UNIVERSITY OF CALIFORNIA,
IRVINE

Numerical Study of Non-Premixed Methane/Air Flames Behavior under Different Body Forces: Buoyancy and Electric Field

DISSERTATION

submitted in partial satisfaction of the requirements
for the degree of

DOCTOR OF PHILOSOPHY

in Civil and Environmental Engineering

by

Claudia-Francisca López-Cámara

Dissertation Committee:
Derek Dunn-Rankin, Chair
Jacob Brouwer
Vince McDonell

2020

DEDICATION

Para mi abuelo, Valeriano Cámara Fernández.
To my grandfather, Valeriano Cámara Fernández.

TABLE OF CONTENTS

LIST OF FIGURES

LIST OF TABLES

ACKNOWLEDGMENTS

First of all, I would like to thank my family, who has been always supporting me. A mi madre y a mi padre, gracias por darlo todo por mi y por mi hermana, por quererme y por enseñarme que con salud, esfuerzo y trabajo puedo llegar a dónde me proponga. A mi hermana, porque cada día me hace sentir más orgullosa de ella y me hace superarme a mi también. A mis abuelos, por enseñarme a querer, a ser fuerte y a ver que las oportunidades hay que ir a buscarlas. Y a mis tios, primos y familia por estar siempre también. Muchas gracias. Evidentment, també vull donar les gràcies al Diego per recolzar-me sempre, sobretot per aquests darrers mesos de tancament a casa escrivint la tesi.

I would like to thank Prof. Dunn-Rankin for the opportunity to carry my research with his advisory during these years. Also, thank to all the professors that have officially formed part of my Dissertation and Ph.D. Defense, Qualifying, and Preliminary Exams committees. For challenging me and helping me to grow as a scientist on the way, I would like to thank Prof. Brouwer, Prof. McDonell, Prof. Abdolhosseini Qomi, Prof. Elghobashi, Prof. Davis, and Prof. Sanders.

Related to the collaborations in this dissertation, I would like to thank Prof. Hong G. Im and his research group at King Abdullah Univeristy of Science and Technology (KAUST) for our collaboration and the use of their computational resources, as well as for inviting and hosting me for a month visit. Moreover, I would like to thank the invaluable help and discussions with Dr. Memdouh Belhi and most recently, the email responses from the graduate student Xiao Shao. During my month-long visit in KAUST I felt like home, so I would like to thank everyone that made that possible, specially to Francisco, Dimitris, Manuel, Cecilia, Davide, Sangeeth, and all the Spaniard group at KAUST.

Also related to the collaborations in this work, I would like to thank Dr. Pitz and his research group – Chiara Saggese, Scott Wagon, and Goutham Kukkadap – at the Lawrence Livermore National Laboratory for our collaboration and for hosting me during six months, and to Lori Greco for all the administrative help. In this case, I would also like to thank the people that made me feel as home while I was there, specially to all Dr. Pitz's research group, Irene, Liza, Matteo C., Mikel, Matteo F., Dean, Victor, Kristen, Tope, Aric, and Tuan.

I would also like to express my gratitude to Prof. William A. Sirignano and Dr. Albert Jordà Juanós from UC Irvine for our collaborative work. Although not featured in this dissertation, our discussions and co-authored work expanded my understanding on other combustion phenomena different than my dissertation topic.

I would also like to thank all the people I have met during different conferences and CEFRC Princeton Combustion Summer Schools, for all the classes, discussions, and friendships. Especially, thanks to the UC Berkeley peers - Prof. Carlos Fernandez-Pello, Maria, Sarah, Charles, Xian, Daniel, and James.

Next, I would like to thank some current and former colleagues from the Lasers, Flames, and Aerosols Laboratory at UC Irvine that have also become friends. For the support during these

years, thank you Rosa Padilla, Michela Vicariotto, Andrea Biasioli, Marco Minniti, and Dorsa Shirazi.

On other side of the world, I would like to thank my friends David Coronado and Kaixi Ye, for keeping our friendship alive through all these years and miles apart. Also to Paula Ferrando, for being an amazing friend since day one at the English Corner. To Orla, Wayne, Max, April, and Holly Baylis, for being my Irish family and helping me during my first experience living in an English-speaking country.

In this side of the world, I would like to further thank Ashley Slack and Melissa Beade and her family, for being great and making me feel at home in California. To my Catalan friends in America, especially to the Friendmily, Anna Papió, Albert Jordà, and Andrés Adam Alberdi. To my international friends in California, especially to Luca Mastropasqua and Chiara Saggese, and all the Italian crew. To the LDOS (Loh Down on Science) Hive, who have kept me sane and cheerful during the quarantine. To the Paradise Perks folks, friends who always cheered me up with their amazing music and wordsmith. Thank you everyone for all our videocalls, talks, and pre-COVID gatherings.

Finally, I would like to thank all the parts that economically contributed to fund me and my research. This work was supported by various grants throughout the years. I would like express my gratitude to the Balsells-Generalitat de Catalunya Fellowship, specially to Pete Balsells and Roger Rangel. The Balsells fellowship granted me the opportunity to come to UCIrvine in the first place, and later, it contributed to stay for my doctorate studies. I would also like to thank the Mechanical and Aerospace Department at UCIrvine, for the learning opportunity working as a teacher assistant during ten quarters, and for the MAE Department Graduate Fellowship during my first year as a Ph.D. student. I want to acknowledge the ACME project from NASA, for their support by NASA's ISS Research (NNX07AB55A) with Dennis Stocker as contact monitor. My appreciation to the National Science Foundation - INTERN program for their funding support that allowed me to conduct part of this work at the Lawrence Livermore National Laboratory. I would like to highly thank the King Abdullah University of Science and Technology (KAUST), particularly the KAUST Supercomputing Laboratory for the use of their computational resources. Lastly, I appreciate the funding received during different periods of my doctorate as Graduate Student Researcher and the CEE Summer Graduate Research Fellowship.

VITA

Claudia-Francisca López-Cámara

EDUCATION

Ph.D. Civil and Environmental Engineering *Dec. 2020*
University of California at Irvine, CA, USA (ACME Project - NASA)
Dissertation: Numerical Simulation of Non-Premixed Flame Behavior
with Electric Fields and Buoyancy.

M.Sc. Nanoscience, Materials and Processes: *Sept. 2015*
Chemical Technology at the Frontier
ETSEQ, University Rovira i Virgili, Tarragona, Spain

M.S. Chemical Engineering *Jul. 2014*
ETSEQ, University Rovira i Virgili, Tarragona, Spain

B.E. Chemical Engineering *Jul. 2014*
ETSEQ, University Rovira i Virgili, Tarragona, Spain

RESEARCH EXPERIENCE

Visiting Ph.D. Student *Jul. 2019 - Dec. 2019*
Lawrence Livermore National Laboratory, CA, USA
Academic Cooperation Program participant at Dr. Pitz research group.
Research performed: Development of reduced combustion kinetic models

Visiting Ph.D. Student *Nov. 2017 - Dec. 2017*
King Abdullah University of Science and Technology, KSA
Collaboration project with Prof. Hong G Im research group.
Research performed: 2D simulations of CH_4/air flames with electric field

Research Scholar - ACME project (NASA) *Feb. 2015 - Aug. 2015*
University of California at Irvine, CA, USA
Master thesis in numerical simulations of a co-flow CH_4/air flame.

Research Scholar *Jan. 2014 - Jul. 2015*
University of California at Irvine, CA, USA
Undergraduate thesis in numerical simulations of a rotational microfluidic channel.

Undergraduate Researcher *Oct. 2013 - Dec. 2013*
University Rovira i Virgili, Tarragona, Spain
Membrane and Process Engineering Technology Centre (METEOR).
Research performed: Production, optimization, and characterization (using SEM/ESEM) of maltodextrin microcapsules employing spray-dryer encapsulation technology.

PUBLICATIONS

REFEREED JOURNAL PAPERS

López Cámara, C.-F., Jordà Juanós, A., Sirignano, W. A. *Normal Strain Rate and Pressure Effects using Detailed and Global Chemistry Models in a CH_4-Air Counterflow Flame*. Combustion and Flame. Volume 221, Nov. 2020, Pages 256-269.

CONFERENCE PAPERS

López Cámara, C.-F., Jordà Juanós, A., Sirignano, W. A. *Normal Strain Rate and Pressure Effects using Detailed and Global Chemistry Models in a CH_4-Air Counterflow Flame* (paper and oral presentation). Paper ID: 912-0023. Western States Section of The Combustion Institute, Alburquerque, NM. Oct.14-15 2019.

López Cámara, C.-F., Belhi, M., Im, H.G., and Dunn-Rankin, D. *Numerical Simulations of Laminar Nonpremixed CH_4-Air Jet Flames Influenced by Varying Electric Fields* (paper and oral presentation). Paper ID: 71LF-0309. 11th US National Meeting of The Combustion Institute, Pasadena, CA. Mar.24-Mar.27 2019.

López Cámara, C.-F., Dunn-Rankin, D. *Numerical Simulations of a Co-Flow Methane/Air Flame including Ions and Excited Species under Different Gravity Conditions* (paper and oral presentation). Paper ID: 29LF-0053. Western States Section of The Combustion Institute, Laramie, WY. Oct.2-3 2017.

López Cámara, C.-F., Eplenier, G., Tinajero, J., and Dunn-Rankin, D. *Numerical Simulation of Methane/Air Flames Including Ions and Excited Species* (paper and oral presentation). Paper ID: 134CK-0055. Western States Section of The Combustion Institute Fall Meeting, Brigham Young University, Provo, UT, October 5-6.

PRESENTATIONS (selection)

ORAL PRESENTATIONS

López Cámara, C.-F., Saggese, C., Pitz, W., Dunn-Rankin, D. *Comprehensive Chemical Kinetic Mechanism for Simple Hydrocarbon Fuels including Excited and Charged Species.* 35th ASGSR Annual Meeting, Denver, CO. Nov.20-Nov.23 2019

López Cámara, C.-F., Belhi, M., Im, H.G., Dunn-Rankin, D. *Numerical simulations of laminar nonpremixed CH_4-Air flames varying buoyancy and applied e-field.* 34th ASGSR Annual Meeting, Bethesda, MD. Oct.30-Nov.4 2018

McBride, S., Munoz Abujder, R.R.R., Putman, E., Bhaskar, R., **López Cámara, C.-F.**, Helmig, J. *A Space Science Curriculum to Initiate Student Interest in STEM.* 34th ASGSR Annual Meeting, Bethesda, MD. Oct.30-Nov.4 2018

López Cámara, C.-F., Tinajero, J., Dunn-Rankin, D. *Numerical Simulations of a Co-Flow Methane/Air Flame under Different Gravity Conditions*. 33th ASGSR Annual Meeting, Lake Washington, WA. Oct.25-29 2017. Rankin, D. *Numerical Simulation of Flames Under the Influence of Electric Field*. 32nd ASGSR, Cleveland, OH, Oct. 26-29 2016.

López Cámara, C.-F., Tinajero, J., Dunn-Rankin, D. *Numerical Simulation of a Co-Flow Methane/Air Flame with an Applied Electrical Field* (oral and poster presentations). 31st ASGSR Annual Meeting, Alexandria, VA, USA, Nov. 11 - 14th 2015.

POSTER PRESENTATIONS

López Cámara, C.-F., Belhi, M., Im, H.G., Dunn-Rankin, D. *Numerical Simulations of CH_4-Air Flames Under the Influence of Buoyancy and Electric Fields.* 37th International Symposium of the Combustion Institute, Dublin, Ireland. Jul.29-Aug.3 2018. Research and Development Conference, San Francisco, Jul. 23-26 2018

López Cámara, C.-F., Dunn-Rankin, D. *Simulation of Combustion Processes with Applied Electric Field in Microgravity.* Princeton CEFRC Combustion Summer School, Princeton, NJ, USA. Jun.24-30 2017

López Cámara, C.-F., Tinajero, J., Dunn-Rankin, D. *Simulation of Combustion Processes with Applied Electric Field in Microgravity.* KAUST Research Conference in New Combustion Concepts (KRCNCC). King Abdullah University of Science and Technology, KSA. Mar.6-8 2017

INVITED TALKS

López-Cámara, C.-F. *May the eForce be with you.* Brews and Brains (TEDtalk style, online), Irvine, CA. Nov. 2 2020.

López-Cámara, C.-F. *Numerical Simulations of Non-Premixed Flame Behavior with Variable Body Forces: Electric Field and Buoyancy.* Seminar at Escola Puigcerver, Reus, Spain. May 2 2019.

López-Cámara, C.-F. *Numerical Simulations of Non-Premixed Laminar Flame Behavior with Electric Fields and Buoyancy.* Seminar at University of Rovira i Virgili, Tarragona, Spain. May 11 2018.

INVITED COLLOQUIA

Colloquia title: *Doing our homework with internet.* Representative of students at the Tarragona Province (Tarragona, Spain. May 20 2009).

COLLABORATIVE ACTIVITY

Lawrence Livermore National Laboratory, California *Ongoing*
Dr. Chiara Saggesse and Dr. William Pitz
Project topic: Reduction of combustion kinetic models including excited and charged species.

King Abdullah University of Science and Technology, Saudi Arabia *Ongoing*
Dr. Memdouh Belhi and Dr. Hong G. Im
Project topic: Numerical study of a CH_4/air laminar diffusion flames with an applied electric field.

TEACHING AND PEDAGOGICAL EXPERIENCE (selection)

Teaching Assistant
University of California at Irvine, CA, USA *Jan. 2017 - Dec. 2020*
MAE 10 Introduction to Engineering Computations - Spring 2017 and 2018.
MAE 189 Senior Project Design - Fall, Winter and Spring 2019, and Spring (online).
MAE 151 Mechanical Engineering Design - Fall 2020 (online), and Winter 2017, 2018, and 2020.
Tasks developed: create syllabus, evaluate pedagogical outcomes, provide feedback to senior projects and to individuals, provide team guidance, hold office hours, create rubrics, grading.

Teens Lab Project Monitor
APQUA - BASF, Tarragona, Spain *Nov. 2014 - Dec. 2014*
Teaching high-school students hands-on activities to characterize chemical and biochemical substances.

INDUSTRY EXPERIENCE

Chemical Engineer Intern *Jul. 2012 - Aug. 2012*
BASF, Tarragona, Spain
Internship as a chemical engineer at the Propane Dehydrogenation plant.
Mass transfer study and optimization and re-design of catalyst regeneration module.

AWARDS AND SCHOLARSHIPS

National Science Foundation Fellowship (INTERN)	*Jul. 2019*
CEE Summer Graduate Research Fellowship 2018	*Jun. 2018*
Clean Combustion Research Center KAUST Fellowship-New Combustion Concepts	*Mar. 2017*
Balsells Fellowship-Generalitat de Catalunya-Spring Quarter	*Mar. 2016*
Department of Mechanical and Aerospace Engineering Fellowship	*Sept. 2015*
Master of Excellence Grant. Catalunya-La Pedrera Foundation	*Sept. 2014*
Undergraduate Mobility-Balsells Fellowship	*Feb. 2014*

PROFESSIONAL DEVELOPMENT AND CERTIFICATES

Certificate in Management Beyond the Classroom	*Nov. 2020*
Certificate in Faculty Careers	*Aug. 2020*
Certificate in Communication Skills for Academics	*Mar. 2020*
Certificate in Teaching Excellence Program (CTEP)	*Feb. 2020*
CIRTL Associate Level	*Mar. 2019*
Mentor Excellence Program	*Jan. 2018*
Course Design Certification Program	*Jul. 2017*
Princeton CEFRC Combustion Summer School, Princeton University, NJ	*Jun. 2017, 2016, 2015*
Excellence in Engineering Comunications	*May 2016*
Monitor Leader - Generalitat de Catalunya	*Sept. 2011*

PROFESSIONAL ASSOCIATION

Membership: The Combustion Institute; The American Society of Gravity and Space Research (ASGSR).

SERVICE

Diversity Engagement: Diverse Educational Community and Doctoral Experience (DECADE - STEM branch, Sept.2015 - Sept.2019) at UCIrvine; Peer mentor at UCIrvine Graduate Intercon-

nect Program (2018); Graduate Program Ambassador for the Civil and Environmental Engineering Department at UCIrvine (2018); Internationalize your education Certificate by Universitat Rovira i Virgili (Mar.-Apr. 2013); International Mentor for new international students at University Rovira i Virgili (2012-2013); Individualized Reading Mentor under the LECXIT program to help primary school students improve their reading skills (Reus, Spain, Apr.2011- Jun. 2011).

Science Communication: Social Media Manager editor at The Loh Down on Science (Nov.2020-Apr.2021); Manager editor at The Loh Down on Science Special Pandemic Edition in Spanish (Apr.- Nov.2020); Trainer at the Science Communication Skills for STEM Scientists Certificate (Sept. 2020); Writer at The Loh Down on Science (Apr.- Sept.2020); Social Media Chair of the Student Chapter at the ASGSR (Nov.2015 - Nov.2018).

Leadership and Coaching: Team leader of a 7 people team to perform a chemical engineering project during the annual course 2013-2014 (University Rovira i Virgili). Project Title: Design of a Vinyl Acetate Monomer Plant (ETSEQ, URV); Coaching Certificate (Tarragona, Spain, 2014); Coaching certificate (Oct.2014, Nov. 2014).

SKILLS

Software: MATLAB, OpenFOAM (C++), ParaView, Tecplot, Chemkin-Pro and Reaction Workbench, Aspen-Hysys, PeleLM, ECDL certificate, LaTeX.

Parallel computing: Experienced using PBS amd Slurm interfaces for high parallel computer simulations (user level).

Languages: Spanish and Catalan (bilingual); English (fluent); Italian (beginner).

Music Studies: Conservatory of Music in Vila-Seca (Spain; Sept.1999 - Jun.2011). Specialty: Piano.

ABSTRACT OF THE DISSERTATION

Numerical Study of Non-Premixed Methane/Air Flames Behavior
under Different Body Forces: Buoyancy and Electric Field

By

Claudia-Francisca López-Cámara

Doctor of Philosophy in Civil and Environmental Engineering

University of California, Irvine, 2020

Derek Dunn-Rankin, Chair

Active control of combustion has always been important given the potential practical applications to improve efficiency and stability, and to reduce unwanted emissions. Body force effects, such as applied electric fields and buoyancy, have been objects of attention given their capability to change small flame behavior. However, distinguishing between different body force effects and then controlling those body forces to affect combustion performance in predictable ways is a challenge that has not yet been solved. In addition to the inherent difficulties defining the flame chemistry in thermally driven buoyant flows, there is the further complication of capturing the relationship between flame charged species chemistry and the ultimate physical influences produced by electromagnetic forces on them.

This work presents the development of numerical simulation tools to provide more insights into the coupling between flame behavior, flame chemistry, and different body force effects. Both buoyancy and electric field effects are explored. Also, the comparison of the resultant flame behavior when these body forces are applied to the flame is analyzed to provide possible equivalences in body force control, as well as to examine what might occur during combustion in alternative gravitational environments.

There are four major parts in this work. The first one relates to the chemical kinetic model for the flame chemistry with charged and excited species; the second looks into the effects that two different jet burner geometries have on a flame that is exposed to different gravity environments; the third section explores the implementation of applied electric fields in the simulations and how this affects a non-premixed flame at 1g; and the last section carries out a comparison between the effects on flame behavior when body forces of different nature, buoyancy and electric field force, are present. This last section also provides insight into the possible similarities and regimes when both forces could be equivalent.

This work starts with the development of a comprehensive chemical kinetic model including excited and charged species. Excited species are rarely included in combustion chemical kinetic models due to their low concentrations and low impact on major chemical pathways in the flame, yet they are crucial for the visual characterization of the flame. Chemiluminescent species CH^* and OH^* are added to the model since they are well-known markers for flame location and heat release. Additionally, naturally produced charged species in the flame are also included in the chemical kinetic model developed in this work since they will be interacting with the electric field when this is applied to the flame. Considered as the first reaction that naturally produces charged species in the flame, the chemi-ionization reaction – as well as the subsequent reactions for charged species – is also included in the chemistry model. Then, the model is validated against detailed chemistry and experimental literature results employing one- and two-dimensional burner geometries. The final reduced model, named Model 1, contains a total of 45 species and 216 reactions.

The second part of this work reproduces how buoyancy forces affect the flame. For that purpose, simulations under gravities that vary from 0g to 2g are performed employing two-dimensional CFD calculations. The results are then contrasted with previous experimental and numerical literature. A comparison between both different gravities and different burners is performed, as well as a non-dimensional analysis of the behavior of the flame.

Next, an implementation of the electric field solver to the 1g two-dimensional flame geometry is explored. The results are compared with experimental literature, showing similarities for the major characteristics, such as for the I-V curves and the downstream ion current spatial distribution. However, a detailed investigation of the electric field characteristics reveals that a non-physical behavior is obtained for the physical distribution of the charged species when employing the solving method proposed for the subsaturation regime, which is also discussed.

Finally, an analogy between body forces and the possible similarities among them is analyzed. This comparison corroborates previous literature mentioning that, even though electric and buoyancy forces are from a different nature, they might be considered equivalent when applying an electric field in a 1g flame to achieve an equivalent supergravity flame. It is concluded that the 2g flame resembles the 1g flame with 0.5kV/cm applied. However, a large regime of supergravity conditions where both forces are equivalent is yet to be explored.

Chapter 1

Introduction

1.1 Background and motivation

Active control of combustion has always been important given the potential practical applications, such as flame synthesis [1], instability control [2], combustion enhancement [3], reduction of exhaust emissions [4], and to avoid unstable or increment stabilities [5].

Body force effects, such as applied electric field and buoyancy, have been objects of attention given their capability to change small flame behavior [6, 7, 8]. The concern of how body forces, particularly electric field force, affect flames was already reported by the combustion community more than half century ago [9, 10, 11, 12, 13, 14]. However, it was unclear how that interaction was occurring. It was not until 1948 that Calcote showed that external electric fields can change hydrocarbon flame behavior by interacting with the naturally produced charged species in the flame's reaction zone [15]. Literally from his paper:

"(...) It is concluded that the observed effect of an electric field on a n-butane-air flame can be almost completely explained by a mechanical interpretation. The high concentration of ions in

the inner cone, adduced from these experiments, is evidence for chemi-ionization and the non-equilibrium conditions existing in the flame front."

The mechanical interpretation that Calcote was referring to was previously reported in 1899 by Chattock [16] and has been given various names such as *ion-driven wind* [17], *ionic wind* [18, 19, 20], *Chattock wind* [20, 21], *electric wind* [16], and *ion drift wind* [22]. In this work, the preferred terminology used is *ion-driven wind* or *ion wind*, which was coined by Weinberg [6], it is extensively used, and more accurately describes the mechanical process produced as a result of a movement of charged species. The ion-wind phenomenon is the generation of a body force that occurs when the naturally produced charged species (ions and electrons) in the flame are accelerated in response to a Lorentz force from the external electromagnetic field. These accelerated species collide with surrounding neutral species, producing a net acceleration in the bulk gas - i.e., the ion wind. Due to the ion wind, the flow behavior is changed; thus, flame performance is altered. Calcote reported the modified flame behavior in his experiments as a deflection of flame shape [15]. He also stated that the primary ion produced in the flame is HCO^+, which quickly reacts to produce H_3O^+. Still, although it is clear that applying a body force – such as an electric field – changes the flame chemistry, it should be considered that the change in flame chemistry also modifies how the flame interacts and how it is affected by the body force, with all these phenomena happening simultaneously. Intriguingly, that interaction between flame chemistry and body forces is still not well understood. Developing tools capable of providing more insights on the coupling between these elements would be highly valuable given the potential for combustion control in practical devices that these body forces have.

Also related to the body forces acting in the flame, the community has always been attracted by the potential for direct electrical control of combustion in practical devices driven by the ion-wind phenomenon [6, 23]. Even though the chemical and physical mechanisms are not fully understood yet, the spectrum of applications that researchers have identified on a laboratory-scale that could benefit from this control includes the stabilization in laminar and turbulent burners [18, 24, 25, 26], the

reattachment and propagation speed of non-premixed laminar jet flames [27, 28], managing heat flux and CO emissions from flames [29], and carbon deposition and reduction of soot formation [6, 30, 31, 32]. Despite the interesting behaviors mentioned, researchers have convincingly shown during the last decades that using naturally produced chemi-ions in hydrocarbon flames as a mechanical actuator is relatively weak in comparison to the enormous thermochemical energy release of the combustion process [29, 33, 34]. Hence, these effects will scale poorly with size. Thus, applying electric field control to industrial-scale flames is challenging, and it should be considered to be employed to modify the behavior of a pilot or nascent flame that later is responsible for the larger heat release in the system. This means that practical and industrial applications of electrical properties of flames cannot use direct forcing but must instead employ subtle levels of sensing and control in critical conditions.

Furthermore, the documented changes that the flame behavior undergoes under different buoyancy forces also showed that these environments are appealing for further investigation and preparation for future space explorations. Therefore, with the aim to understand how the buoyancy force changes the flame, several studies were carried out by previous authors. These studies showed that diffusion flames change their size (width and length), luminosity, extinction conditions, and lift depending on the gravitational body force conditions [7, 8, 35, 36, 37, 38, 39]. Based on that, previous literature has hypothesized the possibility of obtaining similar flame behavior outcomes by tuning both electric and gravitational body forces [33, 34, 40]. Regrettably, the coupling between body forces on Earth makes it difficult to distinguish the contributions from each of them to the flame behavior and the flame chemistry changes when employing experiments at 1g.

Efforts on studying and comparing both body forces effects started in 1987 when Carleton and Weinberg conducted experimental simulations [1] showing for the first time that flame shape changes when an electric field is applied in microgravity and 2g [20]. However, they used a transverse

[1] *Experimental simulations* is a wording used to describe experimental work that employs a particular configuration in order to resemble and achieve similar environmental conditions. E.g., Conducting an experiment on Earth employing the centrifuge force with the expectation to achieve similar results than as running the experiment at low gravity or microgravity in the space.

electric field, so the coupling of effects related to both body forces and how they change the flame chemistry made it challenging distinguish each body force's contribution to the flame behavior. Once a body force alters the flame, it changes its chemistry, which changes the flame response to the body force. Hence, there is the need to understand the contributions of different nature body forces to the behavior of the flame as well as the role that flame chemistry plays, and how body forces and chemistry interact with each other. Also, a comparison between how different body forces impact the flame would bring a better understanding on their individual contribution to the flame changes.

1.2 Goal

The ultimate goal of this work is to develop a numerical simulation tool to understand the role of flame chemistry and the differences and similarities between body forces – density-driven body force and electric body force – affecting the flame behavior. Moreover, this tool aims to provide more insights into the coupling between chemistry and body forces.

1.3 Approach and outline

Figure 1.1 shows the outline followed in this work, based on the meaningful physical parts that the simulation tool considers.

The two primary components of this work are (i) the chemical kinetic model used accounting for the reactions that include important minor species and their corresponding transport and thermodynamic parameters (Chapter 3), and (ii) the effect of the body forces on the flame behavior and their comparison (Chapters 4, 5 and 6). Chapters 7 and 8 summarize the conclusions of this work

and future challenges, respectively. Moreover, it is also necessary to consider the description of the burner geometries studied and how that translates into the simulation (Chapter 2).

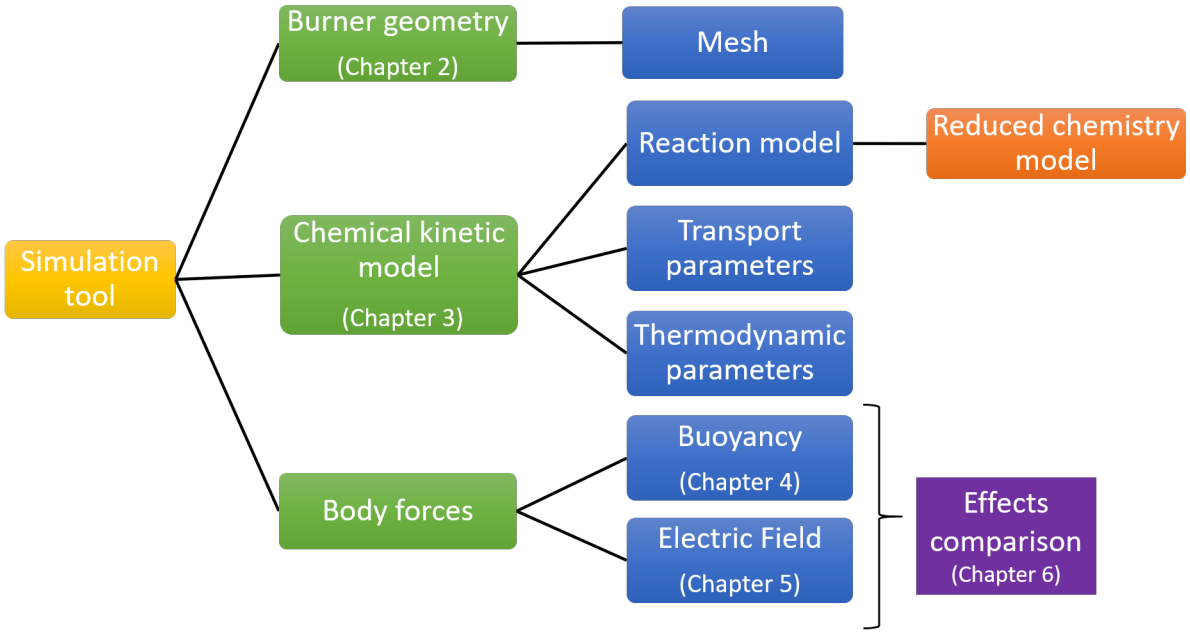

Figure 1.1: Dissertation outline.

Note that by the recommendation in the home page of the FCCM chemical kinetic model [41], the wording *reaction model*, *chemical kinetic model*, and *chemical model* will be preferably used rather than *reaction mechanism*, *chemical kinetic mechanism*, or *chemical mechanism* in this document. The latter have been used traditionally in the reaction chemistry community to describe a model that mimics a certain phenomenon governed by the mechanism of reactions.

Chapter 2

Burner Geometries

Different burner configurations are used in this work, which can be classified as zero-, one- and two-dimensional geometries. This chapter provides an explanation for each of them, stressing the details in software and boundary conditions. The purpose of employing the zero-dimensional simulation is to reduce and validate the chemical kinetic model developed in this work and explained in Chapter 3. The one-dimensional geometry is also used for the validation of the chemical kinetic model explained in Chapter 3. Lastly, two two-dimensional burner geometries are employed for the validation of the chemical kinetic model (Chapter 3) and for predicting the methane-air flame behavior under the influence of different body forces (Chapters 4 and 5).

2.1 Zero-dimensional simulation: PSR

The Perfectly Stirred Reactor (PSR) is the zero-dimensional reactor employed in this work, which is simulated by the PSR module from the Chemkin-Pro® [42] software. Using a zero-dimensional simulation allows achieving faster results than with higher-order dimensions without adding the complication of species transport.

2.1.1 Boundary conditions

The boundary conditions imposed for the PSR simulations are stated in Table 2.1. The choice of these conditions is mostly based on the experimental data from the literature [17, 33, 43, 44, 45, 46] that will be employed for the validation of the model when using higher-dimensional analysis. That is at different temperature regimes typical for a jet flame, in ambient pressure conditions, and in stoichiometric equivalence ratio. The residence and end time are chosen based on the flame stabilization time reported in experimental work for non-premixed laminar diffusion flames [40]; the volume is left as the default value from the Chemkin-Pro®, ensuring a size compromise between lower simulation time and domain being big enough to let complete combustion to occur – which can be secured by checking the simulated profiles obtained for major reactant and product species, as well as heat release and temperature profiles in the domain.

Table 2.1: Boundary conditions for the PSR simulation.

Variables	Value
End time (t_{end})	2s
Residence time (τ)	1s
Volume (V)	8cm^3
Temperature PSR (T_{PSR})	1500K, 2000K, 2500K
Pressure PSR (P_{PSR})	1atm
Pressure inlet stream (P_{in})	1atm
Species mole fraction (inlet stream and PSR)	CH_4 = 0.5; N_2: 0.3835; O_2: 0.1165

2.2 One-dimensional geometry: Counterflow burner

This configuration relates to the counterflow burner geometry. In this case, the Chemkin-Pro® software is used, and the module selected is the opposed-flow flame module (OPPDIF). The counterflow geometry requires the two input files that the PSR simulations need – chemical kinetic model and thermodynamic properties– plus a third file containing the transport properties of the reactants. Therefore, this one-dimensional geometry adds one more factor of complexity to the

simulation, and therefore, it is employed as a tool to ensure that the transport of species is reasonable and derives to simulation results that capture the flame behavior expected from the literature [47, 48].

2.2.1 Boundary conditions

The boundary conditions using this geometry are shown in Table 2.2 and are applicable for all the validation steps explained in Chapter 3. The distance between the two nozzles x is set at 1.27cm, which is chosen based on the literature [49] to prevent flame proximity to the boundaries from affecting too heavily the solution – i.e., zero gradients are desired at boundaries on species mass fraction and temperature curves – while reducing the computational cost.

Two parameters control the adaptive grid refinement in Chemkin-Pro® based on the solution curvature and gradient. The are set to 0.1 and 0.5, respectively. Another two parameters control the solution convergence. They are the absolute and relative tolerances, which are set to 10^{-9} and 10^{-4}, respectively. These parameters have been shown to be sufficient in the author's previous work for counterflow flames in order to obtain converged results within a relative short simulation time [50].

Table 2.2: Boundary Conditions used for Chemkin® simulations.

	Variable	**Value**
Problem	Maximum temperature	3000 K
	Environment temperature	298 K
	Pressure	1 atm
Left nozzle	Inlet velocity	0.12 m/s
	Inlet temperature	298 K
	Species mole fraction	CH_4: 1
Right nozzle	Inlet velocity	0.12 m/s
	Inlet temperature	298 K
	Species mole fraction	N_2: 0.767; O_2: 0.233

2.3 Two-dimensional geometry: Jet burner

Two two-dimensional geometries are employed in this work, which correspond to axysimmetric-jet-burner configurations with different burner heights (see Figure 2.1). The simulation software employed in this case is the OpenFOAM® open-source program [51, 52].

On Figures 2.1(a) and 2.1(b), the configuration is a jet flame with a zero coflow velocity, where the fuel inlet tube is extruded from the nozzle. The second geometry, Figures 2.1(c) and 2.1(d), represent a classical simple jet flame configuration without a coflow mesh platform surrounding the jet. These geometries are designed based on the burner used on the International Space Station (ISS), as part of the Advanced Combustion via Microgravity Experiments (ACME) project [53, 54]. For clarity, the terms *extruded geometry* and *jet geometry* will be used to distinguish the results of the first and second configurations, respectively.

Jet-type burners are axially symmetric 2D burners and have been well-studied in the literature [55, 56, 57, 58] and can retain their symmetry even when ion driven winds are present. Although these similarities between both burner geometries studied, it is important to consider that the difference in burner tube height has previously shown to be crucial on the electric field response of the flame [40]. It is essential to identify that the jet geometry is a simpler case of point to plane electrodes that form an electric field that converges to the thin burner tube. Therefore, the strongest local electric field is expected to be along the centerline – since it is where the shortest field line locates. However, the extruded burner represents a more challenging geometry since it lies between the jet characteristics for the electric field and the case of two charged plates that, in an ideal case scenario (without flame), would form a uniform field with parallel electric field lines. Thus, the electric field lines using the extruded burner will maintain a quasi-parallel form, but its flame structure will be similar to the jet burner flame.

Both meshes are designed based on the OpenFOAM® manual [59]. A representation of a wedge with a 5° arc from the full axisymmetric burner circle is the standard practice [60, 61, 62, 63, 64]

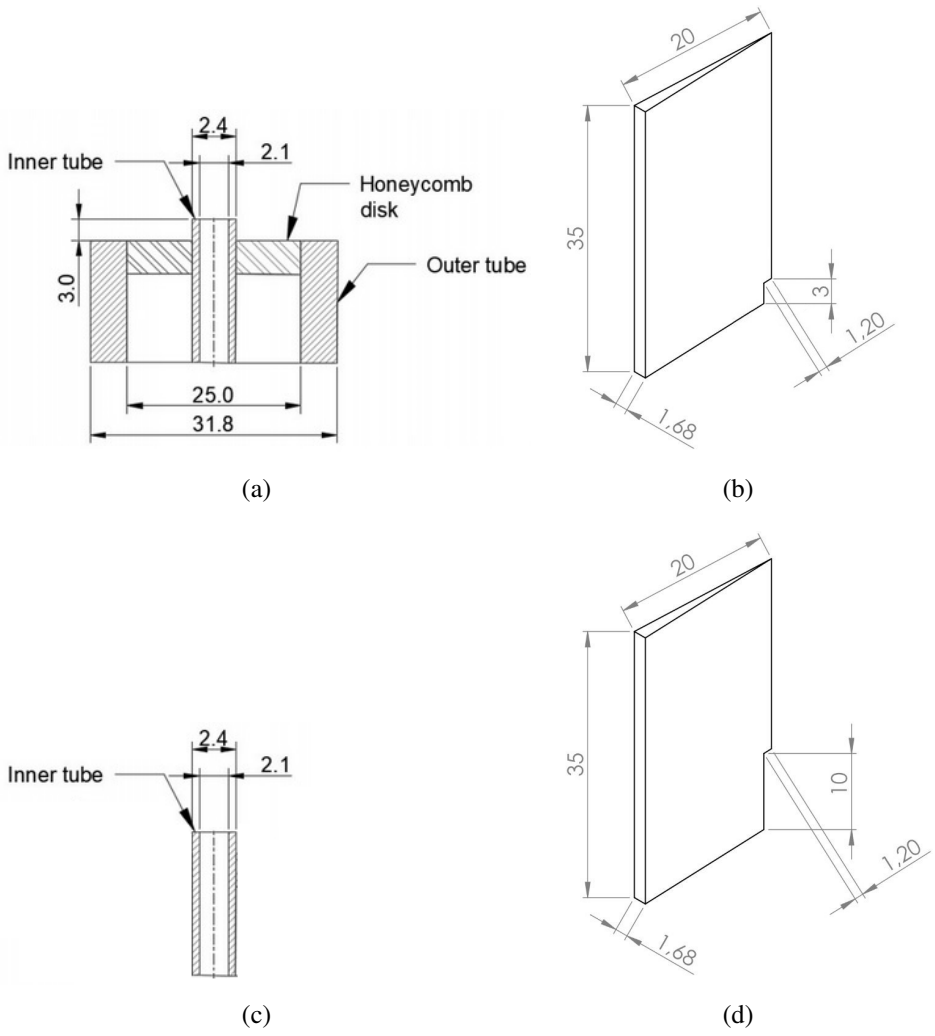

Figure 2.1: Geometries studied and their respective simulated computational domains. (a) Extruded setup, (b) Extruded computational geometry, (c) Jet setup, (d) Jet computational geometry. Dimensions are in millimeters.

for the representation of the entire burner field employing OpenFOAM® (see Figure 2.2). Both meshes have a computational-domain width of 20mm, based on a domain and mesh independence tests that were performed for the extruded geometry and showed that these boundaries and meshing are sufficient to capture the flame behavior without imposing any artificial perturbation (see Figure 2.3 and Appendices A and B). The mesh independency mesh study is completed by performing simulations using smaller and larger hexahedral cells. For the jet geometry configuration, the same spacing as in the extruded geometry mesh was used for all the cells placed above the burner tip

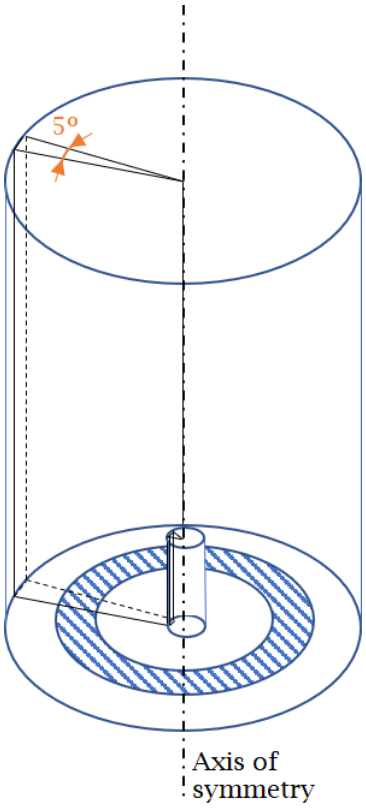

Figure 2.2: Three-dimensional view of the burner geometry and computational domain (not in scale).

(i.e., reaction zone). Therefore, a separate mesh independence test was not carried out for this mesh based on the assumption that reaction zones for jet and burner flames would be similar and that the mesh zone with higher gradients had already been tested for mesh independence.

The final extruded and jet meshes used are formed by 144230 polyhedral blocks – also called cells, which are mostly hexahedral except at the boundaries – created from 289647 points. The mesh details are found in Table 2.3. In both cases, the block distribution is fine in the flame reaction zone and at the burner's tip, and the cells are set to be larger as they are placed further from the reaction zone.

The studied cases with an applied electric field require two electrodes positioned in such a way that the electric field acts axially, that is, aligned with the direction of the bulk downstream flow. Therefore, in these simulations, the burner acts as one of the electrodes and a metallic honeycomb

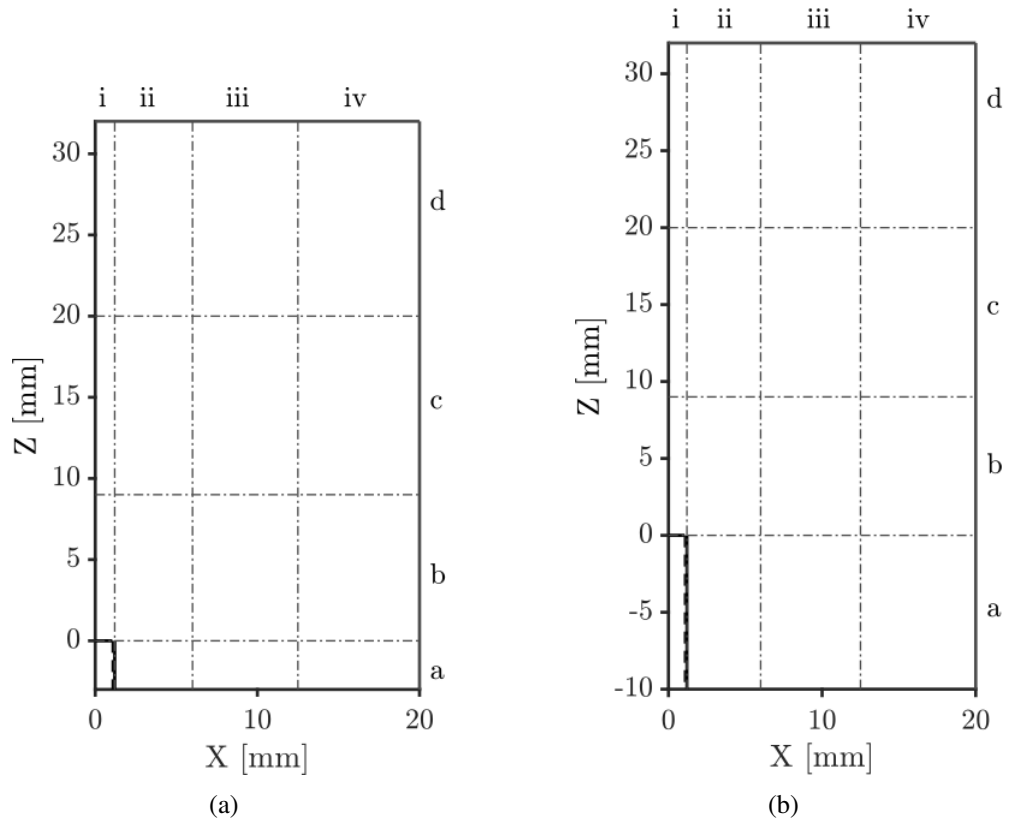

Figure 2.3: OpenFOAM® mesh details. (a) Extruded and (b) Jet geometries.

mesh (not pictured in Figure 2.1) placed horizontally and parallel to the burner at a considerable high, acts as the second electrode. The height of the computational domain is determined based on the placement of the honeycomb mesh electrode, being positioned 32mm downstream of the burner tip in both cases. This distance is selected with the knowledge of the experimental configurations and results that the simulations will eventually be compared with [40, 43, 44].

2.3.1 Boundary conditions

The dynamic and mixture conditions are the same for both jet geometries so that the buoyancy and electric field effects for the two burner configurations can be compared effectively. The boundary

Table 2.3: Mesh grid details

Region	ΔX [mm]	ΔZ [mm]	X range [mm]	Z range [mm]
i	0.033	-	0.00 - 1.20	-
ii	0.033	-	1.20 - 6.00	-
iii	0.083	-	6.00 - 12.5	-
iv	0.150	-	12.5 - 20.0	-
a (extruded)	-	0.033	-	-3.00 - 0.00
a (jet)	-	0.033	-	-10.00 - 0.00
b	-	0.033	-	0.00 - 9.00
c	-	0.150	-	9.00 - 20.0
d	-	0.300	-	20.0 - 32.0

conditions for the different problem's variables are pictured in Figure 2.4 and summarized in Table 2.4.

Notice that in Table 2.4, the conditions referred to electric field (V = ΔV_0 and $\Delta V_0 < 0$, where V represents the voltage) pertain only to the applied electric field cases. Otherwise, the voltage in these boundaries is equal to zero. For the boundaries that $\Delta V_0 < 0$, the electric field is set to be negative – i.e., the voltage at that boundary. Hence, that boundary will act as an anode since the burner, which will act as the second electrode, will be grounded – i.e., more positively charged in comparison, and therefore, acting as a cathode. In these cases, the positively charged particles (which are the majority of charged species in the flame, as seen later in Chapter 3) move rapidly upstream towards the mesh anode while the negatively charged electrons from the anode move downstream towards the burner that acts as the cathode.

Gravity is considered as a negative force in the axial direction. The fuel is considered to enter the domain as a fully-developed flow, with the fully developed parabolic velocity profiles calculated employing the same approach as the literature [40, 65] and considering that the volumetric fuel flow rate (at standard conditions) is equal to 27 mL/min or 20 mL/min (depending on the studied case).

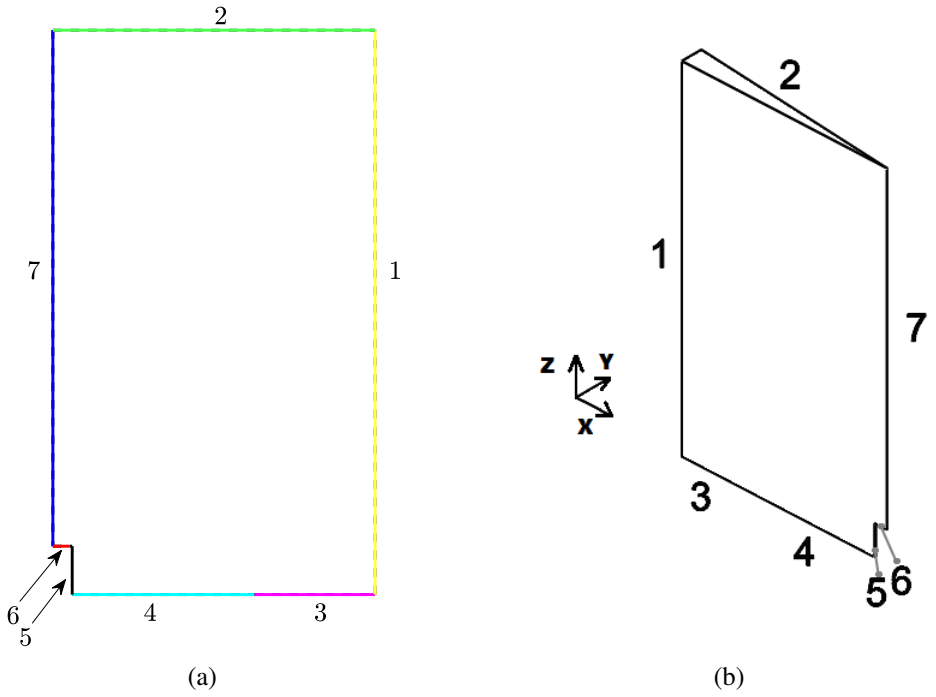

Figure 2.4: Schematic of the computational domain (not in scale). Numbers from 1 to 7 correspond to the boundary conditions shown in Table 2.4. (a) Side view, (b) Three-dimensional view of the domain.

2.3.2 Process to run 2D simulations

For running 2D OpenFOAM® simulations with a large number of species and reactions contained in the chemical kinetic model, it is expeditious to run first the simulation using a smaller chemical kinetic model and, once reached steady-state, change the chemistry to a superior model so that the code can settle more reliably. This is important because it means that some simulation times will not be comparable (e.g., in the mesh independence testing) since each comprehensive simulation departs from a different initial simplified system result. The time step for the iterations can also be tuned manually while the simulation is running in order to obtain faster steady-state results (i.e., when seeing that the simulation results changes by less than a $\approx$10%, the user can increase the time step), which increases the complexity for comparing CPU times. However, this tuning-time-steps approach has not been applied for the cases when a time comparison is shown in this study.

Table 2.4: Boundary conditions corresponding to the computational domain in Figure 2.4. u, v and w are the velocity components in the x, y and x directions. The + and - subscripts denote positively and negatively charged species, respectively.

Boundary	**1**	**2**	**3**	**4**	**5**	**6**	**7**
Description	Normal wall	Mesh (outlet)	Low outer zone	Air coflow	Burner wall	Fuel jet	
Momentum			u = v = w = 0	u = v = w = 0	u = v = w = 0	parabolic profile (u,v,w) [40]	
Energy			T = 300 K	T = 300 K	T = 300 K	T = 300 K	Axial Symmetry
Neutral species				Y_{O_2} = 0.22 Y_{N_2} = 0.78		Y_{CH_4} = 1	
Charged species		$\Delta V < 0$ $Y^- = 0$ $\frac{dY^+}{dr} = 0$		$\Delta V = 0$ $\frac{dY^-}{dx} = 0$ $Y^+ = 0$	$\Delta V = 0$ $\frac{dY^-}{dx} = 0$ $Y^+ = 0$	$\Delta V = 0$ $\frac{dY^-}{dx} = 0$ $Y^+ = 0$	
Poisson		$V = \Delta V_0$			$V = 0$		

All the simulations presented in this work, except for the ones in Chapter 5, require three sequential runs to achieve a steady-state solution employing the final chemical kinetic model of interest. The chemical kinetic model used in the first run is a three-step global chemical kinetic model from the literature [66]. For the second run, the chemistry used is the DRM19 model [67], which is a reduced model from the GRI-Mech 3.0 [68] and only contains neutral species. For the last run, the chemistry used is a detailed chemical kinetic model, which differs depending on the study case. These more detailed models are presented in the next chapters.

Chapter 3

Reduced chemistry reaction model

3.1 Background

During the last sixty years, the combustion community has had a special interest in developing a chemical kinetic model that is able to explain the reaction behavior of hydrocarbon/air flames. Currently, GRI-Mech 3.0 [68] is one of the most accepted models for methane/air flames, and it is widely used in the industry. GRI-Mech 3.0 is based on a survey of the literature and collaborative work that involved advanced experimentation and global constrained optimization. This 325-reactions model is optimized for predicting reactions among neutral non-excited species in natural gas combustion flames. The optimization of the GRI-Mech 3.0 had 77 targets and employed different experimental data such as shock tube ignition delays and laminar flame speeds, as well as thermodynamics sensitivity analysis amongst others (see the complete list in their website [68]). However, previous studies have shown that GRI-Mech 3.0 overestimates the CH radical [69, 70]. This fact has led to inaccurate predictions for CH in excited state (CH^*), which is an important minor specie used as a flame location marker [71]. Other chemical kinetic models have

been proposed throughout the years to predict the flame neutral species reactions. The most used are shown in the Table 3.1.

Table 3.1: Main published chemical kinetic models containing only neutral species. R and S refer to reactions and species, respectively.

Model name	**Year**	#R	#S	**Reference**
GRI-Mech 2.11	unk	277	49	[72]
GRI-Mech 3.0	2000	325	53	[68]
The San Diego Mech.	2018	270	58	[73]

Chemiluminescence is an important feature in flame diagnostics and is produced from the ejection of a photon as one of the pathways of relaxation of excited species to their ground states. It has been shown numerically and experimentally that excited methylidyne (CH^*) and excited hydroxyl (OH^*) in the methane/air flame are spatially coincident with CH in the flame anchoring region [71], showing their highest concentrations in that region [74]. Moreover, CH^* and OH^* concentrations and spatial distributions have been shown to be directly related to the CH and OH concentrations, respectively [71, 75]. The reactions involved in chemiluminescence are not typically included in the reaction models and have not been included in the ones shown in Table 3.1 because of the low concentration of the excited species that makes them not be significant contributors to the major chemical pathways. However, CH^* is the strongest natural chemiluminescent light emitter specie created in hydrocarbon flames [40]. Moreover, since based on Reactions 3.1 and 3.2 from the model proposed by Walsh et al. [71], there is a direct correlation between C_2H and CH^*. Therefore, C_2H is investigated as a possible candidate to capture well the geometry of the flame. Furthermore, recent work has suggested that global chemiluminescence of CH^* emission can be used as a diagnostic tool for total chemi-ion production in the flame [33, 34, 40, 76]. Therefore, for the development of this study, it would be valuable to add to the chemical kinetic model the CH^* production and consumption reactions. The CH^* production is based on Reactions 3.1 and 3.2 and the consumption mostly happens by spontaneous emission (Reaction 3.3, the characteristic blue light of hydrocarbon flames) and collisional quenching. [77, 78].

$$C_2H + O_2 \rightleftharpoons CH^* + CO_2 \tag{3.1}$$

$$C_2H + O \rightleftharpoons CH^* + CO \tag{3.2}$$

$$CH^* \rightarrow CH + h\nu \tag{3.3}$$

Heat release is an important parameter to consider for all combustion systems, and OH^* has been shown to be directly related with it [75, 79, 80, 81] and to CH^* [82]. Hence, OH^* is also included in the chemical kinetic model study. The formation of OH^* is produced by Reaction 3.4. As for CH^*, OH^* can also relaxes to OH ground state by employing different pathways such as spontaneous emission (Reaction 3.5) and quenching (Reaction 3.6) [78, 83].

$$CH + O_2 \rightleftharpoons OH^* + CO \tag{3.4}$$

$$OH^* \rightarrow OH + h\nu \tag{3.5}$$

$$OH^* + M \rightleftharpoons OH + M \tag{3.6}$$

Further in this study, the behavior of non-premixed flames with an external electric field applied is characterized (Chapter 5). For that purpose, including the naturally produced charged species within the flame (chemi-ions and electrons) in the chemical kinetic model has to be considered. Although chemical kinetic models that include either chemi-ions [76, 84, 85, 86] or excited species [46, 80] are available in the literature, there are only two published models that contain both chemi-ions and excited species [84, 87]. The Pedersen and Brown model [84], however, is for premixed methane/air flames and the products of the reaction between $C_3H_3^+$ and an electron e^- (Reaction 84 in the model and Reaction 3.7 here) is undefined. All versions of the Saudi Aramco Mechanism [87] have too large a number of species and reactions to permit a full CFD simulation in a two-dimensional geometry with an electric field applied. That is, the computational demand for an

electrically active system with detailed transport (either by diffusion or advection) and comprehensive chemical reaction modeling is prohibitive even with current supercomputing resources. As an orientating number, using the methodology from Belhi et al. [19], a two-dimensional simulation with an electric field applied at 1g with a reaction model containing only 24 species needs to run for at least 72h hours using 512 CPU-cores to reach steady-state – i.e., 36864 CPU hours. Therefore, a target number of species for the new reduced chemical kinetic model would be below 50 to still have a model that current supercomputing resources can handle comfortably when employing two-dimensional simulations with an electric field applied. Moreover, from personal communications with Dr. Pitz and his team at Lawrence Livermore National Laboratory, it is known that the number of reactions does not affect the simulation time too much, but so it does the number of species.

$$\mathrm{C_3H_3^+ + e^- \rightleftharpoons products} \tag{3.7}$$

The chemi-ionization reaction of formyl cation (HCO^+; Reaction 3.8) is generally accepted by the combustion community to be the principal source of flame ions, as proposed by Calcote [88]. This reaction is also important because of its direct relation with Reaction 3.9, which produces hydronium ion (H_3O^+). Hydronium ion is the most important naturally produced charged specie in methane/air stoichiometric mixtures [76, 84], and it is produced and consumed by Reactions 3.9 and 3.10, respectively.

$$\mathrm{CH + O \longrightarrow HCO^+ + e^-} \tag{3.8}$$

$$\mathrm{HCO^+ + H_2O \longrightarrow CO + H_3O^+} \tag{3.9}$$

$$\mathrm{H_3O^+ + e^- \longrightarrow H_2O + H} \tag{3.10}$$

This Chapter 3 explores the development of a new comprehensive reduced reaction model that includes neutral, excited, and charged species.

3.2 Purpose

The goal of this chapter is to describe a reduced chemical kinetic model for methane/air flames that includes the naturally-produced ions in the flame (H_3O^+ and HCO^+) and excited species (primarily CH^* and OH^*) and predicts the steady-state flame when implemented in a two-dimensional numerical simulation. The developed reduced reaction model is validated against a detailed model and experimental data for different burner geometries. Once validated, the new reduced model is employed for the simulations presented in the rest of this work.

3.3 Methodology

This section comprises the procedure and tools used for (i) the reduction of the detailed chemical kinetic model and (ii) the validation of the reduced model developed.

For the reduction of the detailed chemical kinetic model, a zero-dimensional geometry is chosen to proceed. This choice avoids the complication of two-dimensional species transport while needing less time to reach a steady-state solution than higher-dimensional geometries. After reducing the chemical model and the addition of the charged species sub-model, the validation of the resultant reduced model is made by comparison to the fully detailed model.

To further validate the reduced model and the species' transport coefficients after the zero-dimensional geometry validation is achieved successfully, one-dimensional and two-dimensional geometries are simulated employing the reduced chemistry. In the one-dimensional geometry, the validation is similar to the one done previously for the zero-dimensional geometry: the results obtained em-

ploying the reduced model are contrasted with the ones obtained from using the detailed model. The two-dimensional configuration is also used to validate the results obtained using the reduced model against the ones from the detailed model. In this case, the validation is also done by comparison with experimental data from the literature. This last comparison with experiments is crucial since one of the well-known issues with adding reactions from one chemical kinetic model into another is that models are often tuned within themselves, and adding other components could break that self-consistency. Therefore, a validation with experiments ensures that the addition of these minor species takes into account this characteristic and keeps the chemistry kinetics self-consistent.

3.3.1 Reduction of the detailed chemistry

Firstly, a simulation is carried out using the perfectly stirred reactor module (PSR). Once the simulation reaches the steady-state, the Workbench module in Chemkin-Pro® software is used to reduce the chemical kinetic model.

Initial chemical kinetic model

The neutral species constitute the majority of reactants in a hydrocarbon combustion process. Thus, the neutral chemical kinetic model's choice is crucial for the further prediction of charged and excited minor species and their interactions. The San Diego Mechanism [73] is chosen as "the detailed model" for neutral species since it is the most effective balance between size and accuracy – i.e., low number of species– while it is still a recently-published chemical kinetic model of for small hydrocarbon combustion with air (see Figure 3.1 from [89]). Even though a zero-dimensional geometry already helps provide a faster simulation approach, obtaining a low number of species in the chemical kinetic model also aids in reducing the computational time and resources.

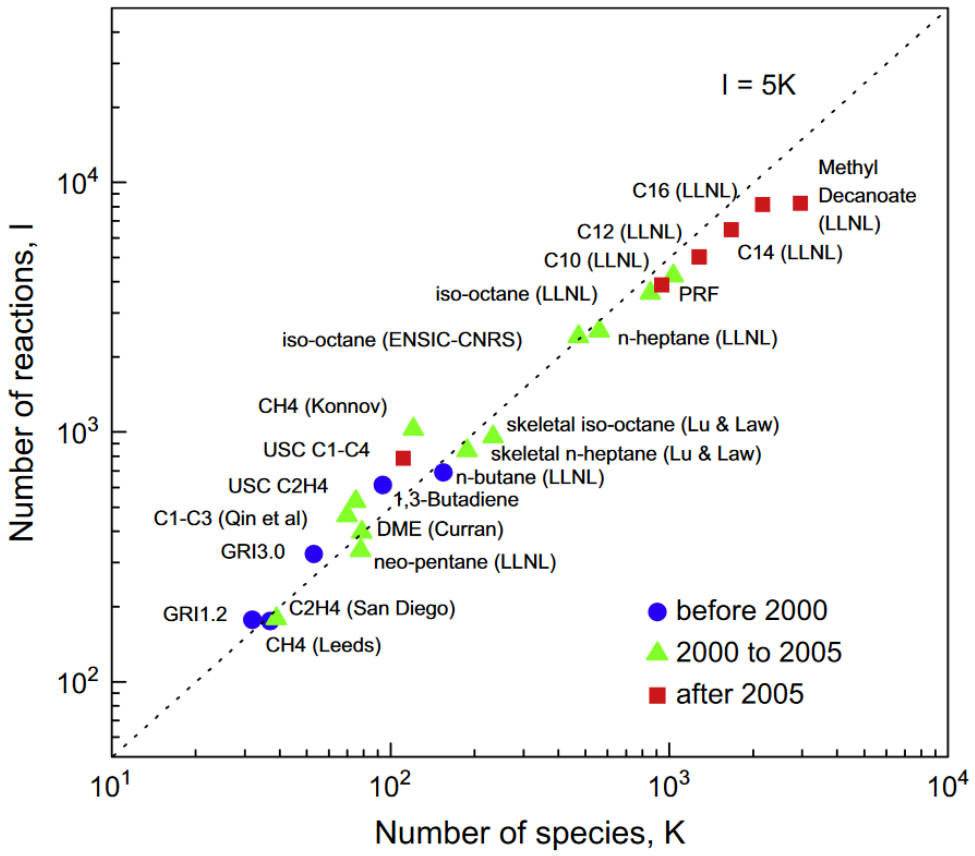

Figure 3.1: Size of selected detailed and skeletal mechanisms for hydrocarbon fuels, together with the approximate years when the chemical models were compiled. From [89].

For the prediction of CH^* and OH^*, the sub-model for the CH^* and OH^* from K.T. Walsh [71] (Appendix C.1.1) is added to the San Diego Mechanism to account for these species. A recent review of sub-models to predict CH^* and OH^* chemiluminescence was considered while choosing the model [80]. However, the final decision is based on the closeness of mole fractions and profiles for these species for non-premixed coflow jet flames, which was also experimentally validated [46].

The resultant chemical kinetic model containing neutral and excited species has 70 species and 330 reactions. That is the initial detailed chemical kinetic model that should be reduced, ideally and as previously mentioned, under 50 species.

Pre-reduction process

The Workbench tool from Chemkin-Pro® is used for the reduction of the chemical kinetic model. Before starting with the reduction process, this tool requires the user to run a simulation employing one of the provided burner geometries from Chemkin-Pro® in order to identify the sensitivity of each reaction and specie. The zero-dimensional PSR module is chosen to be used for this simulation.

The nature of this simulated reactor geometry requires two input files: the chemical kinetic model and the thermodynamic properties for the species are included in the model. The former has been discussed in the previous section. For the latter, Chemkin® accepts the thermodynamic data file given in NASA polynomial format. These NASA polynomial coefficients allow calculating the heat capacity, enthalpy, and entropy at standard state using temperature polynomial fits.

For all the neutral species, the NASA polynomial coefficients are obtained from the San Diego Mechanism. For species that are not contained in the San Diego Mechanism, the NASA polynomial is obtained from Burcat [90]. To ensure that the thermodynamic properties for the neutral and excited species do not have any data discontinuity leading to excessive times of simulation, the Mech Checker online tool developed by Lawrence Livermore National Laboratory is used [91]. This tool refits the NASA polynomial coefficients such that discontinuities between temperature ranges are removed while minimizing changes to the temperature dependence. In this work, only the thermodynamic coefficients of C_2H_4OOH and N_2 were found out of compliance, which had little impact (see Appendix D).

Once the detailed chemical kinetic model (without charged species) and the repaired thermodynamic properties are obtained, the PSR simulation is solved for a fixed gas temperature using a transient solver (see details of the simulation in Chapter 2).

Reduction process

After the PSR simulation reaches steady-state, the chemical kinetic model reduction is performed using the Workbench Chemkin-Pro® software. The reduction procedure minimizes the number of species and reactions present in the model simultaneously while targeting and keeping the species that the user defines as either "target" or "species to keep" when setting up the reduction process. Hence, the target species for the reduction are chosen to be the precursors of the chemiluminescent and ionic species of interest, which are C_2H, CH, H_2, O, O_2, and OH. That is because directly targeting minor species at this step led to reduced model results that were differing significantly from the detailed model results (by at least one order of magnitude) for the minor species of interest. Therefore, major precursors of minor species of interest are set as targets. Simultaneously, the species that are marked to be kept in the reduced model are CH_4, CH^*, CO, CO_2, H_2O, N_2, OH^*, and the previously-mentioned precursors. This is done to ensure that the reduced model accounts for the minor species of interest.

The Directed Relation Graph with Error Propagation (DRGEP) method is used for the reduction process [92, 93, 94], which consists of an automated iterative procedure that reduces the chemical kinetic model by identifying unimportant species in the reaction model by resolving species coupling – i.e., analyzing the importance of each specie to the production rate of the rest of the species and tracking on how this affects to the model reduction. For this work, the relative tolerance maximum for the target species is set to 8% and the absolute tolerance to 1e-5 mole fraction. This indicates that below 1e-5 mole fraction, it is not essential that the model resolves the values with the same precision as the detailed model. These tolerances are chosen based on a trial-and-error approach that provided the lowest number of species in the reduced model while keeping a reasonable agreement for the target species prediction.

The reduced model using the DRGEP method is achieved on a time scale that is linearly proportional to the number of reactions in the chemical kinetic model. The species sensitivity analysis

is set to be used automatically by Workbench Chemkin-Pro® to further reduce the resultant model after running the DRGEP reduction method. The lumping of isomers – i.e., not distinguishing between compounds with the same formula but a different arrangement of atoms – is given as default by the program, and it is maintained to ensure obtaining the most reduced chemistry possible in terms of the number of species and reactions, which is the standard practice while reducing chemical kinetic models [95].

This first version of the reduced chemical reaction model obtained contains 36 species. However, since this model is meant to predict a reactive environment without helium or argon, these two species and their participation in third body reactions are eliminated after the reduced model is created. Moreover, NO, N, and N_2H species are further removed since (i) the chemistry of the nitrogen is not taken into account in this study since nitrogenated species are not a target of the study and (ii) reducing the number of species leads to a further reduction on computational time. In principle, these reactions could have been erased previous to proceeding with the DRGEP method used by the Workbench software. However, they are eliminated after reducing the model because now it is clearer which branching of reactions are accounting for these species. Moreover, at this stage of the process, there are fewer possibilities to dismiss reactions that contribute indirectly to the formation or creation of target species in the chemical kinetic model. Therefore, the final version of the reduced model without charged species has 31 species and 152 reactions.

At this time, a first validation round is made using zero- and one-dimensional geometries. This validation process is explained in Section 3.3.2 and ensures that the reduced model is capturing the same features as the detailed model.

Once the first validation round using zero- and one-dimensional geometries is finalized, the sub-model for chemiions and electrons from Belhi et al. [96] is added to both the reduced and detailed chemical kinetic models. The Belhi et al. sub-model for charged species is originally based on the model proposed by Prager et al. [86], although with updated thermodynamic data. Following the classification from Lawton and Weinberg [6], the ionic chemical kinetic sub-model from

Belhi et al. accounts for electron transfer ionization reactions (example Reaction 3.11), chemi-ionization reactions (example Reactions 3.12 and 3.13), three-body attachment reactions (example Reaction 3.14), dissociative attachment reactions (example Reaction 3.15), electron transfer charge-exchange reactions (example Reaction 3.16), charge transfer with chemical rearrangement reactions (example Reaction 3.17), and three-body recombination reactions (example Reactions 3.18 and 3.19).

$$A + B \longrightarrow A^+ + B^- \tag{3.11}$$

$$A + B \longrightarrow C^+ + D + e^- \tag{3.12}$$

$$A + B \longrightarrow C^+ + D^- \tag{3.13}$$

$$e^- + A + X \longrightarrow A^- + X \tag{3.14}$$

$$AB + e^- \longrightarrow A + B^- \tag{3.15}$$

$$A + B^+ \longrightarrow A^+ + B \tag{3.16}$$

$$A^+ + B \longrightarrow C^+ + D \tag{3.17}$$

$$A^+ + e^- + M \longrightarrow A + M \tag{3.18}$$

$$A^+ + B^- + M \longrightarrow A + B + M \tag{3.19}$$

The addition of the Belhi et al. sub-model [96] to the previously-developed detailed and reduced models completes them from the species-of-interest point of view. Both now account for neutral, excited (CH^*, OH^*) and charged species (H_3O^+, HCO^+, $C_2H_3O^+$, CH_5O^+, O_2^-, OH^-, e^-, CO_3^-, CHO_2^-, O^-, CHO_3^-), and their correspondent reactions.

For clarity, the detailed and reduced chemical kinetic models developed in this work will be called Model 0 and Model 1, respectively. Model 0 contains 83 species and 394 reactions (see Appendix C.1.2). Table 3.2 shows Model 1, which contains a total of 45 species and 216 reactions. Even though this looks like a relatively small change, the computational cost is enormously reduced

since computation time scales more than three times faster when employing this reduced model than when using the detailed one for two-dimensional simulations (see Section 3.4.3).

Table 3.2: Model 1. From the modified Arrhenius expression $k = AT^b exp(-E_a/RT)$. Pre-exponential factor A in $[cm^3\, mole^{-1}\, s^{-1}]$; activation energy Ea in $[cal\, mol^{-1}]$.

Model 1. Reactions	**A**	**b**	**E_a**
Neutral species reactions			
H+O2 ⇌ OH+O	3.52E16	-0.7	1.706979E4
H2+O ⇌ OH+H	5.06E4	2.67	6.29063E3
H2+OH ⇌ H2O+H	1.17E9	1.3	3.63528E3
H2O+O ⇌ 2OH	7.0E5	2.33	1.454828E4
2H+M ⇌ H2+M	1.3E18	-1.0	0.0E0
H2/2.5/H2O/12.0/CO/1.9/CO2/3.8/			
H+OH+M ⇌ H2O+M	4.0E22	-2.0	0.0E0
H2/2.5/H2O/12.0/CO/1.9/CO2/3.8/			
2O+M ⇌ O2+M	6.17E15	-0.5	0.0E0
H2/2.5/H2O/12.0/CO/1.9/CO2/3.8/			
H+O+M ⇌ OH+M	4.71E18	-1.0	0.0E0
H2/2.5/H2O/12.0/CO/1.9/CO2/3.8/			
H+O2(+M) ⇌ HO2(+M)	4.65E12	0.44	0.0E0
H2/2.5/H2O/16.0/CO/1.2/CO2/2.4/C2H6/1.5/			
LOW /5.75E19 -1.4E0 0.0E0/			
TROE /5.0E-1 1.0E-30 1.0E30/			
HO2+H ⇌ 2OH	7.08E13	0.0	2.9493E2
HO2+H ⇌ H2+O2	1.66E13	0.0	8.229E2
HO2+H ⇌ H2O+O	3.1E13	0.0	1.72084E3
HO2+O ⇌ OH+O2	2.0E13	0.0	0.0E0
HO2+OH ⇌ H2O+O2	7.0E12	0.0	-1.09465E3

Table 3.2: Model 1. From the modified Arrhenius expression $k = AT^b exp(-E_a/RT)$. Pre-exponential factor A in $[cm^3\, mole^{-1}\, s^{-1}]$; activation energy Ea in $[cal\, mol^{-1}]$.

Model 1. Reactions	**A**	**b**	**E_a**
DUPLICATE			
HO2+OH ⇌ H2O+O2	4.5E14	0.0	1.092973E4
DUPLICATE			
2OH(+M) ⇌ H2O2(+M)	9.55E13	-0.27	0.0E0
H2/2.5/H2O/6.0/H2O2/6.0/CO/1.5/CO2/2.0/			
LOW /2.76E25 -3.2E0 0.0E0/			
TROE /5.7E-1 1.0E30 1.0E-30/			
2HO2 ⇌ H2O2+O2	1.03E14	0.0	1.104207E4
DUPLICATE			
2HO2 ⇌ H2O2+O2	1.94E11	0.0	-1.40894E3
DUPLICATE			
H2O2+H ⇌ HO2+H2	2.3E13	0.0	7.95005E3
H2O2+H ⇌ H2O+OH	1.0E13	0.0	3.58509E3
H2O2+OH ⇌ H2O+HO2	1.74E12	0.0	1.43403E3
DUPLICATE			
H2O2+OH ⇌ H2O+HO2	7.59E13	0.0	7.27294E3
DUPLICATE			
H2O2+O ⇌ HO2+OH	9.63E6	2.0	3.9914E3
CO+O(+M) ⇌ CO2(+M)	1.8E11	0.0	2.38408E3
H2/2.5/H2O/12.0/CO/2.0/CO2/4.0/			
LOW /1.55E24 -2.79E0 4.19097E3/			
TROE /1.0E0 1.0E0 1.0E7 1.0E7/			
CO+OH ⇌ CO2+H	4.4E6	1.5	-7.4092E2
CO+HO2 ⇌ CO2+OH	2.0E13	0.0	2.294455E4

Table 3.2: Model 1. From the modified Arrhenius expression $k = AT^b exp(-E_a/RT)$. Pre-exponential factor A in $[cm^3\, mole^{-1}\, s^{-1}]$; activation energy Ea in $[cal\, mol^{-1}]$.

Model 1. Reactions	**A**	**b**	**E_a**
CO+O2 ⇌ CO2+O	1.0E12	0.0	4.770005E4
HCO+M ⇌ CO+H+M	1.86E17	-1.0	1.700048E4
H2/1.9/H2O/12.0/CO/2.5/CO2/2.5/			
HCO+H ⇌ CO+H2	5.0E13	0.0	0.0E0
HCO+O ⇌ CO+OH	3.0E13	0.0	0.0E0
HCO+O ⇌ CO2+H	3.0E13	0.0	0.0E0
HCO+OH ⇌ CO+H2O	3.0E13	0.0	0.0E0
HCO+O2 ⇌ CO+HO2	7.58E12	0.0	4.0989E2
HCO+CH3 ⇌ CO+CH4	5.0E13	0.0	0.0E0
H+HCO(+M) ⇌ CH2O(+M)	1.09E12	0.48	-2.6004E2
H2/2.0/H2O/6.0/CO/1.5/CO2/2.0/CH4/2.0/C2H6/3.0/			
LOW /1.35E24 -2.57E0 4.2495E2/			
TROE /7.824E-1 2.71E2 2.755E3 6.57E3/			
CH2O+H ⇌ HCO+H2	5.74E7	1.9	2.74857E3
CH2O+O ⇌ HCO+OH	3.5E13	0.0	3.51338E3
CH2O+OH ⇌ HCO+H2O	3.9E10	0.89	4.0631E2
CH2O+O2 ⇌ HCO+HO2	6.0E13	0.0	4.0674E4
CH2O+HO2 ⇌ HCO+H2O2	4.11E4	2.5	1.021033E4
CH4+H ⇌ H2+CH3	1.3E4	3.0	8.03776E3
CH4+OH ⇌ H2O+CH3	1.6E7	1.83	2.78203E3
CH4+O ⇌ CH3+OH	1.9E9	1.44	8.67591E3
CH4+O2 ⇌ CH3+HO2	3.98E13	0.0	5.689054E4
CH4+HO2 ⇌ CH3+H2O2	9.03E12	0.0	2.464149E4
CH3+H ⇌ T-CH2+H2	1.8E14	0.0	1.510516E4

Table 3.2: Model 1. From the modified Arrhenius expression $k = AT^b exp(-E_a/RT)$. Pre-exponential factor A in $[cm^3\, mole^{-1}\, s^{-1}]$; activation energy Ea in $[cal\, mol^{-1}]$.

Model 1. Reactions	**A**	**b**	**E_a**
CH3+H ⇌ S-CH2+H2	1.55E14	0.0	1.347992E4
CH3+OH ⇌ S-CH2+H2O	4.0E13	0.0	2.50239E3
CH3+O ⇌ CH2O+H	8.43E13	0.0	0.0E0
CH3+T-CH2 ⇌ C2H4+H	4.22E13	0.0	0.0E0
CH3+HO2 ⇌ CH3O+OH	5.0E12	0.0	0.0E0
CH3+O2 ⇌ CH2O+OH	3.3E11	0.0	8.9412E3
CH3+O2 ⇌ CH3O+O	1.1E13	0.0	2.782003E4
2CH3 ⇌ C2H4+H2	1.0E14	0.0	3.200287E4
2CH3 ⇌ C2H5+H	3.16E13	0.0	1.469885E4
H+CH3(+M) ⇌ CH4(+M)	1.351E14	0.091	8.7721E1
H2/2.0/H2O/16.0/CO/1.5/CO2/2.0/CH4/4.0/			
LOW /1.59E33 -4.761E0 2.43229E3/			
TROE /8.34E-1 3.68E1 7.78E2 2.4643E3/			
2CH3(+M) ⇌ C2H6(+M)	1.81E13	0.0	0.0E0
H2/2.0/H2O/6.0/CO/1.5/CO2/2.0/CH4/2.0/C2H6/3.0/			
LOW /1.27E41 -7.0E0 2.76291E3/			
TROE /6.2E-1 7.3E1 1.2E3/			
S-CH2+OH ⇌ CH2O+H	3.0E13	0.0	0.0E0
S-CH2+O2 ⇌ CO+OH+H	3.13E13	0.0	0.0E0
S-CH2+CO2 ⇌ CO+CH2O	3.0E12	0.0	0.0E0
S-CH2+M ⇌ T-CH2+M	6.0E12	0.0	0.0E0
H2/2.4/H2O/15.4/CO/1.8/CO2/3.6/			
T-CH2+H ⇌ CH+H2	6.02E12	0.0	-1.78776E3
T-CH2+OH ⇌ CH2O+H	2.5E13	0.0	0.0E0

Table 3.2: Model 1. From the modified Arrhenius expression $k = AT^b exp(-E_a/RT)$. Pre-exponential factor A in $[cm^3\, mole^{-1}\, s^{-1}]$; activation energy Ea in $[cal\, mol^{-1}]$.

Model 1. Reactions	**A**	**b**	**E_a**
T-CH2+OH ⇌ CH+H2O	1.13E7	2.0	2.99952E3
T-CH2+O ⇌ CO+2H	8.0E13	0.0	0.0E0
T-CH2+O ⇌ CO+H2	4.0E13	0.0	0.0E0
T-CH2+O2 ⇌ CO2+H2	2.63E12	0.0	1.4914E3
T-CH2+O2 ⇌ CO+OH+H	6.58E12	0.0	1.4914E3
2T-CH2 ⇌ C2H2+2H	1.0E14	0.0	0.0E0
CH+O ⇌ CO+H	4.0E13	0.0	0.0E0
CH+O2 ⇌ HCO+O	1.77E11	0.76	-4.7801E2
CH+H2O ⇌ CH2O+H	1.17E15	-0.75	0.0E0
CH+CO2 ⇌ HCO+CO	4.8E1	3.22	-3.22658E3
CH3O+H ⇌ CH2O+H2	2.0E13	0.0	0.0E0
CH3O+H ⇌ S-CH2+H2O	1.6E13	0.0	0.0E0
CH3O+OH ⇌ CH2O+H2O	5.0E12	0.0	0.0E0
CH3O+O ⇌ OH+CH2O	1.0E13	0.0	0.0E0
CH3O+O2 ⇌ CH2O+HO2	4.28E-13	7.6	-3.53728E3
CH3O+M ⇌ CH2O+H+M	7.78E13	0.0	1.351338E4
H2/2.0/H2O/6.0/CO/1.5/CO2/2.0/CH4/2.0/			
C2H6+H ⇌ C2H5+H2	5.4E2	3.5	5.21033E3
C2H6+O ⇌ C2H5+OH	1.4E0	4.3	2.77247E3
C2H6+OH ⇌ C2H5+H2O	2.2E7	1.9	1.12333E3
C2H6+CH3 ⇌ C2H5+CH4	5.5E-1	4.0	8.2935E3
C2H6(+M) ⇌ C2H5+H(+M)	8.85E20	-1.23	1.0222275E5
H2/2.0/H2O/6.0/CO/1.5/CO2/2.0/CH4/2.0/C2H6/3.0/			
LOW /4.9E42 -6.43E0 1.0716993E5/			

Table 3.2: Model 1. From the modified Arrhenius expression $k = AT^b exp(-E_a/RT)$. Pre-exponential factor A in $[cm^3\, mole^{-1}\, s^{-1}]$; activation energy Ea in $[cal\, mol^{-1}]$.

Model 1. Reactions	**A**	**b**	**E_a**
TROE /8.4E-1 1.25E2 2.219E3 6.882E3/			
C2H6+HO2 ⇌ C2H5+H2O2	1.32E13	0.0	2.046989E4
C2H5+H ⇌ C2H4+H2	3.0E13	0.0	0.0E0
C2H5+O ⇌ C2H4+OH	3.06E13	0.0	0.0E0
C2H5+O ⇌ CH3+CH2O	4.24E13	0.0	0.0E0
C2H5+O2 ⇌ C2H4+HO2	7.5E14	-1.0	4.79995E3
C2H5+O2 ⇌ C2H4OOH	2.0E12	0.0	0.0E0
C2H4OOH ⇌ C2H4+HO2	4.0E34	-7.2	2.3E4
C2H5(+M) ⇌ C2H4+H(+M)	1.11E10	1.037	3.676864E4
H2/2.0/H2O/6.0/CO/1.5/CO2/2.0/CH4/2.0/			
LOW /3.99E33 -4.99E0 4.0E4/			
TROE /1.68E-1 1.2E3 1.0E-30/			
C2H4+H ⇌ C2H3+H2	4.49E7	2.12	1.336042E4
C2H4+OH ⇌ C2H3+H2O	5.53E5	2.31	2.96367E3
C2H4+O ⇌ CH3+HCO	2.25E6	2.08	0.0E0
C2H4+O ⇌ CH2CHO+H	1.21E6	2.08	0.0E0
2C2H4 ⇌ C2H3+C2H5	5.01E14	0.0	6.470005E4
C2H4+O2 ⇌ C2H3+HO2	4.22E13	0.0	5.762309E4
C2H4+M ⇌ C2H3+H+M	2.6E17	0.0	9.656812E4
H2/2.0/H2O/6.0/CO/1.5/CO2/2.0/CH4/2.0/			
C2H4+M ⇌ C2H2+H2+M	3.5E16	0.0	7.153203E4
H2/2.0/H2O/6.0/CO/1.5/CO2/2.0/CH4/2.0/			
C2H3+H ⇌ C2H2+H2	4.0E13	0.0	0.0E0
C2H3(+M) ⇌ C2H2+H(+M)	6.38E9	1.0	3.762667E4

Table 3.2: Model 1. From the modified Arrhenius expression $k = AT^b exp(-E_a/RT)$. Pre-exponential factor A in $[cm^3\, mole^{-1}\, s^{-1}]$; activation energy Ea in $[cal\, mol^{-1}]$.

Model 1. Reactions	**A**	**b**	**E_a**
H2/2.0/H2O/6.0/CO/1.5/CO2/2.0/CH4/2.0/			
LOW /1.51E14 1.0E-1 3.268595E4/			
TROE /3.0E-1 1.0E30 1.0E-30/			
C2H3+O2 $\rightleftharpoons$ CH2O+HCO	1.7E29	-5.312	6.50311E3
C2H3+O2 $\rightleftharpoons$ CH2CHO+O	7.0E14	-0.611	5.26243E3
C2H3+O2 $\rightleftharpoons$ C2H2+HO2	5.19E15	-1.26	3.31262E3
C2H2+O $\rightleftharpoons$ HCCO+H	4.0E14	0.0	1.065966E4
C2H2+O $\rightleftharpoons$ T-CH2+CO	1.6E14	0.0	9.89484E3
C2H2+O2 $\rightleftharpoons$ CH2O+CO	4.6E15	-0.54	4.493308E4
C2H2+OH $\rightleftharpoons$ CH2CO+H	1.9E7	1.7	9.9904E2
C2H2+OH $\rightleftharpoons$ C2H+H2O	3.37E7	2.0	1.400096E4
CH2CO+H $\rightleftharpoons$ CH3+CO	1.5E9	1.43	2.68881E3
CH2CO+O $\rightleftharpoons$ T-CH2+CO2	2.0E13	0.0	2.29446E3
CH2CO+O $\rightleftharpoons$ HCCO+OH	1.0E13	0.0	2.00048E3
CH2CO+CH3 $\rightleftharpoons$ C2H5+CO	9.0E10	0.0	0.0E0
HCCO+H $\rightleftharpoons$ S-CH2+CO	1.5E14	0.0	0.0E0
HCCO+OH $\rightleftharpoons$ HCO+CO+H	2.0E12	0.0	0.0E0
HCCO+O $\rightleftharpoons$ 2CO+H	9.64E13	0.0	0.0E0
HCCO+O2 $\rightleftharpoons$ 2CO+OH	2.88E7	1.7	1.00143E3
HCCO+O2 $\rightleftharpoons$ CO2+CO+H	1.4E7	1.7	1.00143E3
C2H+OH $\rightleftharpoons$ HCCO+H	2.0E13	0.0	0.0E0
C2H+O $\rightleftharpoons$ CO+CH	1.02E13	0.0	0.0E0
C2H+O2 $\rightleftharpoons$ HCCO+O	6.02E11	0.0	0.0E0
C2H+O2 $\rightleftharpoons$ CH+CO2	4.5E15	0.0	2.50956E4

Table 3.2: Model 1. From the modified Arrhenius expression $k = AT^b exp(-E_a/RT)$. Pre-exponential factor A in $[cm^3\, mole^{-1}\, s^{-1}]$; activation energy Ea in $[cal\, mol^{-1}]$.

Model 1. Reactions	**A**	**b**	**E_a**
C2H+O2 $\rightleftharpoons$ HCO+CO	2.41E12	0.0	0.0E0
CH2CHO $\rightleftharpoons$ CH2CO+H	1.047E37	-7.189	4.434034E4
CH2CHO+H $\rightleftharpoons$ CH3+HCO	5.0E13	0.0	0.0E0
CH2CHO+H $\rightleftharpoons$ CH2CO+H2	2.0E13	0.0	0.0E0
CH2CHO+O $\rightleftharpoons$ CH2O+HCO	1.0E14	0.0	0.0E0
CH2CHO+OH $\rightleftharpoons$ CH2CO+H2O	3.0E13	0.0	0.0E0
CH2CHO+O2 $\rightleftharpoons$ CH2O+CO+OH	3.0E10	0.0	0.0E0
CH2CHO+CH3 $\rightleftharpoons$ C2H5+CO+H	4.9E14	-0.5	0.0E0
CH2CHO+HO2 $\rightleftharpoons$ CH2O+HCO+OH	7.0E12	0.0	0.0E0
CH2CHO $\rightleftharpoons$ CH3+CO	1.17E43	-9.8	4.379995E4
Excited species reactions			
C2H+O $\rightleftharpoons$ CH*+CO	1.08E13	0.0	0.0E0
C2H+O2 $\rightleftharpoons$ CH*+CO2	2.17E10	0.0	0.0E0
CH* $\rightarrow$ CH	1.85E6	0.0	0.0E0
CH*+N2 $\rightleftharpoons$ CH+N2	3.03E2	3.4	-3.81E2
CH*+O2 $\rightleftharpoons$ CH+O2	2.48E6	2.1	-1.72E3
CH*+H2O $\rightleftharpoons$ CH+H2O	5.3E13	0.0	0.0E0
CH*+H2 $\rightleftharpoons$ CH+H2	1.47E14	0.0	1.361E3
CH*+CO2 $\rightleftharpoons$ CH+CO2	2.4E-1	4.3	-1.694E3
CH*+CO $\rightleftharpoons$ CH+CO	2.44E12	0.5	0.0E0
CH*+CH4 $\rightleftharpoons$ CH+CH4	1.73E13	0.0	1.67E2
CH+O2 $\rightleftharpoons$ OH*+CO	3.25E13	0.0	0.0E0
OH* $\rightarrow$ OH	1.45E6	0.0	0.0E0

Table 3.2: Model 1. From the modified Arrhenius expression $k = AT^b exp(-E_a/RT)$. Pre-exponential factor A in $[cm^3\, mole^{-1}\, s^{-1}]$; activation energy Ea in $[cal\, mol^{-1}]$.

Model 1. Reactions	**A**	**b**	**E_a**
OH^*+N2 $\rightleftharpoons$ OH+N2	1.08E11	0.5	-1.238E3
OH^*+O2 $\rightleftharpoons$ OH+O2	2.1E12	0.5	-4.82E2
OH^*+H2O $\rightleftharpoons$ OH+H2O	5.92E12	0.5	-8.61E2
OH^*+H2 $\rightleftharpoons$ OH+H2	2.95E12	0.5	-4.44E2
OH^*+CO2 $\rightleftharpoons$ OH+CO2	2.75E12	0.5	-9.68E2
OH^*+CO $\rightleftharpoons$ OH+CO	3.23E12	0.5	-7.87E2
OH^*+CH4 $\rightleftharpoons$ OH+CH4	3.36E12	0.5	-6.35E2
Charged species reactions			
CH + O $\rightleftharpoons$ HCO^+ + e^-	1.746E+18	-2.190	327.889
HCO^+ + e^- $\rightleftharpoons$ CO + H	7.399E+18	-0.690	0.00
HCO^+ + H2O $\rightleftharpoons$ $H3O^+$ + CO	2.608E+16	-0.500	0.00
$H3O^+$ + e^- $\rightleftharpoons$ H2O + H	7.395E+017	-0.500	0.00
$H3O^+$ + e^- $\rightleftharpoons$ OH + H + H	3.181E+018	-0.500	0.00
$H3O^+$ + e^- $\rightleftharpoons$ H2 + OH	5.601E+017	-0.500	0.00
$H3O^+$ + e^- $\rightleftharpoons$ O + H2 + H	5.841E+016	-0.500	0.00
$H3O^+$ + C $\rightleftharpoons$ HCO^+ + H2	6.022E+12	0.000	0.00
HCO^+ + CH2CO $\rightleftharpoons$ $C2H3O^+$ + CO	1.259E+15	-0.048	0.00
HCO^+ + CH3 $\rightleftharpoons$ $C2H3O^+$ + H	7.763E+14	-0.006	0.00
$C2H3O^+$ + e^- $\rightleftharpoons$ CH2CO + H	3.129E+18	-0.500	0.00
$H3O^+$ + CH2CO $\rightleftharpoons$ $C2H3O^+$ + H2O	2.086E+16	-0.500	0.00
$C2H3O^+$ + e^- $\rightleftharpoons$ CO + CH3	3.129E+18	-0.500	0.00
$C2H3O^+$ + O $\rightleftharpoons$ HCO^+ + CH2O	2.000E+14	0.000	0.00
HCO^+ + CH3OH $\rightleftharpoons$ $CH5O^+$ + CO	2.816E+16	-0.500	0.00

Table 3.2: Model 1. From the modified Arrhenius expression $k = AT^b exp(-E_a/RT)$. Pre-exponential factor A in $[cm^3\, mole^{-1}\, s^{-1}]$; activation energy Ea in $[cal\, mol^{-1}]$.

Model 1. Reactions	**A**	**b**	**E_a**
$H3O^+ + CH3OH \rightleftharpoons CH5O^+ + H2O$	2.608E+16	-0.500	0.00
$CH5O^+ + e^- \rightleftharpoons CH3OH + H$	4.653E+17	-0.590	0.00
$CH5O^+ + CH2CO \rightleftharpoons C2H3O^+ + CH3OH$	1.486E+15	-0.077	-82.93
$O2^- + H2 \rightleftharpoons H2O2 + e^-$	6.022E+14	0.000	0.00
$O2^- + H \rightleftharpoons HO2 + e^-$	7.226E+14	0.000	0.00
$O2^- + OH \rightleftharpoons OH^- + O2$	6.022E+13	0.000	0.00
$O2^- + H \rightleftharpoons OH^- + O$	1.084E+15	0.000	0.00
$OH^- + O \rightleftharpoons HO2 + e^-$	1.204E+14	0.000	0.00
$OH^- + H \rightleftharpoons H2O + e^-$	8.431E+14	0.000	0.00
$OH^- + C \rightleftharpoons HCO + e^-$	3.011E+14	0.000	0.00
$OH^- + CH \rightleftharpoons CH2O + e^-$	3.011E+14	0.000	0.00
$OH^- + CH3 \rightleftharpoons CH3OH + e^-$	6.022E+14	0.000	0.00
$CO3^- + H \rightleftharpoons OH^- + CO2$	1.020E+14	0.000	0.00
$CO3^- + O \rightleftharpoons O2^- + CO2$	4.600E+13	0.000	0.00
$CHO2^- + H \rightleftharpoons CO2 + H2 + e^-$	1.159E+14	0.000	0.00
$OH^- + HCO \rightleftharpoons CHO2^- + H$	2.959E+15	-0.140	-105.3
$O^- + C \rightleftharpoons CO + e^-$	3.011E+14	0.000	0.00
$O^- + H2 \rightleftharpoons OH^- + H$	1.807E+13	0.000	0.00
$O^- + CH4 \rightleftharpoons OH^- + CH3$	6.022E+13	0.000	0.00
$O^- + H2O \rightleftharpoons OH^- + OH$	8.431E+14	0.000	0.00
$O^- + CH2O \rightleftharpoons OH^- + HCO$	5.601E+14	0.000	0.00
$O^- + CH2O \rightleftharpoons CHO2^- + H$	1.307E+15	0.000	0.00
$O^- + C2H6 \rightleftharpoons C2H5 + OH^-$	6.130E+15	-0.500	0.00
$O^- + H \rightleftharpoons OH + e^-$	3.011E+14	0.000	0.00

Table 3.2: Model 1. From the modified Arrhenius expression $k = AT^b exp(-E_a/RT)$. Pre-exponential factor A in $[cm^3\, mole^{-1}\, s^{-1}]$; activation energy Ea in $[cal\, mol^{-1}]$.

Model 1. Reactions	**A**	**b**	**E_a**
O^- + H2 $\rightleftharpoons$ H2O + e^-	4.215E+14	0.000	0.00
O^- + CH $\rightleftharpoons$ HCO + e^-	3.011E+14	0.000	0.00
O^- + CH2 $\rightleftharpoons$ CH2O + e^-	3.011E+14	0.000	0.00
O^- + CO $\rightleftharpoons$ CO2 + e^-	3.914E+14	0.000	0.00
O^- + O $\rightleftharpoons$ O2 + e^-	1.144E+14	0.000	0.00
O^- + C2H2 $\rightleftharpoons$ CH2CO + e^-	7.226E+14	0.000	0.00
O^- + H2O $\rightleftharpoons$ H2O2 + e^-	3.613E+11	0.000	0.00
$O2^-$ + O $\rightleftharpoons$ O^- + O2	1.987E+14	0.000	0.00
$O2^-$ + $C2H3O^+$ $\rightleftharpoons$ O2 + CH2CO + H	1.000E+18	0.000	0.00
$O2^-$ + $CH5O^+$ $\rightleftharpoons$ O2 + CH3 + H2O	1.000E+18	0.000	0.00
O^- + $C2H3O^+$ $\rightleftharpoons$ O + CH2CO + H	1.000E+18	0.000	0.00
O^- + $C2H3O^+$ $\rightleftharpoons$ O + CH2CHO	1.000E+18	0.000	0.00
O^- + $CH5O^+$ $\rightleftharpoons$ O + CH3 + H2O	1.000E+18	0.000	0.00
$CHO3^-$ + $CH5O^+$ $\rightleftharpoons$ CH3OH + H2O + CO2	2.000E+18	0.000	0.00
O2 + e^- + O $\rightleftharpoons$ $O2^-$ + O	3.627E+16	0.000	0.00
O2 + e^- + O2 $\rightleftharpoons$ $O2^-$ + O2	1.523E+21	-1.000	1191.9
O2 + e^- + H2O $\rightleftharpoons$ $O2^-$ + H2O	5.077E+18	0.000	0.00
O2 + e^- + N2 $\rightleftharpoons$ $O2^-$ + N2	3.590E+21	-2.000	139.0
e^- + OH + M $\rightleftharpoons$ OH^- + M	1.088E+17	0.000	0.00
H2/1.0/ H2O/6.5/ O2/0.4/ N2/0.4/ CO/0.75/ CO2/1.5/ CH4/3.0/			
OH^- + CO2 + O2 $\rightleftharpoons$ $CHO3^-$ + O2	2.760E+20	0.000	0.00
OH^- + CO2 + H2O $\rightleftharpoons$ $CHO3^-$ + H2O	1.104E+21	0.000	0.00
e^- + O + O2 $\rightleftharpoons$ O^- + O2	3.627E+16	0.000	0.00
e^- + O + O $\rightleftharpoons$ O^- + O	3.021E+17	0.000	0.00

Table 3.2: Model 1. From the modified Arrhenius expression $k = AT^b exp(-E_a/RT)$. Pre-exponential factor A in $[cm^3\, mole^{-1}\, s^{-1}]$; activation energy Ea in $[cal\, mol^{-1}]$.

Model 1. Reactions	**A**	**b**	**E_a**
O^- + CO2 + O2 $\rightleftharpoons$ $CO3^-$ + O2	1.123E+20	0.000	0.00
C2H6 + CH $\rightleftharpoons$ C2H5 + CH2	1.1E14	0.0	-2.6E2

Figure 3.2 shows the schematic of the approach used to reduce the chemical kinetic model and the resultant Model 0 and Model 1.

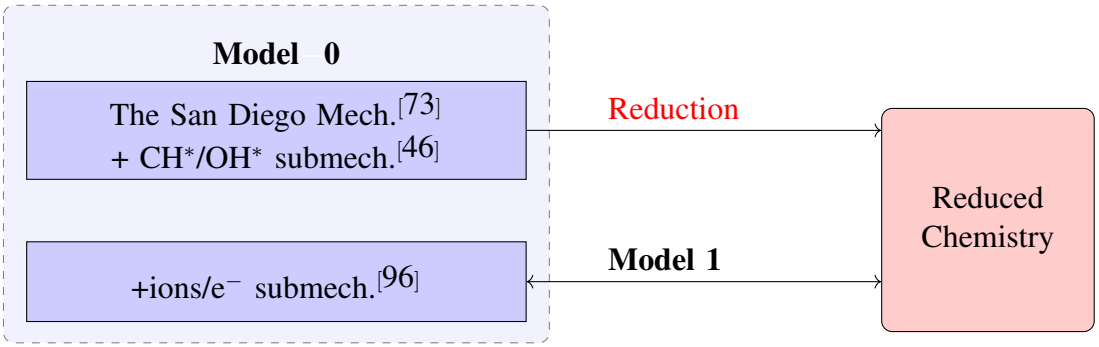

Figure 3.2: Reduction process schema.

3.3.2 Validation of the reduced chemistry

There are two stages where validation of the reduced model is needed: (i) after the reduction of the model when charged species are not added yet and (ii) after adding charged species into the model. The first validation is done using zero- and one-dimensional simulations. The second stage validation uses one- and two-dimensional burner geometries. In all cases, the validation consists of analyzing the species' profiles - trend and peak- obtained using the same simulation for Model 0 and Model 1. Moreover, some other crucial parameters – i.e., temperature – are checked using the same validation approach. Due to the availability of experimental data in the literature for the

extruded burner geometry, the validation of CH^* location by comparison of the models with the literature is also accomplished.

The criteria of success established for the validations is that the zero- and one- dimensional simulation comparison between detailed and reduced model should differ by less than 5% for the temperature profile – i.e., at 2000K and above for the zero-dimensional geometry – and major species (CH_4, O_2, H_2O, N_2, CO_2, and CO) and qualitatively and quantitatively predict the peak for the minor species (CH^*, OH^*, H_3O^+, HCO^+, and electrons) to be within the same order of magnitude and at less than 10% difference in location. For the cases where C_2H is considered, the same validation criterion as for the minor species is followed.

For the two-dimensional simulations, the criteria of success is that the previously mentioned major and minor species should be mapped within a 5% and 10% of the location from the detailed model, respectively. Moreover, the minor specie CH^* has to differ by equal or less than 10% on the location from the experimental literature.

These criteria of success values are chosen to achieve a similar behavior for minor target species for detailed and reduced models considering the possible experimental error coming from the sources used for the comparison.

Zero-dimensional geometry (PSR)

The zero-dimensional geometry is only employed for the first validation round since it gives faster results than simulations with higher dimensional order. The simulation employing this geometry only requires two input files that have been discussed previously: the chemical kinetic model and the thermodynamic properties for the species. Even though the positive results on the zero-dimensional validation (see Section 3.4), these are considered preliminary since the model should be challenged against higher order dimensional simulations and experimental data as well.

One-dimensional burner geometry (Counterflow burner)

This geometry is used in both validation processes because (i) it is faster than the two-dimensional simulations since it does not include two-dimensional transport, and (ii) it is still a geometry widely used to understand fundamental flame behavior. Note that the use of the counterflow geometry is appropriate to study the chemical kinetic model of flames without electric fields applied. However, this geometry will not be employed in the simulations with the addition of an electric field since the flow field cannot retain its one-dimensional character.

These counterflow simulations require the two input files that the PSR simulations need – chemical kinetic model and thermodynamic properties– plus a third file containing the transport properties of the species.

Chemkin-Pro® offers two detailed formulations to estimate the transport properties: mixture-averaged and multicomponent. Since the latter is theoretically more accurate and does not add significant computational cost to the simulation, it is chosen herein. The ideal gas law is used as the equation of state. For more details on the formulation for thermophysical and transport properties, see the Chemkin-Pro® theory manual [42].

The transport properties of each species contained in the model should be defined in a specific Chemkin-Pro® format. These values are used to calculate the transport properties, such as viscosity, conductivity, and diffusion coefficient [97]. The transport coefficients' values are obtained from the referenced models and are found in Appendix F. For the excited species, CH^* and OH^*, the transport coefficients are approximated as the same as those of the ground state species. This approximation is commonly used in the literature [80] without apparent detriment.

Two-dimensional burner geometry (Jet burner)

The two-dimensional burner geometry used for validation employing the completed models with excited and charged species corresponds to an axisymmetric-jet-burner configuration with two different burner heights (see explanation in Chapter 2). In all the two-dimensional geometry comparisons in this Chapter 3, the inlet fuel velocity was set to be a fully-developed parabolic profile corresponding to 20mL/min of fuel flow rate.

The two-dimensional geometry is the most complex configuration employed in this work, requiring more time and computational resources. Hence, the one-dimensional burner geometry is used first to validate the chemical kinetic model, and once the results are within the accepted tolerances, the two-dimensional geometry simulations are run.

As in the one-dimensional geometry case, the two-dimensional simulations also require three files related to the chemical kinetic model, the thermodynamic, and the transport properties for the species contained in the model. Therefore, the charged species properties are added to these files in order to proceed with the simulation. Appendices D and F show the thermodynamic and transport properties used for these simulations.

The OpenFOAM® simulation of the jet burner flame also allows comparison against experimental data for excited species location for one of the jet heights.

3.4 Results and discussion

As mentioned in Section 3.3.2, there are two stages where validation of the reduced model is needed: (i) after the reduction of the model when charged species are not added yet and (ii) after adding charged species into the model. The first validation is done using zero- and one-dimensional simulations. The second stage validation uses one- and two-dimensional burner geometries.

Therefore, the zero-dimensional simulation results shown below are only preliminary because they do not count with the complete Model 0 and Model 1 – i.e., they account for Model 0 and Model 1 without the addition of the charged species. The results of the validation using one- and two-dimensional geometries include the complete Model 0 and Model 1 – i.e., the chemistry of charged species is already included. These geometries correspond to the counterflow and jet burner geometry, respectively.

3.4.1 Zero-dimensional validation (PSR)

To determine if the reduction process using the Workbench module in Chemkin-Pro ® is successful, a comparison between the different outcomes using the detailed and reduced models using a zero-geometry reactor (i.e., PSR) is made. At this stage, there are no charged species included in the chemical kinetic models.

The major species profiles – CH_4, N_2, O_2, CO_2, and CO profiles – differ by less than 1% qualitatively and quantitatively, and therefore, they are considered identical and within the acceptable validation criteria. Figures 3.3 and 3.4 show that the minor species CH^* and OH^*, respectively, are within the acceptable validation of criteria by having their peak values at the same order of magnitude and the profiles differing by less than 5% and 10% for high temperatures (2000K-2500K) and lower temperature (1500K), respectively. The discrepancies at lower temperature in Figures 3.3, 3.4, and 3.5 are not significant for the approach of this work since the reactive region of the methane-air flames investigated here is shown to remain always above 1500K – even in microgravity environments (see Chapter 4, Figures 4.3 and 4.4) – and the concentrations for these species are very low as well.

The C_2H mapping is also considered for comparison, as it is a CH^* precursor and a potential flame zone marker. Figure 3.5 shows the trends for C_2H specie, which are found to be within less than 5% difference in location for temperatures higher than 2000K, which are typical temperatures for

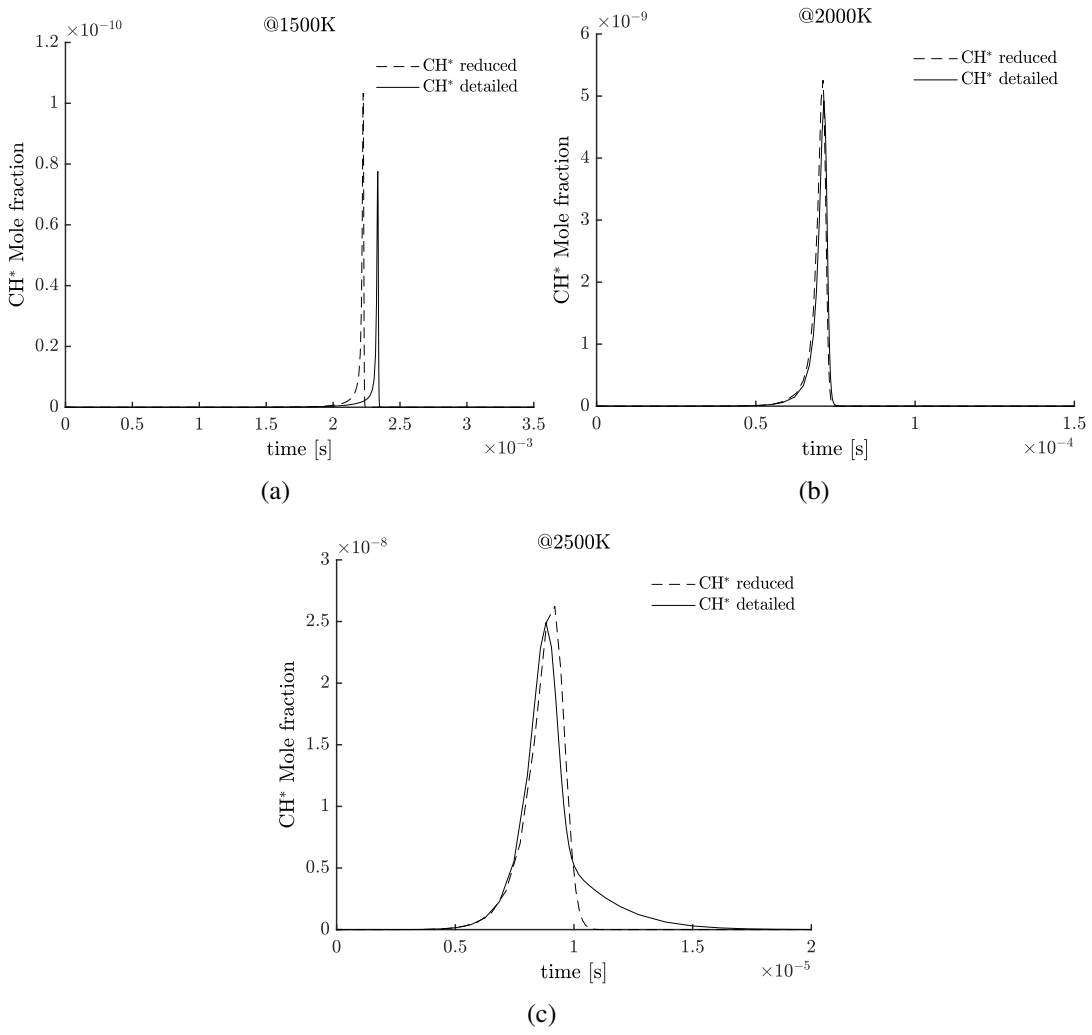

Figure 3.3: PSR configuration. CH^* specie comparison between detailed and reduced chemical kinetic models (Models 0 and 1 without charged species reactions added).

a methane diffusion jet flame. For this work, the reduced chemistry model capturing similar trends and locations for the species as the detailed model is more important than the quantitative results related to the particular values for these characteristics.

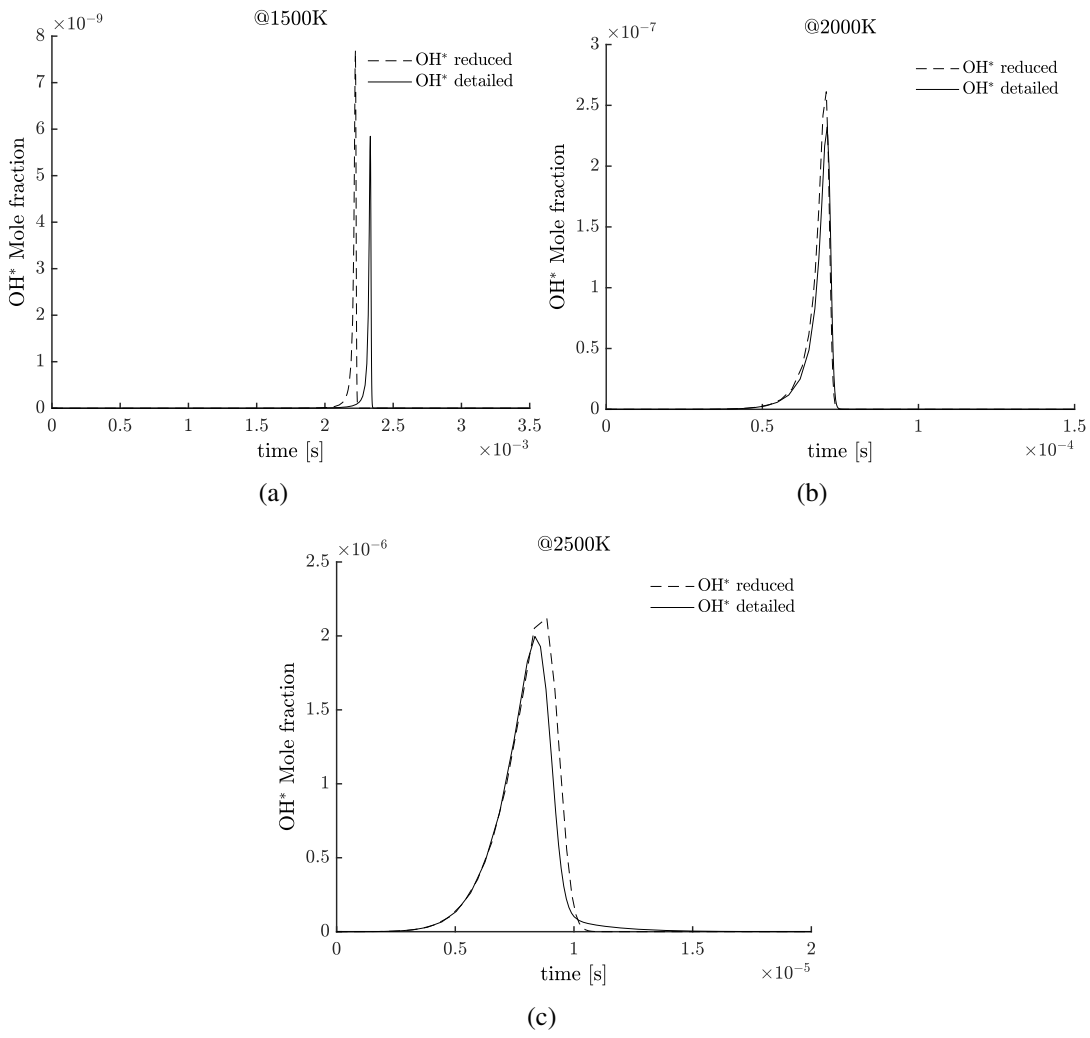

Figure 3.4: PSR configuration. OH^* specie comparison between detailed and reduced chemical kinetic models (Models 0 and 1 without charged species reactions added).

3.4.2 Counterflow burner validation

The details of the counterflow simulation are shown in Chapter 2 Section 2.3. Fuel (methane) flows at 0.12m/s from the left nozzle, while the oxidizer (air) does it at the same velocity from the right nozzle.

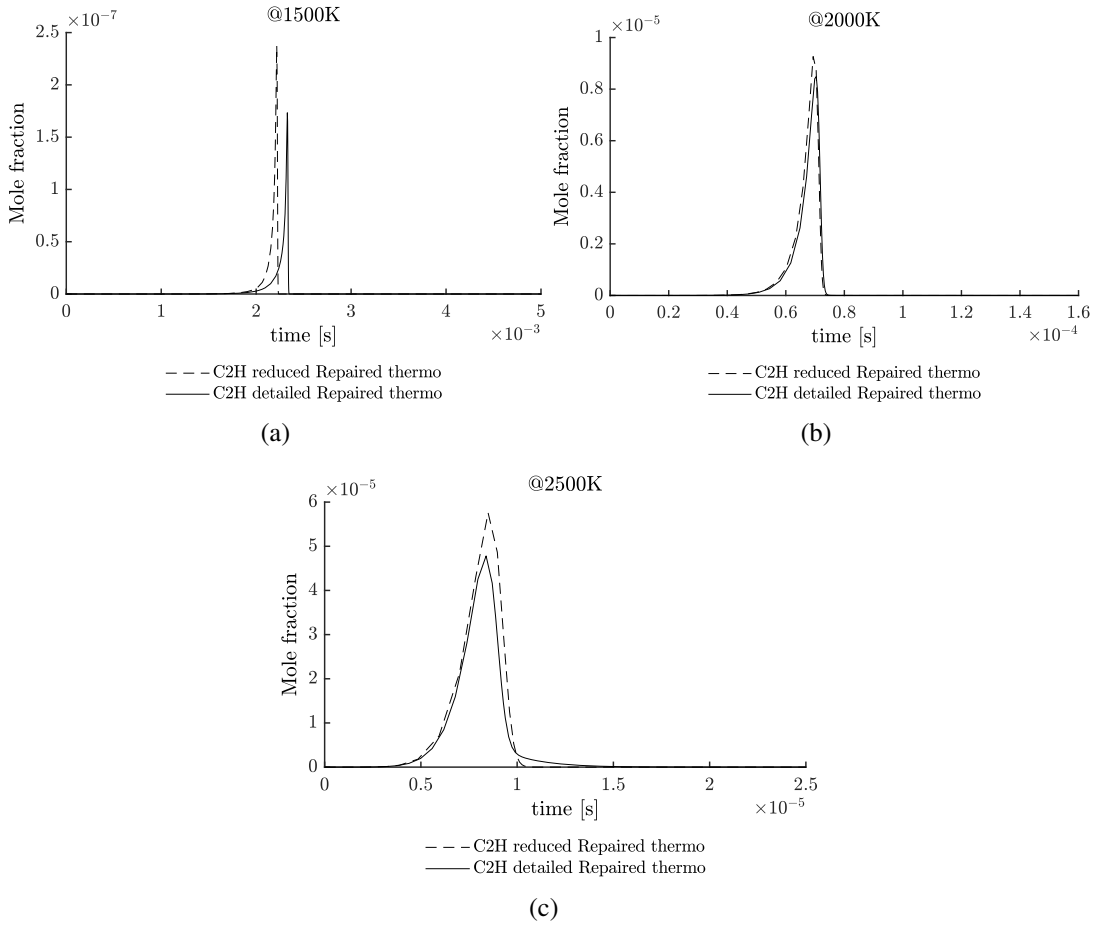

Figure 3.5: PSR configuration. C_2H specie comparison between detailed and reduced chemical kinetic models (Models 0 and 1 without charged species reactions added).

The x-axis in the following figures is standardized by dividing the distance at each point of the domain x_i by the distance x between nozzles (Equation 3.20).

$$\chi = x_i/x \tag{3.20}$$

Temperature and major species profiles

Figure 3.6 shows the temperature and major neutral species profiles in the flame for the models tested. Using either chemistry model, the differences in all profiles are less than 1%.

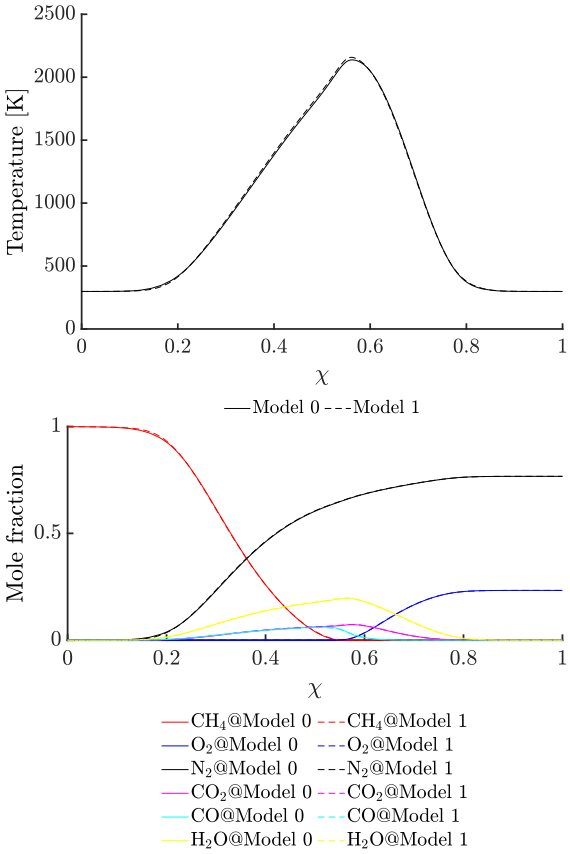

Figure 3.6: Temperature (top) and main species distribution (bottom) using Model 0 (detailed) and Model 1 (reduced) in a counterflow geometry.

Excited species profiles, CH* and OH*

Figure 3.7 shows the profiles for the excited species CH* and OH*. The temperature profile is also plotted to give a sense of the location of these species as relative information in the flame. For both species, the reduced model under-predicts the peak mole fraction. However, the position of the peak and the order of magnitude for both species are the same using either model. Notice that the absolute concentration of these species is very low. Therefore, the compromise of accepting these differences is assumed considering the decrease on species' number – i.e., the expected reduction of needed computational resources; as mentioned later in this Chapter 3, the computational time is achieved to be reduced by more than three times of CPU time for a two-dimensional geometry simulation.

CH* Previous literature has shown that the CH* mole fraction peak is in the order of 2e-9 and 6e-11 for experimental results and between 1.2e-10 and 2.3e-10 for simulated results in methane-air counterflow and coflow jet flames [71, 98]. In the simulations from this work, the CH* mole fraction is on the order of magnitude expected for both detailed and reduced models. The two-dimensional simulations will allow further quantitative and qualitative comparison with experiments since the burner geometry and coflow, if any, may affect the production of these chemiluminescent minor species.

OH* The OH* mole fraction peak shown by literature is in the order of 1.3e-8 and 9e-10 for experimental results and between 1.1e-8 and 1e-9 for simulated results in methane-air counterflow and coflow jet flames [71, 98]. Likewise in this case, compromise between CH*, OH*, and other species prediction is going to be tested later with two-dimensional simulations in order to evaluate the significance and agreement of the models. However, also in this case, the order of magnitude of OH* mole fraction is consistent with the prior work. It is important to remark that the reduced chemistry model capturing a similar location of peak mole fraction and trend for OH* in comparison to the results obtained with the detailed chemistry model is more important than the quantitative results for the mole fraction obtained for these minor species.

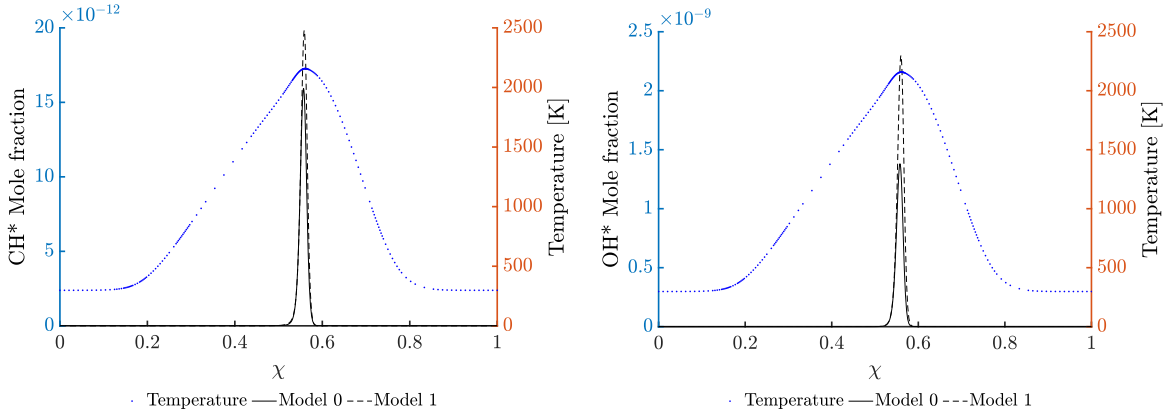

Figure 3.7: CH (left) and OH* distribution (right) using Model 0 (detailed) and Model 1 (reduced) in a counterflow geometry.*

Charged species profiles, H_3O^+, HCO^+ and e^-

Figure 3.8 shows the profiles for the major charged species HCO^+, H_3O^+, and electrons. In this case, the temperature profile is also plotted to give more relative information to the flame. As for the excited species, the reduced model under-predicts the charged species peak mole fraction. However, also here, the position of the peak and the order of magnitude of them are the same using either chemical kinetic model. Previous literature for methane premixed flames using jet-type burners in stoichiometric combustion conditions [99] found the H_3O^+ peak was produced at $\approx$ 500K below the maximum flame temperature, which agrees with the prediction for the detailed Model 0 from this work. Moreover, Prager et al. [86] numerically showed that using a flat, fuel-lean, and laminar methane-oxygen flame, the electron mole fraction peak was found to be $\approx$ 1.5e-9, which agreed with Goodings et al. [100] experimental findings. In contrast, the electron mole fraction peak is predicted to be one order of magnitude higher in this work. The disparity between results might be given by the lean character of the flame that Prager et al. used in comparison to the stoichiometric flame studied here since the stoichiometric flame would produce more reactants for the chemi-ionization reaction to occur and produce more chemi-ions and electrons.

At this stage, the threshold between the quantitative results from the detailed and the reduced model for charged species is currently assumed in expectancy to evaluate its impact in Section 3.4.3.

3.4.3 Jet burner validation

The first step in this validation is to compare the time to reach the same steady-state simulation using both detailed and reduced models. This is made for informative purposes and verifies that the reduced model requires less time to reach a steady-state solution. Identical jet burner geometries, software, hardware, boundary, and initial conditions are set for the comparison.

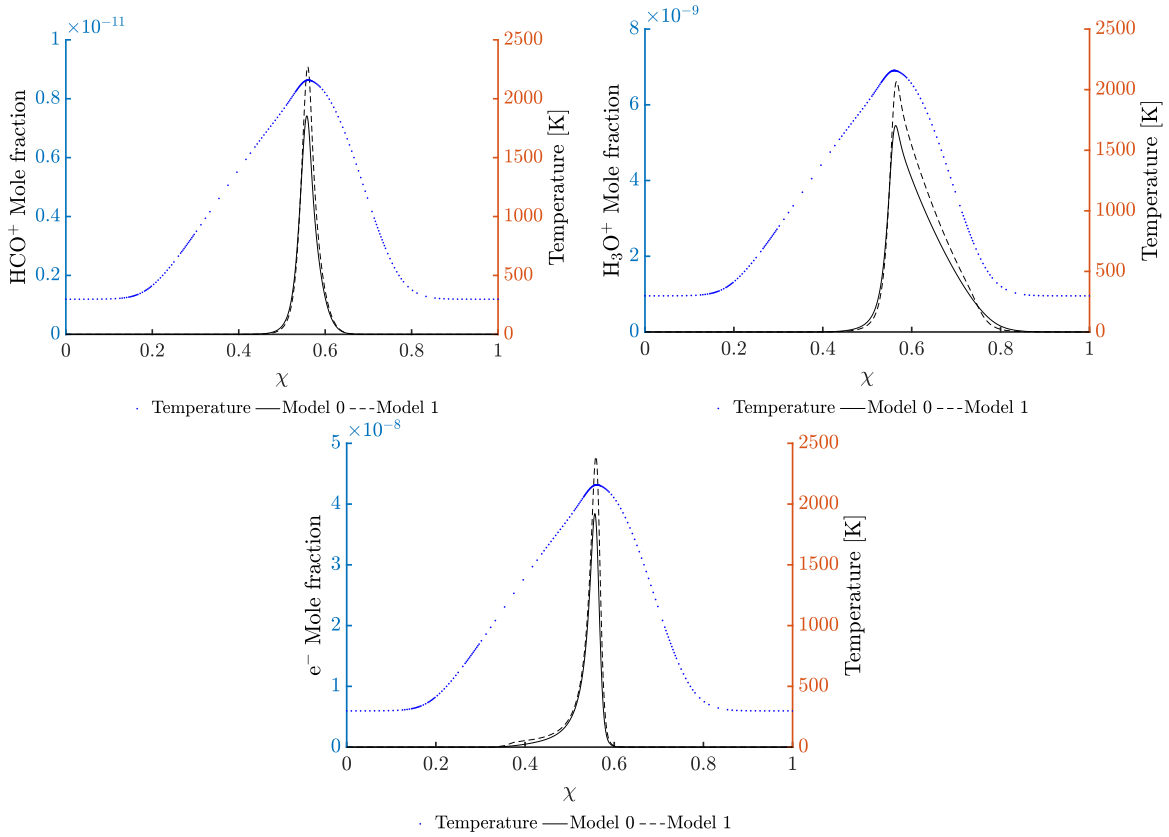

Figure 3.8: HCO^+ (top left), H_3O^+ distribution (top right), and electrons (bottom) using Model 0 (detailed) and Model 1 (reduced) in a counterflow geometry.

As expected, the reduced model effectively decreases the computational resources and time needed to perform the same simulation. For the extruded burner, the simulation using Model 1 (reduced chemistry) is 3.67 times faster than one employing Model 0. When using the jet burner, the Model 1 simulation is 3.30 times faster than the Model 0 simulation. Notice that this factor is nearly the same as the product of the number of species and reactions difference in a linear way, so this suggests how much improvement could be expected from further reduction – Model 0: 83 species and 394 reactions; Model 1: 45 species and 216 reactions.

The domain plotted in the following results is only half of the experimental domain, as explained in Chapter 2. However, since the jet burners simulated are axisymmetric, the symmetry axis placed at X = 0 mm shows that the non-plotted experimental domain (left side of the y-axis) would mirror the plotted results.

Temperature profile

Figures 3.9, 3.10, and 3.11 show the comparison between the temperature profiles obtained using Model 0 (detailed) and Model 1 (reduced) chemical kinetic models for the extruded and jet burner geometries with a temperature legend going up to 1900K.

The two chemistry models show differences of less than 1% for the trend and distribution of temperature. The peak temperature, placed in the center of the reaction region in all cases, has shown to be $\approx$ 2014K (Model 0) and $\approx$ 2013K (Model 1) for the extruded burner, and $\approx$ 1999K (Model 0) and $\approx$ 2001K (Model 1) for the extruded burner. The difference of 1-2K between reaction models is inside the uncertainty of the calculation, and therefore, the peak on temperature profiles are taken as equal for each burner geometry. Moreover, previous literature showed that for a coflow diffusion methane flame, the temperature at the reaction region is 1977K for a 1g flame [101]. It can be considered that the results obtained using either chemistry model for both burner geometries in this work and the results from the literature are the same since they only differ by less than 2%.

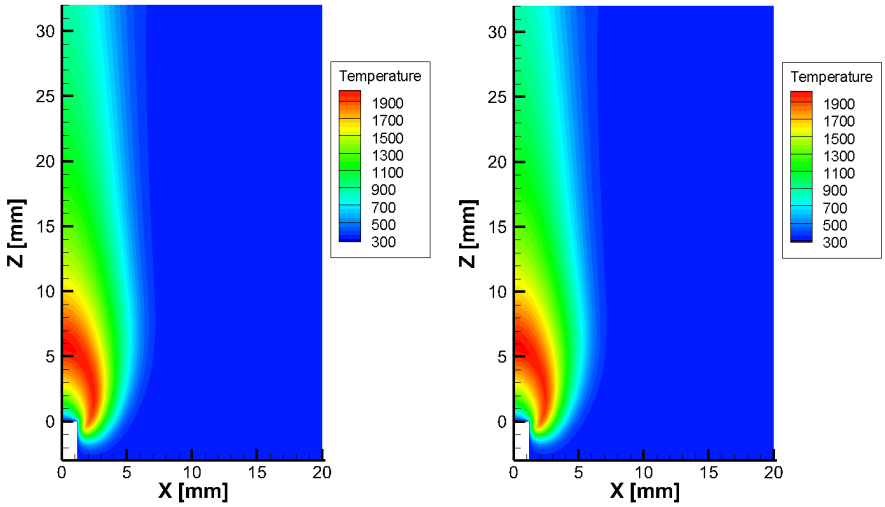

(a) Model 0 (b) Model 1

Figure 3.9: Extruded burner. Temperature of 1g extruded burner flame without e-field applied at steady-state. (a) Model 0, (b) Model 1.

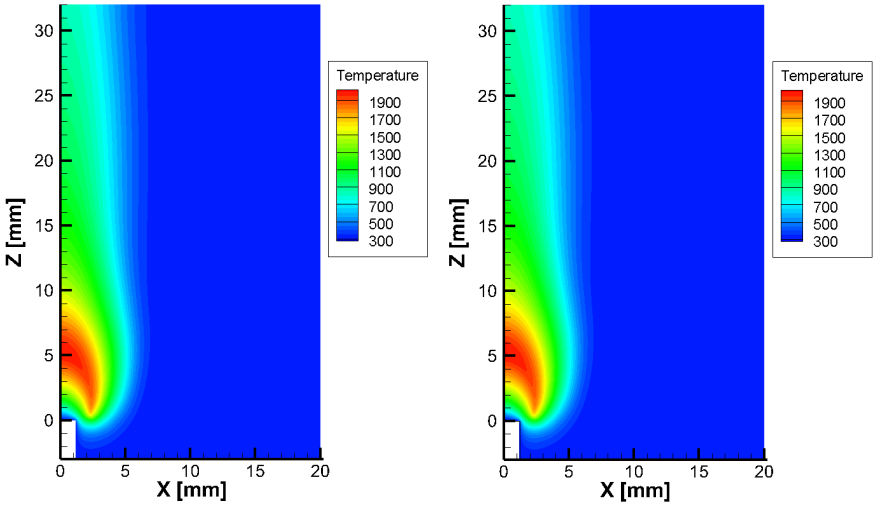

(a) Model 0 (b) Model 1

Figure 3.10: Jet burner (close-up). Temperature of 1g extruded burner flame without e-field applied at steady-state. (a) Model 0, (b) Model 1.

Major species profiles

The profiles of major species H_2O, O_2, CO and CO_2 using both chemistry models are also compared in Figures 3.12 and 3.13. Most of the comparisons for main species either overlap using either chemistry model or display a difference of less than 5% in position for the same mass fraction distribution.

Notice that looking at the O_2 concentrations obtained when employing the extruded or the jet geometries, there is an intrusion of O_2 close to the burner rim. That is because the separation between the burner tip and burner base (3mm and 10mm, respectively) allows more air entrainment in the jet burner case.

Also, looking at the results for the jet geometry, the carbon monoxide CO profile displays a high concentration *bubble* in the upper-middle of the reaction zone. This is also shown in experimental work from the literature [102], and it is attributed to the diffusion process from zones closer to the flame.

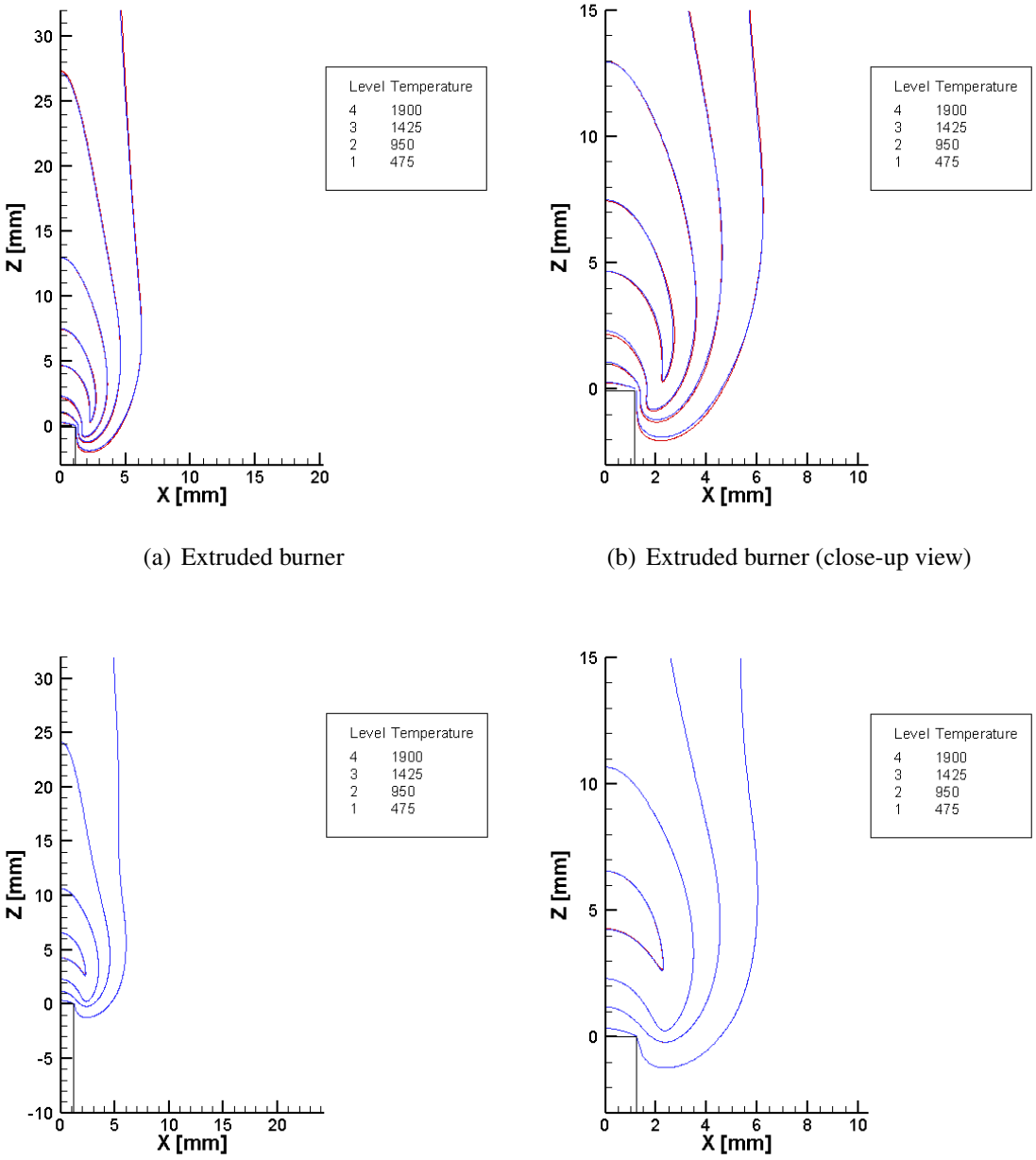

(a) Extruded burner

(b) Extruded burner (close-up view)

(c) Jet burner

(d) Jet burner (close-up view)

Figure 3.11: Temperature contours of 1g flame without e-field applied at steady-state. Model 0 (red) and Model 1 (blue). Extruded burner (top) and Jet burner (bottom). Highest value contour (level 13) is in the center.

Since Model 1 is developed to capture the main features of the flame with special interest on minor excited and charged species, and the larger quantitative differences for temperature and major

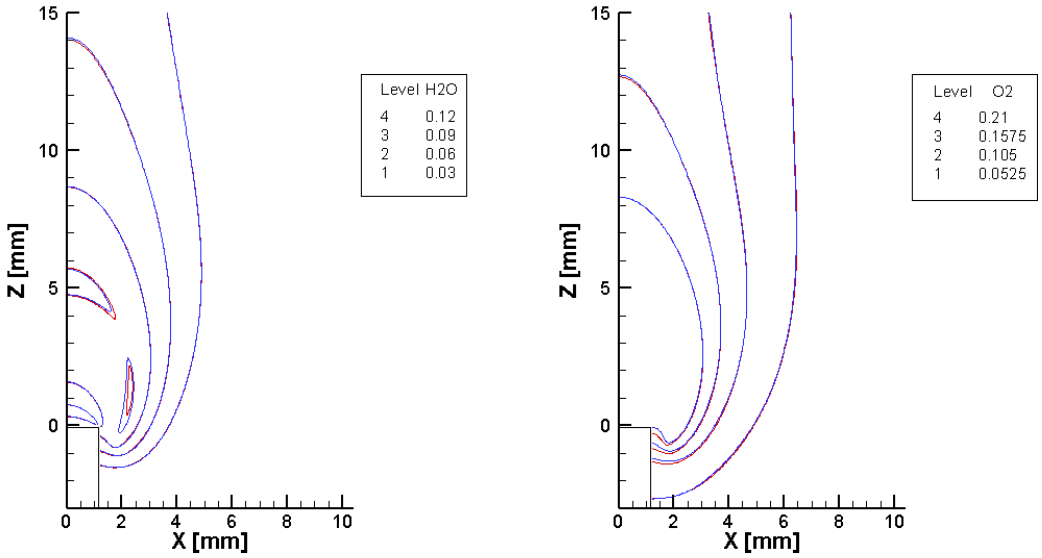

(a) H_2O

(b) O_2

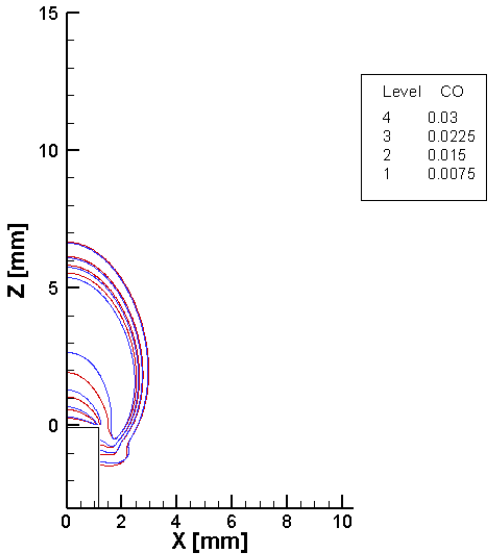

(c) CO

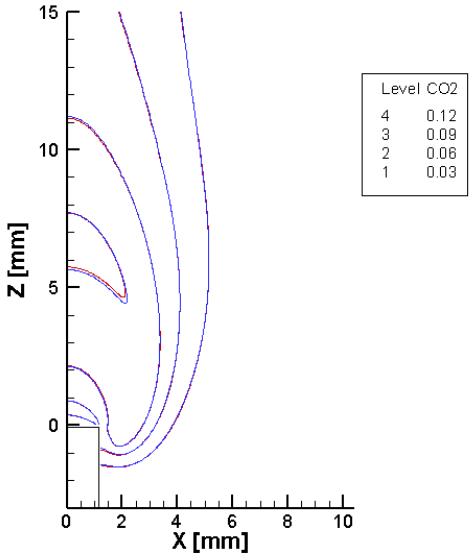

(d) CO_2

Figure 3.12: Contours of 1g flame without e-field applied at steady-state. Extruded geometry (close-up view). Model 0 (red) and Model 1 (blue). (a) H_2O, (b) O_2, (c) CO, (d) CO_2. Highest value contour (level 11) is in the center except for O_2 (combustion reactant), that the lowest value contour (level 1) is in center.

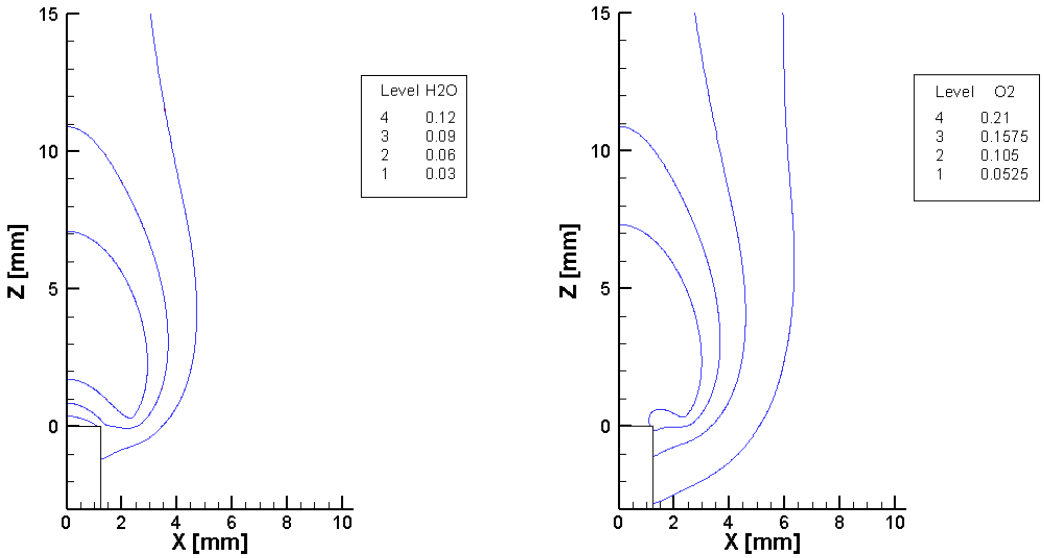

(a) H_2O

(b) O_2

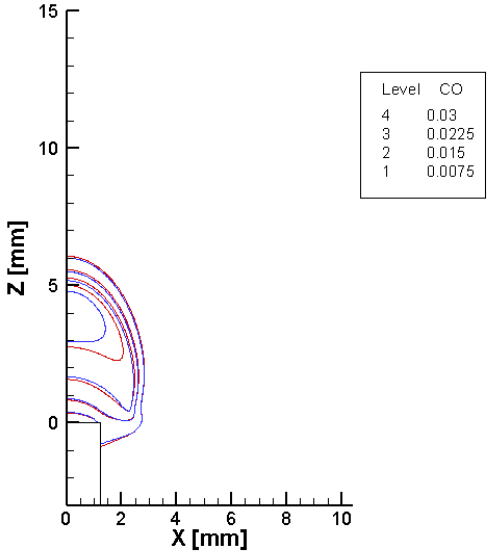

(c) CO

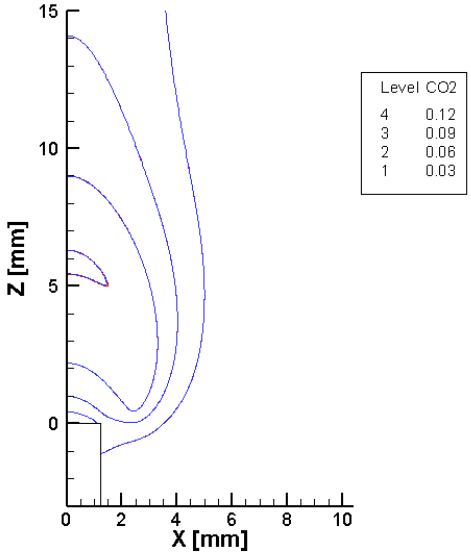

(d) CO_2

Figure 3.13: Contours of 1g flame without e-field applied at steady-state. Jet geometry (close-up view). Model 0 (red) and Model 1 (blue). (a) H_2O, (b) O_2, (c) CO, (d) CO_2. Highest value contour (level 11) is in the center except for O_2 (combustion reactant), that the lowest value contour (level 1) is in center.

species mole fraction distributions are below the 5%, it is decided to continue with the validation of the model to understand its limitations and capabilities.

C_2H profile

From the reaction pathways shown in Model 1, it is observed that C_2H could also be a potential flame marker given that it is a reactant in the reactions that produce CH^* (Reactions 3.8 and 3.9) and Figure 3.14 corroborates it. Its maximum mass fraction at each height Z aligns with the inside of the CH^* experimental contour from [43], as clearly seen in Figures 3.15(a) and 3.15(b). Therefore, using C_2H as reaction zone marker, Figure 3.15 shows that the location of the flame is the same using either chemistry. There are minor differences in the distribution of the mass fraction of C_2H, especially at the tip of the flame when using both burner geometries. To not become liable to these differences between the chemistry used, the C_2H maximum mass fraction obtained in the simulation can be taken as a marker for the flame location.

Excited species profiles, CH^* and OH^*

For the extruded geometry, the CH^* location is validated by comparison with the simulation results employing the detailed chemical kinetic model (Model 0) as well as against experiments from the literature [40]. Depending on the light collection optics, the system sensitivity of which concentration of CH^* can be seen will vary. So, the simulation identifies the contour that seems to best match the experiment assuming that this represents the sensitivity of that particular experiment.

OH^* profiles are validated by comparison between reduced and detailed chemistry model steady-state solutions. Moreover, experimental literature for coflow methane diffusion flames shows profiles for CH^* and OH^* (see Figure 3.16 reproduced from Walsh et al. [71]), where the maximum values are used for a comprehensive comparison with the Model 1 results.

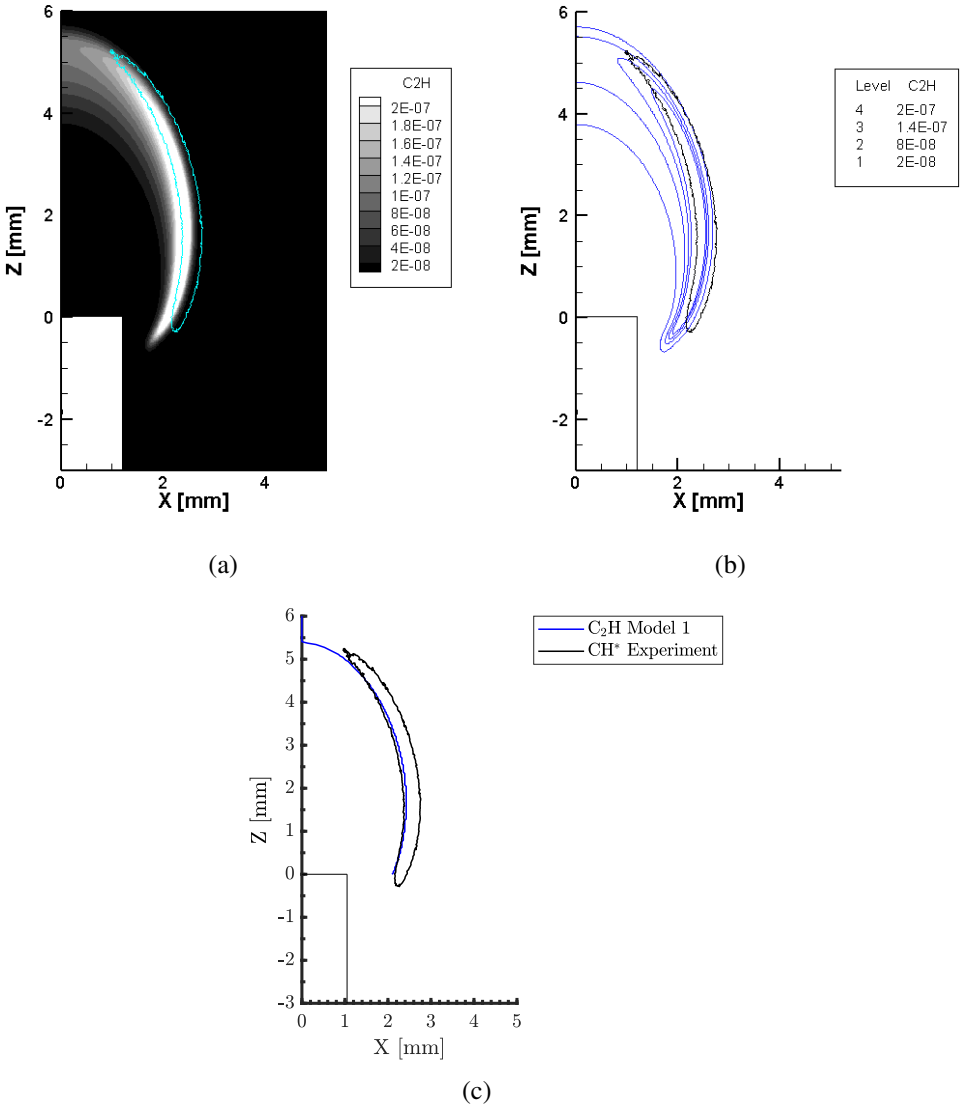

Figure 3.14: Flame location in the extruded burner. (a) Simulated C_2H mapping with experimental CH^* cyan isoline, (b) Simulated C_2H blue isolines with experimental CH^* black isoline, and (c) Simulated C_2H maximum mass fraction (threshold [C_2H] = 1e-12) with experimental CH^* black isoline.

Figures 3.17 and 3.18 show the comparison between the CH^* results obtained from the Model 1 simulation from this work and the experiments from [43, 103]. The simulation CH^* mappings are normalized by its maximum (CH^*/CH^*_{max}), while the contour line shown in Figure 3.18 is

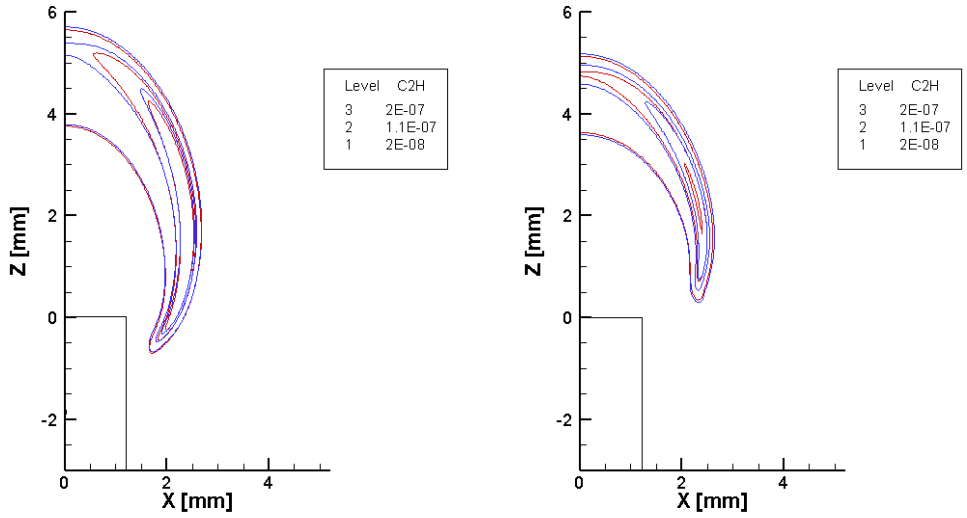

(a) (b)

Figure 3.15: C_2H contours of 1g flame without e-field applied at steady-state (close-up views). Model 0 (red) and Model 1 (blue). Inner to outer contours go from higher concentration to lower concentration. (a) Extruded, (b) Jet.

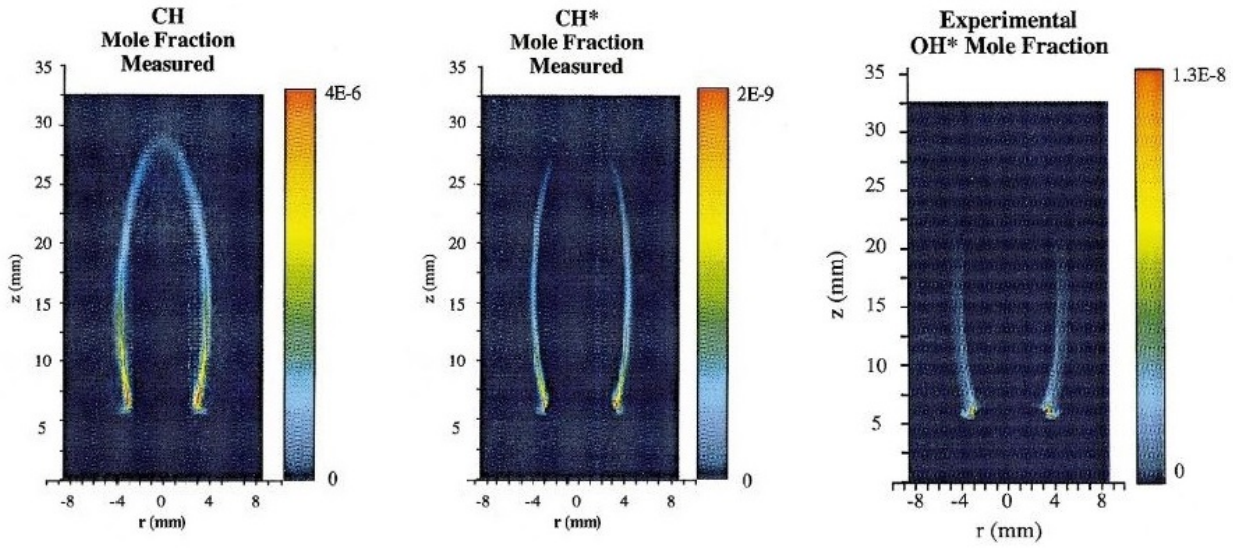

Figure 3.16: Experimental values obtained using a coflow methane-air configuration from Walsh et al. [71]. From left to right: CH, CH, and OH* mole fraction mapping.*

taken from the literature experiments for CH* chemiluminescence at the same burner and boundary conditions as in the simulation (Figure 3.17(b)).

These results indicate that the reduced model captures well the CH^* distribution on the flame except for the disagreement closer to the tip of the burner. That region has already been challenging to observe and predict in previous experimental and numerical studies due to the interaction between the flame and the jet burner that can cause perturbations in the flame itself, leading to studies that purposefully lift the flame to avoid these challenges [71, 74, 104, 105]. For the purpose of further comparisons in the next Chapters, Figure 3.19 shows the black and white mapping corresponding to the simulated CH^*/CH^*_{max} ratio, and the different subfigures show the comparison between different ratios and the literature experiments for CH^* chemiluminescence.

Following the results from Figure 3.19, the simulated CH^* contour that is taken as the most representative of the experiment results is at CH^*/CH^*_{max} = 0.05. While the discrepancy is not ideal, the overall flame shape and size where the most robust reaction occurs (as shown by the brightest CH^* signal) show reasonable agreement with the simulation. We expect this to be the same region where most ion species production occurs as well, so it is essential that the high-intensity regions are captured effectively in a global sense. Further analysis will determine if the discrepancy ultimately produces significant errors in the electrical response flame predictions using these chemical models.

Figures 3.20 and 3.21 show that both models reach similar steady-state solutions for the excited species mass fraction distribution – i.e., less than 1% difference on the different mass fraction distribution for both extruded and jet geometries – as well as for the trends and location where these species are placed.

Focusing on the quantitative results, the experimental literature [71, 98] shows that the measured peak level for CH^* was found to be between 2e-9 to 5e-11 for jet flames (with coflow air and methane with pure oxygen premixed, respectively), while the obtained in this work for the extruded and jet burners is 1.8e-11 and 3.7e-11, respectively. The disparity in the values can be explained because the experimental literature values are obtained from a premixed methane flame with pure oxygen, and since pure oxygen enhances the reactivity of the combustion more than when methane

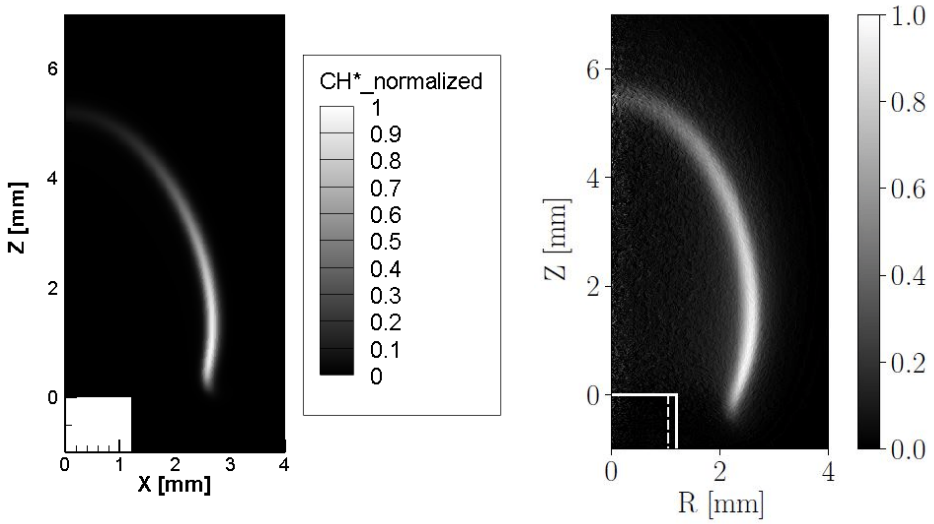

(a) Simulation (Model 1) (b) Experiment [40]

Figure 3.17: Extruded burner without external electric field applied at 1g with inlet fuel velocity of 27 mL/min. (a) CH chemiluminescence from simulation using Model 1; (b) Experimental CH* chemiluminescence (R is X in the simulations).*

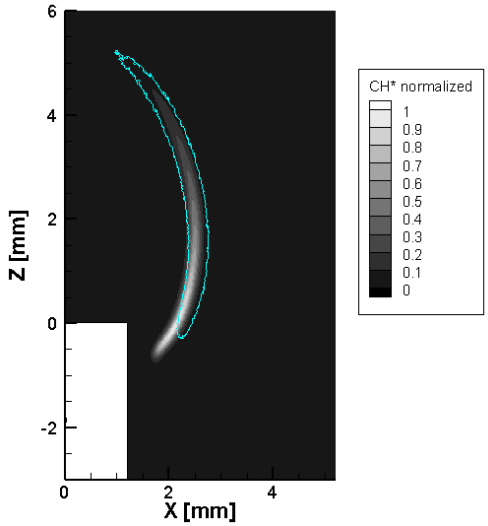

Figure 3.18: Extruded burner without external electric field applied at 1g with inlet fuel velocity of 20 mL/min. CH^*/CH^*_{max} mapping (simulation) and contour of CH chemiluminescence (experiment, [43])*

is mixed with air, the studied cases in his work have less reactivity – and, therefore, a lower concentration of CH* – than in the case studied in the literature.

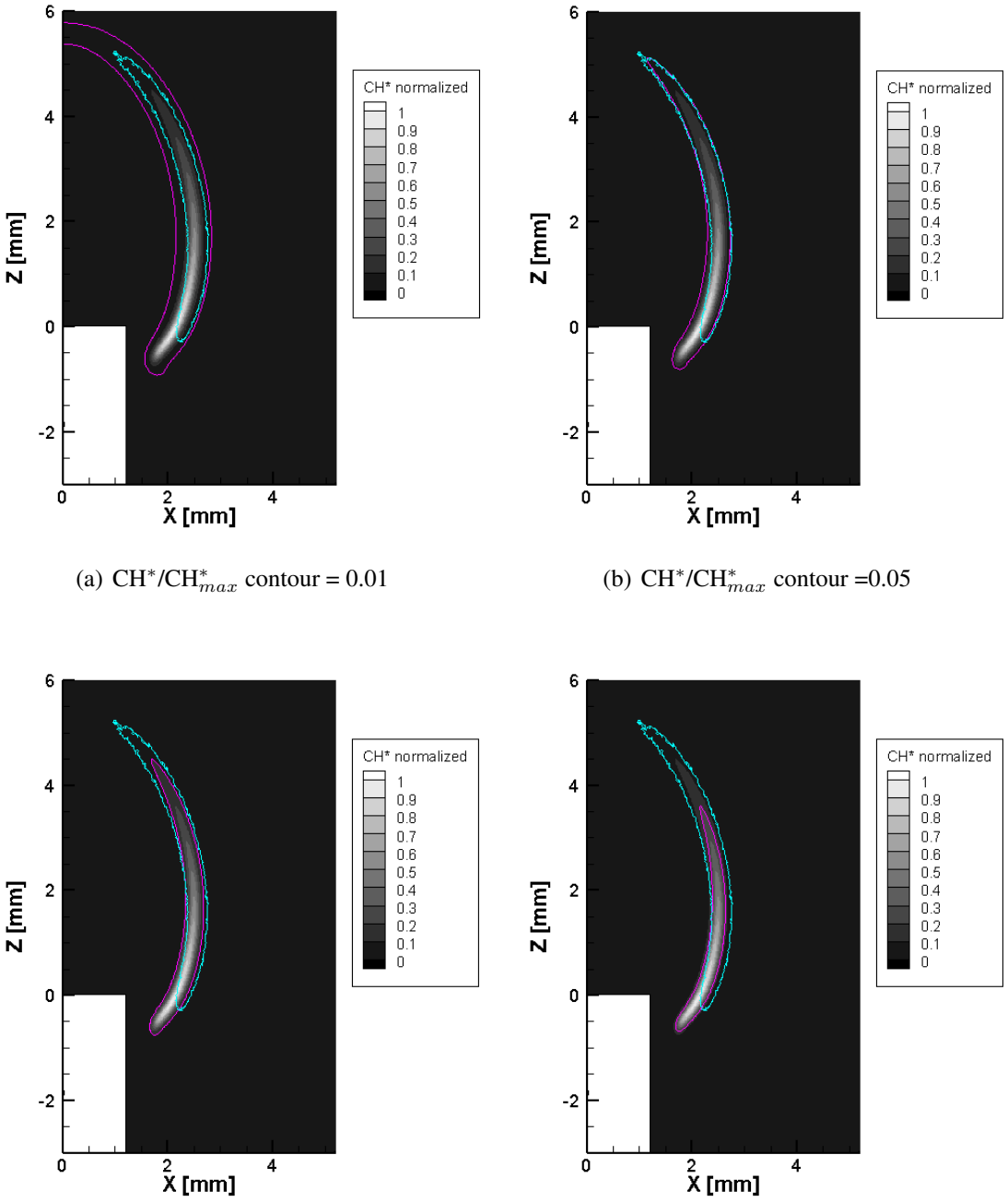

(a) CH^*/CH^*_{max} contour = 0.01

(b) CH^*/CH^*_{max} contour =0.05

(c) CH^*/CH^*_{max} contour = 0.1

(d) CH^*/CH^*_{max} contour = 0.2

Figure 3.19: CH^*/CH^*_{max} mapping (simulation), simulation CH^* contour (pink), and experimental CH^* contour from [43] (cyan).

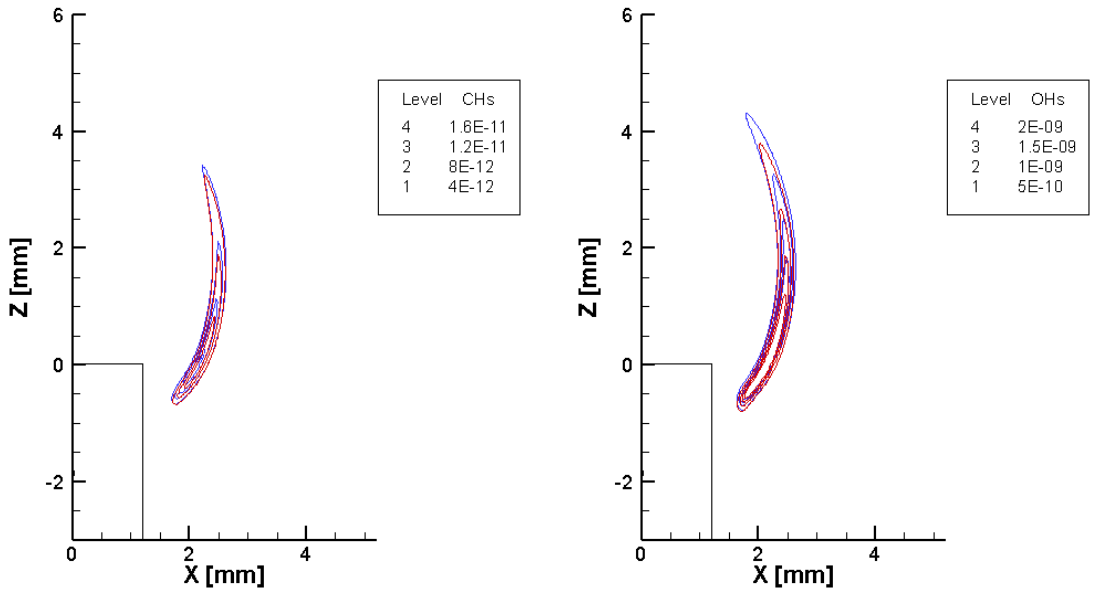

(a) (b)

Figure 3.20: Contours of 1g flame without e-field applied at steady-state. Extruded geometry. Model 0 (red), Model 1 (blue). Levels correspond to the mass fractions. Inner to outer levels go from higher level (1.6e-11 and 2e-09 for CH^* and OH^*, respectively) to lower level (4e-12 and 5e-10 for CH^* and OH^*, respectively). (a) CH^*; (b) OH^*.

The contours for OH^* elongate 0.5mm-0.9mm – for extruded and jet burner, respectively – for the top of the foremost external contour isoline using the detailed model. That isoline corresponds to the smallest concentration of OH^*. This elongation is more noticeable in the jet geometry case. Figure 3.22 shows that when normalizing the OH^* for both chemistry models, the location of OH^* differs by less than 5% for the jet geometry. Hence, the OH^* chemistry at the top of the flame is not majorly affected in trend and location, but in mass fraction distribution when the flame is placed further from the burner base (jet burner). This means that the species that react to produce/consume OH^* and that have not been targeted in the reduction process to obtain Model 1 – i.e., OH is excluded from these – are being predicted differently in Model 0 than in Model 1 and are causing the discrepancy in that region for OH^*.

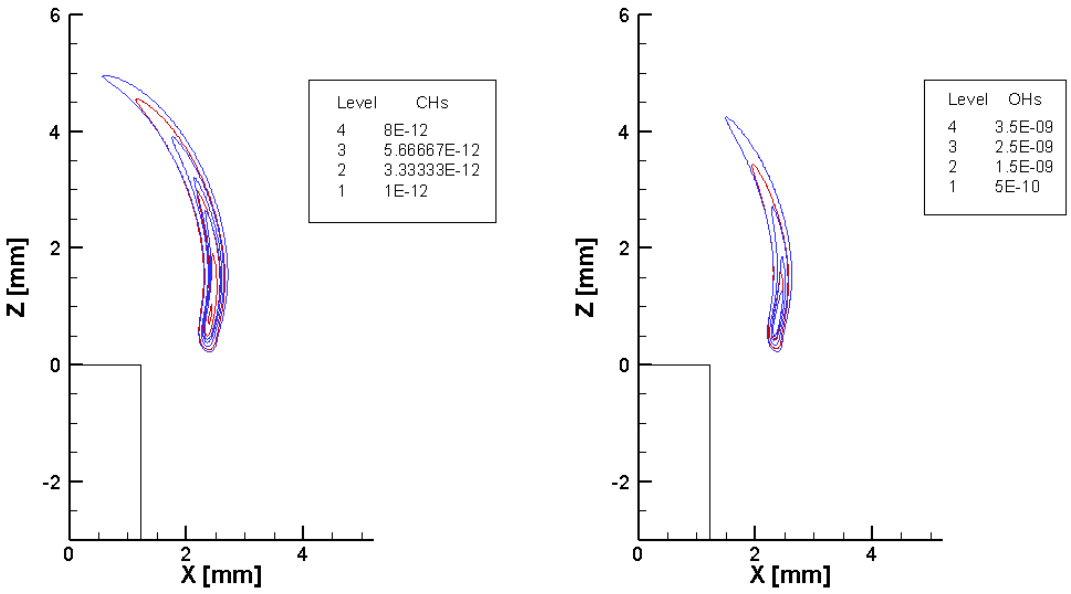

(a) (b)

Figure 3.21: Contours of 1g flame without e-field applied at steady-state. Jet geometry (close-up view). Model 0 (red), Model 1 (blue). Levels correspond to the mass fractions. Inner to outer levels go from higher level (8e-12 and 3.5e-9 for CH^* and OH^*, respectively) to lower level (1e-12 and 5e-10 for CH^* and OH^*, respectively). (a) CH^* (b) OH^*.

Focusing on the quantitative prediction of OH^* the mole fraction distribution, the peak mole fractions obtained when employing the extruded and jet geometries with Model 1 chemistry (Figure 3.23) are 6.1e-9 and 7.3e-9, respectively. The locations of the OH^* peak mole fractions in these simulations are at the bottom of their corresponding OH^* profiles, which agrees with the experimental results from Walsh et al. [71] (Figure 3.16). The comparison between the literature and simulation results shows that the profile of OH^* follows a similar trend in its distribution in the flame. However, the OH^* mole fraction peak measured in the experiments [71] is 1.3e-8, which differs by 6.9e-9 and 5.7e-9 from the values obtained in this work when employing Model 1 chemistry and the extruded and jet burners, respectively. This under-prediction of OH^* in comparison to the experimental value might be given by the fact that the experimental work purposely lifts the flame to avoid any perturbation from the closeness of the flame to the burner. Therefore, the lifting

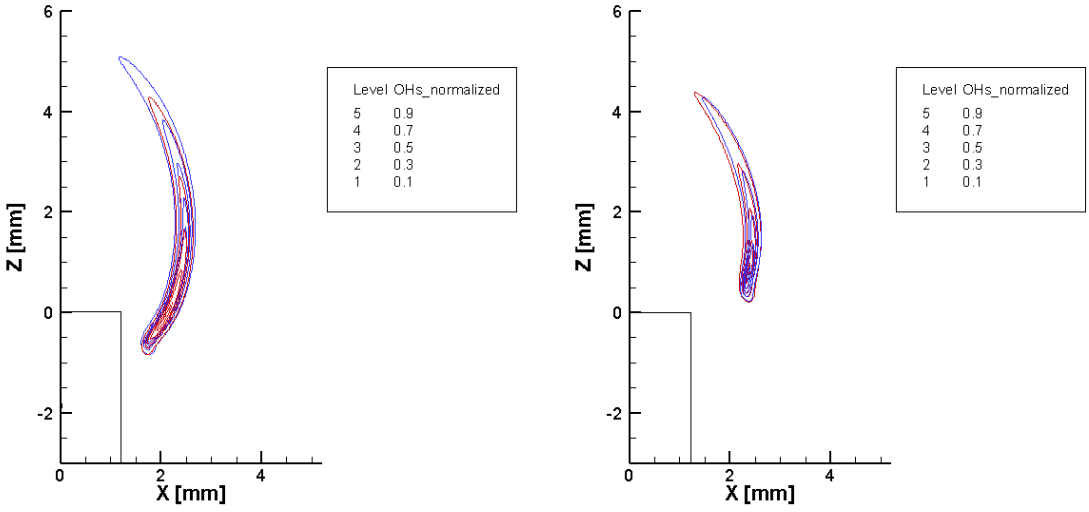

(a) (b)

Figure 3.22: OH contours for the 1g flame without e-field applied at steady-state. Close-up views. Model 0 (red), Model 1 (blue). The highest value contour (level 9) is the outer isoline. (a) Extruded burner (b) Jet burner.*

of the flame would allow more air entrainment from the bottom of the flame, which would directly affect the production of OH^* based on Reaction (Reaction 3.21).

$$CH + O_2 \longrightarrow OH^* + CO \tag{3.21}$$

In conclusion, for the scope of this study, the differences in CH^* and OH^* are considered to be a product of the accepted tolerance for the reduced model. Further analysis will determine if the discrepancy ultimately produces significant errors in the electrical response flame predictions using these chemical models.

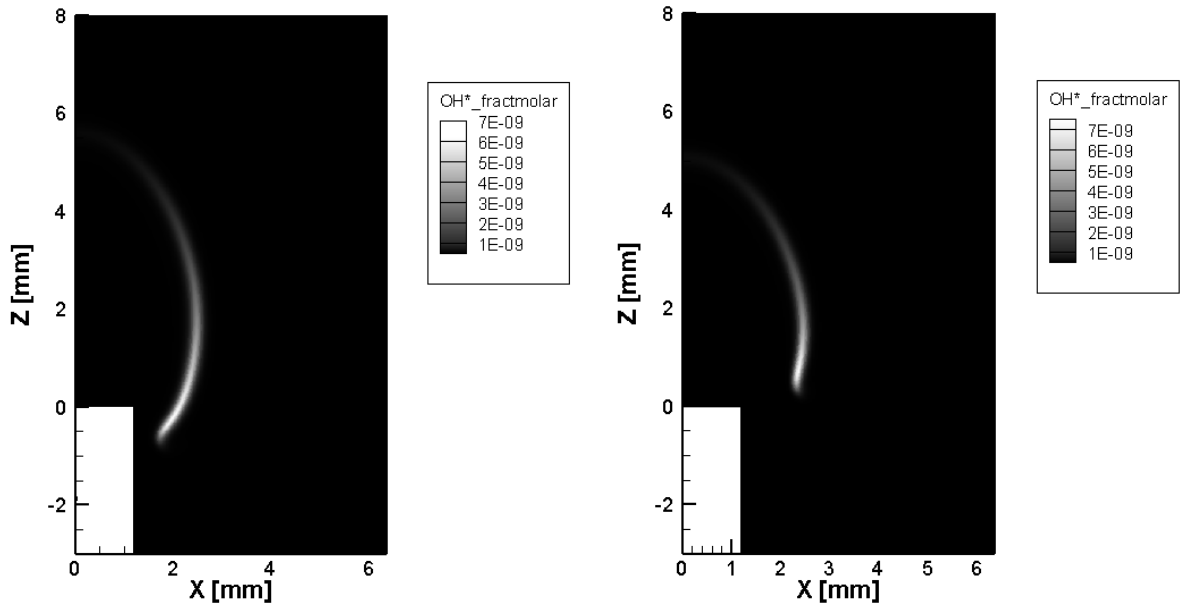

(a) (b)

Figure 3.23: (a) Extruded and (b) Jet burner configurations without external electric field applied at 1g with inlet fuel velocity of 20 mL/min. OH^* the mole fraction.

Charged species profiles, H_3O^+, HCO^+ and electrons

Figures 3.24 and 3.25 qualitatively compare the main charged species in the flame for both studied geometries using Model 0 and Model 1 chemistry simulations.

In all the cases and for both Model 0 and Model 1, there is a large region at the top where charged particles are present, while less charged species are present in the region closer to the burner tip. Nevertheless, the literature for premixed flames in lean combustion conditions found the H_3O^+ mole fraction peak was located at approximately 2mm above from the burner when employing a McKenna burner and a flat flame [99], which is similar to the results obtained here when employing Model 1 here (see Figure 3.26, CH^* contour from experiments plotted as guidance). Figure 3.26 also shows that the H_3O^+ specie is transported further away from the flame sheet, which does not occur for the HCO^+ specie. This is a major trend explained in the literature [6] and that Model 1 predicts.

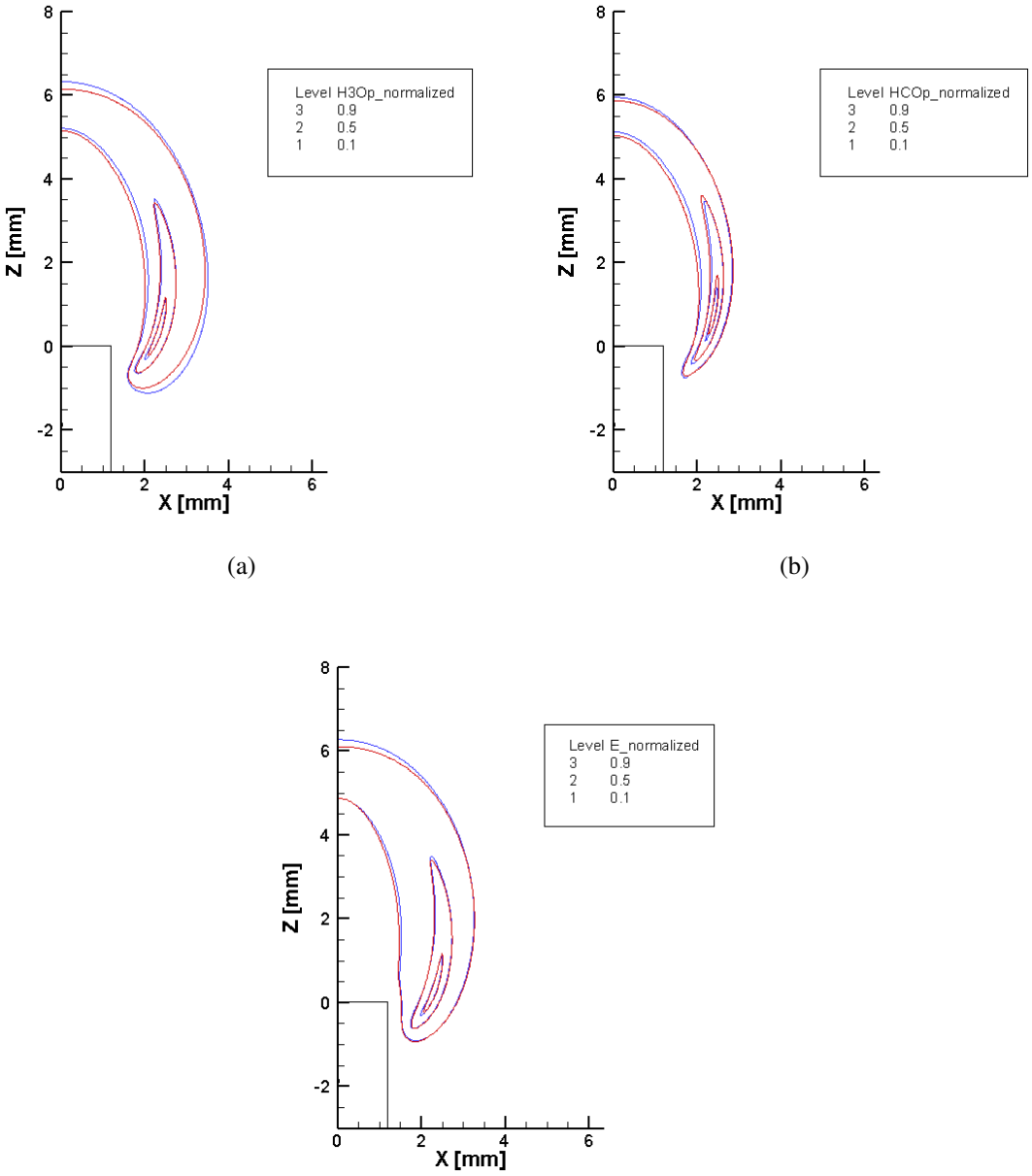

Figure 3.24: Normalized contours of 1g flame without e-field applied at steady-state. Extruded geometry. Model 0 (red), Model 1 (blue). Inner to outer levels go from higher level to lower level. (a) H_3O^+ (b) HCO^+ (c) electrons.

The disparity between the results from Model 0 or Model 1 in the jet burner case is less than 6% in location for the same mass fraction contours, which is similar to the error obtained in the literature

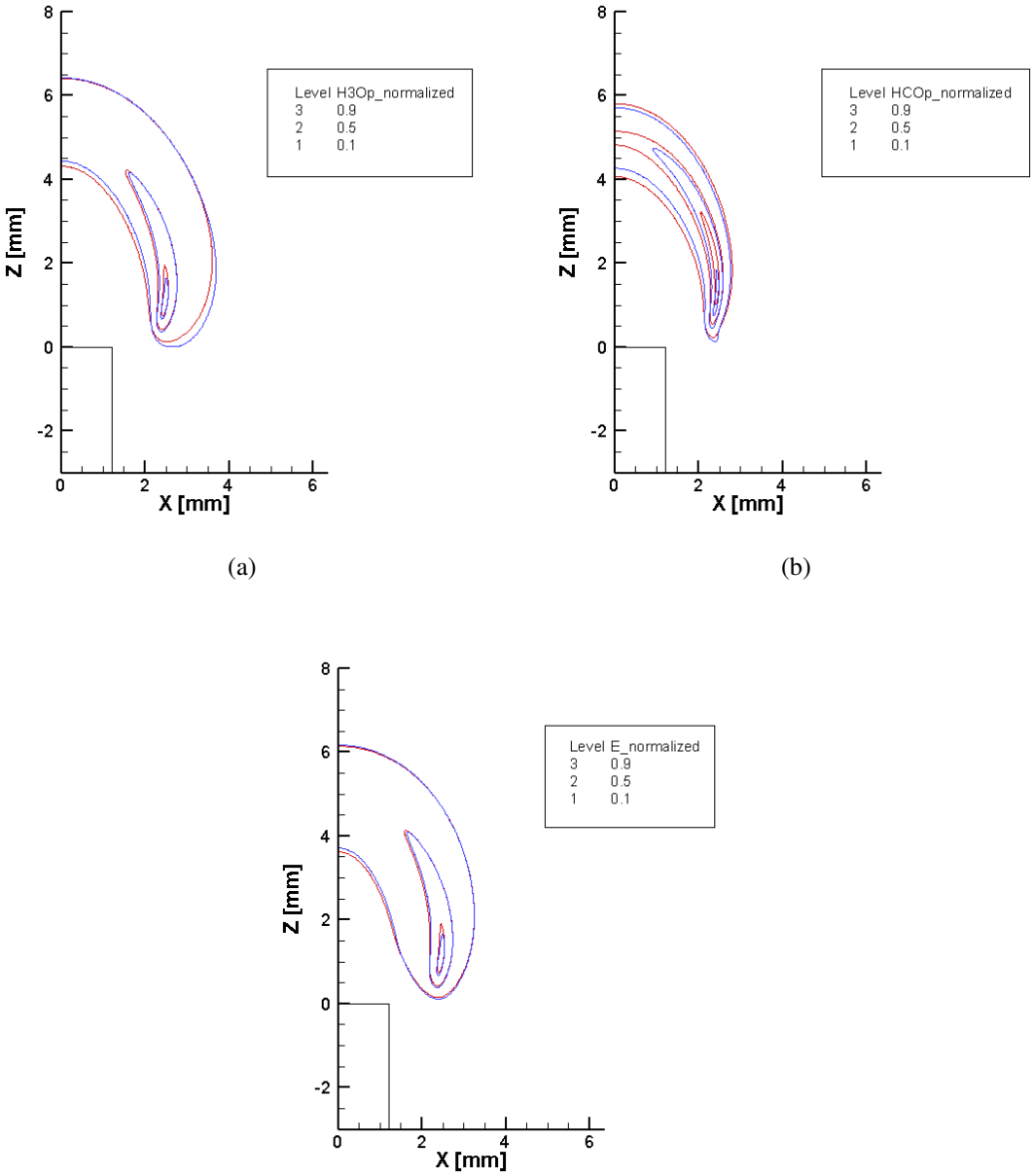

Figure 3.25: Normalized contours of 1g flame without e-field applied at steady-state. Jet geometry (close-view). Model 0 (red), Model 1 (blue). Inner to outer levels go from higher level to lower level. (a) H_3O^+ (b) HCO^+ (c) electrons.

from employing novel machine learning approaches for the reduction of chemical kinetic models [106]. This is an acceptable error considering that the concentration of these species is very low.

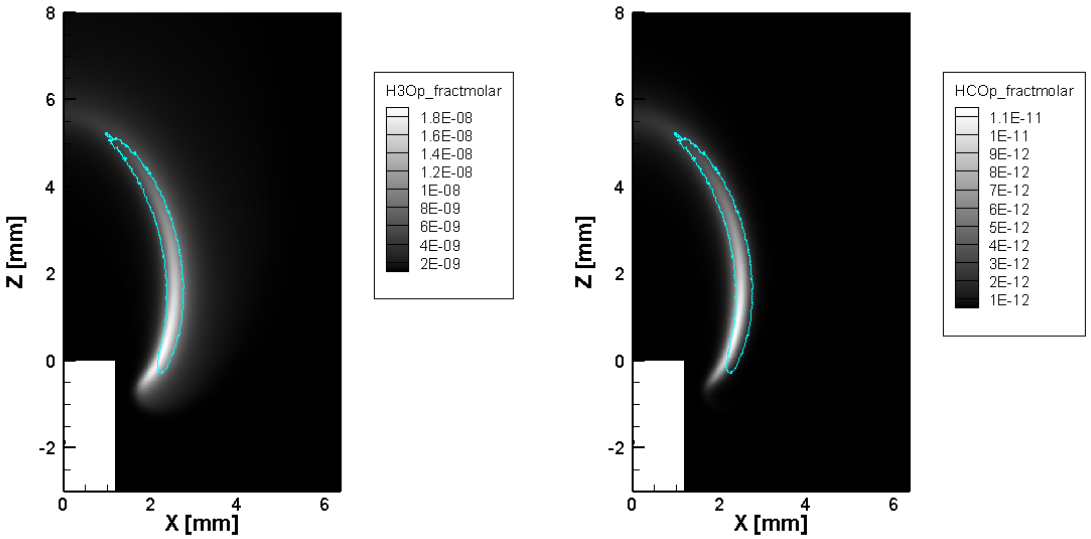

(a) (b)

Figure 3.26: Extruded geometry of the 1g flame without e-field applied at steady-state employing Model 1. Mole fractions of (a) H_3O^+ and (b) HCO^+ (mappings) with the experimental CH^* contour from [43] (cyan).

The prediction of the maximum charged species peaks and locations – shape and size – show reasonable agreement between Model 0 and Model 1.

Density gradients

Shadowgraphs are visuals of the Laplacian of the density, whose experimental equivalent representations are schlieren images. The experimental difference between shadowgraphs and schlieren images is subtle but distinct. Both show thermal gradients, but the shadowgraph is maximum contrast at the second derivative of density while the schlieren contrast matches the first derivative of density, making schlieren imaging more sensitive in most cases [107]. However, since flames generally have very sharp thermal gradients, the location of these two is not significantly different and, therefore, comparable between both image classes [108, 109]. Due to the importance of schlieren images in the experimental work and for the comparison between simulations and experiments

under applied electric field forces in Chapter 5, Model 1 must perform similarly to Model 0 under a shadowgraph comparison to be valid for this research study. In this case, the most important is where the outer boundary of the shadowgraphs is placed since that will be the information used to compare the shadowgraph contours from the simulations against the schlieren images from the experiments (see Chapter 5).

Figure 3.27 shows the comparison between the shadowgraph representations between using Model 0 and Model 1, only for the outer contour. As a clarification, the vertical and horizontal straight lines observed in these figures are an artifact of the change in mesh size that the software is unable to process. Moreover, because the resolution is artificially much higher in these simulations than can occur in real systems, the shadow contour contains spurious edges and spikes that do not occur in physical shadowgraph images.

The Model 0 and Model 1 isolines overlap in the outer contour, differing by less than 1% for both geometries. Therefore, it is concluded that both chemistry models produce the same shadowgraph outcomes. This is not surprising since we have also seen that the temperatures match very closely for both chemistry models, and the density in flames is almost entirely controlled by the temperature.

3.5 Conclusions

Generally, the predictions for the temperature and the relevant major species coincide between detailed and reduced chemical kinetic models.

There is a good agreement for the CH^* chemiluminescence location with experimental literature work. These results indicate that the reduced model captures well the CH^* qualitative and quantitative distribution on the flame, except for the divergence closer to the tip of the burner. That region has already been challenging to observe and predict in previous experimental and numeri-

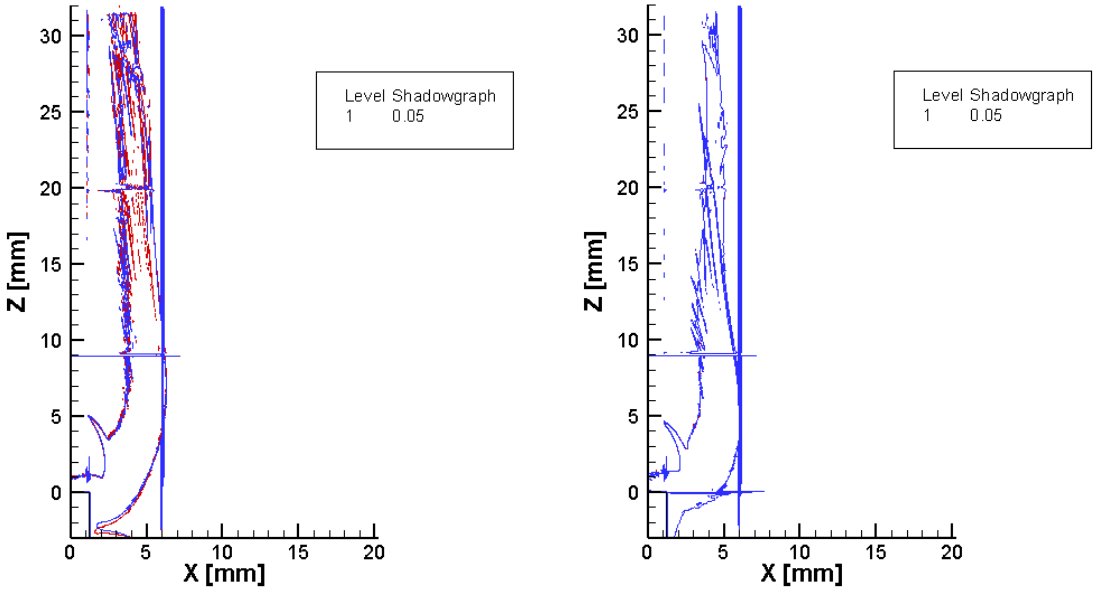

(a) (b)

Figure 3.27: Shadowgraph contours of 1g flame without e-field applied at steady-state. Model 0 (red) and Model 1 (blue). (a) Extruded burner (b) Jet burner.

cal studies due to the interaction between the flame and the jet burner that can cause perturbations in the flame itself, leading to studies that purposefully lift the flame to avoid these challenges.

The maximum of C_2H in the flame is shown to be able to be used as a reaction zone marker if there is an advantage to leaving the excited species out of the reaction model. That would be when the chemical kinetic model does not account with CH^* or if an even more reduced model wants to be developed for speeding up the simulations by removing the reactions related to CH^* keeping the capability to predict flame location considering C_2H specie.

The reduced Model 1 developed in this work reasonably captures the major desired features from the detailed Model 0 while reaching steady-state solutions more than three times faster than using the detailed chemistry kinetics.

Chapter 4

Buoyancy effects

4.1 Background

Studying flames in a variety of gravitational environments can help demonstrate the role of the gravitational body force in combustion, and by extension, it can help guide an understanding of the potential role of more general body forces on non-premixed flames. Several studies have shown how diffusion flames are affected by buoyancy forces. These studies show that the flame temperature is lower in microgravity flames [35]; flame length increases and flame radius decreases when increasing buoyancy forces, creating flames noticeably longer and narrower than their 1g counterparts – the narrowing of the flame is a consequence of the radially inward convection near the flame front [7, 8, 35, 39, 110, 111]; flame luminosity reduces at elevated gravity (supergravity conditions) due to the soot interference – i.e., carbon luminosity decreases with increasing buoyancy [38, 39]; flames eventually separate from the burner rim and finally extinguish depending on gravity conditions [38]; and microgravity sooting flames show lower soot temperatures and higher soot volume fraction, shifting its distribution from the centerline of the flame (1g) to the wings (in microgravity) [35, 56, 111]. None of these studies performed two-dimensional simulations show-

ing the effects of different gravity environments including chemi-ion chemistry, and so the current work explores if these phenomena can be replicated in numerical simulation. Additionally, the change in gravity affects the density field, which then affects the buoyant flow further. Simulations can help describe the complexity of this phenomena.

4.2 Purpose

This section aims to numerically predict the behavior of non-premixed methane/air jet flames under different gravity environments. The two jet geometries of interest examined in this chapter have been presented in Chapter 2 (extruded and jet burner geometries).

4.3 Methodology

4.3.1 Solver

The reactingFoam solver is the combustion solver for transient, compressible flows, pressure-based, and that allows chemical reactions, which makes it suitable for this work. This solver is included in the OpenFOAM® package [112]. However, the reactingFoam solver used in this work has been modified for the mass transport equation by imposing a fixed Schmidt number equal to 0.7 since previous studies showed that this assumption better captures flame characteristics such as its location as compared to the more standard assumption of Lewis number equal to 1 – which is the original approach in reactingFoam [40, 64, 113, 114, 115, 116].

The time marching scheme for the first and second-time derivatives is the default Euler method provided by OpenFOAM's subdictionaries. Linear Gaussian finite-volume integration is used for the spatial derivatives, which is also provided by OpenFOAM's subdictionaries.

The equations included in the modified reactingFoam comprise the conservation of mass (Equation 4.1), momentum (Equation 4.2), total energy (Equation 4.3), and species densities (Equation 4.4). In these equations, the variables represented are the velocity (u), the total energy (E), the mass fractions (Y_k) of N reacting species (neutral, excited, and charged), the time (t), the pressure calculated by equation of state (p), the heat flux calculated by Fourier's law (q), the viscous stress (τ), the identity tensor (I), the molar mass (W_k), the diffusion velocity (V_k), the molar source term ($\dot{w}_k$), the enthalpy formation of the species k (h_k), and the volume force acting on species k (f_k).

$$\frac{\partial \rho}{\partial t} + \bigtriangledown \cdot (\rho u) = 0 \tag{4.1}$$

$$\frac{\partial \rho u}{\partial t} + \bigtriangledown \cdot (\rho u \bigotimes u + pI - \tau) = \rho \sum_{k}^{N} Y_k f_k \tag{4.2}$$

$$\frac{\partial \rho E}{\partial t} + \bigtriangledown \cdot [\rho u E + q - (\tau - pI) \cdot u] = -\sum_{k}^{N} h_k \dot{w}_k + \rho \sum_{k}^{N} Y_k f_k \cdot (u + V_k) \tag{4.3}$$

$$\frac{\partial \rho Y_k}{\partial t} + \bigtriangledown \cdot [\rho (u - V_k) Y_k] = W_k \dot{w}_k \tag{4.4}$$

4.3.2 Computational hardware

The simulations performed in this Chapter 4 were carried out in serial using an Intel® Core™ i7-5820K processor with a frequency of 3.30GHz x 12 and in parallel using the HPC cluster at UC Irvine employing one node of 40 CPUs. The steps to run these cases are described in Section 2.3.2, being the third and last simulation run using the reduced Model 1 (see Chapter 3). The time to complete one simulation was approximately between 4464 to 8928 CPU hours – one to two months in actual calendar time running on an i7-5820K processor in series, although running times varied depending on the CPUs used and the buoyancy force considered.

For more efficiently obtaining runs at different gravities, subsequent cases use a base case steady-state solution as their starting point. The first case run is set at 1g. The final steady-state result from that case is used as an initial condition for running two new cases at higher or lower gravity, respectively. Once those two cases reach steady-state solutions, the same procedure is repeated to run even higher or lower gravity scenarios. The example schema of this is shown in Figure 4.1.

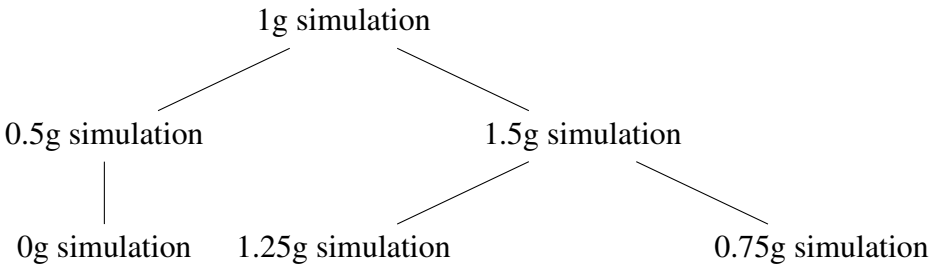

Figure 4.1: Example initial conditions schema.

In all simulations, the applied initial conditions are crucial to lead to new steady-state solutions. To avoid a possible systematic error coming from the stepwise change in gravitational force, a random case is run beginning with perturbed initial conditions to be certain that the steady-state solution is not affected.

4.3.3 Reaction model details and boundary conditions

The chemical kinetic model used is Model 1 (shown in Table 3.2), which includes excited and charged minor species. These minor species are excited methylidyne (CH^*), excited hydroxyl (OH^*), hydronium cation (H_3O^+), formyl cation (HCO^+), acetyl radical cation ($C_2H_3O^+$), protonated methyl alcohol (CH_5O^+), oxygen anion (O_2^-), hydroxyl anion (OH^-), electrons (e^-), carbonate ion (CO_3^-), formate anion (CHO_2^-), atomic oxygen anion (O^-), bicarbonate anion (CHO_3^-).

The boundary conditions and burner geometry for these simulations have been specified in Chapter 2 (reproduced again in Figure 4.2).

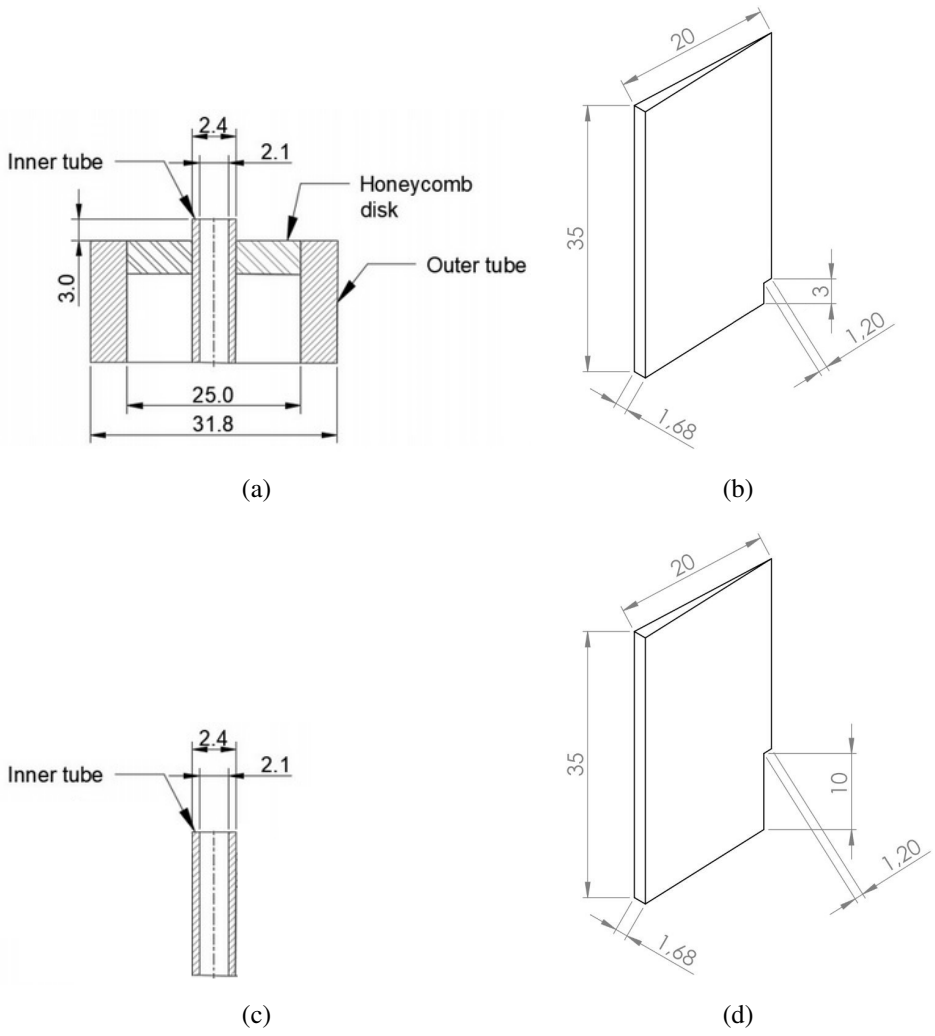

Figure 4.2: From Figure 2.1. Geometries studied and their respective simulated computational domains. (a) Extruded setup, (b) Extruded computational geometry, (c) Jet setup, (d) Jet computational geometry. Dimensions are in millimeters.

4.4 Results and discussion

The simulated flame behavior is studied under microgravity (0g), partial gravity (0.5g), gravity (1g), and supergravity (1.5g and 2g) conditions. Temperature and important minor species profiles (CH^*, H_3O^+ and HCO^+) are shown in Figures 4.3 and 4.4 for the extruded and jet burner geometries, respectively. The understanding of the minor species CH^*, H_3O^+, and HCO^+ has been

prioritized. Therefore, OH^* and the rest of the charged species included in the chemical kinetic model have been left out from the discussion at this time. The discussion of the results follows.

4.4.1 Flame temperature

Table 4.1 shows that the simulated microgravity flames' temperature is lower than the flame temperature at higher gravities –except fot the 1g extruded burner. However, the difference is less than 1K, which is well within the numerical error of the simulation. Microgravity flames also showed lower maximum temperatures in the literature [35, 101]. For the quantitative comparison, previous literature found that the highest temperature in a coflow diffusion methane flame is around 1900K (1g) and 1700K (0g) [101], which differs from the results found in this work by a maximum of ≈117 (1g) and ≈237 (0g). There are several differences in the experiments in comparison to the simulations presented in this work that can produce these differences in the temperatures, such as the jet fuel velocity and the coflow that the experiments have. Therefore, flame temperatures for 0g and 1g similar order of magnitude as when comparing them with the literature results, and the general temperature trend is to increase as gravity increases for both burner geometries.

Table 4.1: Maximum temperatures [K] for different gravities using Model 1 and the extruded or jet burner geometries.

	Burner geometry	
Gravity	**Extruded** v_{fuel} = 20mL/min	**Jet** v_{fuel} = 20mL/min
0g	2018.65	1937.85
0.5g	2046.7	1999.69
1g	2017.33	2001.24
1.5g	–	2029.98
2g	2053.37	2087.35

This work shows that when in gravity (extruded burner) and supergravity (jet burner), the higher-temperature reaction region is expanded as the flame length increases due to the gravity increment.

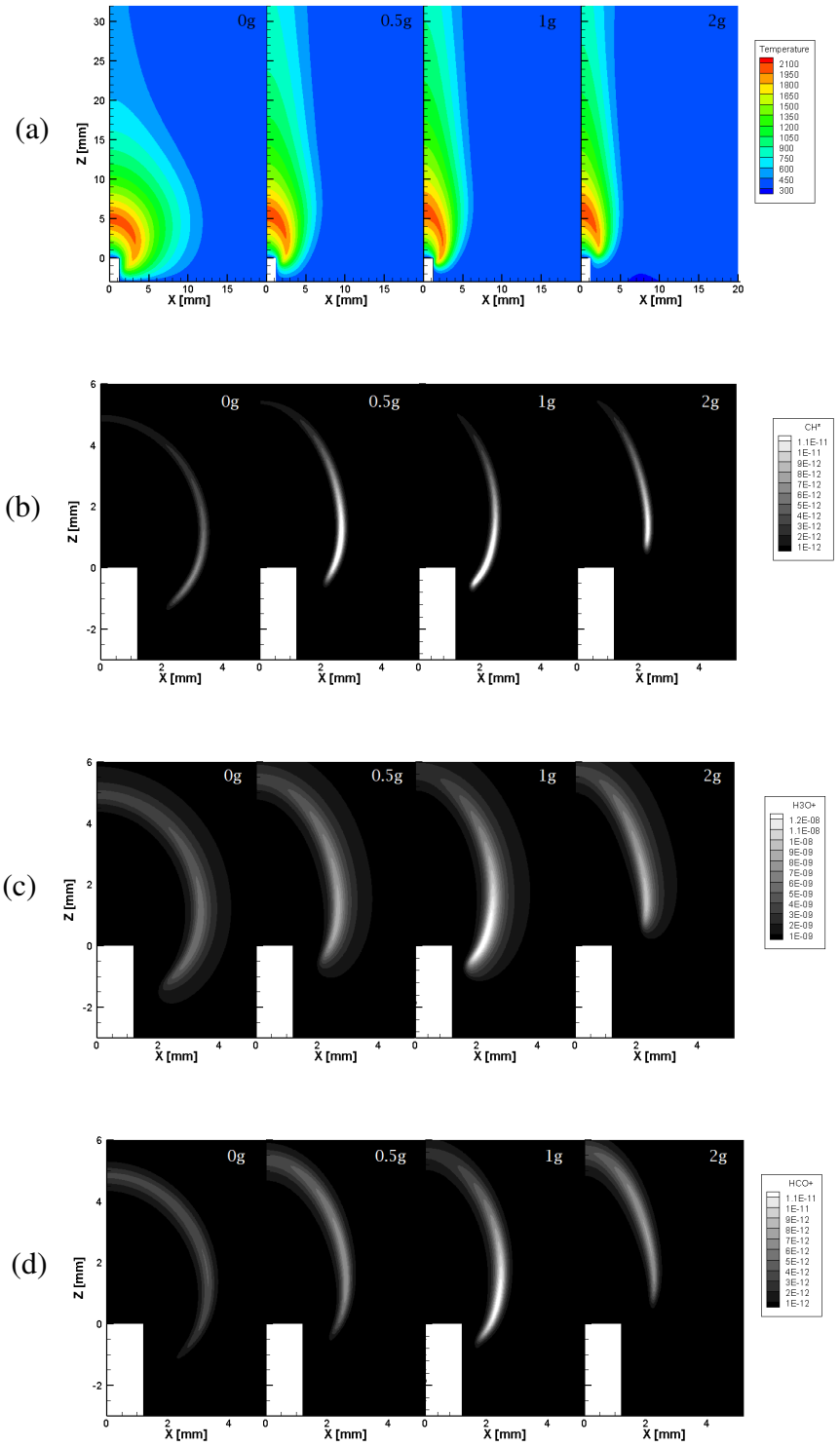

Figure 4.3: Results for (a) Temperature (full-domain), and mass fractions of (b) CH^*, (c) H_3O^+, (d) HCO^+ in the extruded burner geometry. Inlet fuel flow rate = 20mL/min. From left to right: 0g, 0.5g, 1g, and 2g. Zero in the axial direction placed at the burner tip.

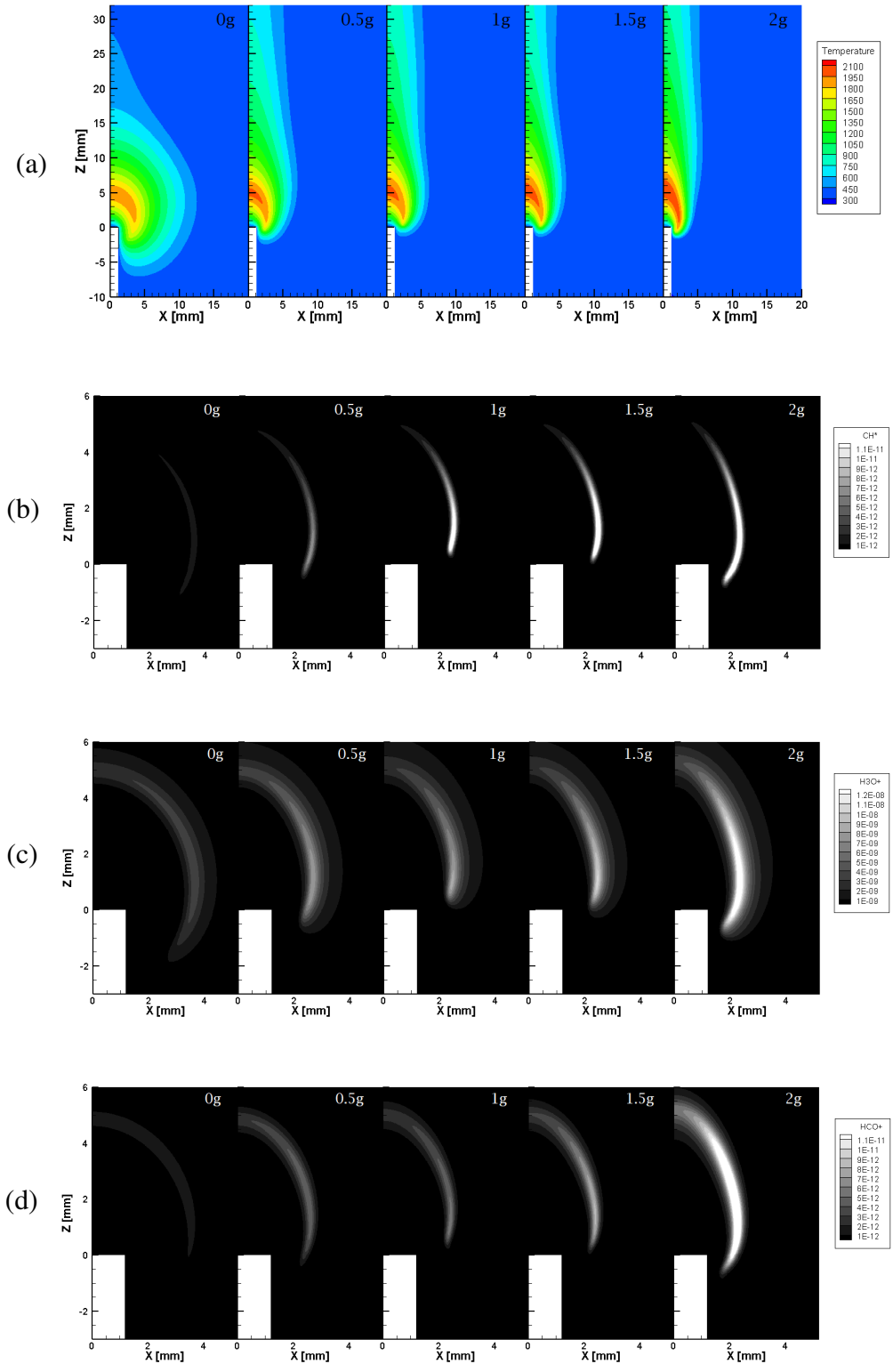

Figure 4.4: Results for (a) Temperature (full-domain), and mass fractions of (b) CH^*, (c) H_3O^+, (d) HCO^+ in the jet burner geometry (close-up view). Inlet fuel flow rate = 20mL/min. From left to right: 0g, 0.5g, 1g, 1.5g, and 2g. Zero in the axial direction placed at the burner tip.

This temperature profile trend is not reported in previous literature, but it is shown to be directly related to the enhancement of the chemiluminescent specie CH^* presence in the flame.

4.4.2 Flame structure

The discussion related to the flame structure is based on the CH^* location since, as stated before, this chemical specie is used as a flame position marker. Figure 4.5 shows the contours of the normalized CH^* specie for both burner geometries at different gravity scenarios. The contours have been taken at CH^*/CH^*_{max} = 0.05 as it showed good qualitative results in comparison with the experimental literature (see Section 3.4.3). Figure 4.6 shows the difference observed when the inlet fuel flow rate is increased by 35% in the extruded geometry burner configuration. The structure observed in both extruded and jet geometries is similar and explained next.

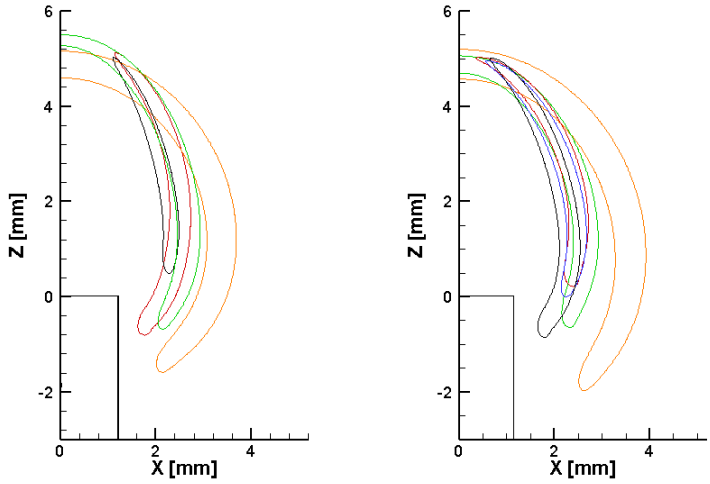

(a) Extruded burner (b) Jet burner

Figure 4.5: Simulated CH^*/CH^*_{max} contour = 0.05 at different gravity (close-up views; 0g orange, 0.5g green, 1g red, 1.5g blue, 2g black). Inlet fuel flow rate = 20mL/min

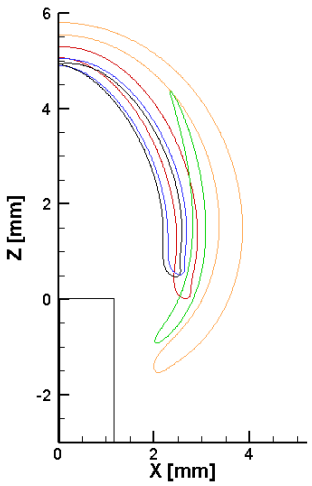

Figure 4.6: Simulated CH^*/CH^*_{max} contour = 0.05 at different gravity (close-up views; 0g orange, 0.5g green, 1g red, 1.5g blue, 2g black). Extruded geometry. Inlet fuel flow rate = 27mL/min.

Flame height and length

The definition of flame height and length is inconsistent in the literature. For this work, the flame height (h) is defined as the distance from the burner tube rim to the top of the flame, while the flame length (L) is the distance from the base of the flame to the top of the flame, based on the CH^* location.

Both Figures 4.5(a) and 4.5(b) show that flame height remains constant for buoyant flames while an increase in gravity makes the flame base move upwards, sometimes even above the burner tip. The flame height is taken as the highest point where 5% of the normalized CH^* specie is found. In these simulations, the tip of the flame is observed to be between 5mm and 5.75mm height in all cases and for all gravity environments, differing by a maximum of ±0.5mm between different gravity environments for each studied case. Unaffected flame height by gravity forces is manifested more clearly when either the jet geometry burner or a higher inlet fuel flow rate are employed. This agrees with a widely-used theoretical model developed by Roper [57], which predicted that flame height should be independent of gravity since an increase in flow acceleration caused by buoyancy

in the axial direction is compensated for by narrowing the width of the flame (i.e., narrowing the boundary layer thickness in the transverse direction).

Based on the works from Roper [57] and Altenkirch et al. [38], Sunderland et al. [39] demonstrated that the jet flame length could be scaled based on the burner diameter (d) and the non-dimensional Reynolds (Re) and Froude (Fr) numbers. The scaling follows Equations 4.5 and 4.6 for non-buoyant and buoyant flames, respectively.

$$L/d \sim Re^{2/3} \qquad \text{For non-buoyant flames} \tag{4.5}$$

$$L/d \sim Re^{2/3}Fr^{1/3} \qquad \text{For buoyant flames} \tag{4.6}$$

Based on these definitions, Sunderland et al. [117] showed that buoyant methane flames follow the trend of $(L/d)Re^{-2/3}Fr^{-1/3} = 0.486Fr^{-0.2596}$, which is similar to the trends observed in this work. For the buoyant flames employing the extruded burner geometry with an inlet fuel flow rate of 20mL/min, the trend is $(L/d)Re^{-2/3}Fr^{-1/3} = 0.5366Fr^{-0.3159}$ with an $R^2 = 0.9969$ (see Table 4.2 and the fitting in Figure 4.7). Likewise, Table 4.3 shows the parameters corresponding to the jet burner geometry at different gravities, which resolve to a flame length trend of $(L/d)Re^{-2/3}Fr^{-1/3} = 0.4389Fr^{-0.4096}$ with an $R^2 = 0.8321$.

In contrast to the buoyant flames where the flame height remains constant, non-buoyant flames are found to be shorter (Figure 4.5(a)) as long as their counterparts (Figure 4.5(b)), or longer than their counterparts at 1g (Figure 4.6), depending on the burner geometry and fuel flow rate. The disparity between results is due to competitive effects between the jet momentum and diffusion phenomena that occur at non-buoyancy environments, the former having more importance when the inlet fuel flow is higher. The proportionality proposed by the literature for non-buoyant flames (Equation

Table 4.2: Extruded burner. $Q_{inletfuel}$=20mL/min. Parameters and adimensional numbers.

Relative gravity to Earth (G)	**0**	**0.5**	**1**	**2**
g [m/s]	0	4.905	9.81	19.62
h [m]	0.0057	0.0050	0.0065	0.0063
L [m]	0.0070	0.0060	0.0060	0.0058
d [m]	0.0021	0.0021	0.0021	0.0021
L/d	3.338	2.843	2.880	2.781
u [m/s] at nozzle outlet	0.10	0.10	0.10	0.10
Re	12.417	12.397	12.395	12.321
Fr	-	1.009	0.504	0.249
$(L/D)Re^{-2/3}Fr^{-1/3}$	-	0.5291	0.6755	0.8286

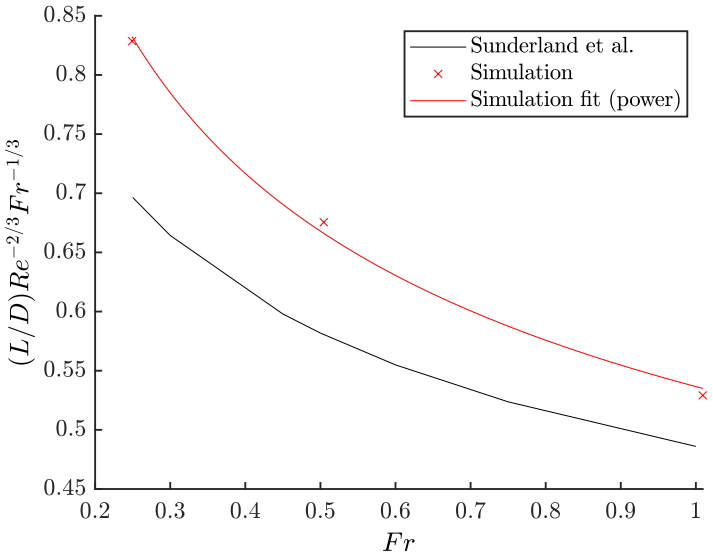

Figure 4.7: Adimensional parameters trend and fitting $(L/d)Re^{-2/3}Fr^{-1/3} = 0.5366Fr^{-0.3159}$, $R^2 = 0.9969$ (red). Sunderland et al. prediction [117] (black). Extruded burner geometry. Inlet fuel flow rate = 20mL/min.

Table 4.3: Jet burner. $Q_{inletfuel}$=20mL/min. Parameters and adimensional numbers.

Relative gravity to Earth (G)	**0**	**0.5**	**1**	**1.5**	**2**
g [m/s]	0	4.905	9.81	14.715	19.62
h [m]	0.0051	0.0050	0.0052	0.0052	0.0052
L [m]	0.0061	0.0055	0.0048	0.0049	0.0059
d [m]	0.0021	0.0021	0.0021	0.0021	0.0021
L/d	2.905	2.610	2.262	2.333	2.810
u [m/s] at nozzle outlet	0.10	0.10	0.10	0.10	0.10
Re	12.407	12.358	12.232	12.343	12.369
Fr	-	1.003	0.491	0.333	0.251
$(L/D)Re^{-2/3}Fr^{-1/3}$	-	0.488	0.540	0.630	0.832

4.5) is also followed in both burner geometries studied, showing that $L/d \approx 0.647Re^{2/3}$ for the extruded burner and $L/d \approx 0.542Re^{2/3}$ for the jet burner.

Flame width

As previously mentioned, narrower flames are obtained for higher gravity environments due to the radial convective inflow near the flame front, which agrees with the literature [7, 8, 35, 37]. Thus, the non-buoyant flames are wider due to the absence of convective flow and the radial diffusion being more significant relative to any radial inflow driven by the non-buoyant jet flow. As gravity increases, the convective flow starts to evolve, and the mechanisms of species transport, radial convection (inwards), and diffusion (outwards) start to compete, up to a time that the radial inward flow overcomes the diffusion outflow more strongly, leading to a thinner flame.

Flame position with respect to the rim of the burner

The results shown for the reaction region closer to the burner are constrained by the assumption that the burner wall boundary condition is set to 300K during the simulation. Consequently, observations related to the lifting of the flame base from the burner tip or obtaining a flame sheet that moves below the burner tip should be used only in relative terms, recognizing the numerical model limitations.

Flame lifting is expected from the burner tip occurring at higher gravity environments following literature results from Altenkirch et al. [38] when higher air flows are being injected (200-600 cm^3/s, which correspond to 12000-36000 mL/min). The flow velocity is several orders of magnitude lower in this work, and therefore, no lifted flames appear.

In addition, anchoring of the flames in microgravity and partial gravity – and Earth gravity in the extruded burner geometry – is observed (see Figures 4.5 and 4.6). This is because, for these

cases, there is a flammable mixture at the region below the burner rim due to the dominance of radial diffusion while approaching microgravity environments, which allows flames to anchor to the burner. A similar explanation about anchoring a flame with a flammable mixture around the burner region is found in the literature [38]. For the flames studied in this work, the flame anchoring behavior can also be attributed to the effect of low velocities – and diffusion – playing a dominant role and causing the flames to locate below the burner, as previous literature described [37].

Flame surface area

Karnani [34] calculated the 0g flame surface area by idealizing the flame as an oblate spheroid. His work with an experimental jet methane flame at 0g, without coflow or electric field applied, and with the mean jet flow at 24cm/s, showed a computed surface area of 750 mm^2 approximately. Using the same oblate spheroid assumption, the microgravity extruded burner flame obtained in this work – without coflow or electric field applied, and for a fuel velocity of 13.7cm/s (27mL/s) – is 496 mm^2 approximately. Some of the difference is attributable to the 10% higher flow velocity used by Karnani. The remaining 15% difference is within the combined uncertainty of the experiment and the simulation.

4.4.3 CH^* profile

Chemiluminescence associated with the relaxation of CH^* to CH is directly correlated with the luminosity of the flame – when there is no incandescent soot – and how the flame looks to the eye. As shown in Section 3.4.3, the flame structure and location of CH^* are predicted accurately for the 1g flame in comparison to the experimental data from the literature [40]. The integrated CH^* for each of the cases is shown in Table 4.4.

Table 4.4: Integral of CH (half flame) in the plane X-Z for different gravities using Model 1 and the extruded and jet burner geometries.*

Gravity	Burner geometry		
	Extruded v_{fuel} = 20mL/min	**Extruded** v_{fuel} = 27mL/min	**Jet** v_{fuel} = 20mL/min
0g	8.23e-012	5.04e-012	3.36e-012
0.5g	1.25e-011	8.66e-012	6.19e-012
1g	1.17e-011	1.01e-011	9.05e-012
2g	7.93e-012	1.05e-011	1.55e-011

The general trend observed (except for an anomaly described below for the low velocity supergravity case) is that, as gravity increases, brighter flames are obtained due to CH^* chemiluminescence. This contrasts with previous studies that described a reduction of flame luminosity due to a reduction of carbon (soot) luminosity at elevated gravity [38, 39]. Since the simulation presented in this work does not account for soot reactions, this work suggests that even though the CH^* chemiluminescence increases with buoyancy, the overall luminosity of the flame is decreased in experimental observations due to the soot luminosity masking the CH^* chemiluminescence contribution. In addition to CH^* and soot, other sources that could be contributing to the overall flame luminosity because they also emit in the visible range (such as C_2*, CO_2*, that emit at 516.5nm and 455nm, respectively) have not been considered in this work. Including these species in the simulation would modify the overall integrated luminescence obtained in the flames presented in this work, but considering that all excited species are intensified at higher temperatures, the general finding of increasing luminosity with increasing gravity are likely to persist..

The extruded burner geometry seems to present a singular behavior when injecting the fuel at a lower velocity and increasing the gravity environment up to 2g. Since the 1g simulation employing the extruded burner has been successfully validated against numerical and experimental data in Chapter 3, the out-of-trend behavior in CH^* mass fraction might be given by either (i) the simulation reached a steady-state that is not truly the final steady-state, or (ii) the inlet fuel velocity is too small that the buoyancy forces have a bigger effect than the convective forces at supergravity and cause the flame to lift, changing the expected CH^* mass fraction trend. As Figure 4.6 showed

a comprehensible and consistent trend behavior of the CH^* location, it is concluded that the out-of-trend prediction of CH^* mass fraction in the flame is caused by an intermediate steady-state solution coming from the simulation. This inaccuracy in the CH^* quantitative prediction for the supergravity environment computed is directly correlated with the production of charged species (as seen in the next section), and therefore, neither excited nor charged species can be taken as quantitatively accurate at supergravity for this particular studied case.

4.4.4 H_3O^+ and HCO^+ profiles

The main chemi-ions naturally produced by the flame, H_3O^+, and HCO^+, are shown to be in similar or higher mass concentrations than CH^*. Moreover, the charged species' location overlaps with the excited CH^*, and the peak concentrations also converge in the same flame location. Previous literature has hypothesized a possible proportionality between ion production and CH^* reaction intensity, implying that if true, one could measure only one and infer the other [34]. Since the prediction in excited species at supergravity is not accurate for the fuel inlet velocity of 20mL/min, Table 4.5 shows the results obtained in this work for the jet burner flame. These results are used to challenge the hypothesis that both excited and charged species are related by looking into the possible relation between temperature, CH^*, and H_3O^+.

Table 4.5: Values obtained from the region with the highest H_3O^+ and within the CH^*/CH^*_{max} = 0.05

Gravity [G]	X [mm]	Z [mm]	T [K]	CH^*	H_3O^+
0	3.6429	0.003645	1793.03	1.54E-12	3.62E-09
0.5	2.605	0.4836	1765.42	6.50E-12	7.59E-09
1	2.44	0.898	1752.218	1.68E-11	8.41E-09
1.5	2.42	0.6219	1735.345	1.71E-11	9.52E-09
2	2.259	0.2991	1906.657	1.93E-11	1.50E-08

Examining a multivariable regression analysis of the values shown in Table 4.5, the relation between temperature, CH^*, and H_3O^+ is obtained (Equation 4.7, where T states for temperature and Y_i is the mass fraction of the species i, being i = CH^*, H_3O^+). The adjusted R^2 (which is obtained

for multivariable regressions) is equal to 0.837. This adjusted R^2 value is generally considered to show a strong correlation between the multiple variables, which confirms the literature's hypothesis. Nonetheless, a more exhaustive analysis is recommended as future work to observe if when including other variables into the analysis, the adjusted R^2 value increases – i.e., a more precise multivariable trend is obtained.

$$Y_{H_3O^+} = -4.57e-08 + 2.78e-11 \cdot T + 389 \cdot Y_{CH^*} \quad \text{R}^2 \text{ (multivariable) = 0.837} \qquad (4.7)$$

Moreover, and as seen in Table 4.5 and Figures 4.3 and 4.4, higher mass fractions of H_3O^+ are obtained under stronger gravity environments – with the previously mentioned exception of the 2g extruded case due to a numerical inaccuracy on the steady-state predicted. Also, from Figures 4.3 and 4.4, it is confirmed that H_3O^+ is transported further away from the peak generation region in comparison to the other ions considered. These results are consistent with expectations that: (i) HCO^+ is produced but is very short-lived and reacts very quickly into H_3O^+; and (ii) H_3O^+ has a much longer lifetime and is able to diffuse outside the reaction zone.

As previously mentioned, flame temperature increases with gravity, making reaction rates increase as the shear layers become thinner. It is known that a higher temperature can produce more ions with the same carbon influx, which correlates with the observations of this work.

4.4.5 Schlieren images and shadowgraphs

As mentioned in Chapter 3, schlieren and shadowgraph imaging are optical techniques used for visualizing non-homogeneous density gradients in flows. Since a flame environment is characterized by large density gradients, these techniques can provide information about the flame thermal plume.

In this case, a comparison between the simulated schlieren calculations from Tinajero [40] and this work's simulated shadowgraphs is performed for the extruded geometry. The major difference between the simulations from Tinajero and the ones from this work is the chemical kinetic model used: the Tinajero simulations did not consider charged species in the chemical kinetic model used, plus the GRI-Mech 3.0 [68] was employed for the predictions of the neutral species reactions – which has already been discussed in Chapter 3 to predict CH differently, which then affects the CH^* presence in the flame. Also, it is unclear the jet fuel flow that the Tinajero simulations used. The inlet fuel flow employed for this comparison in this work's simulation is set at 20mL/min (Figure 4.8(a)).

Figure 4.8 shows (a) the results of this work, (b) the results from Tinajero [40], and (c) the comparison of results from both works in superposition. Based on Figure 4.8(c), the simulations from this work predict the 1g flame shadowgraph being similar to the result for the 2g schlieren. There is no apparent reason for this beyond the possible difference in boundary conditions and the different chemical model used. However, Tijanero already pointed out that the thermal boundary layer reduction obtained in his results was under-predicted, yet it is captured by the results from this work's simulation – i.e., larger separation between different shadowgraph profiles for buoyant flames.

4.5 Conclusion

Simulations including excited species and chemi-ions reproduce successfully many of the main flame characteristics. The temperature of the microgravity flames is generally lower than for buoyant flames. Flame height is not affected by a change in the gravity field while flame width decreased. Wider flames have been observed at lower gravity environments due to radial diffusion being more significant relative to any radial inflow driven by the only weakly rising buoyant plume. For lower gravity environments, the flame sheet anchors below the burner tip.

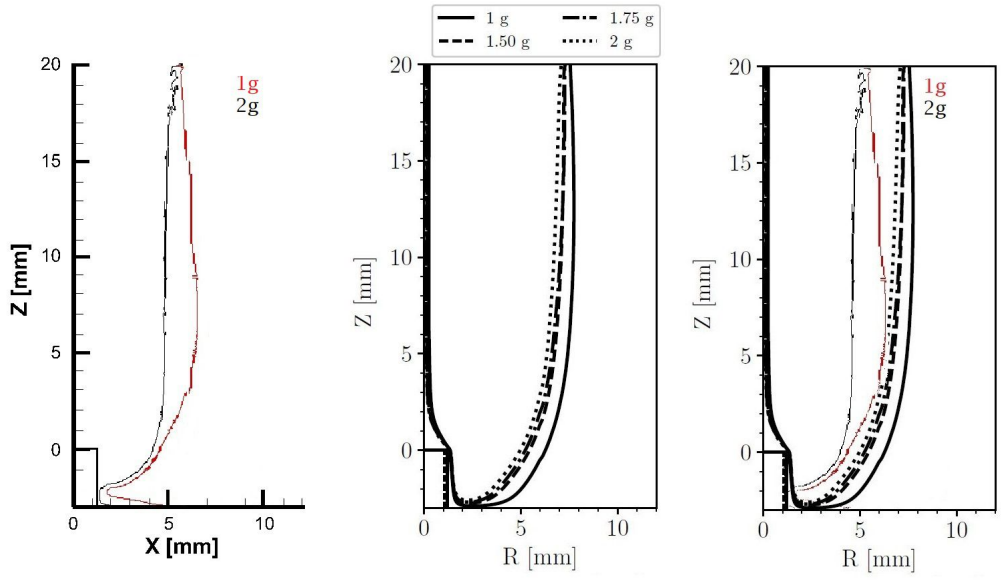

(a) (b) (c)

Figure 4.8: (a) Shadowgraph profiles from this work at different gravities; (b) Schlieren profiles from Tinajero [40].; (c) Comparison by superposition of (a) and (b).

Even though supergravity flames have been seen in past work to show a lower luminosity, these calculations suggest that the flame CH^* luminosity is increased when increasing buoyancy due to the expansion of the high-temperature region in the flame.

Non-buoyant flames are shown to follow the trend $L/d \approx 0.647Re^{2/3}$ for the extruded burner and $L/d \approx 0.542Re^{2/3}$ for the jet burner. For buoyant flames, the trend followed is $(L/d)Re^{-2/3}Fr^{-1/3} = 0.5366Fr^{-0.3159}$, $R^2 = 0.9969$ for the extruded burner and $(L/d)Re^{-2/3}Fr^{-1/3} = 0.4389Fr^{-0.4096}$, $R^2 = 0.8321$ for the jet burner.

A correlation between the major naturally produced ion in the flame (H_3O^+) and the CH^* chemi-luminescence specie has been achieved, confirming the literature hypothesis predicting a relation between ions and excited species in the flame.

Lastly, chemi-ion profiles show that H_3O^+ can be transported further than other chemi-ions without recombination. Moreover, a higher concentration of naturally produced chemi-ions occurs under

supergravity conditions, which makes these conditions interesting for future investigation of flame control by using electric fields. However, it is too early to predict the flame behavior under these conditions since competing effects of buoyant driven convection are stronger at higher gravities, and the net competition between buoyant and electric field effects can go in either direction.

Chapter 5

External electric field effects

5.1 Background

Understanding the electric body force driven flame behavior might allow more efficient combustion applications such as electrolysis processes to deposit ions on electrodes or to traverse gas while inducing chemical effects in the flame, the movement of charge in methods of detection and measurement – e.g., analyzing changes in an electric field to detect flame presence – [6, 23], and also for nanomaterial synthesis to avoid carbon agglomeration when creating nanocarbon materials by flame synthesis (at times called thermal vapor deposition processes) [1]. External electric fields act upon the naturally produced charged species (chemi-ions and electrons) within a hydrocarbon flame and thereby change flame behavior (e.g., flame shape, luminosity, soot tendency) [6, 23, 34, 118, 119]. While the observed behavior is generally attributed to the ion-wind effect[1] [6], how the ion-driven convection feeds back to the ion production of the flame– which is the driver of the ion-driven wind – is not well understood. The coupling between the chemistry and

[1] As explained in Chapter 1, the *ion wind* is the generation of a body force that occurs when the naturally produced charged species (ions and electrons) in the flame are accelerated in response to an external electromagnetic field and collide with surrounding neutral species, producing a net acceleration in the bulk gas – i.e., the ion wind.

the ion-driven flow field is too complex to clearly differentiate both contributions without employing simulations.

Most of the work done to understand flame behavior under weak applied electric fields has been performed experimentally [20, 28, 29, 33, 34, 119] due to the numerical challenge and computational resources required to achieve multi-dimensional simulation results. However, computational tools have evolved rapidly during the last decade, and there are now powerful machines capable of handling high volumes of parallelized coding data and allowing numerical and experimental work to complement each other. Reinforcing previous experimental observations [20, 28], Belhi et al. developed a two-dimensional simulation for a counterflow non-premixed methane/air flame under the influence of an electric field [96, 120]. A similar study was also published by Di Renzo et al. [121]. Later, Belhi et al. [19] also investigated the behavior of a three-dimensional jet flame configuration with an applied DC electric field positioned transversely to the flame jet flow employing the same numerical tool as was used in their previous two-dimensional study. However, these studies employ a premixed fuel mixture, and the configuration used does not permit evaluation of the electric flow feedback described previously – the coupling between the chemistry and the ion-driven flow field – because the counterflow flame is constrained by continuity to prevent the feedback and the transverse calculation is not symmetric, and so it is less feasible to trace the connections.

Therefore, the challenges to predict flame behavior under the configurations studied in this work are due to the non-premixing of the reactants (fuel and air) and the flow field being in the same direction as the electric field. On the one hand, the former has been avoided in the literature by either employing premixed flames [122] or by reducing the problem to one dimension using non-premixed counterflow configurations and analyzing the non-premixed flame challenges along the centerline [96, 120, 123, 124]. On the other hand, the applied e-field being positioned in the same direction as the jet flow leads to fundamentally different outcomes on flame behavior than the ones

provided in the previously-mentioned literature, as seen in the experiments [40]. In that context, two major aspects of this work's configurations should be highlighted:

- Firstly, the two different jet burner geometries used in this work (called extruded and jet burners) represent two different electric field distributions [40]: for the jet burner, the strongest local electric field is expected to be along the centerline – since it is where shortest field line locates; for the extruded burner, the electric field lines will maintain a quasi-parallel form, but its flame structure will be similar to the jet burner flame (see explanation in Section 2.3 in Chapter 2).
- Secondly, the chemistry and electric field effects are coupled in these configurations as both the convective flow field and electric field are aligned in the same direction. This is distinct from previous computational works where the electric field is placed in the transverse direction with respect to the flow field, which makes difficult the distinction between chemical and electric field effects [19].

The five available numerical works in the literature that employ a similar e-field configuration are from Papac et al. [125], Yamashita et al. [118], Sayed-Kassem et al. [126], Ren et al. [127], and Belhi et al. [96]. A summary of the major findings from these studies follows.

- The studies from Papac et al. [125] and Yamashita et al. [118] were two-dimensional axisymmetric simulations of a downward pointing jet, whose burner base and burner acted as one electrode and a metallic plate or mesh placed below the burner tip was the second electrode. Papac's work describes the flow field of entrained gases and exhaust surrounding a gaseous fuel flame exposed to electric fields. In contrast, Yamashita's study describes the underlying mechanisms responsible for the voltage–current characteristic response of a capillary-fed methane diffusion flame with an electric field applied, testing its numerical simulation for voltages as high as 3.4kV. These studies showed (i) the existence of a competition between buoyant and electric body forces leading to a complex flow situation [125];

(ii) the presence of flow recirculation vortex anchored just outside of the ion conduction path and sustained by an upward flow being entrained into the buoyant plume above the flame, which was caused by a prevailing buoyant flow accelerated by an upward ion driven wind at the top of the flame [125]; (iii) the time it takes for the flame to respond to electrical actuation, which is found to be the time it takes the convective flow to form above the flame while sustaining the lower vortex by flow entrainment ($\approx$ 100 and 200 ms) [125]; (iv) air around the flame becomes entrained in the pre-flame zone, resulting from changes in the flow field due to the ion-driven wind [118]; (v) local increases in air entrainment change the pure diffusion flame to a partially premixed flame [118]; and that (vi) the chemical reaction pathways are changed by the inflow of air creating an enhancement of ion production.

- Sayed-Kassem et al. [126] carried out experimental work and numerical simulations of a coflow non-premixed ethylene flame to see how soot particles were affected by a DC electric field. They grounded the coflow burner and placed a downstream electrode mesh that was positively charged with a maximum voltage of 20kV. This work reached similar conclusions as previous studies, claiming that the ionic wind is the main cause of the geometrical modifications of the flame due to the increase in the burning rate. Also, they concluded that the electric field has a strong influence on soot formation and emission, which is likely caused by the electric field affecting the residence time and the environment of soot formation and growth.

- Ren et al. [127] showed both experiments and numerical calculations of DC electric fields acting on a premixed methane-air stagnation flame employing a one-dimensional flat flame and a conical flame under -1.36kV applied. The electric field configuration employed had the jet burner grounded and acting as one electrode, and a copper plate placed downstream of the nozzle acting as the second electrode. This study's main point was to show that both modes (flat flame and conical flame) can be obtained when an applied DC field is present due to the two-way interaction between the electric and hydrodynamic responses of the flame.

- Belhi et al. [96] proposed a very similar configuration as the one from this work, with a jet burner acting as one electrode and a mesh placed above the burner acting as the second electrode, and they calculated it for positive and negative polarities. However, they used premixed methane/air. This paper's objective was to develop a detailed modeling framework – in terms of transport and chemical kinetic predictions – for the quantitative prediction of the I–V curves in methane/air flames.

The current study presents a two-dimensional simulation of a non-premixed methane/air flame for two different jet burner geometries, where the position of the electrodes aligns the electric field force, the flame jet flow, and the natural convective flux. Distinctly from previous studies, this work identifies the contributions of the chemistry and electric field effects in flame behavior and explains the coupling between them.

5.2 Purpose

The main reason for carrying out these simulations is to be able to calculate the feedback of ion-wind effects on flames to pursue, in the future, an active control of the flame by driving the ion wind. Therefore, this Chapter 5 aims to obtain a numerical prediction of the behavior of methane/air jet flames in the two jet geometries of interest (presented in Chapter 2) under different applied electric field conditions at 1g. In doing so, it will be possible to trace the feedback link between the ion-driven convection in these systems and the changes to the flame that create this wind. By demonstrating a high-fidelity simulation of these phenomena, it will facilitate the design of new electrode and burner configurations that can maximize the electric field control of combustion.

5.3 Methodology

Negative voltages were applied to the upper downstream electrode (anode) while the burner was grounded (cathode). As such, the positive ions are drawn upwards toward the anode (which would represent a metallic mesh in experiments). Positive voltages will be considered in future simulations after understanding if the negative voltage simulations give trustworthy results. All the simulations in this Chapter 5 have the inlet fuel flow $Q_{inletfuel}$ set at 27mL/min, except if specified differently.

5.3.1 Solver

The modified version of the reactingFoam solver in OpenFOAM® proposed by Belhi et al. [96] is used. Description of the modifications implemented in the solver to allow for the simulation of ionized flames in electric fields can be found in the literature [96]. In contrast to the Belhi work, where the diffusion coefficients of neutral species are approximated using a constant Lewis number assumption [19, 96], this work assumes that the Schmidt number is constant and set equal to 0.7. As previously mentioned in Chapter 4, Schmidt number equal to 0.7 is the most suitable assumption for different combustion processes [40, 113, 114, 115], including the one investigated in this work. The time marching scheme for the time derivatives is set to the default Euler scheme, and the linear Gaussian finite-volume integration is used for the spatial derivatives.

The equations included in the modified reactingFoam correspond to the conservation of mass equation (Equation 4.1), momentum (Equation 4.2), total energy (Equation 4.3), and species densities (Equation 4.4). Moreover, the expressions related to the application of electric field are also implemented in the solver (Equations 5.1, 5.2, and 5.3). In these equations, the variables represented are the electric force (F), the charge number (q_k), the number density of charged species k (n_k), the number of species considered in the chemical kinetic reaction model (N), the elementary charge

($e = 1.602 \cdot 10^{19}$ C), the electric field vector (E, defined by Gauss law in Equation 5.2), the electric potential (V), the vacuum permittivity ($\epsilon_0 = 8.854 \cdot 10^{12}$ F/m), the species diffusion velocity vector (V_k), the mass fraction of species k (Y_k). the mole fraction of species k (X_k), the molar mass of species k (W_k), the diffusion coefficient of species k (D_k), the electric mobility (μ_k).

$$F = \sum_{k}^{N} q_k e E n_k \tag{5.1}$$

$$\bigtriangledown \cdot E = - \bigtriangledown^2 V = \frac{\sum\limits_{k} q_k e n_k}{\epsilon_0} \tag{5.2}$$

$$\rho Y_k V_k = -\rho D_k \frac{W_k}{W} \bigtriangledown X_k + \frac{q_k}{|q_k|} \rho Y_k \mu_k E \tag{5.3}$$

Moreover, the electric current reaching the upper boundary of the domain (anode) is calculated in the post-processing of the simulation by computing the sum of current density (J) over the surface area where the current flows (S, the anode surface) employing Equation 5.4. In this equation, i is the electric current, and U is the bulk velocity vector.

$$i = \int_S J dS = e \int_S \sum_{k}^{N} n_k E \mu_k dS = e \int_S \sum_{k}^{N} q_k n_k (U + V_k) dS \tag{5.4}$$

For the further discussion, it is important to notice that Equations 5.1 and 5.4 indirectly show the inverse proportionality between the electric field force and the mobility of species μ_k in the flame (see Equation 5.5, where ν is the velocity of gas). This inverse proportionality is valid up to the *breakdown field*, when secondary ionization happens [6]. This relationship explains why the electron contribution to the ion-wind effect is small compared to the charged clusters – i.e., since electrons have much higher mobility, the electric force they carry is small, producing a less

pronounced dragging effect than in the case of species with lower mobility. This is a known fundamental aspect of electrically actuated flames.

$$\mu_k = \frac{\nu}{E} = \frac{U + V_k}{E} = \frac{\sum_k^N q_k e n_k (U + V_k)}{\sum_k^N q_k e E n_k} = \frac{J}{F} \tag{5.5}$$

However, and as pointed out from previous literature [96], electrons are also important because they can attach to neutrals and create negative ions which then have low mobility and do create force. In that regard, Felix Weinberg's et al. [6] showed that the electrons do not travel far in the unburned gas before they attach, but they can travel quite a distance in the burned gas plume as electrons. This has an effect relative to detecting flames electrically.

5.3.2 Computational hardware

Simulations are performed using 512 CPU-cores in the Shaheen Supercomputer from the Supercomputing Laboratory from the King Abdullah University of Science and Technology (KAUST) in Saudi Arabia. Shaheen Supercomputer is a 36 rack Cray-XC40 system.

5.3.3 Reaction model details

The chemical kinetic model proposed by Belhi et al. [96] is used, which accounts for 17 neutral species, one positive ion, five negative ions, and electrons. The Sutherland constants related to the viscosity of each specie are predicted by Tinajero [40] using Cantera® software. The ion mobilities and diffusivities are determined using the mixture-average rules with interaction potentials, which are appropriate for collisions involving charged species. The ion transport coefficients (ion-neutral and ion-charge interactions) are determined using the (n,6,4) and Coulomb interaction potentials,

respectively [128, 129]. Electron transport coefficients are computed as a function of temperature, and mixture composition [130]. The thermodynamic properties of the charged species are extracted from Burcat's database [90] and are the same ones employed by Belhi et al. [96].

On the other hand, because the chemical kinetic model proposed by Belhi et al. [96] does not contain C_2H nor CH^* to predict the flame location, the only possible specie that can be used as a marker for the flame location that shows a relative low deviation from the CH^* position – if that specie would have been included in the model – is the monoatomic hydrogen (H). As shown by Figure 5.1, which displays the results for the 1g flame simulation without an electric field applied (see Chapter 4), the simulated H/H_{max} = 0.65 contour overlaps the CH^*/CH^*_{max} = 0.05 from the simulation in $\approx$75% of it, while it overlaps the experimental CH^* contour by $\approx$70%. Thus, this is taken as a marker for flame location when employing this chemical kinetic model. As a further validation that atomic hydrogen can be taken as a flame marker, Figure 5.2 shows that even though CH^* and H mole fractions are quantitatively different, the peak location of these species differs by 4% employing a counterflow burner without an electric field applied (same counterflow simulations as in Chapter 3). The mole fraction peaks for CH^* and H are found approximately at the same place as the peak temperature occurs.

As in Belhi et al. [96], for speeding up the numerical simulation, the CH specie and its reactions are not included in these simulations. Therefore, the chemi-ionization reaction (Reaction 3.8) and the HCO^+ ion are neglected in this chemical kinetic model. However, since HCO^+ is transformed very rapidly into H_3O^+ by Reaction 3.9, the molar ion production rate (ω_p^i) can be calculated as shown in Equation 5.6, where $\omega_p^{H_3O^+}$ is the molar H_3O^+ production and k_c is the chemi-ionization rate. Moreover, Belhi et al. [19] showed that $[CH] \propto [CH_3][OH]$. Therefore, they demonstrated numerically that the molar ion production rate can be approximated by Equation 5.7, where C is an optimization parameter constant that depends on the initial mixture equivalence ratio and the reaction mechanism used in the simulations. In other words, because the ions produced in the flame depend on the chemistry of the flame, the C will vary depending on the reactants and the

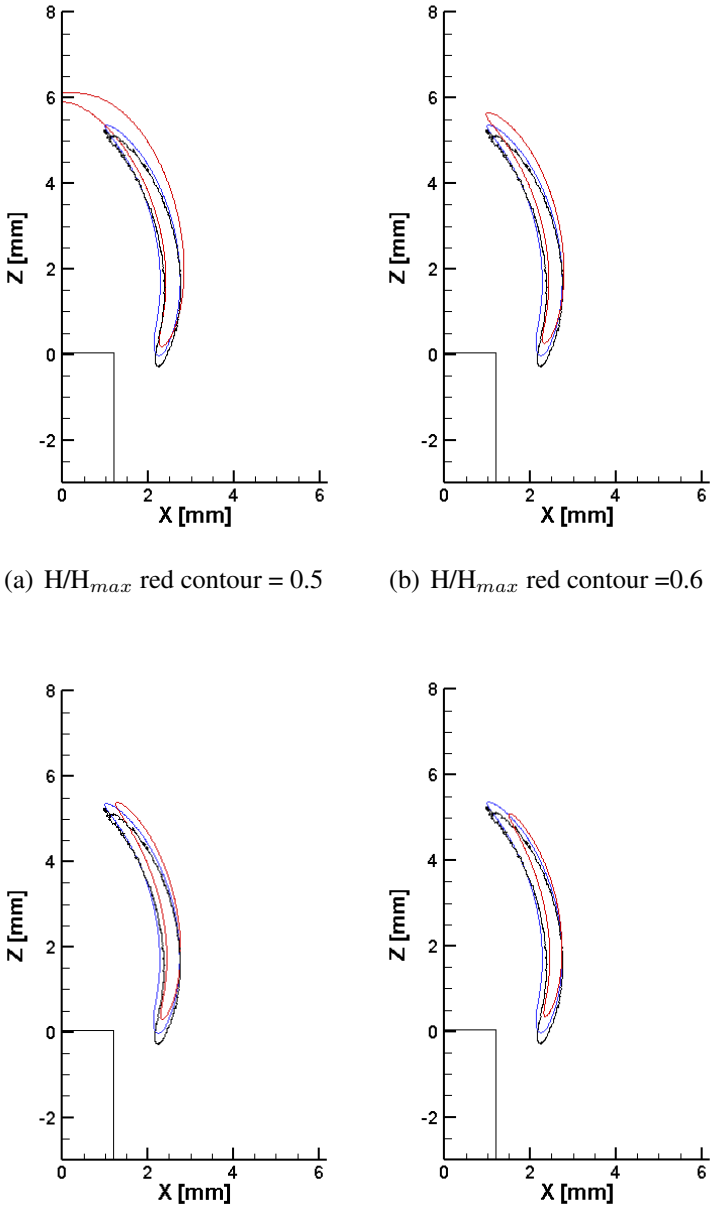

(a) H/H$_{max}$ red contour = 0.5 (b) H/H$_{max}$ red contour =0.6

(c) H/H$_{max}$ red contour = 0.65 (d) H/H$_{max}$ red contour = 0.7

Figure 5.1: Extruded burner without an electric field applied at 1g. H/H$_{max}$ red line from simulation using Model 1, CH*/CH$^*_{max}$= 0.05 blue line from simulation using Model 1, and experimental CH* contour from [43] (black).

chemical reactions occurring at the flame. Equation 5.7 has been implemented in the solver and the

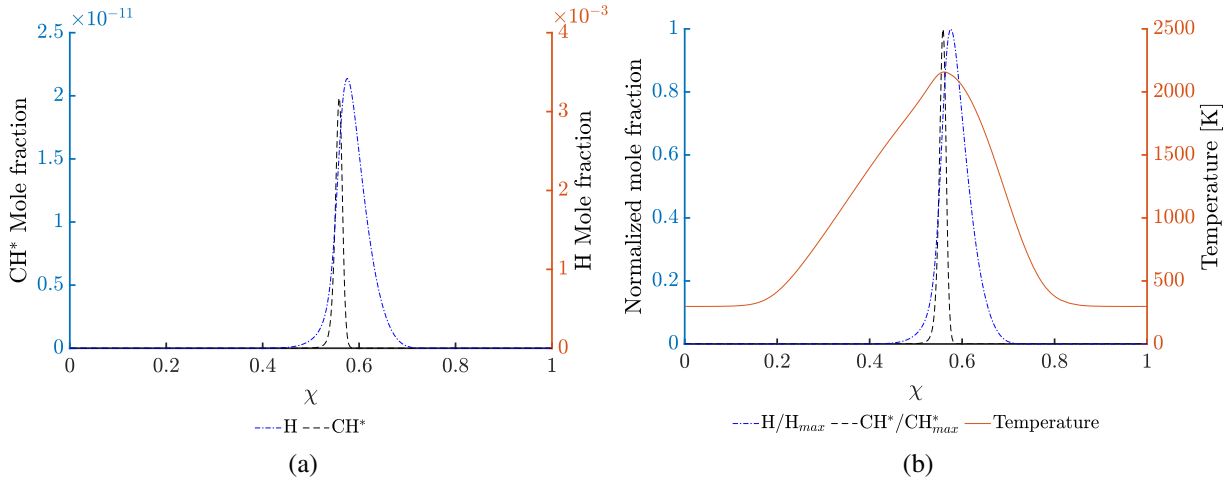

Figure 5.2: Comparison between CH and H using Model 1 chemistry. Counterflow burner without an electric field applied at 1g (velocity fuel inlet 20mL/min). (a) CH* and H mole fractions (no normalized), (b) Normalized mole fractions by their respective maximums (temperature plotted for reference).*

C parameter is tuned based on experimental data, following the methodology proposed by Belhi et al. [19].

The methodology from Belhi et al. [19] consists of determining the value of the ion production optimization constant C for each of the studied burner geometries based on tuning this parameter to obtain the same saturation point in the current-voltage curve – also called I-V curve or VCC (Voltage Current Curve) – as the previously measured saturation point from the experiments. Thus, this methodology carries the implicit disadvantage of needing, beforehand, experimental results employing a similar burner-electrodes setup as the one in the simulation.

$$\omega_p^i = \omega_p^{H_3O^+} = k_c[CH][O] \tag{5.6}$$

$$\omega_p^i = Ck_c[CH_3][OH][O] \tag{5.7}$$

The I-V curve represents the relation between the imposed electric field strength and current collected at the electrode. Typically, the ion current increases gradually until it reaches a plateau (saturation). At saturation, the total rate of chemi-ions extracted from the flame is equal to the rate at which chemi-ions are produced in the flame, so that field strengths above this saturation point cannot increase the ion current (see Figure 5.3). However, another gradually increasing current region has been observed by previous researchers [44, 131, 132] in hydrocarbon flames after the saturation regime for the extruded burner geometry, which is attributed to a secondary ionization process generated by the electron impact reactions. This phenomenon is not considered in the present work, but it will be added in the future.

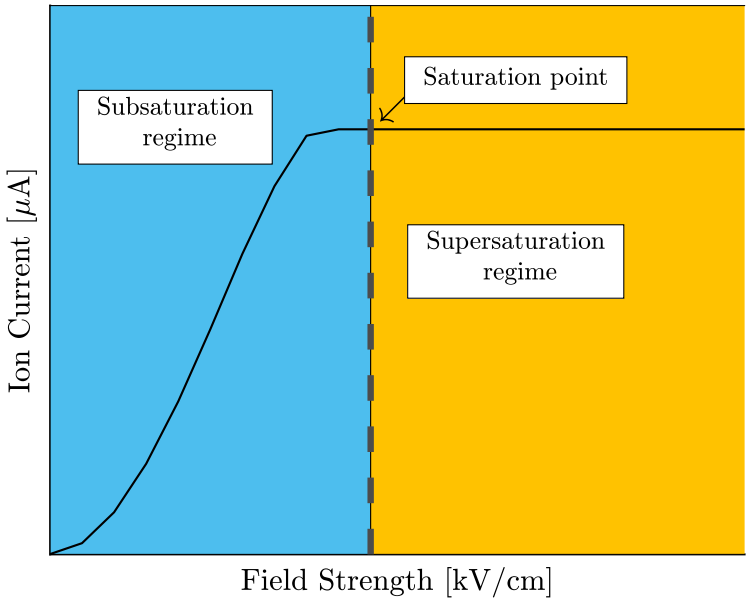

Figure 5.3: Schematic of simple voltage current curve

The next general steps should be followed to determine and tune the ion production optimization constant C and to be able to start obtaining the simulation results for the different expected points on the I-V curve:

1. Have the experimentally obtained I-V curve defined for your studied burner configuration. In this work, the experimental I-V curves for both extruded and jet burner geometries are obtained from Tinajero et al. [44].

2. Have solved the CFD simulation without an electric field applied on steady-state. In this work, these are obtained from the simulations shown in Chapter 4.

3. Implement the steady-state solution from the CFD simulation into the modified reactingFoam solver – the one that includes the application of electric field – and modify the electric potential applied in the simulation to match the saturation current obtained in the experimental I-V curve from the literature.

4. Run the CFD simulation with the electric field applied.

5. Tune the ion optimization parameter until the saturation point matches in both numerical and experimental I-V curves.

6. Run the study case with the optimized C parameter (this step can take $>$27456 CPU hours).

For the extruded and jet burner configurations of the diffusion flame studied, an averaged value of C = 3 x 10^{-2} m^3/mole and 505 x 10^{-4} m^3/mole are used, respectively. These are the values obtained from following the methodology mentioned above. Once the simulation at saturation with the tuned parameter C reaches steady-state, this steady-state solution is used as a base case for running two simulation cases: one at an upper field strength and another at a lower field strength with respect to the electric potential at saturation –i.e., upper mesh set at +500V or -500V relative to the electric potential at saturation. It is important to consider that for all cases, the changes in electric potential between a previous case to the new running case should be small enough, and the time step for the iteration should be adequate – i.e., the time step must not be too big to be able to capture the behavior of the electrons and other charges, but it should not be too small so the computational resources used are not more than the ones needed to run the simulation showing reasonable results.

This tuning approach methodology has been found to give reasonable results for flames that remain fundamentally the same when an electric field is applied, which refers to flames where the chemical

and electric field effects are not coupled. However, when the feedback occurs and the ion-driven wind modifies the flame behavior, it is unclear if the assumption remains reasonable, as it will be discussed in the next sections based on the results obtained.

5.4 Results and Discussion

Figure 5.4 displays the simulated distributions of H_3O^+ mass fractions, electric potential, and force lines at the saturation condition for the extruded burner geometry. The concentration of positive ions (H_3O^+) is higher at the flame's reaction zone than in the surroundings, where the location of the reaction zone is marked by the H/H_{max}=0.65 contour. These distributions agree with the hypothesis that H_3O^+ is created in the reaction zone of the flame, and when a negative electric field is applied, H_3O^+ is transported far away from the reaction zone [40]. Figure 5.4 (left) shows the equipotential lines from -4500V to 0V with an decrease of -200V per isoline.

The electric potential isolines obtained are normal with the direction of the electric field force, as expected by its definition. Also by definition, the electric field force flows from high to low potential, as seen in Figure 5.4. It is known that the flame is a conductor and can be considered as an equipotential surface. Figure 5.4 (right) shows that only the region where H_3O^+ is showing its maximum mass concentration is an equipotential surface. This means that the overall electrical balance in the flame is not correct since the whole flame should be acting as an equipotential surface. This will affect the local electric field prediction outcome.

5.4.1 Voltage current curves

The I-V curves obtained for the two studied geometries are shown in Figure 5.5, in comparison to the experimental data from Tinajero et al. [44].

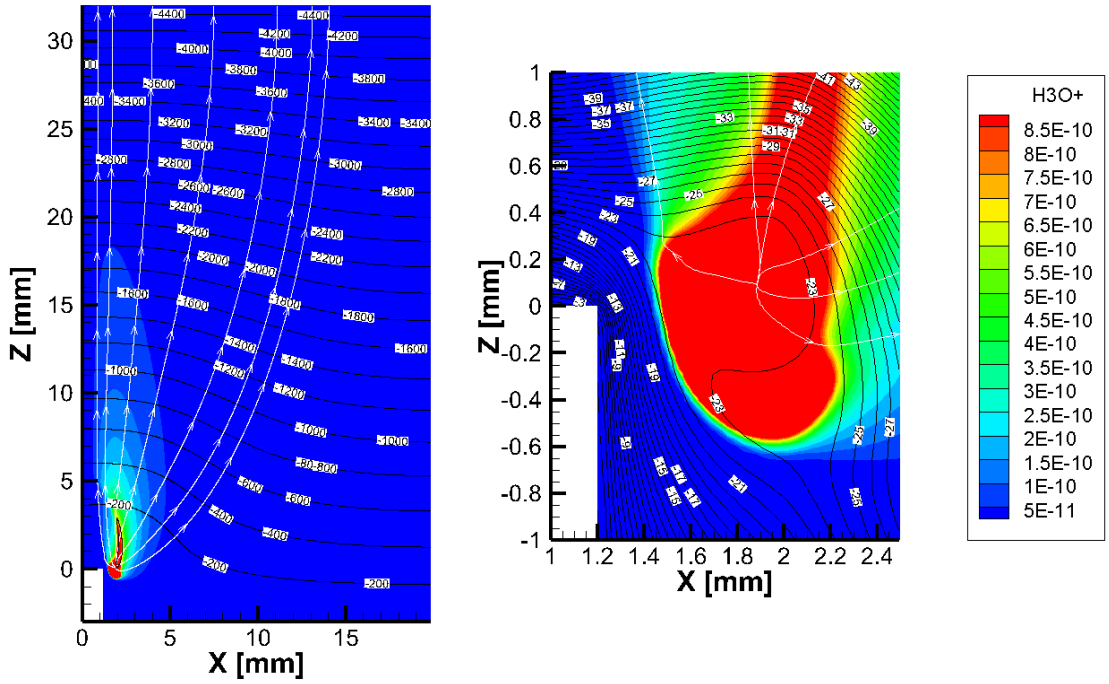

Figure 5.4: Extruded burner at electric field saturation conditions (1.29kV/cm) and 1g. Distribution of the H_3O^+ mass fraction, potential isolines (horizontal lines), electric force lines (white lines), and H/H_{max}=0.65 contour (black contour). General view (left), close-up view (right).

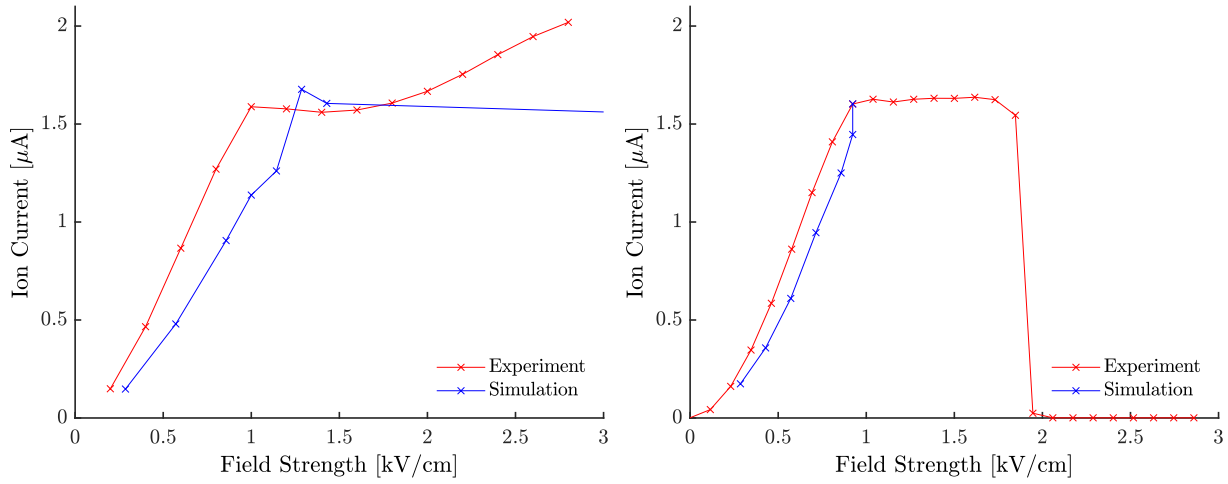

(a) Extruded geometry

(b) Jet geometry

Figure 5.5: I-V curves for extruded and jet geometries. Experimental values are from [44]. $Q_{inlet,fuel}$ = 27mL/min in both experiment and simulation. Result at 5.71kV/cm not pictured for Figure 5.5(a).

The simulated I-V curves follow similar trends for both experimental and numerical results and for both studied geometries. As the secondary ionization (electron impact) reactions are not considered in the reaction model, the simulation cannot predict the experimental behavior in the post-saturation regime (supersaturation). Notice that for the extruded geometry, even though the difference in ion current at saturation from the experimental to the numerical value is $\approx 15\%$, the field strength required to reach the saturation point in the simulation is $\approx 50\%$ higher than the one observed on the experimental literature for the experimental saturation point – i.e., which translates into 0.5kV of difference. This over-prediction is caused by the prediction quality of H_3O^+ electrical mobility in the simulation. Figure 5.6 shows the distribution of positive and negative ions and electrons at saturation (1.29kV/cm) from the simulation for the extruded burner.

Although higher field strengths are required in the jet simulations in order to predict the supersaturation region, the model does follow the basic trends. With this global matching of total ion current behavior, the following sections look into how the ion driven wind affect the flame shape and behavior.

5.4.2 Flame shape at supersaturation

Considering the overall flame shape when an electric field is applied to the flame, a direct comparison against the literature from Tinajero [40] is presented in Figure 5.7. For reference, the differences between experiments and simulations are that

1. the experimental results from Tinajero [40] have the Q_{fuel} = 20mL/min, and this work's simulations are at Q_{fuel} = 27mL/min,
2. the gap between electrodes in the Tinajero experiments is 25mm, while in this work's simulation is set to 35mm, and
3. the field strength applied in both compared contours is slightly different.

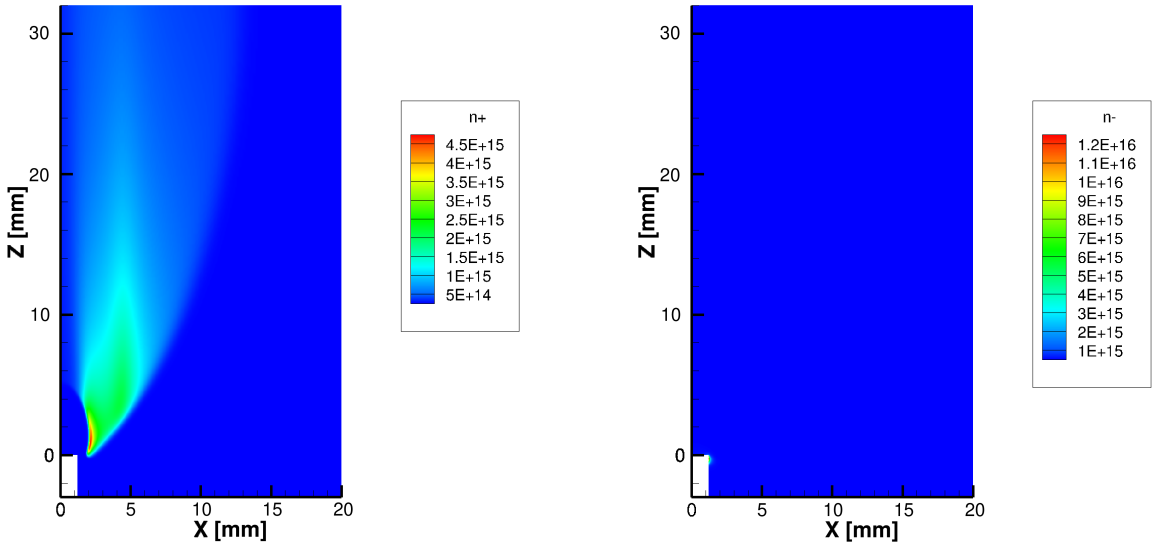

(a) Positive ions

(b) Negative ions

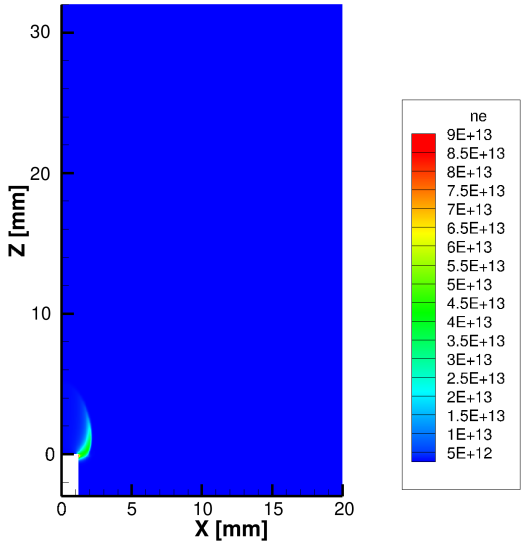

(c) Electrons

Figure 5.6: Distribution of the number density for positive and negative ions, and electrons at saturation for the extruded burner geometry (1.43kV/cm).

Despite the differences mentioned above between the experiments and the simulations, the flame is located at the same position when in supersaturation for both experiments and simulations –

before the secondary ionization takes place in the experiment. Notice that both experimental and numerical results plotted have an implicit error due to the contour chosen, and since the contours compared are from two different species, it is expected that the simulated normalized contour for H will not predict the experimental CH^* contour in its totality – as seen in Figure 5.1 for the 1g flame without an electric field applied.

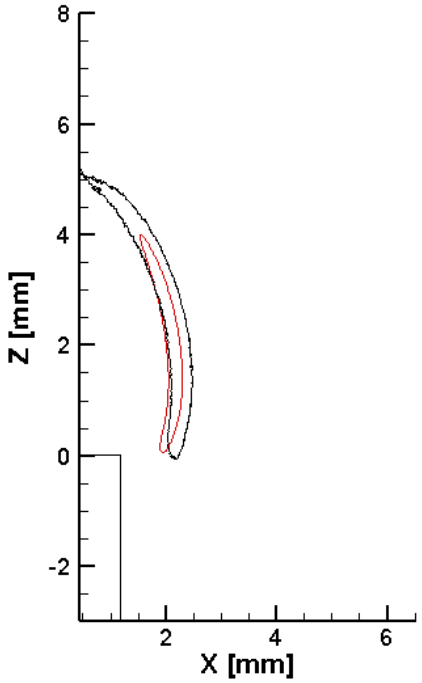

Figure 5.7: Extruded burner flame locations. Flame at 1g and supersaturation. Black contour from experimental CH^* chemiluminescence of a flame with 1.5kV/cm applied [40]. Red contour represents the H/H_{max} = 0.65 from this work's simulations of a flame under 1.43kV/cm applied.

Supposing that the quantity of CH^* chemiluminescence is well captured by the contours from the experimental literature [40], CH^* shows to be more affected than H by the applied electric field when comparing Figures 5.1 and 5.7. Since the electric field does change the flame shape via the ion-driven wind, there will also be a change in the relative locations of H and CH^*, but this change does not affect the general conclusions of the work.

5.4.3 Schlieren images and shadowgraphs

Schlieren and shadowgraph imaging are optical techniques used for visualizing non-homogeneous density gradients in flows. Because a flame environment is characterized by large density gradients, these techniques can provide information about the flame thermal plume. Experimentally, both techniques depend on the variation of refraction index in the flow (flame and surroundings, in this case) and the resulting effect on a light beam passing through it. Theoretically, the shadowgraph image is used to indicate the variation of the second derivatives (normal to the light beam) of the index of refraction, while the schlieren technique indicates the variation on the first derivative of the index of refraction. As explained in Section 3 Chapter 3, in this case, the shadowgraph images obtained from the simulations and the physical schlieren images can be considered equivalent and therefore, they can be used for direct comparison.

Apart from the simple validation of the physical behavior of the flame employing the simulations of this work against the experimental data from the literature, this comparison aims to provide insights on the uncoupling of the chemistry and electric field contributions.

Figure 5.8(a) shows the steady-state location contours of the shadowgraphs obtained from the simulations at 1g and different e-field applied with the extruded geometry. For comparison, Figure 5.8(b) is reproduced from the literature [40] and shows the experimental schlieren image boundary results as a function of electric field strength. Both literature experiment and this works' simulation used the same extruded geometry burner and the same inlet fuel flow equal to 27 mL/min.

Increasing the electric field strength makes the density plume narrow in the simulation, which can be explained by an electric field forced enhancement to the upwards and radially-inwards convection when a stronger electric field is applied. This effect is also seen in the experimental literature (see Figure 5.8(b)). In both cases, the high-density plume width also narrows after saturation has been reached (see Figure 5.5(a) for references on the saturation). Differently, the *opening* of the schlieren profile at the top is not observed in the numerical profiles. This is likely because the

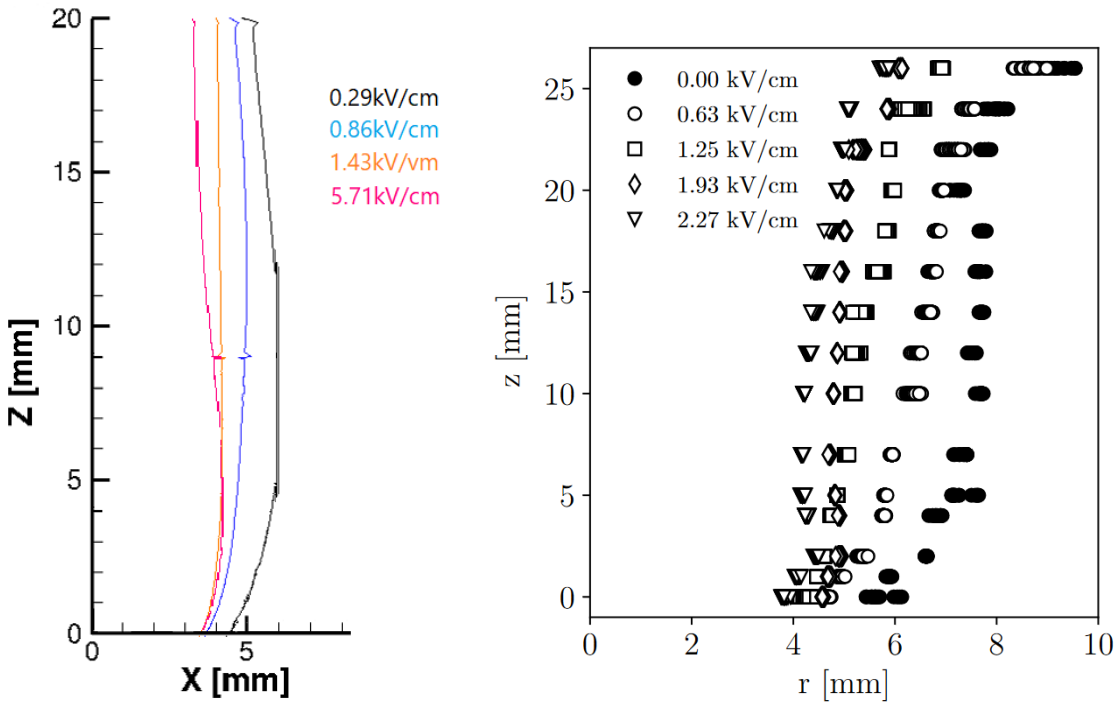

(a) This work (simulations)

(b) From [40] (experiments)

Figure 5.8: Final steady-state location of the schlieren and shadowgraph image boundary as a function of electric field strength. Negative electrode placed 3.5 cm from burner tip (burner tip at Z=0). $Q_{inletfuel}$= 27 mL/min. Identical extruded burner employed in both experiment and simulation.

honey-comb mesh placement at 32mm from the burner rim impacts the flame behavior from 16mm up. Previous literature determined that the upper mesh electrode affected the experimental flame in the same way as a metallic plate placed above the flame: quenching the ions at the mesh – i.e., no additional momentum – and creating an impinging flame [33]. Since the simulation does not consider a solid mesh or plate placed at the top of the simulation domain, the outlet gases move freely without producing this effect.

Since the shadowgraph is a second derivative, the temperature plots shown in Figure 5.9 facilitate the flame behavior comparison to the schlieren experimental data from Figure 5.8(b). For the cases where an electric field is applied, the model results follow the general trends of the flame behavior from the schlieren images: in the axial direction, the flame plume widens from 0mm up

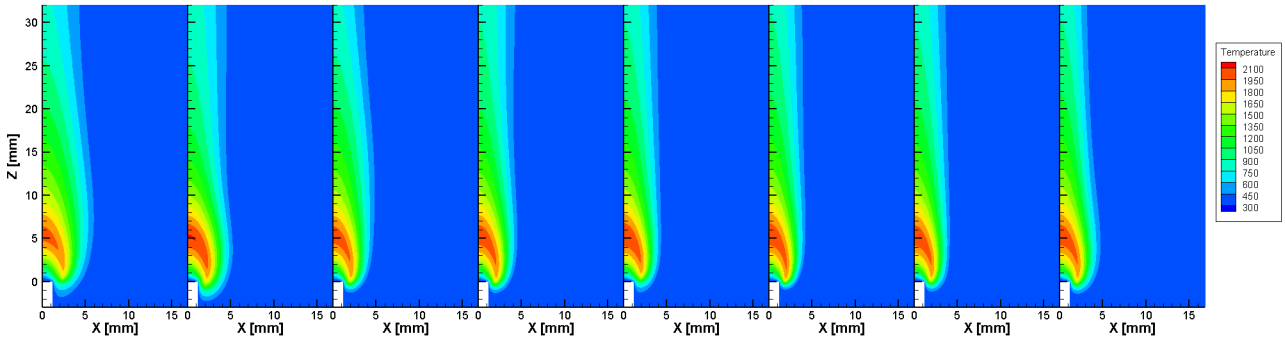

Figure 5.9: Final steady-state temperature mapping for the extruded burner configuration at different applied electric field cases. From left to right: 0.29kV/cm, 0.57kV/cm, 0.86kV/cm, 1kV/cm, 1.14kV/cm, 1.29kV/cm, 1.43kV/cm, and 5.71kV/cm.

to 5mm approximately, then it narrows from 5mm to 10mm approximately, and then it widens again. The only case that does not follow this trend is at 0.86kV/cm. Similar behavior is shown in the experimental data (Figure 5.8(b)), where the schlieren profile at 1.93kV/cm resembles the 0.86kV/cm profile from this work's shadowgraph. It is interesting to observe that the experimental ion current obtained at 0.86kV/cm corresponds to the sub-saturation regime in the I-V curve, yet the 1.93kV/cm field strength corresponds to the super-saturated regime (refer to Figure 5.5). This indicates that at a certain field strength closer to saturation but still in the sub-saturation regime, the spatial distribution of density – and therefore of the species – remains independent of the ion current collected downstream.

5.4.4 H_3O^+ and e^- profiles

Figures 5.10, 5.11, and 5.12 show the H_3O^+ molar fraction mapping and the contours at steady-state for different applied electric fields employing the extruded burner geometry. The difference between Figures 5.10 and 5.11 is that the latter has the same color legend for all the plots to clearly compare the H_3O^+ presence by employing the same plotting color scale. On Figure 5.12, the H_3O^+ molar fraction contours have been normalized by their corresponding H_3O^+ mole fraction maximum and the displayed ones are at $H_3O^+/H_3O^+_{max}$ = 0.05 for the purpose of qualitative com-

parison of location of the majority of H_3O^+ in each case studied. To provide more insights, the electrons location is shown in Figure 5.13.

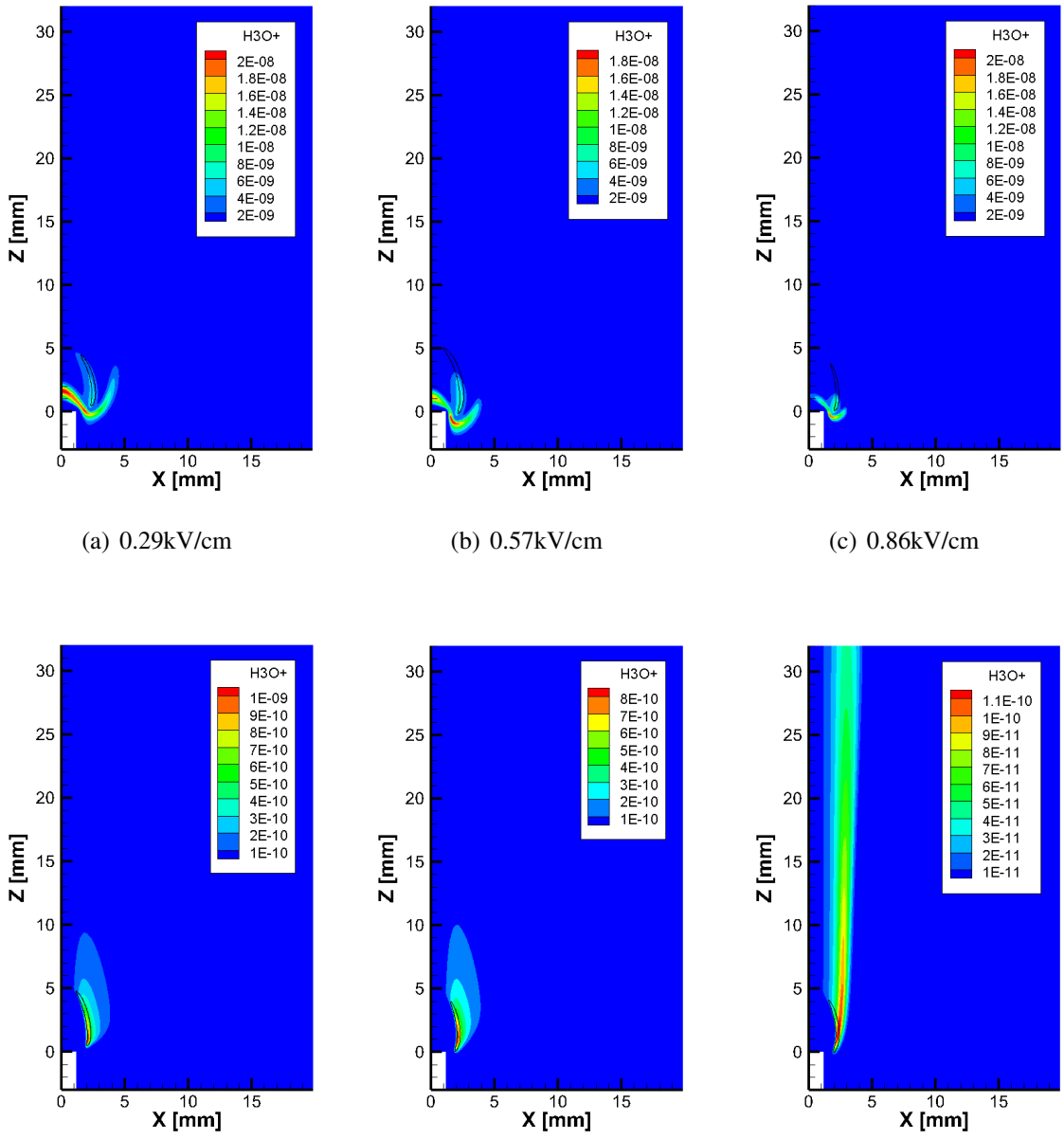

(a) 0.29kV/cm (b) 0.57kV/cm (c) 0.86kV/cm

(d) 1.14kV/cm (e) 1.43kV/cm (f) 5.71kV/cm

Figure 5.10: Final steady-state H_3O^+ mass fraction mapping and corresponding H/H_{max}=0.65 contours (black, flame location marker) for the extruded burner configuration at different applied electric field cases. Different color-legend in each sub-figure.

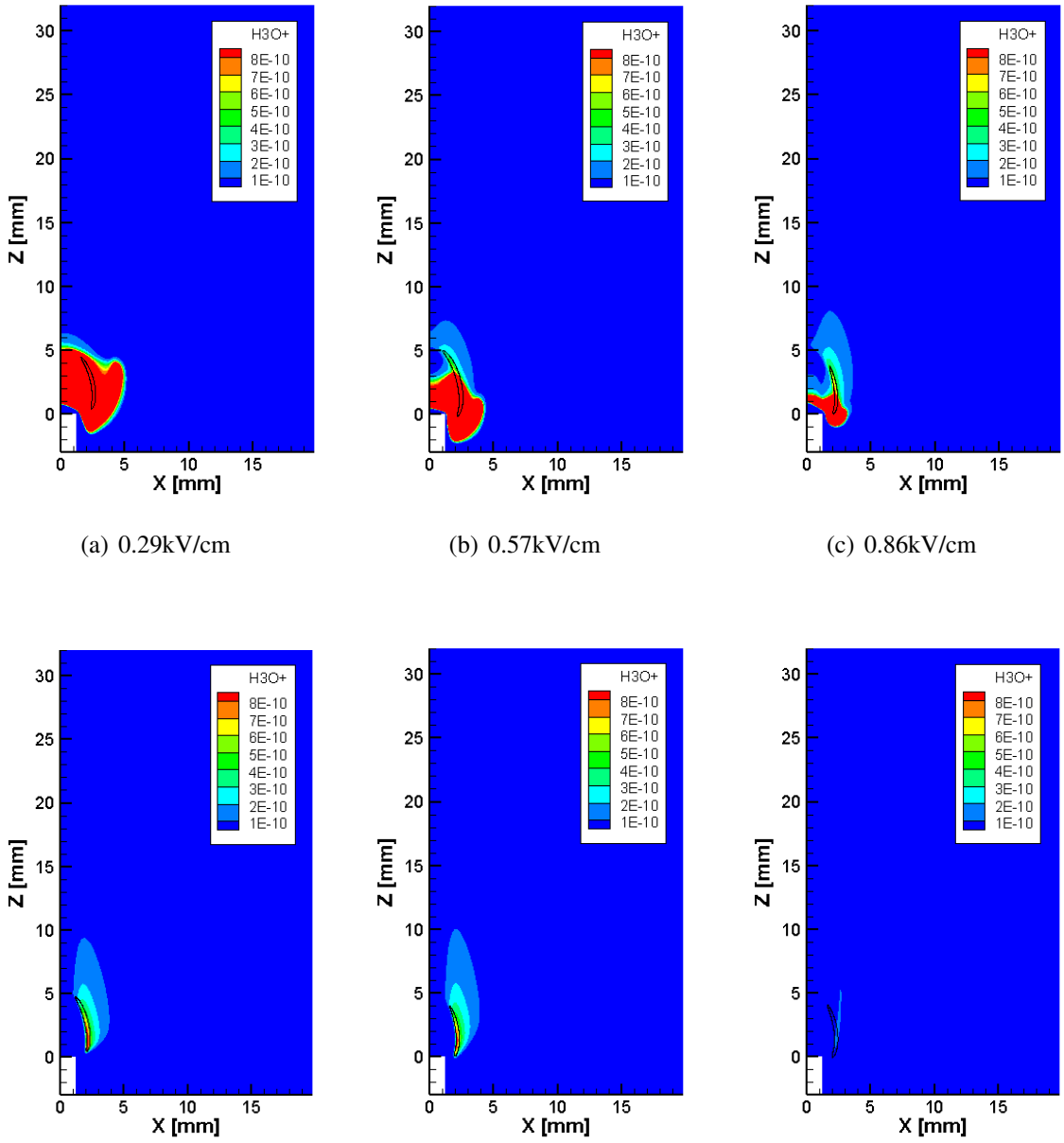

(a) 0.29kV/cm (b) 0.57kV/cm (c) 0.86kV/cm

(d) 1.14kV/cm (e) 1.43kV/cm (f) 5.71kV/cm

Figure 5.11: Final steady-state H_3O^+ mass fraction mapping and corresponding H/H_{max}=0.65 contours (black, flame location marker) for the extruded burner configuration at different applied electric field cases. Identical color-legend for all sub-figures.

The physical understanding of these results is based on the fact that the cations (mainly H_3O^+) are moving by attraction forces towards the anode electrode, which is placed at 32mm downstream

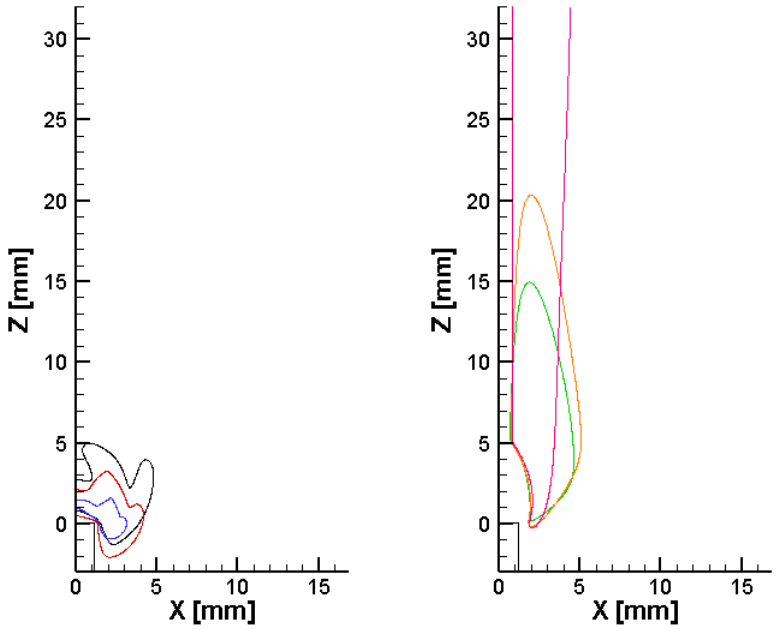

(a) Before saturation point (b) After saturation point

Figure 5.12: Final steady-state H_3O^+ mass fraction contours for the extruded burner configuration at different applied electric field cases. Color code: 0.29kV/cm (black), 0.57kV/cm (red), 0.86kV/cm (blue), 1.14kV/cm (green), 1.43kV/cm (orange), and 5.71kV/cm (pink).

from the burner tip, and they are repelled from the cathode electrode (burner). The mapping and contours of H_3O^+ follow that behavior at higher field strengths, showing that more positive ions are drained towards the negative electrode while increasing the electric field. After the saturation point, the anode keeps receiving positive ions forming a *weak* column of ions – i.e., low concentration of ions. Aligned with the previous explanation about the movement of H_3O^+ towards the sides of the flame, the description for this phenomena is that at high electric fields, the velocity of the ions being dragged to the anode – and charge-neutralized there – is higher than the formation of cations in the flame. At the same time, since the cations are mostly in the sides of the flame, there is no obstruction to arrive faster to the anode. Hence, as soon as cations are formed, they move rapidly towards the sides of the flame and towards the anode, so the steady-state solution achieved shows a low presence of H_3O^+ at high electric fields (saturation and supersaturation conditions).

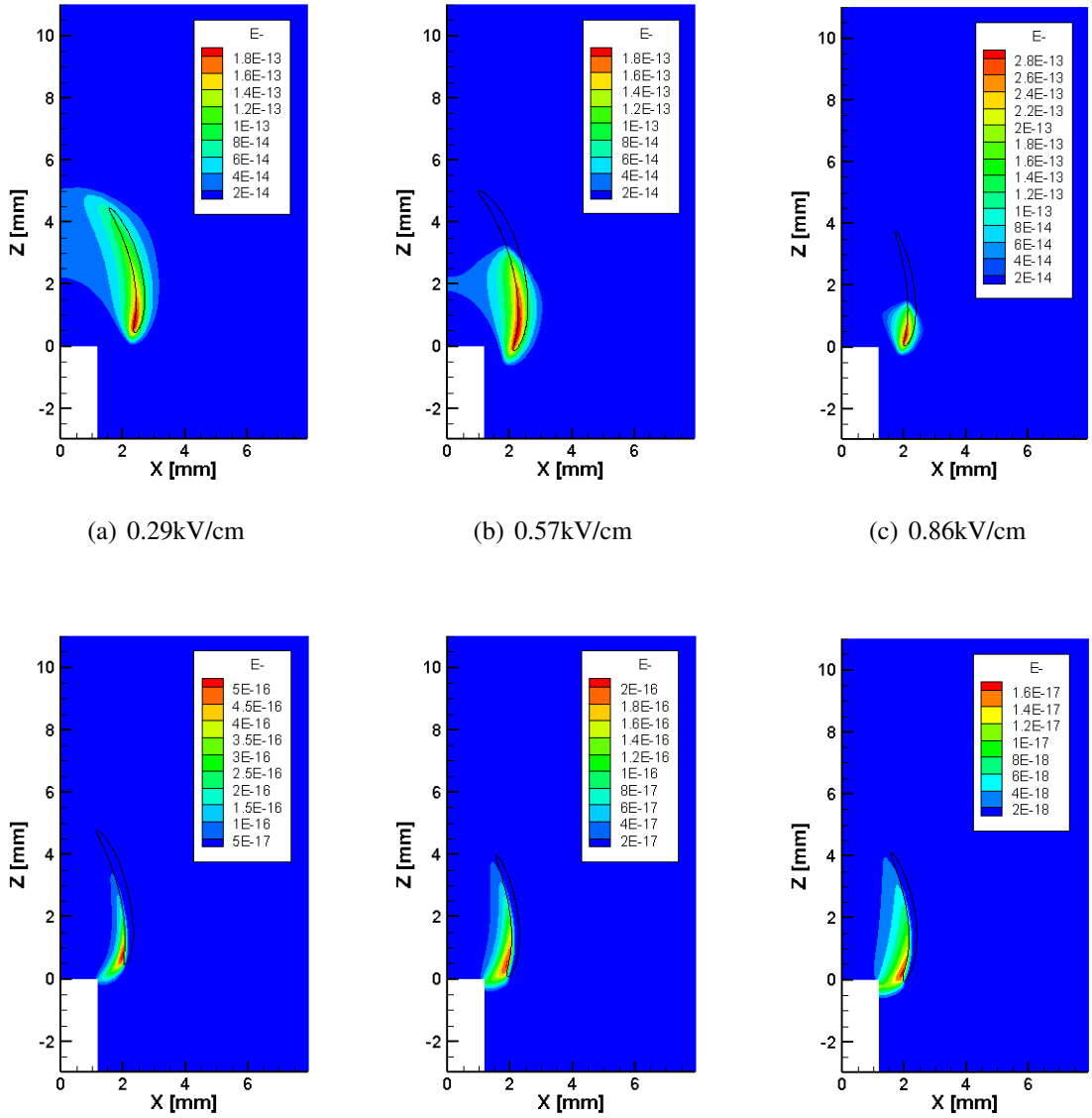

(a) 0.29kV/cm (b) 0.57kV/cm (c) 0.86kV/cm

(d) 1.14kV/cm (e) 1.43kV/cm (f) 5.71kV/cm

Figure 5.13: Final steady-state e^- mass fraction mapping and corresponding H/H_{max}=0.65 contours (black, flame location marker) for the extruded burner configuration at different applied electric field cases. Close-up view. Identical color-legend for all sub-figures.

It should be noticed that for these cases, the positive ions are not touching the cathode due to repulsion forces, while electrons and negative ions move towards the cathode (burner walls) (see Figure 5.10). Negative charges, such as the electrons, travel rapidly towards the cathode (burner),

with a tendency to get localized at the sharp edge of burner rim, particularly at higher electric fields, as shown by Figure 5.13 and in previous literature [34].

Focusing on the predicted flame behavior below the saturation point, an unexpected behavior is observed. Figure 5.12 shows that when a weak electric field is applied, the H_3O^+ moves towards the cathode. This non-physical prediction is a consequence of the local ion distribution at low electric field strengths not being well predicted in the simulation, most drastically close to or at the reaction zone.

5.4.5 Z-Current in radial direction

In the previous section it has been seen that the electric field simulations show non-physical behaviors at lower applied electric fields. However, the downstream electrode position is placed far from the source of ions (flame). Thus, even though the pathways that the ions follow to get to the downstream field is not physically correct, as long as the total ion production is predicted correctly (as shown by the I-V curve, Figure 5.5), the downstream ion current appears to provide acceptable predictions.

Figure 5.14 displays the current density distribution on the anode surface along the radial axis for different bias voltages.

There is a valley in the current density at the center of the flame at higher electric fields, showing the maximum current density to be displaced around 2-3mm from the center of the flame for both extruded and jet geometries. That valley, hence the current density peak, is more pronounced as the electric field increases. This can be clearly seen in Figure 5.15, which is the same figure as Figure 5.14(a) but with the addition of the field strength at 5.71kV/cm. Additionally, Figure 5.16 shows the H_3O^+ mass fraction profiles for the extruded burner with 1kV and 4kV applied (0.29kV/cm and 1.14kV/cm, respectively), which is directly related to the Z-current density. The valley obtained

in the higher electric field simulations in this work was also observed in the Tinajero experimental work [43] for a flush tube burner geometry (Figure 5.17). The Tinajero flush tube burner was meant to represent the electric field distribution of two charged plates that would ideally form a uniform field with parallel electric field lines, where the burner was acting as the cathode and the mesh placed 35mm above the burner tip was acting as an anode. As shown in Figure 5.17(c) by the I-V curve of the Tinajero flush burner, the saturation point employing that configuration was reported to be at $\approx$1.4μA for an inlet fuel flow of 27mL/min, which is in the same order of magnitude as the saturation ion current found for the jet burners studied in this work (both extruded and jet). Yet, the current density peak in the flush geometry is one order of magnitude above the current density peak obtained in the numerical simulations for the extruded and jet geometries, even for the saturation at the cases. Several factors are conditioning these outcomes and can explain the disparity in orders of magnitude between the experimental ion current density collection at the downstream electrode and the calculated values obtained for it from this work:

1. **Overestimation in Tinajero's Z-current density results.** Considering that these are axisymmetric flames, the integral of the Z-current density at 1.14kV/cm from the Tinajero flush geometry plot gives a value of $\approx 4.6\mu A$. From the Tinajero I-V curve for that flame (methane at 27mL/min), the total ion current collected at the downstream electrode at 1.14kV/cm is $\approx 1.3\mu A$. Therefore, it is seen that the measurement method based on fixed points of collection from Tinajero appears to overestimate the local Z-current density by a factor of 3.5.

2. **Tail values consideration in this work.** The downstream electrode in both flush burner experiments from Tinajero and this work's simulations have the same dimensions. However, notice that the current density at the tail of the curves (between a radial distance of 10mm to 20mm) was not considered in the Tinajero experiments, yet it is considered in this work. The experiment shows a more rapid drop-off of ion current near the domain boundary, while the simulation shows a slower decay in ion current density. Accounting for this low collection

of current density over a large area also contributes to the differences observed between both works.

3. **Upper electrode geometry and material.** The downstream electrode in the experiments from Tinajero is a honeycomb mesh of 101.6mm in diameter. In this work's simulations, the downstream electrode diameter is 80mm, and it is set as a zero gradient for the velocity– i.e., there is nothing that perturbs the departing gases. These differences in the downstream electrode are potentially contributing to the disparities observed.

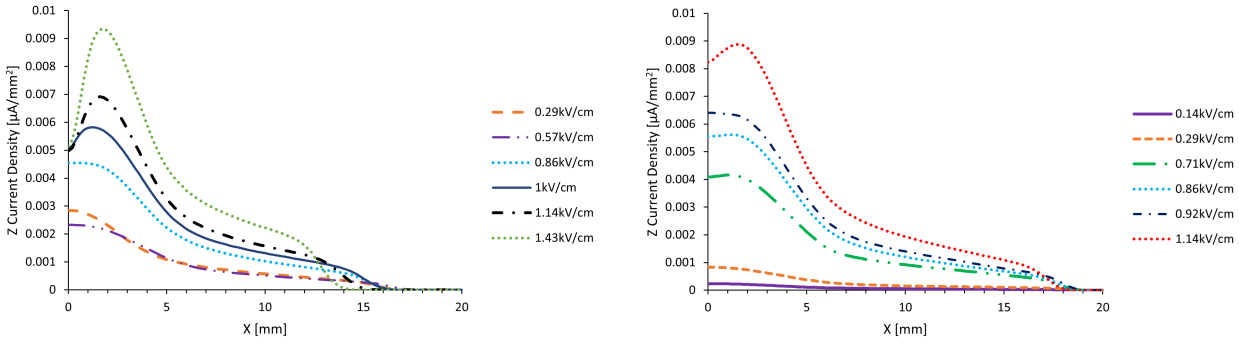

(a) Extruded geometry

(b) Jet geometry

Figure 5.14: Downstream ion current density (anode). (a) Extruded geometry, (b) Jet geometry.

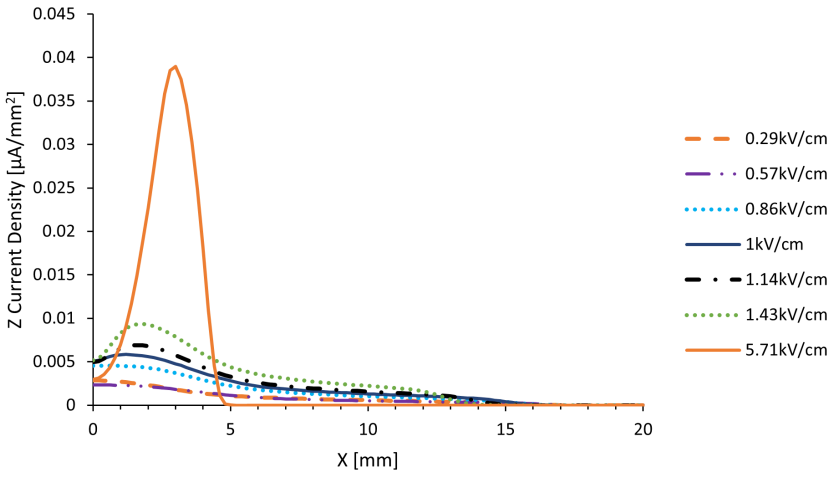

Figure 5.15: Downstream ion current density (anode) for the extruded geometry.

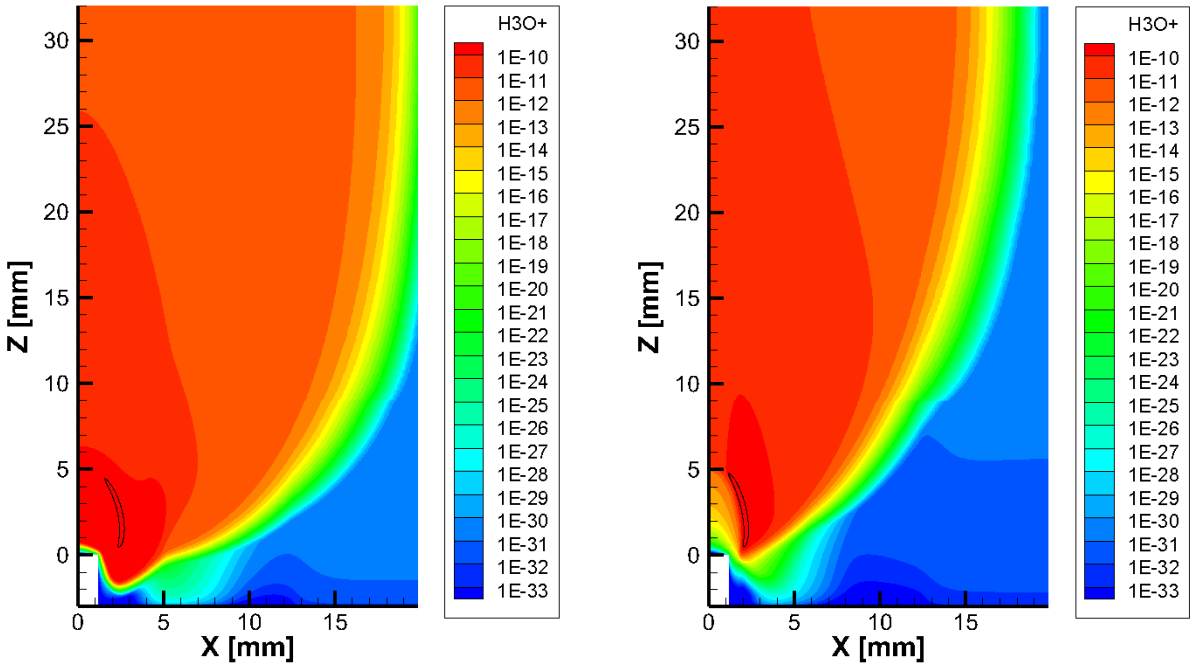

(a) 0.29kV/cm

(b) 1.14kV/cm

Figure 5.16: Extruded geometry with an electric field applied. H_3O^+ mass fraction. (a) 0.29kV/cm (b) 1.14kV/cm.

Notice that for both simulated extruded burner (Figure 5.14(a)) and experimental flush burner (Figure 5.17), the downstream ion current density profiles are showing maximum current density in the center of the downstream electrode (Warburg distribution) for field strengths lower or equal to 0.86kV/cm – i.e., low subsaturation regimes. That is because the ion current profile can be treated as a point-source to plate configuration at these conditions. The Warburg distribution – described in Equation 5.8, where $\frac{j(x)}{j_0}$ is the Z current density at a certain radial distance x; b and m are the scaling factor and the Warburg exponent, which are empirically determined; and H is the separation between electrodes – predicts that the majority of positive charge collection will happen at the center of the downstream electrode by treating the current discharge as a space charge expansion in a unipolar system. A previous study from Papac [33] also showed that the Warburg distribution profile was followed for a configuration designed to emulate a point-to-plane

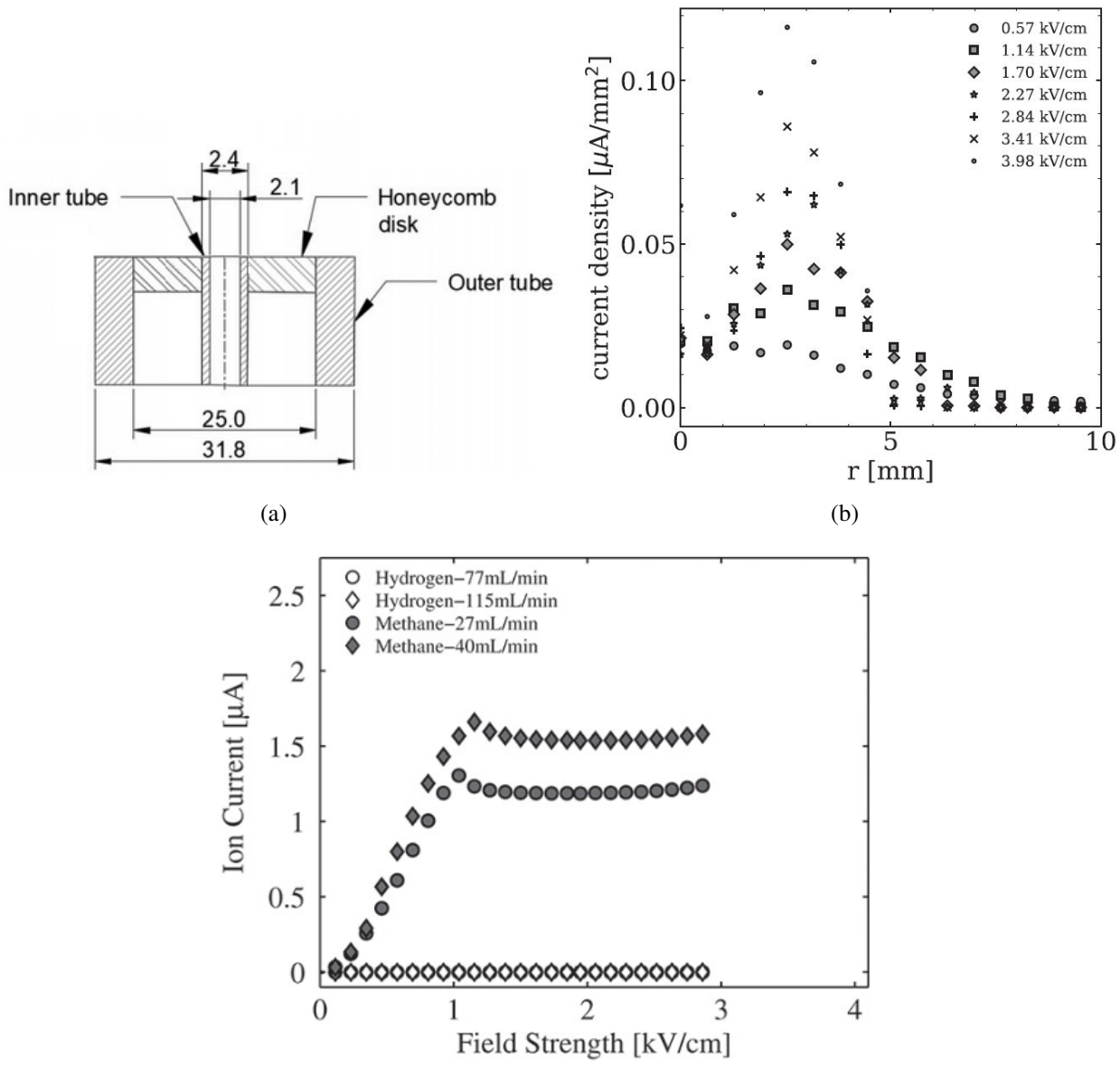

Figure 5.17: (a) Flush burner employed by Tinajero et al. [43], (b) Downstream ion current density (anode) from Tinajero et al. [43], (c) I-V curve for the flush burner geometry from Tinajero et al. [44] for the flush tube burner geometry with a spacing of 35mm between burner and downstream electrode.

electrode/burner geometry with a capillary burner and a distance between electrodes (H) equal to 35mm (see Figure 5.18).

$$\frac{j(x)}{j_0} = b\left(\frac{H}{\sqrt{H^2 + r^2}}\right)^m \tag{5.8}$$

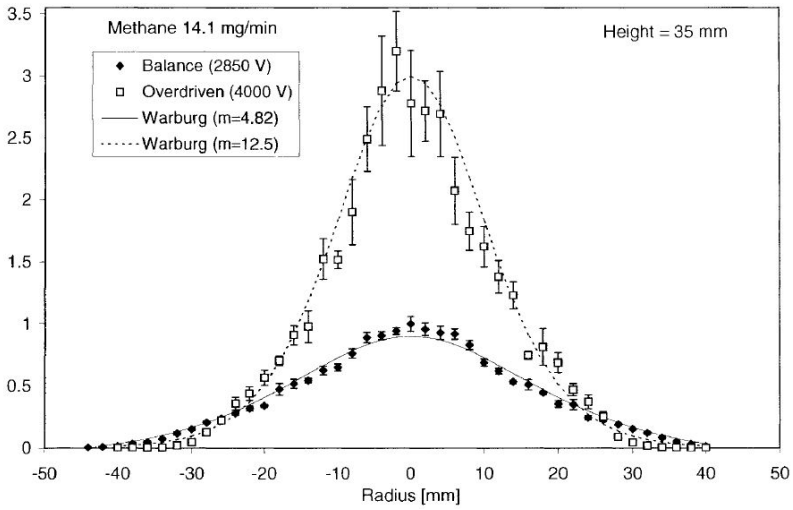

Figure 5.18: Downstream ion current from Papac [33] at 2850V and 4000V employing a capillary-to-plane electrode configuration with a spacing of 35mm (same spacing as this work simulations).

Considering the current densities that reach the upper electrode (Figure 5.14), the outer part of the cathode receives a negligible amount of current density (in the order of 1e-6 to 6e-22 μA/m^2, depending on the field strength case and the radial position).

5.4.6 Feedback of the ion wind to the flame

The crucial behavior to study in these simulations is the feedback of ion-wind effects, which is directly tied to the ion-wind force – i.e., electric force. However, Figure 5.12 shows that at subsaturation regimes, the clouds of charges are distributed in a way that seems non-physical since the cations are moving towards the cathode. However, the simulations at saturation can still provide some insights about the feedback of the ion wind to the flame.

On the one hand, Figure 5.19 shows that at a low electric field, there are vectors going in both directions in the reaction zone, which means that the net ion wind is not strong in that region. Moreover, the flame does not perturb the electric field much except in the region very close to the burner tip.

On the other hand, that same Figure 5.19 shows that once far away from the reaction zone (i.e., source of ions), the H_3O^+ ions are being received by the downstream electrode following the distribution shown in Figure 5.19 and in the previous Section 5.4.5. This leads to the conclusion that the behavior of charges very near the flame is less important for the overall ion wind. That is because the overall ion-wind behavior acts as a sort of buoyant plume that generates an overall flow – i.e., bulk gas movement. That explains why the behavior close to the reaction zone does not affect the overall behavior of the upper ion wind. Thus, and as previously mentioned, as long as the total amount of charge that reaches the downstream mesh is well predicted (shown by the I-V curves in Figure 5.5), the overall ion-wind behavior will be reasonable for these symmetric configurations.

Figure 5.20 shows that the magnitude of the local electric field force (vectors) is 100 times larger than in Figure 5.19. Also, it demonstrates that the positive charges produced at the wings of the flame at high electric fields are dragged to the downstream electrode in a vertical pathway. This would not happen in a symmetric charge-source such as the one seen in the work by Papac [33] and explains the peak of current charges reaching the downstream electrode being displaced by 2-3mm from the center of the electrode (see Section 5.4.5).

Even though the ion wind's general behavior is captured by the simulation, the charge distribution and the small changes in the electric field near the burner are still too convoluted questions to answer at this time, and further investigation should be performed towards that goal.

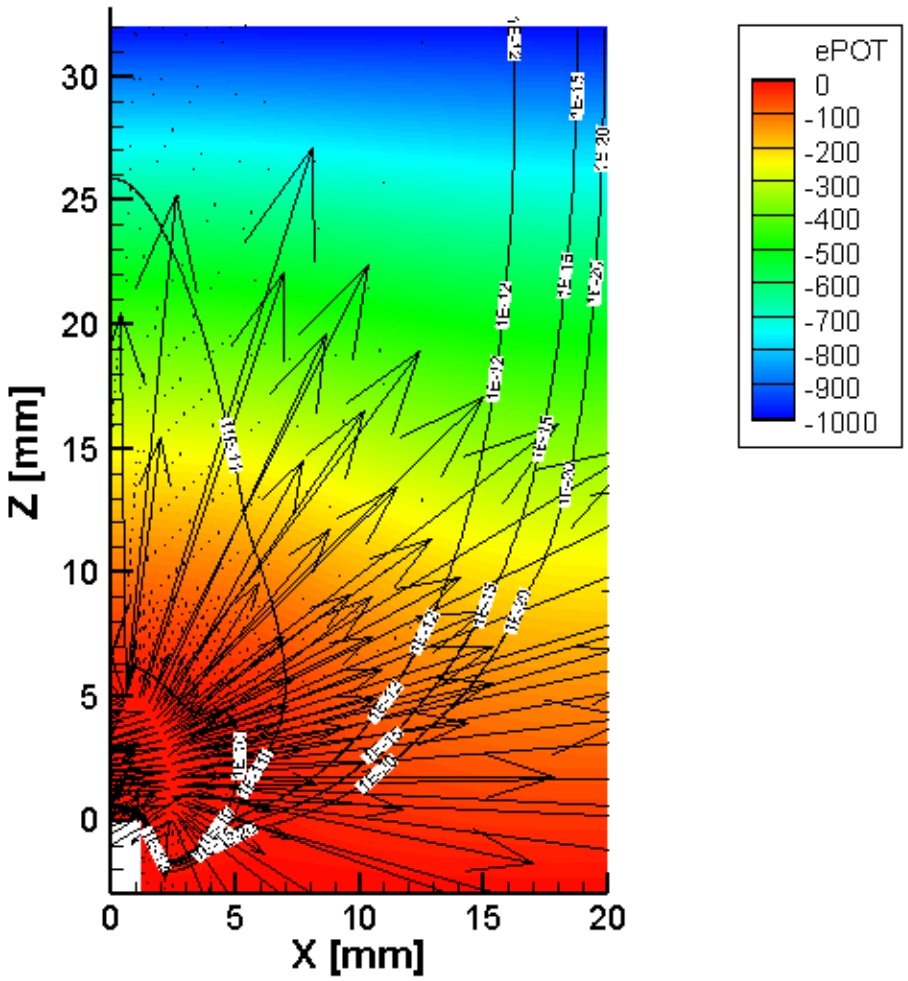

Figure 5.19: Extruded burner configuration at 0.29kV/cm applied (subsaturation). Electric potential mapping; H_3O^+ mass fraction contour (black); Local electric field force vectors are scaled relative length: grid units/magnitude = 80.

5.5 Conclusions

There are indications that the model will be able to accurately reproduce the I-V curves obtained experimentally. The methodology using the tuning of the ion production constant C exhibited promising results for obtaining the characteristic I-V curve.

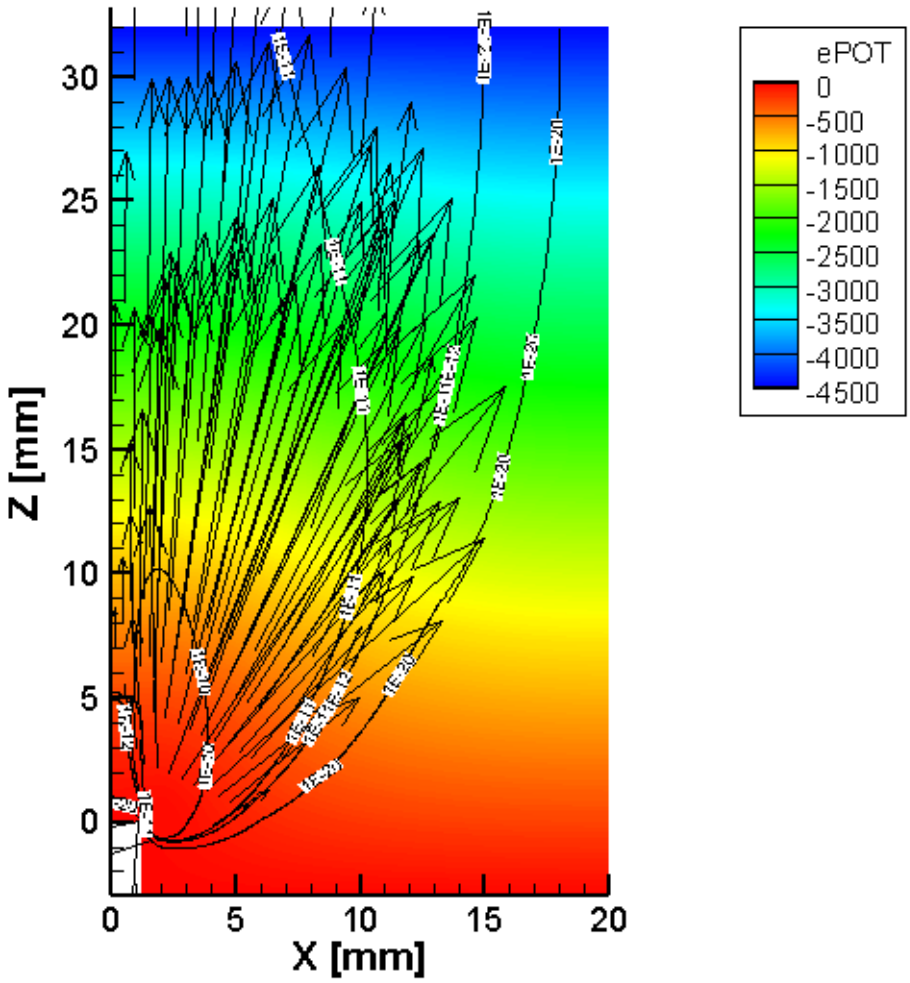

Figure 5.20: Extruded burner configuration at 1.27kV/cm applied (saturation). Electric potential mapping; H_3O^+ mass fraction contour (black); Local electric field force vectors are scaled relative length: grid units/magnitude = 0.8.

At the moment, the I-V curves obtained are capturing the trend in the sub-saturation domain, but there remains some work needed to accurately capture the transition to complete saturation and supersaturation in the jet burner case.

The downstream ion current density readings showed that as the applied electric field increases, the maximum ion current density reaching the anode is located 2-3mm from the burner center. It

was shown consistently that the positive charges produced at the wings of the flame at high electric fields were dragged to the downstream electrode in almost direct vertical paths. This would not happen in a symmetric charge-source approximation as was a simplification employed in the past [33]. In contrast, at lower electric fields, the system behaves much more as the charges were distributed throughout the internal reaction zone, which produces a distribution of charges that follows the Warburg distribution, where the maximum charges are collected at the center of the downstream electrode.

Since current characterization of the behavior of ions at sub-saturation regimes has shown to be faulty for predicting the charge distribution near the reaction zone, further understanding of the simulation flaws will grant more insights on the interactions that are occurring between chemistry and electric field. However, the general behavior of the charges transported towards the downstream electrode by the ion-wind effect is shown not to be affected by the charge distribution at the reaction zone, and the total amount of charges that reach the downstream electrode is well-predicted (as shown by the I-V curves). This is due, in part, to the strategy of the tuning parameter based on the saturation ion current collected experimentally.

Chapter 6

Comparison between different body forces

6.1 Background

An indication of how different nature body forces affect the flame comes from comparing flames under such body forces' influence. Previous studies have looked into the similarities or even equivalences between buoyancy and electric field body forces driving ion winds.

Carleton and Weinberg [20] reported candle flame experiments with an applied electric field configuration placed in a transverse position with respect to the convective flow. They carried these experiments out while in a parabolic flight – during the period when the aircraft pulls out of the parabola (supergravity) as well as during free-fall (microgravity). Although the orientation of buoyancy and electric field was different in these experiments, they showed that both body forces were capable of changing the flame shape and directing its hot flame gases.

As a continuation of this work, Strayer et al. [133] showed that, by employing a capillary diffusion flame – i.e., capillary-to-plane electrode geometry – it was possible to balance convection by the use of electric fields acting on flame ions to generate a body force on the gas in order to simulate

microgravity conditions for small diffusion flames over extended periods of time in steady-state. Using that same capillary-to-plane geometry, Papac et al. [17] examined the coupling between the ion wind and the thermofluid flow field in a buoyant flame. They found that the microbuoyant condition for methane – i.e., when the buoyant flame shape is modified to resemble a microgravity flame – coincided with ion current saturation when the capillary-to-plane distance was varied. From that outcome, the authors suggested a numerical modeling simplification considering that the recombination in the domain is negligible. Later works from Papac et al. [125, 134] demonstrated that, even though buoyancy and ion-wind forces do not always behave identically, the electric field can cancel buoyancy to a large degree over a reasonable part of the domain. They showed that the limitation on the situations where buoyancy and electric field force can be treated equivalently depends on the flow recirculation (vortex) anchored just outside of the ion conduction path. However, when under that limit, electric fields can effectively cancel buoyancy over a ± 15 degree angle of the flame. It can produce, in this way, a spherical flame arc even in 1g.

Aligned with the previous findings, Karnani et al. [34, 45] employed microgravity drop-tower experiments – i.e., negligible buoyancy effects – with a similar electrode-burner configuration as the one studied in this work to show that negative electric fields could be used to change the flame shape to resemble a flame under gravity conditions. Figure 6.1 shows the results from Karnani et al. work when a small coflow flame in a microgravity drop-tower is subjected to an applied electric potential between -1kV to -5kV over a varying gap between the burner and the downstream electrode. These images demonstrated that, based on flame area measurements, a coflow velocity equal to the mean jet-flow (24 cm/s) or a 0.6 kV/cm applied electric field to the microgravity flame will create a flame area similar to a flame in 1g. Note that there remain some differences in the precise flame shape, but the overall appearance is similar, suggesting some equivalence level between the body force of buoyancy and the body force of electric fields.

More recently, Tinajero [40] tried to quantify the similarity between buoyancy and electric field effects on flames based on CH^* chemiluminescence. He used the same extruded burner/downstream

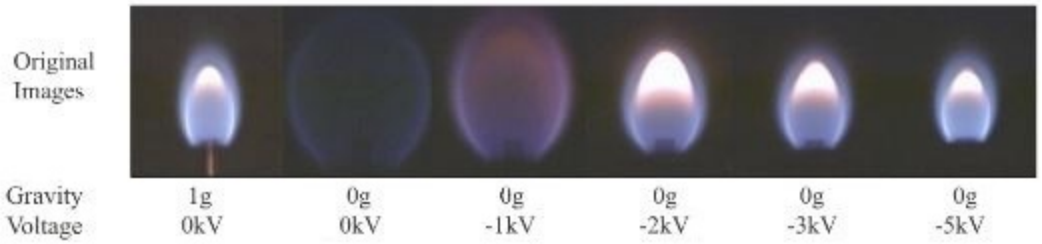

Figure 6.1: Pictures of 1g flame without an electric field applied and microgravity flames with an electric field from Karnani et al. [45].

electrode geometry configuration as the one employed in this work to make comparisons between (i) simulations at different gravities and without an electric field applied and (ii) experiments at 1g with different electric force applied. The chemical kinetic model used for neutral species in those simulations was the GRI-Mech 3.0 [68], which likely captures the thermal aspects very similarly to the current simulations but the details of the minor species, particularly CH^*, may differ.

From these works and their conclusions, it can be distilled that similarities between buoyancy and electric field forces in flames exist, but they will not overlap precisely because there is no formal reason that the locations of high current density align with regions of high-temperature gas. The overall impact on the flame, however, which depends on the more global flows driven by the body forces, can be comparable.

The results exposed in this Chapter 6 intend to clarify how the buoyancy and electric body forces compare over the domain, highlighting the regions where one or the other force dominates for the electrode-burner geometry studied. These results will help show which range of electric field or buoyancy forces cause equivalent flame shape responses. Furthermore, this Chapter 6 also investigates the possibility to employ electric fields in 1g flames to simulate supergravity without an electric field being applied.

6.2 Purpose

The purpose of this section is to compare the effects of different forces – gravity and electric field – on non-premixed diffusion methane/air flames. The OpenFOAM® software is used to simulate these scenarios, as described in previous chapters. The comparison of effects should provide more insights on possible similarities between body forces of a different nature.

6.3 Results and Discussion

The results used for the comparisons are from the simulations explained and shown in previous chapters of this work, and the experimental data from Tinajero et al. [40, 43] and Karnani et al. [34, 45]. These experimental results are suitable for comparison since they employed the same burner geometries as the ones explored in this work's simulations plus, in some cases, they used the same fuel flow rate.

6.3.1 CH^* location and flame structure

At saturation, the experimental expectation is that the overall electric field force will be approximately five to ten times larger than the overall buoyancy force. Also, there is experimental evidence that, in a downward point-to-plane configuration, the buoyancy is approximately balanced at saturation, which suggests that electric body force and buoyancy are about the same in magnitude. Therefore, these experimental expectations suggest that somewhere between half of the saturation voltage and 20% of the saturation voltage is equivalent to 1g. This means that for the comparison of gravity and electric field forces explored in the previous chapters of this work, the simulations that should be considered to carry on with the comparison are the computed flames at 1g to 2g without electric field and the computed flames at 1g with 0kV/cm to 0.5 kV/cm of field strength.

Having the previous experimental expectations in mind, Figure 6.2 compares CH^* contours from the current simulations of a flame under different gravity conditions with CH^* contours of a flame at 1g but with additional electric fields applied from [43]. Figure 6.3 provides the same information but separately overlaps the computed CH^* greyscale contours with the experimental CH^* line contour representing the flame location.

Figure 6.3(b) shows that the CH^* contour of the flame exposed to a 2g environment without an electric field applied is affected similarly as if the flame were exposed to a 0.5kV/cm electric force field at 1g.

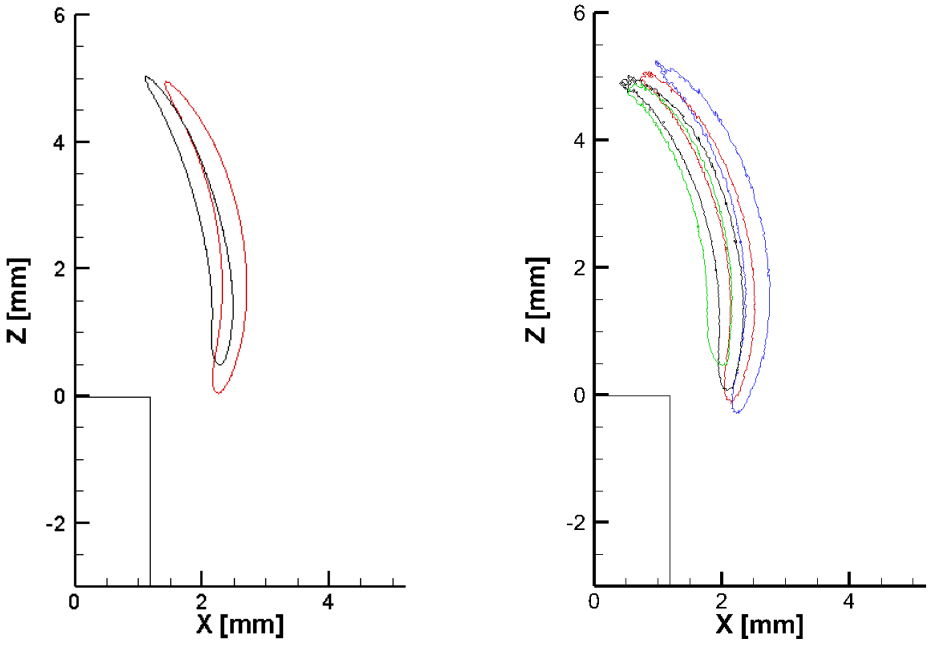

(a) Buoyancy body force (from this work). (b) Electric field body force (from [43])

Figure 6.2: Comparison of body forces effect on CH^* mapping in the methane-air diffusion flame. Extruded burner (close-up views). Inlet fuel flow rate = 20mL/min. (a) Different gravity (1g red; 2g black). (b) Different electric field applied at 1g flame (0kV/cm blue, 0.5 kV/cm red; 1kV/cm black; 3kV/cm green).

Based on the CH^* profiles, Figure 6.4 displays the detachment (lifting) of the flame from the burner base, having the burner base placed at $H_{b,0}$. Standing on the reasonable scaling mentioned before,

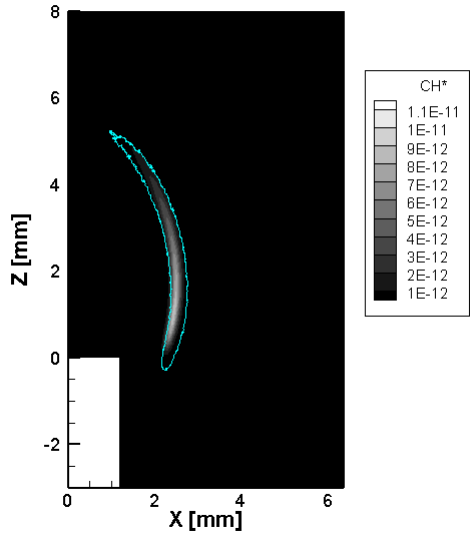

(a) 1g, 0kV/cm (sim.) v.s. 1g, 0kV/cm (exp.)

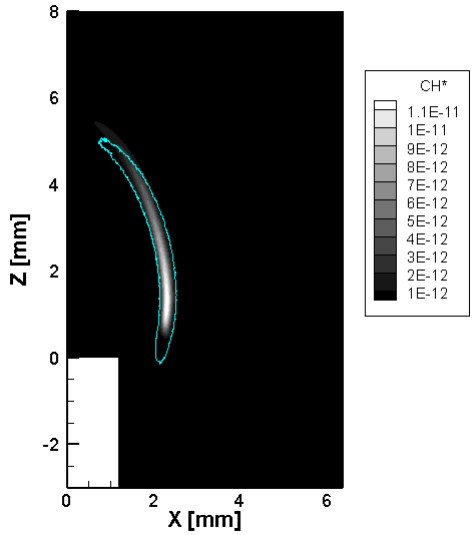

(b) 2g,0kV/cm (sim.) v.s. 1g, 0.5kV/cm (exp.)

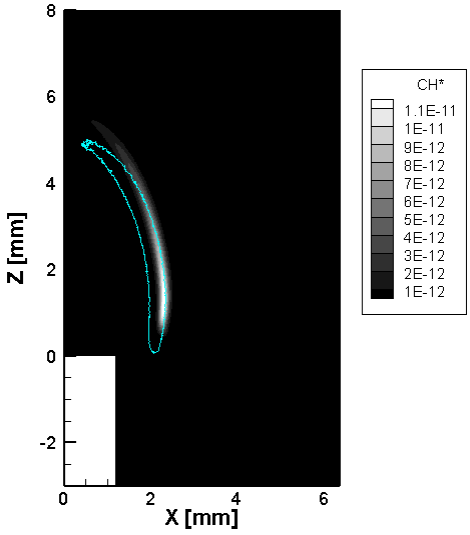

(c) 2g , 0kV/cm (sim.) v.s. 1g, 1kV/cm (exp.)

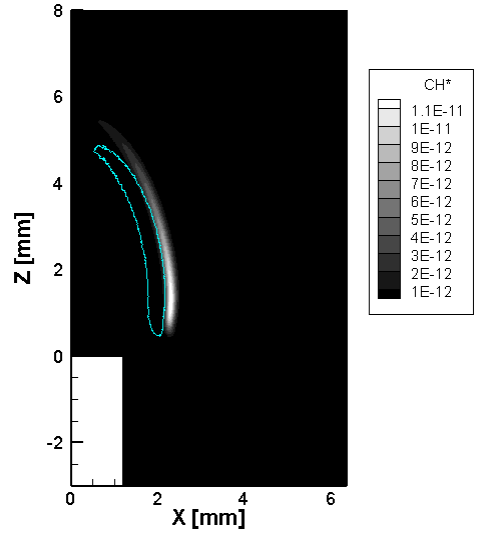

(d) 2g, 0kV/cm (sim.) v.s. 1g, 3kV/cm (exp.)

Figure 6.3: Comparison of different body force effects. Buoyancy effects without an electric field applied (CH^* grey-scale mapping) and electric field forces at 1g (CH^* blue contour from [43]). Extruded burner (close-up views). Inlet fuel flow rate = 20mL/min. "Sim." and "Exp." state for simulations and experiments, respectively.

the base behavior beyond 1kV/cm is not relevant for the comparison. Interestingly, the flame does not seem to change its lifting distance from 1.5g to 2g. Two hypotheses arise (i) the flame heats the burner tube, producing the opposite effect (flame attachment), or (ii) the 2g flame is in a mid-steady state. Supposing that the second hypothesis is not occurring since that flame was already perturbed once and left to reach steady state again – which is the solution displayed –, the first hypothesis would be happening. Appendix G numerically shows that the change of the burner wall temperature by less than 100K will not impact the flame lifting by much. Because previous experimental observations – informally reported – regarding burner tip temperature when the flame is lifted upwards showed that the burner wall temperature rises less than 100K, it remains unclear why increasing buoyancy does increase the flow velocity (as shown in Figure 6.5) but does not increase the flame detachment.

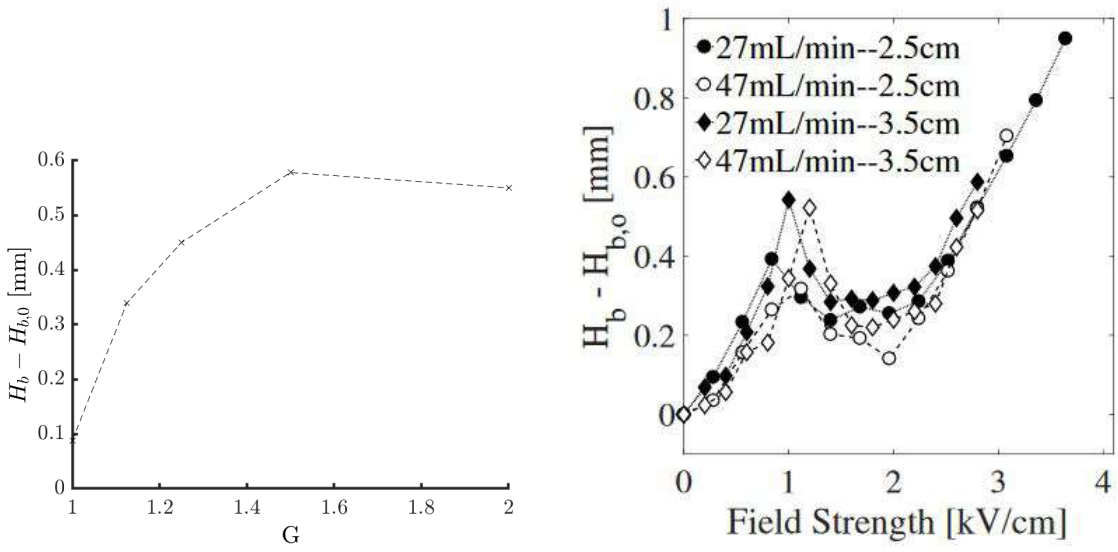

(a) Flame detachment from burner tip ($H_{b,0}$) (simulations)

(b) From [40] (experiments)

Figure 6.4: Effect of body forces in flame structure. Extruded burner geometry. Simulations for Subfigure 6.4(a) have an inlet fuel flow rate of 27mL/min and is based on simulations.

It is concluded that more data about buoyant flames at supergravity >2g is needed to extend the discussion regarding flame attachment behavior.

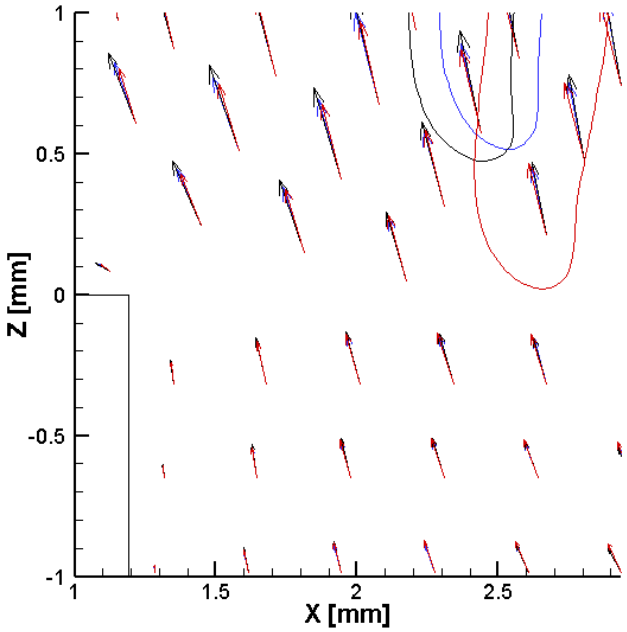

Figure 6.5: Extruded burner flame at 1g (red), 1.5g (blue) and 2g (black). Q_{fuel}=27mL/min. CH^*/CH^*_{max}=0.05. Velocity vectors plotted with the corresponding colors (1g red; 1.5g blue; 2g black) and relative vector length grid units/ magnitude = 1.

To further understand the detailed differences between buoyancy and electric field forces, the next Section 6.3.2 compares the 1g flame at saturation and the ones obtained at supergravity environments (>1g) without an electric field applied.

6.3.2 Flame temperature and species H_2O, OH, and H

Figure 6.6 compares the numerically predicted 1g flame with an electric field applied at saturation (from Chapter 5) with the simulations of flames at supergravity without an electric field applied (from Chapter 4). This figure shows the different contours for temperature, H_2O, OH, and H. The species contours have been normalized for each case. The value of the contours has been chosen to show at least 50% of the species contour since the species plotted are present at higher concentrations in the flame, so similar distribution and location of these species contribute to improved

predictions for minor species too – i.e., at least 50% of their mass fractions should be showing similar outcomes in the comparison between flames in order predict similarly the species that are in minor concentrations. For the hydrogen, the 0.65 number was picked based on Chapter 5, which showed that atomic hydrogen is an acceptable parameter to see the flame contour, and its normalized contour at 0.65 provided a reasonable flame location.

From Figure 6.6, it can be recognized that there is no buoyant flame at supergravity and without an electric field applied that captures a behavior similar to the 1g flame at saturation. Here the target for matching is the agreement with a difference of less than 20% in at least one of the subfigures for temperature or major flame species. This was expected based on the previous Figure 6.4, and it reinforces the conclusion that buoyancy force effects should be studied at even higher gravities in order to provide more insights about its equivalent repercussions in the flame relative to the electric field effects. At the moment, and for the range of buoyancy and electric field forces studied, the control of flames employing different body forces results in different flame behaviors, even in the major flame characteristics.

Previous work from Karnani et al. [34] compared the isolated effects of buoyancy and electric fields in the flame by looking at flames in microgravity with an electric field applied or flames at 1g without an electric field applied. In this work, when an electric field is applied to the flame, the flame is always exposed to a 1g environment. Higher gravity simulations and/or experiments are needed to see if it is possible to obtain a low electric field 1g flame. Thus, the outcomes from the Karnani study as well as this work suggest that the similarity between electric field and buoyancy body forces only occur when (i) the contribution of buoyancy force is substituted by an equivalent electric field force (in microgravity environments, Karnani et al. work), or when (ii) the buoyancy forces with no electric field overcome the contribution of both electric field and buoyancy forces when these forces are coupled (in partial gravity and gravity environments, this work).

Because the 2g flame without an electric field applied has a similar flame shape as the 1g 0.5kV/cm flame, a further comparison of the temperature and major species obtained in these two flames is

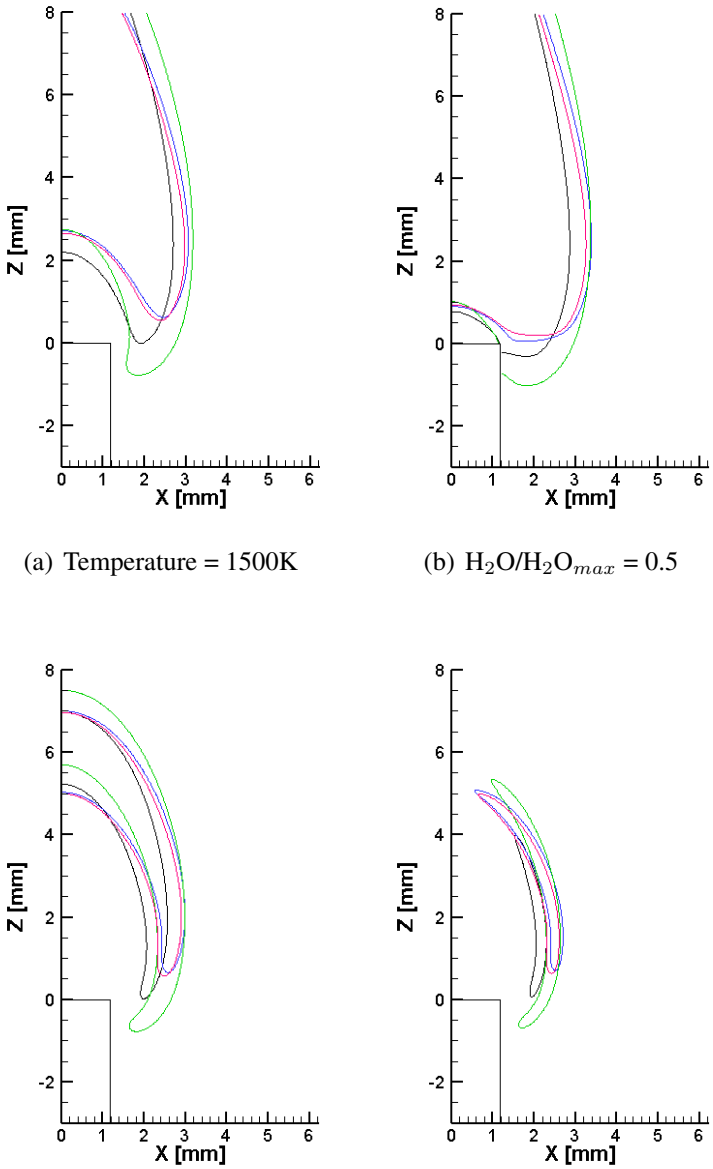

(a) Temperature = 1500K

(b) H_2O/H_2O_{max} = 0.5

(c) OH/OH_{max} = 0.5

(d) H/H_{max} = 0.65

Figure 6.6: Extruded burner with inflow fuel velocity = 27 mL/min. Case at 1g and 5kV electric field applied (supersaturation, black contour); Cases without an electric field applied at 1.5g, 1.75g, 2g (blue, green and pink contour, respectively). (a) Temperature, (b) H_2O/H_2O_{max}, (c) OH/OH_{max}, (d) H/H_{max}.

carried out. For that, the simulation from this work at 1g and 0.57kV/cm is taken as similar to the 1g 0.5kV/cm experiment. The 1g 0.57kV/cm simulation is in the subsaturation regime, and

therefore, the distribution of charges is faulty – see Chapter 5 for more details. Nevertheless, the temperature and major species in the flames are not affected. Figure 6.7 shows that the profile of the species is different for both cases, but these variations are not sufficient to be noticeable for CH^* – that is why the flame profiles look similar.

6.3.3 Body forces magnitude

This section compares the body forces magnitude employing the simulations at subsaturation and saturation for the extruded geometry presented in Chapter 5.

The buoyancy forces are always in opposition to gravity, so the vector will always point opposite to the direction of gravity. Hence, the direction of the buoyancy body forces is known and, in the studied cases from this work, it points upwards. For the calculation of the buoyancy magnitude, the density has been multiplied by the gravity. The units of the resultant buoyancy force magnitude are [N m^{-3}].

In Section 6.3.1 it has been seen that the extruded burner simulation at 2g and 0kV/cm showed a very similar CH^* location as the experimental contour at 1g and 0.5kV/cm. As in the previous section, the simulation from this work at 1g and 0.57kV/cm is taken as a similar result as the 1g and 0.5kV/cm experiment, and it is used to compare the body forces against the simulation at 2g and 0kV/cm from this work. Even though the distribution of charges is faulty in that simulation at subsaturation – see Chapter 5 for more details – the overall magnitude and distribution of electric field forces away from the near-burner region is expected to be reasonable since the overall current and current density at the downstream electrode were consistent with prior work.

Figure 6.8 shows that in the 1g simulated flame with 0.57kV/cm applied, the buoyancy and electric field forces are of the same order of magnitude at the buoyant plume. Figure 6.9 shows the logarithmic plot for the ratio between the electric field and buoyancy forces magnitude for this study case.

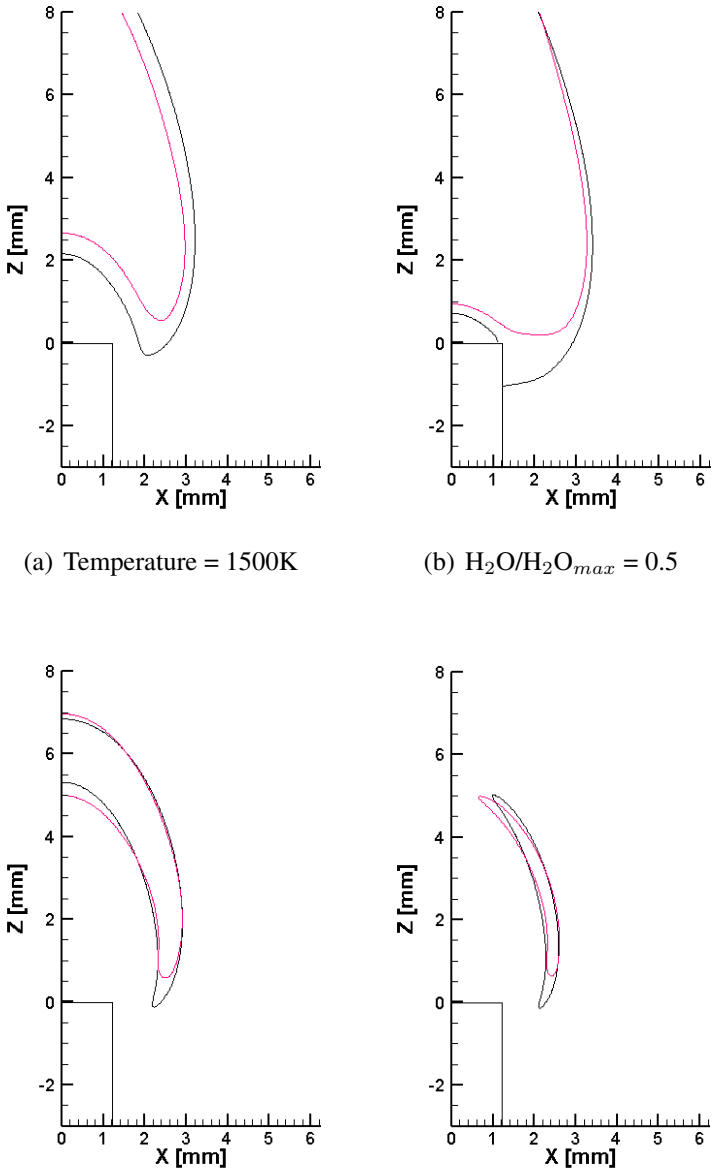

(a) Temperature = 1500K

(b) H_2O/H_2O_{max} = 0.5

(c) OH/OH_{max} = 0.5

(d) H/H_{max} = 0.65

Figure 6.7: Extruded burner with inflow fuel velocity = 27 mL/min. Case at 1g and 2kV electric field applied (0.57kV/cm, subsaturation, black contour); Case without an electric field applied at 2g (pink contour). (a) Temperature, (b) H_2O/H_2O_{max}, (c) OH/OH_{max}, (d) H/H_{max}.

In that figure, zero means that the electric field force and buoyancy force are equal in magnitude; above zero means that the electric field force is larger in magnitude than the buoyancy force; below zero means buoyancy force is larger. The mapping has been limited to zones where buoyancy force

is larger than 0.05N m^{-3} and logarithms that are larger than -2 (ratio between forces equal to 1e-2, which avoids plotting regions where electric field force is approximately zero). Hence, Figure 6.9 shows that, in fact, electric field magnitude predominates in comparison to buoyancy forces in the center axis of symmetry. Buoyancy forces are larger than the electric field moving further from the center line. These figures reinforce the fact that the influence of small electric fields applied to a 1g flame – when the electric field is applied in the same direction as the buoyant plume – is often masked by the buoyant convection since both body forces have very similar values.

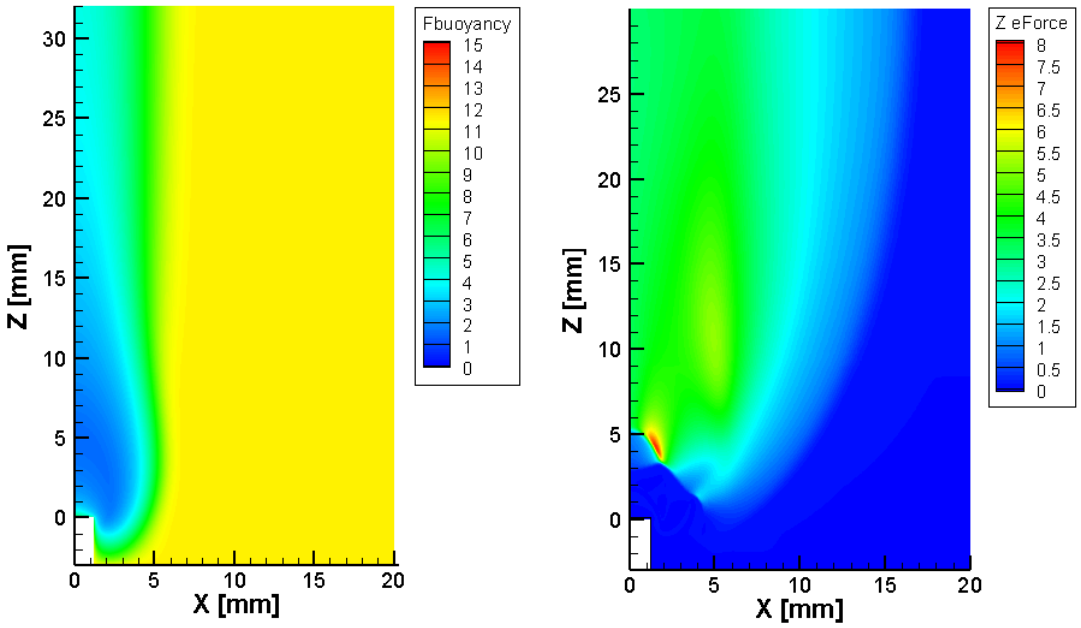

(a) Buoyancy body force

(b) Electric field body force

Figure 6.8: Comparison of body forces magnitude for the simulation at 1g and 0.57kV/cm (subsaturation). Q_{fuel}=27mL/min. Both forces are expressed in [N m^{-3}].

Because the 2g flame without an electric field applied was similarly located to the 1g flame with 0.5kV/cm applied, Figure 6.10 shows the buoyancy force for the 2g case at 0kV/cm. To compare all the body forces acting in that flame, Figure 6.11 shows the body forces acting in the 2g 0kV/cm flame (Fig.6.11 at left, only buoyancy force) and in the 1g 0.57kV/cm flame (Fig.6.11 at right, sum of buoyancy and electric field forces). Therefore, even though the CH^* profiles of a simulated 2g flame without an electric field applied and an experimental flame at 1g with 0.5kV/cm applied

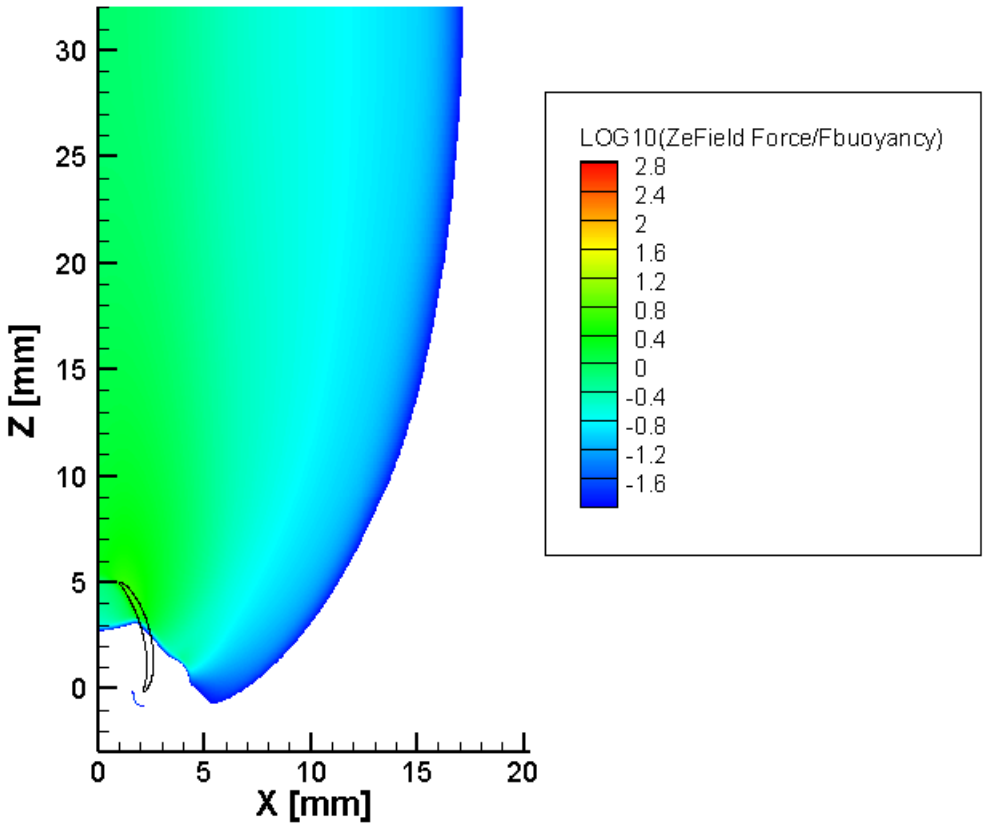

Figure 6.9: Logarithm of the ratio between buoyancy and electric field forces for the simulation results at steady-state, 1g, and 0.57kV/cm (subsaturation). Both forces are expressed in [N m^{-3}]. H/H$_{max}$ = 0.65 black contour. Whitened parts where $F_{buoyancy} < 0.05$ N m^{-3} and/or forces ratio< 1e-2 (i.e., electric field force $\approx$ 0 N m^{-3}).

overlapped, the magnitude of the forces and their distribution in the flame region is very different based on Figure 6.11. This shows that the flame shape is not a sensitive measure to locally distributed forces but instead responds to global changes in the flow field driven by the integral of body forces at work. This is equivalent to what Papac proposed [33], where the electric body force produced a downward wind that then creates a flow field in which the flame resides, so there is a complex interaction. This also explains why the time response of the flame to changes in the electric field is slower than it would be expected by an instantaneous change in local forces: the ion drift has to first set up a flow to which the flame responds. An alternative to the flame shape as a way of indicating the influence on the combustion process should be investigated for future comparisons.

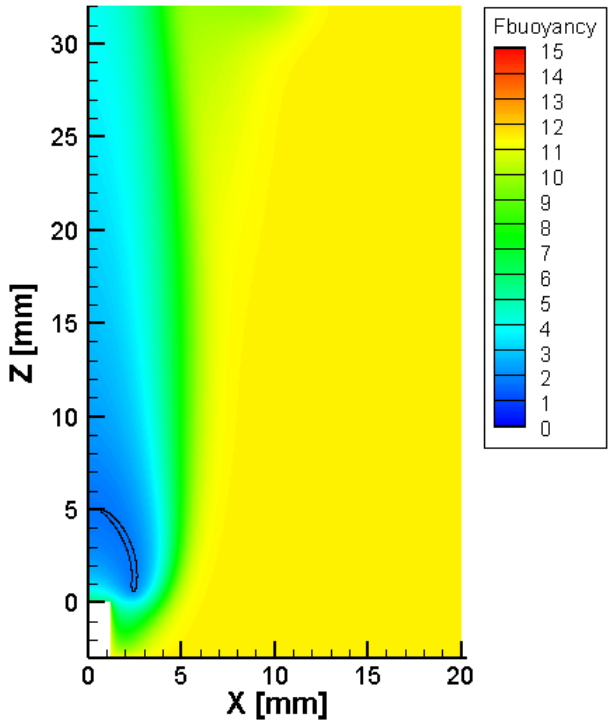

Figure 6.10: Buoyancy body force magnitude for the extruded burner simulation at 2g without an electric field applied. Buoyancy units [N m^{-3}]. H/H_{max} = 0.65 contour has been plotted as a reference to show where the flame resides. Q_{fuel}=27mL/min.

When increasing the electric field applied to the flame up to saturation (Figure 6.12) the buoyancy force shows a similar distribution, while the electric field force is still shown to be acting on the flame side and above and *expanding* sideways – as in an inverted cone shape – from the flame but more focused towards ≈3mm from the center of the burner. This explains why the current density peak is displaced by 3mm from the burner center, as shown in Chapter 5. In this saturation case, the electric field force is 4.5 times larger than the buoyancy force when these two overlap. That is clearly shown in Figure 6.13 by the green region, where the logarithm of the ratio between body forces is ≈0.45. Figure 6.13 also shows that at almost any point of the buoyant plume, the electric force magnitude is larger than the buoyant force. This suggests that at a high enough electric field applied, the buoyancy forces would not be important anymore, and the flame would be mainly driven by the electric field force. Interestingly, this point is clearly shown but it occurs at flame

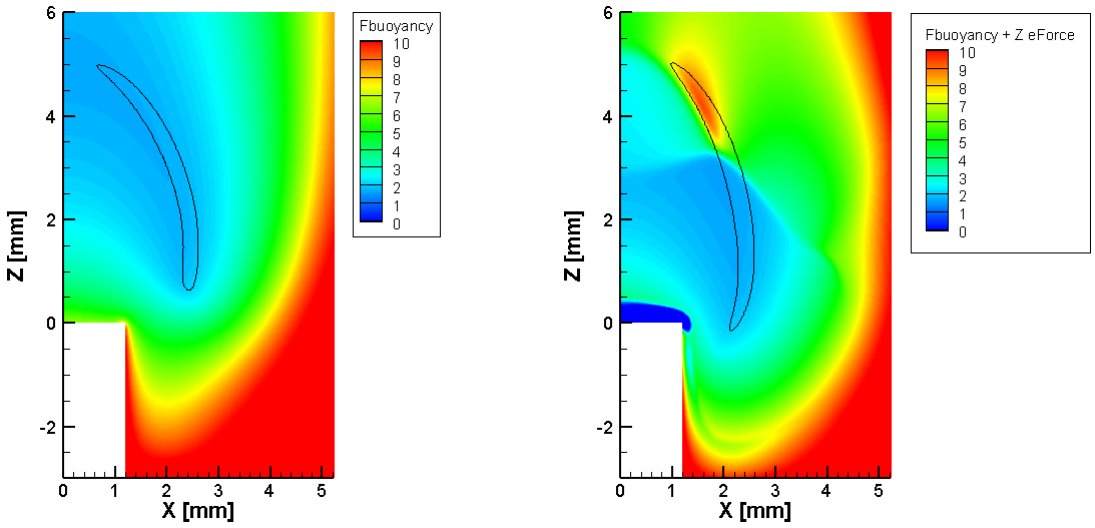

(a) Buoyancy force

(b) Buoyancy + e-field forces

Figure 6.11: Comparison of body forces magnitude acting in the flame.for the (a) Simulation at 2g and 0kV/cm, and (b) 1g and 0.57kV/cm (subsaturation). Q_{fuel}=27mL/min. Both forces are expressed in [N m^{-3}]. H/H_{max} = 0.65 contour has been plotted as a reference to show where the flame resides.

blow-off, so it turns out to be difficult to go to very high field strengths while keeping the flame stable.

6.3.4 Body forces equivalence at reduced gravity

A previous work by Karnani et al. [45] tried to show an equivalence between 1g flames (without an electric field applied) and 0g flames with an electric field applied. Figure 6.14 (extension from Figure 6.1) shows the images that Karnani used as a similarity measurement between flames, based on the intensity subtraction of the flame images. In short, the lower the computed root-mean-square (RMS) value obtained, the more similar the reduced gravity flame is presumed to the 1g flame without an electric field applied. From these images and based on the RMS obtained, Karnani concluded that 1g was about equal to the 1kV/cm. Hypothesizing that both forces scale linearly, it

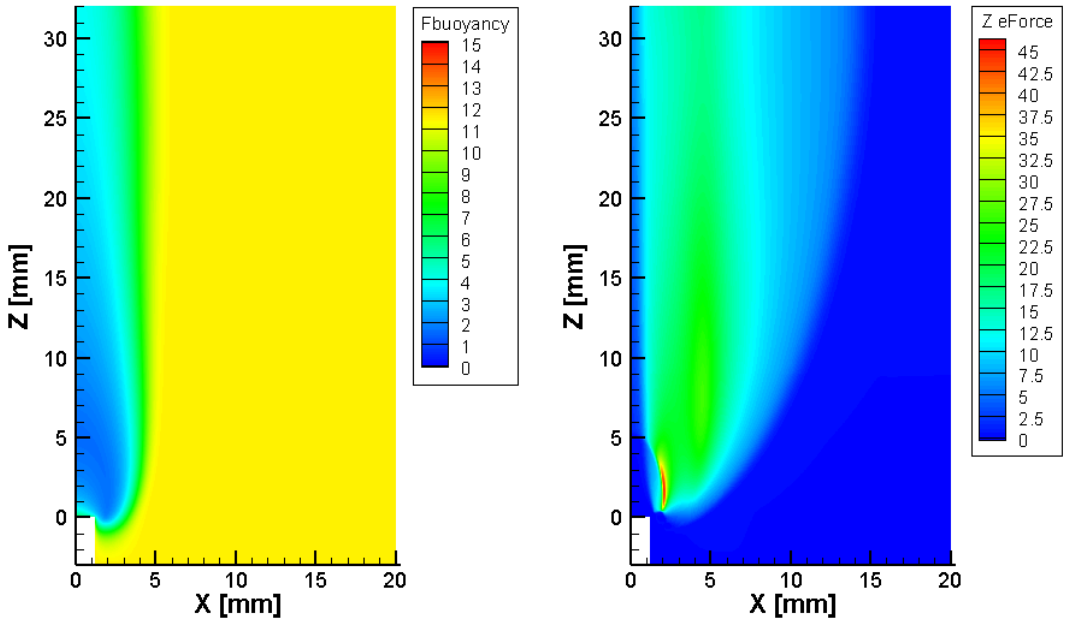

(a) Buoyancy body force

(b) Electric field body force

Figure 6.12: Comparison of body forces magnitude for the simulation at 1g and 1.29kV/cm (saturation). Both forces are expressed in [N m^{-3}].

would be expected that 0.5g equals 0.5kV/cm for a flame with coflow velocity equal to the mean jet flow (24cm/s in the Karnani case).

Figure 6.15 shows the comparison between the 1g flame without an electric field obtained from the simulations in this work (no coflow and jet velocity set at 10cm/s) and the 1g flame without an electric field from Karnani et al. [45] (with coflow and a jet velocity of 24cm/s). The flames are at the same scale based on the fact that both simulation and experimental jet diameters have the same dimensions. Unfortunately, the two flames turn out to be too dissimilar to provide an effective quantitative comparison as they used different jet velocity and the Karnani 1g flame had coflow applied leading to a sooting tip – the simulation in this work does not account for either coflow or soot chemistry.

Although conditions between both cases are too dissimilar to reach a strong conclusion, a similar general trend is observed from Figure 6.16. That is, when increasing electric field in a 0g flame,

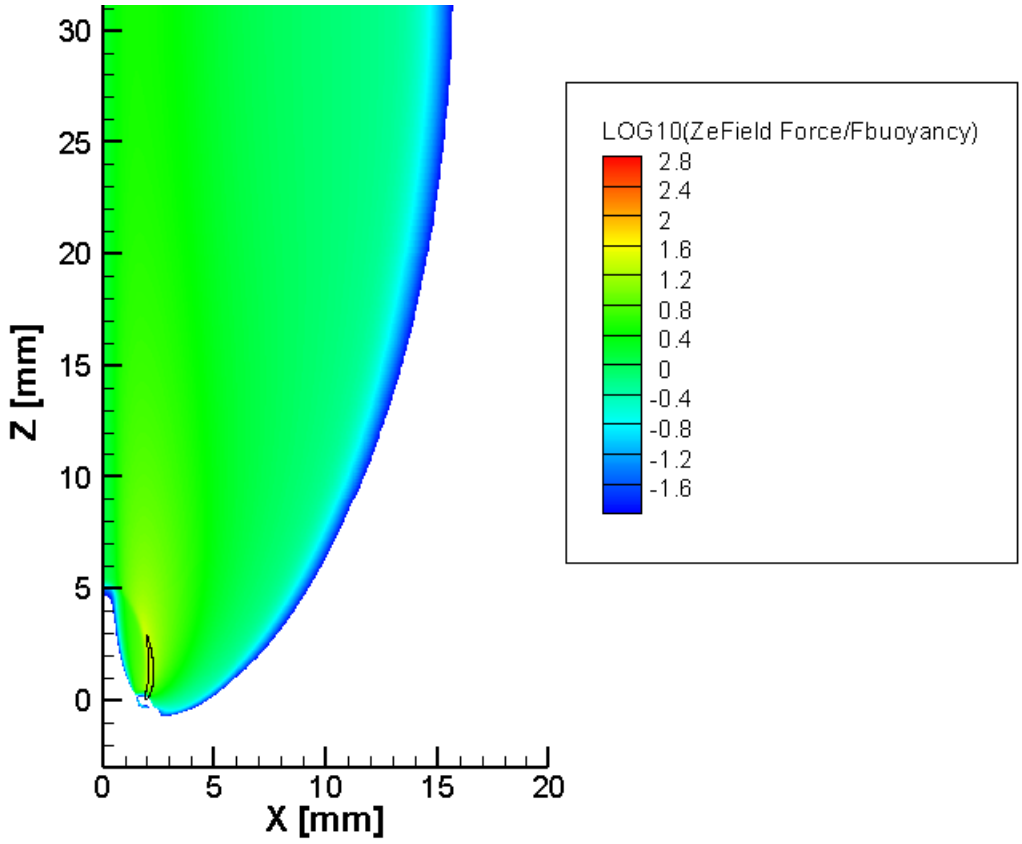

Figure 6.13: Logarithm of the ratio between buoyancy and electric field forces for the simulation results at steady-state, 1g, and 1.29kV/cm (saturation). Both forces are expressed in [N m^{-3}]. H/H_{max} = 0.65 black contour. Whitened parts where $F_{buoyancy} < 0.05$ N m^{-3} and/or forces ratio< 1e-2 (i.e., electric field force $\approx$ 0 N m^{-3}).

the inner chemiluminescent part of the flame – which is the one this work's simulations account for, without representing the halo in the exterior part of the flame – gets thinner in width. This is the same general behavior that had been observed in Chapter 3 when increasing gravity from microgravity to partial gravity.

6.4 Conclusions

It has been seen that the flame exposed to an electric field of 0.5kV/cm at 1g is equivalent in CH^* chemiluminescence (flame location) as the same flame without an electric field in a 2g environ-

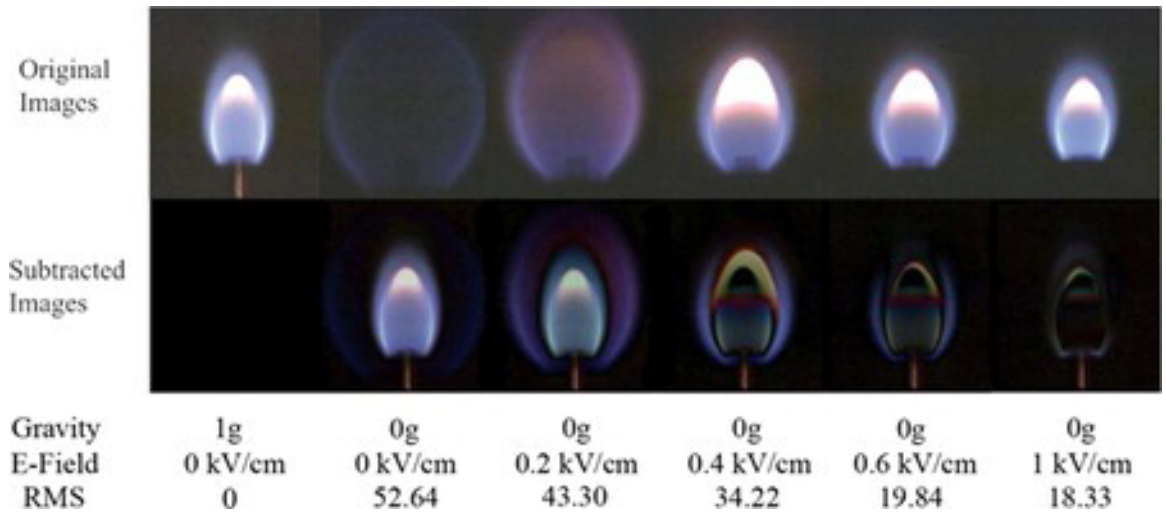

Figure 6.14: Pictures of 1g flame without an electric field applied and microgravity flames with an electric field from Karnani et al. [45].

ment. This is reasonable since the buoyancy forces in the 2g flame must compensate for the 1g force in the flame with an electric field applied plus the electric field forces. However, the main species are predicted with some differences, particularly in the region closer to the burner. This is because the magnitude of the forces acting at the flame region in a 2g 0kV/cm flame or at the 1g 0.5kV/cm is noticeably different, especially at the upper part of the flame sheet.

Buoyancy forces and electric field forces are shown to be similar in magnitude in a subsaturated 1g flame. This reinforces the fact that the influence of an electric field on these flames is going to be masked by how the buoyant forces affect the flame if the electric field is not strong enough to saturate the flame. In contrast, when the flame reaches saturation, electric field forces are one order of magnitude larger than buoyancy forces in most of the buoyant plume region.

The current data sets for microgravity flames under electric field forces and partial gravity flames without electric field forces applied are too dissimilar to reach a strong conclusion between the equivalence of buoyancy and electric field forces. However, it is clearly shown that the magnitude and distribution of both body forces in the domain are different, even when flames look similar – i.e., for the 0.5kV/cm at 1g and 2g without an electric field applied cases.

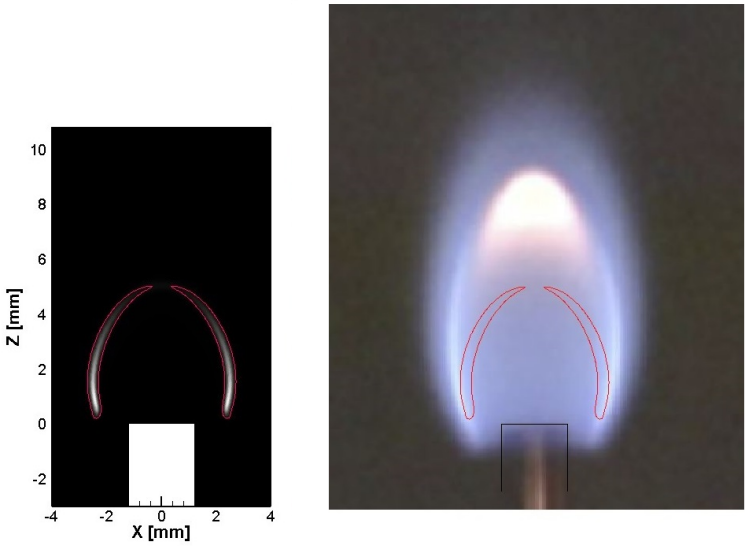

Mapping	1g 0kV/cm Simulation	1g 0kV/cm Experiment
Contour (pink)	CH*/CH*_max = 0.05	CH*/CH*_max = 0.05 (from simulation)

Figure 6.15: CH chemiluminescence of a 1g flame without an electric field applied. Left: Jet burner simulation (normalized CH*/CH^*_{max} where white = 1 and black = 0; Q_{fuel}=20mL/min); Right: Experimental flame from [45]. Pink contours represent the normalized CH*/CH^*_{max} = 0.05 from the simulation of this work.*

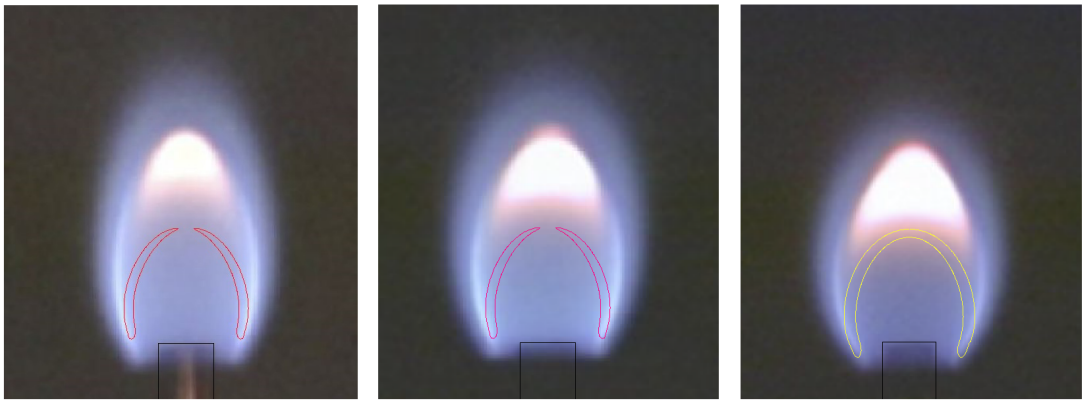

Figure 6.16: CH^* chemiluminescence. Mappings (pictures) represent the flames from Karnani et al. [45]. Contours represent the normalized CH^*/CH^*_{max} = 0.05 from the simulation of this work without an electric field applied at 1g (pink) and 0.5g (yellow).

Chapter 7

Final conclusions

The conclusions of this work have been disclosed at the end of each chapter and they are also summarized next.

Reduced chemistry reaction model

- A comprehensive reduced model, named Model 1, that includes excited species (CH* and OH*) and charged species (H_3O^+, HCO^+, $C_2H_3O^+$, CH_5O^+, O_2^-, OH^-, e^-, CO_3^-, CHO_2^-, O^-, CHO_3^-) has been achieved. Model 1 contains a total of 45 species and 216 reactions and has been reduced from a detailed model (Model 0) that contained 83 species and 394 reactions.

- The reduced Model 1 developed in this work reasonably captures the major desired features from the detailed Model 0 while reaching steady-state solutions more than three times faster than using the detailed chemistry kinetics.

- The maximum of C_2H in the flame is shown to be able to be used as a reaction zone marker if there is an advantage to leaving the excited species out of the reaction model.

Buoyancy effects

- The temperature of the microgravity flames is generally lower than for buoyant flames. Flame height is not affected by a change in the gravity field while flame width decreased. Wider flames have been observed at lower gravity environments due to radial diffusion being more significant relative to any radial inflow driven by the only weakly rising buoyant plume. For lower gravity environments, the flame sheet anchors below the burner tip.

- Even though supergravity flames have been seen in past work to show a lower luminosity, these calculations suggest that the flame CH^* luminosity is increased when increasing buoyancy due to the expansion of the high-temperature region in the flame.

- Non-buoyant flames are shown to follow the trend $L/d \approx 0.647Re^{2/3}$ for the extruded burner and $L/d \approx 0.542Re^{2/3}$ for the jet burner. For buoyant flames, the trend followed is $(L/d)Re^{-2/3}\ Fr^{-1/3} = 0.5366Fr^{-0.3159}$, $R^2 = 0.9969$ for the extruded burner and $(L/d)Re^{-2/3}Fr^{-1/3} = 0.4389Fr^{-0.4096}$, $R^2 = 0.8321$ for the jet burner.

- A correlation between the major naturally produced ion in the flame (H_3O^+) and the CH^* chemiluminescence specie has been achieved, confirming the literature hypothesis predicting a relation between ions and excited species in the flame.

- Chemi-ion profiles show that H_3O^+ can be transported further than other chemi-ions without recombination. Moreover, a higher concentration of naturally produced chemi-ions occurs under supergravity conditions, which makes these conditions interesting for future investigation of flame control by using electric fields. However, it is too early to predict the flame behavior under these conditions since competing effects of buoyant driven convection are stronger at higher gravities, and the net competition between buoyant and electric field effects can go in either direction.

External electric field effects

- The methodology using the tuning of the ion production constant C exhibited promising results for obtaining the characteristic I-V curve.
- The downstream ion current density readings showed that as the applied electric field increases, the maximum ion current density reaching the anode is located 2-3mm from the burner center. However, at lower field strengths, the Warburg distribution applies, and the maximum charges are collected at the center of the downstream electrode.
- Since the current characterization of the behavior of ions at sub-saturation regimes has shown to be faulty for predicting the charge distribution near the reaction zone, further understanding of the simulation flaws will grant more insights on the interactions that are occurring between chemistry and electric field. However, the general behavior of the charges transported towards the downstream electrode by the ion-wind effect is shown not to be affected by the charge distribution at the reaction zone, and the total amount of charges that reach the downstream electrode is well-predicted (as shown by the I-V curves). This is due, in part, to the strategy of the tuning parameter based on the saturation ion current collected experimentally.

Comparison between different body forces effects

- Based on the CH^* profiles, the position of the 2g flame without an electric field applied resembles the experimental flame at 1g with 0.5kV/cm applied. However, even in this case where the CH^* profile overlaps, it is shown that there are differences in the temperature, the major species, the body forces magnitudes, and the distribution of both body forces.
- Buoyancy forces and electric field forces are shown to be similar in magnitude in a subsaturated 1g flame. This reinforces the fact that the influence of an electric field on these flames is going to be masked by how the buoyant forces affect the flame if the electric field is not

strong enough to saturate the flame. In contrast, when the flame reaches saturation, electric field forces are one order of magnitude larger than buoyancy forces in most of the buoyant plume region.

- The current data sets for microgravity flames under electric field forces and partial gravity flames without electric field forces applied are too dissimilar to reach a strong conclusion between the equivalence of buoyancy and electric field forces.

Chapter 8

Further Challenges

Once the electric field solver provides physical solutions for the subsaturation regime, some future challenges to explore related to the research developed in this work could be:

- To further evaluate if it is possible to obtain a better trend prediction in the relation between H_3O^+ in the flame and CH^* by adding more variables to the multivariable regression analysis.
- To challenge the electric field solver by changing the chemical kinetic model onto the Model 1 developed in this work.
- To develop the electric field solver to include the secondary ionization impacts in the flame.
- To carry a numerical investigation of microgravity flames under different electric fields to bring light to a better comparison between purely driven ion-wind flames behavior and buoyant flames behavior.
- To further validate the numerical model developed by comparison with the International Space Station (ISS) experiments.

- To run simulations for positive electric fields –i.e. downstream electrode mesh acting as the cathode and burner acting as the anode.

Apart from the previous items, in the further future, some of the fundamental understanding challenges that could be investigated by using electric fields to control flame behavior are:

- Managing heat flux from flames by focusing their hot gas impingement, helping to develop more efficient devices.
- Controlling flame shape to avoid incomplete combustion, leading to less CO emissions.
- Electric field applied at different gravity environments (further than microgravity and 1g).
- Controlling soot tendency in the flame using e-fields to reduce or create soot at convenience. Similar to plasma synthesis, flame synthesis controlled by e-fields could lead to state-of-the-art materials such as carbon nanomaterials from soot deposition.

Bibliography

[1] Hong Zhao, Xiaofei Liu, and Stephen D. Tse. Control of nanoparticle size and agglomeration through electric-field-enhanced flame synthesis. *Journal of Nanoparticle Research*, 10(6):907–923, 2008.

[2] K.R. McManus, T. Poinsot, and S.M. Candel. A review of active control of combustion instabilities. *Progress in Energy and Combustion Science*, 19(1):1 – 29, 1993.

[3] J. Brouwer, B.A. Ault, J.E. Bobrow, and G.S. Samuelsen. Active control for gas turbine combustors. *Symposium (International) on Combustion*, 23(1):1087 – 1092, 1991. Twenty-Third Symposium (International) on Combustion.

[4] M. Asano, T. Kuma, M. Kajitani, and M. Takeuchi. Development of new ion current combustion control system. In *SAE Technical Paper*. SAE International, 02 1998.

[5] N. Docquier and S. Candel. Combustion control and sensors: a review. *Progress in Energy and Combustion Science*, 28(2):107 – 150, 2002.

[6] J. Lawton and F.J. Weinberg. *Electrical aspects of combustion*. Oxford University Press, 1970.

[7] S. Cao, B. Ma, B.A.V. Bennett, D. Giassi, D.P. Stocker, F. Takahashi, M.B. Long, and M.D. Smooke. A computational and experimental study of coflow laminar methane/air diffusion flames: effects of fuel dilution, inlet velocity, and gravity. *Proceedings of the Combustion Institute, 35 1 897-903*, 2015.

[8] P. B. Sunderland, B. J. Mendelson, Z.G. Yuan, and D. L. Urban. Shapes of buoyant and nonbuoyant laminar jet diffusion flames. *Combustion and Flame 116 376-386*, 1999.

[9] A.E. Malinovskii and coworkers. (series of papers).

[10] W.A. Bone, R.P. Fraser, and W.H. Wheeler. Further experiments upon flame propagation through dry carbonic oxide-oxygen mixtures in an electric field. *Proc. Roy. Soc. A132, 1*, 1931.

[11] W.A. Bone, R.P. Fraser, and W.H. Wheeler. A photographic investigation of flame movements in gaseous explosions part 7 the phenomenon of spin in detonation. *Trans. Roy. Soc. 235, 29*, 1935.

[12] W.E. Garner and S.W. Saunders. Investigations on gaseous explosions. part i. ionisation in hydrogen and oxygen explosions. *Transactions of the Faraday Society 22, 2981, 324*, 1926.

[13] E.N. Guenault and R.V. Wheeler. The propagation of flame in electric fields. part i. distortion of the flame surface. *J. Chem. Soc. 134, 195*, 1931.

[14] E.N. Guenault and R.V. Wheeler. The propagation of flame in electric fields. part ii. the effects of transverse fields. *J. Chem. Soc. 135, 2788*, 1932.

[15] H.F. Calcote. Electrical properties of flames. *3rd Symposium on Combustion and Flame, and Explosion Phenomena, 1 245-253*, 1948.

[16] A.P. Chattock. On the velocity and mass of the ions in the electric wind in air. *The Philosophical Magazine, Fifth Series, vol. 48, no. 294, pp. 401–421*, 1899.

[17] M. J. Papac and D. Dunn-Rankin. Canceling buoyancy of gaseous fuel flames in a gravitational environment using an ion-driven wind. *Annals of the New York Academy of Sciences*, 1077(1):585–601, 2006.

[18] M. K. Kim, S. H. Chung, and H. Ho Kim. Effect of electric fields on the stabilization of premixed laminar bunsen flames at low ac frequency: Bi-ionic wind effect. *Combustion and Flame*, 159(3):1151 – 1159, 2012.

[19] M. Belhi, B. J. Lee, M. S. Cha, and H. G. Im. Three-dimensional simulation of ionic wind in a laminar premixed bunsen flame subjected to a transverse dc electric field. *Combustion and Flame*, 202:90 – 106, 2019.

[20] F.B. Carleton and F.J. Weinberg. Electric field-induced flame convection in the absence of gravity. *Nature*, 330(1):635 – 636, 1987.

[21] A. P. Chattock. XXVI. on the electrification of steel needle-points in air. *The London, Edinburgh, and Dublin Philosophical Magazine and Journal of Science*, 32(196):285–304, 1891.

[22] Yu-Chien Chien and Derek Dunn-Rankin. Electric field induced changes of a diffusion flame and heat transfer near an impinging surface. *Energies*, 11(5):1235, 2018.

[23] A. B. Fialkov. Investigations on ions in flames. *Progress in Energy and Combustion Science*, 23(5):399 – 528, 1997.

[24] R.I. Noorani and R.E. Holmes. Effects of electric fields on the blowoff limits of a methane-air flame. *AIAA Journal Vol. 23 No. 9, pp. 1452-1454*, 1985.

[25] S.M. Lee, C.S. Park, M.S. Cha, and S.H. Chung. Effect of electric fields on the liftoff of non-premixed turbulent jet flames. *IEEE Transactions on Plasma Science, vol. 33, no. 5, pp. 1703-1709*, 2005.

[26] M.K. Kim, S.K. Ryu, S.H. Won, and S.H. Chung. Electric fields effect on liftoff and blowoff of nonpremixed laminar jet flames in a coflow. *Combustion and Flame*, 157(1):17 – 24, 2010.

[27] S.H. Won, M.S. Cha, C.S. Park, and S.H. Chung. Effect of electric fields on reattachment and propagation speed of tribrachial flames in laminar coflow jets. *Proceedings of the Combustion Institute*, 31(1):963 – 970, 2007.

[28] S.H. Won, S.K. Ryu, M.K. Kim, M.S. Cha, and S.H. Chung. Effect of electric fields on the propagation speed of tribrachial flames in coflow jets. *Combustion and Flame*, 152(4):496 – 506, 2008.

[29] Yu-Chien Chien. *PhD Dissertation. Electrical Aspects of Impinging Flames*. PhD thesis, 2015.

[30] L. Xie, T. Kishi, and M. Kono. The influences of electric fields on soot formation and flame structure of diffusion flames. *J. of Thermal Science 2, 288*, 1993.

[31] Y. Wang, G.J. Nathan, Z.T. Alwahabi, K.D. King, K. Ho, and Q. Yao. Effect of a uniform electric field on soot in laminar premixed ethylene/air flames. *Combustion and Flame. Volume 157, Issue 7, Pages 1308-1315*, 2010.

[32] M. Saito, T. Arai, and M. Arai. Control of soot emitted from acetylene diffusion flames by applying an electric field. *Combustion and Flame*, 119(3):356 – 366, 1999.

[33] M.J. Papac. *PhD Dissertation. Electrical aspects of gaseous fuel flames for microgravity combustion and combustion control*. PhD thesis, 2005.

[34] S.V. Karnani. *PhD Dissertation. Electric Field-Driven Flame Dynamics*. PhD thesis, 2011.

[35] M.R.J. Charest, C.P.T. Groth, and O.L. Gulder. Effects of gravity and pressure on laminar coflow methane–air diffusion flames at pressures from 1 to 60 atmospheres. *Combustion and Flame, 158 860–875*, 2011.

[36] P.B. Sunderland, S.S. Krishnan, and J.P. Gore. Effects of oxygen enhancement and gravity on normal and inverse laminar jet diffusion flames. *Combustion and Flame, 136 254–256*, 2004.

[37] P. Bhatia, V.R. Katta, S.S. Krishnan, Y. Zheng, P.B. Sunderland, and J.P. Gore. Simulations of normal and inverse laminar diffusion flames under oxygen enhancement and gravity variation. *Combustion Theory and Modelling, 16 5 774–798*, 2012.

[38] R. A. Altenkirch, R. Eichhorn, N. N. Hsu, A. B. Brancic, and N. E. Cevallos. Characteristics of laminar gas jet diffusion flames under the influence of elevated gravity. *Proceedings of the Combustion Institute 16 (1165-1174)*, 1976.

[39] P. B. Sunderland, D. L. Urban, and V. Nayagam. Scaling of gas-jet flame lengths in elevated gravity. *Progress in Scale Modeling, 269-279*, 2008.

[40] J.A. Tinajero. *PhD Dissertation. Flame dynamics and chemi-ion flows driven by applied electric fields.* PhD thesis, 2017.

[41] G. P. Smith, Y. Tao, and H. Wang. Foundational Fuel Chemistry Model Version 1.0 (FFCM-1). https://web.stanford.edu/group/haiwanglab/FFCM1/pages/FFCM1.html.

[42] ANSYS, Inc. Chemkin theory manual 17.0 (15151), 2015. Reaction Design: San Diego.

[43] J. Tinajero and D. Dunn-Rankin. Non-premixed axisymmetric flames driven by ion currents. *Combustion and Flame*, 199:365 – 376, 2019.

[44] J. Tinajero, G. Bernard, L. Autef, and D. Dunn-Rankin. Characterizing i-v curves for non-premixed methane flames stabilized on different burner configurations. *Combustion, Science and Technology, 189:10 1739-1750*, 2017.

[45] S. Karnani, D. Dunn-Rankin, F. Takahashi, Z.G. Yuan, and D. Stocker. Simulating gravity in microgravity combustion using electric fields. *Combustion Science and Technology 184 (10-11), 1891-1902*, 2012.

[46] K. T. Walsh. *PhD Dissertation. Quantitative Characterizations of Coflow Laminar Diffusion Flames in a Normal Gravity and Microgravity Environment*. PhD thesis, 2000.

[47] H. Bufferand, L. Tosatto, B. La Mantia, M.D. Smooke, and A. Gomez. Experimental and computational study of methane counterflow diffusion flames perturbed by trace amounts of either jet fuel or a 6-component surrogate under non-sooting conditions. *Combustion and Flame*, 156(8):1594 – 1603, 2009.

[48] D. Urzica and E. Gutheil. Counterflow combustion modeling of ch_4/air and ch_4/o_2 including detailed chemistry. 2008.

[49] R.E. Padilla. *PhD Dissertation. Structure and Behavior of Water-laden Methane/Air Flames.* PhD thesis, 2016.

[50] Claudia-F. López-Cámara, Albert Jordà Juanós, and William A. Sirignano. Strain rate and pressure effects on multi-branched counterflow flames. *Combustion and Flame*, 221:256 – 269, 2020.

[51] Openfoam Foundation ltd, Version: 2.4.0.

[52] Openfoam Foundation ltd, Version: 4.0.

[53] D.P. Stocker, F. Takahashi, J.M. Hickman, and A.C. Suttles. Gaseous non-premixed flame research planned for the international space station. 2014.

[54] T.F. O'Malley, W.A. Sheredy, and D.P. Stocker. Combustion research on the international space station. 2008.

[55] S.P. Burke and T.E.W. Schumann. Diffusion flames. *Proceedings of the Symposium on Combustion*, 1-2:2 – 11, 1948.

[56] B. Ma, Su Cao, D. Giassi, D. P. Stocker, F. Takahashi, B. A. V. Bennett, M. D. Smooke, and M. B. Long. An experimental and computational study of soot formation in a coflow jet flame under microgravity and normal gravity. *Proceedings of the Combustion Institute*, 35(1):839 – 846, 2015.

[57] F.G. Roper. The prediction of laminar jet diffusion flame sizes: Part i. theoretical model. *Combustion and Flame*, 29:219 – 226, 1977.

[58] M.D. Smooke, P. Lin, J.K. Lam, and M.B. Long. Computational and experimental study of a laminar axisymmetric methane-air diffusion flame. *Symposium (International) on Combustion*, 23(1):575 – 582, 1991. Twenty-Third Symposium (International) on Combustion.

[59] Chris Greenshields. Openfoam v6 user guide: 5.3 mesh generation with blockmesh. `https://cfd.direct/openfoam/user-guide/v6-blockmesh/`.

[60] Rafalzietara. OpenFOAM wiki (Main ContribExamples/AxiSymmetric). `https://openfoamwiki.net/index.php/Main_ContribExamples/AxiSymmetric`, 2008.

[61] OpenCFD Ltd. OpenFOAM. The open source CFD toolbox. `https://www.openfoam.com/documentation/user-guide/boundaries.php`, 2008.

[62] M. Johansson. *Master thesis. Evaluation of RANS turbulence models for the hydrodynamic analysis of an axisymmetric streamlined body with special consideration of the velocity distribution in the stern region*. PhD thesis, 2012.

[63] V. Ricchiuti. *Master thesis. OpenFOAM simulations of impinging coflow flames, including chemi-ionization and electric fields*. PhD thesis, 2016.

[64] D. Escofet Martin. *PhD Dissertation. Laser diagnostics for high pressure combustion.* PhD thesis, 2017.

[65] White. *Viscous Fluid Flow*. McGraw Hill, 1991.

[66] L. Acampora, F. S. Marra, and E. Martelli. Comparison of different ch4-air combustion mechanisms in a perfectly stirred reactor with oscillating residence times close to extinction. *Combustion Science and Technology*, 188(4-5):707–718, 2016.

[67] A. Kazakov and M. Frenklach. DRM19 model. `http://combustion.berkeley.edu/drm/`, 1994.

[68] G. P. Smith, D. M. Golden, M. Frenklach, N. W. Moriarty, B. Eiteneer, M. Goldenberg, C. T. Bowman, R. K. Hanson, S. Song, W. C. Gardiner, Jr., V. V. Lissianski, and Z. Qin. GRI-3.0 Mech. `http://www.me.berkeley.edu/gri_mech/`, 1999.

[69] C. Gibaud, J.A. Snyder, V.Sick, and R.P. Lindstedt. Laser-induced fluorescence measurements and modeling of absolute CH concentrations in strained laminar methane/air diffusion flames. *Proceedings of the Combustion Institute, 30 (455-462)*, 2005.

[70] C-F. López-Cámara. Master's thesis. numerical simulation of a non-premixed co-flow methane/air flame including ions and excited species, 2015.

[71] K.T. Walsh, M.B. Long, M.A. Tanoff, and M.D. Smooke. Experimental and computational study of ch, ch*, and oh* in an axisymmetric laminar diffusion flame. *Symposium (International) on Combustion*, 27(1):615 – 623, 1998. Twenty-Seventh Sysposium (International) on Combustion Volume One.

[72] C.T. Bowman, R.K. Hanson, D.F. Davidson, W.C. Gardinera Jr., V. Lissianski, G.P. Smith, D.M. Golden, M. Frenklach, and M. Goldenberg. GRI 2.11 Mech. `http://http://combustion.berkeley.edu/gri-mech/new21/version21/text21.html`.

[73] Chemical-kinetic mechanisms for combustion applications, San Diego Mechanism web page, Mechanical and Aerospace Engineering (Combustion Research), University of California at San Diego. `http://combustion.ucsd.edu`, 2018.

[74] K. T. Walsh, J. Fielding, M. D. Smooke, M. B. Long, and A. Liñán. A comparison of computational and experimental lift-off heights of coflow laminar diffusion flames. *Proceedings of the Combustion Institute*, 30(1):357 – 365, 2005.

[75] L. He, Q. Guo, Y. Gong, F. Wang, and G. Yu. Investigation of oh* chemiluminescence and heat release in laminar methane–oxygen co-flow diffusion flames. *Combustion and Flame*, 201:12 – 22, 2019.

[76] D. Kim, F. Rizzi, K.W. Cheng, J. Han, F. Bisetti, and O.M. Knio. Uncertainty quantification of ion chemistry in lean and stoichiometric homogenous mixtures of methane, oxygen, and argon. *Combustion and Flame. 162, 2904–2915*, 2015.

[77] K. Devriendt, H. van Look, B. Ceusters, and J. Peeters. Kinetics of formation of chemiluminescent CH(A2Delta) by the elementary reactions of C2H(X2Epsilon+) with O(3P) and O2(X3Epsilong): A pulse laser photolysis study. *Chemical Physics Letter, 261 (450-456)*, 1996.

[78] M. Tamura, P.A. Berg, J.E. Harrington, J. Luque, J.B. Jeffries, G.P. Smith, and D.R. Crosley. Collisional quenching of CH(A), OH(A), and NO(A) in low pressure hydrocarbon flames. *Combustion and Flame, 114 (503-514)*, 1998.

[79] Martin Rolf Werner Lauer. *PhD Dissertation. Determination of the Heat Release Distribution inTurbulent Flames by Chemiluminescence Imaging*. PhD thesis, 2011.

[80] C.S. Panoutsos, Y. Hardalupas, and A.M.K.P. Taylor. Numerical evaluation of equivalence ratio measurement using OH* and CH* chemiluminescence in premixed and non-premixed methane–air flames. *Combustion and Flame*, 156(2):273 – 291, 2009.

[81] Y. Hardalupas and M. Orain. Local measurements of the time-dependent heat release rate and equivalence ratio using chemiluminescent emission from a flame. *Combustion and Flame*, 139(3):188 – 207, 2004.

[82] D. Giassi, S. Cao, B. A. V. Bennett, D. P. Stocker, F. Takahashi, M. D. Smooke, and M. B. Long. Analysis of ch* concentration and flame heat release rate in laminar coflow diffusion flames under microgravity and normal gravity. *Combustion and Flame*, 167:198 – 206, 2016.

[83] R.P. Porter, A.H. Clark, W.E. Kaskan, and W.E. Browne. A study of hydrocarbon flames. *Eleventh Symposium (International) on Combustion, The Combustion Institute (907-917)*, 1996.

[84] T. Pedersen and R. C. Brown. Simulation of electric field effects in premixed methane flames. *Combustion and Flame*, 94(4):433 – 448, 1993.

[85] Fred L. Jones, Philip M. Becker, and Robert J. Heinsohn. A mathematical model of the opposed-jet diffusion flame: Effect of an electric field on concentration and temperature profiles. *Combustion and Flame. 19, 3, 351–362*, 1972.

[86] J. Prager, U. Riedel, and J. Warnatz. Modeling ion chemistry and charged species diffusion in lean methane–oxygen flames. *Proceedings of the Combustion Institute*, 31(1):1129 – 1137, 2007.

[87] W. K. Metcalfe, S. M. Burke, S. S. Ahmed, and H. J. Curran. A hierarchical and comparative kinetic modeling study of c1-c2 hydrocarbon and oxygenated fuels. *Intl. J. Chemical Kinetics*, 45:638 – 675, 2013.

[88] Hartwell F. Calcote. Electrical properties of flames: Burner flames in transverse electric fields. *Symposium on Combustion and Flame, and Explosion Phenomena*, 3(1):245 – 253, 1948. Third Symposium on Combustion and Flame and Explosion Phenomena.

[89] T. Lu and C. K. Law. Toward accommodating realistic fuel chemistry in large-scale computations. *Progress in Energy and Combustion Science*, 35(2):192 – 215, 2009.

[90] A. Burcat. Prof. Burcat's Thermodynamic Data. `http://garfield.chem.elte.hu/Burcat/burcat.html`.

[91] Nick J. Killingsworth, Matthew J. McNenly, Russell A. Whitesides, , and Scott W. Wagnon. Cloud based tool for analysis of chemical kinetic mechanisms. *Combustion and Flame*, 2020.

[92] Perrine Pepiot and Heinz Pitsch. Systematic reduction of large chemical mechanisms. 2005.

[93] P. Pepiot-Desjardins and H. Pitsch. An efficient error-propagation-based reduction method for large chemical kinetic mechanisms. *Combustion and Flame*, 154(1):67 – 81, 2008.

[94] ANSYS, Inc. ANSYS Chemkin-Pro Reaction Workbench User's Manual, 2018.

[95] A. Stagni, A. Cuoci, A. Frassoldati, T. Faravelli, and E. Ranzi. Lumping and reduction of detailed kinetic schemes: an effective coupling. *Industrial & Engineering Chemistry Research*, 53(22):9004–9016, 2014.

[96] M. Belhi, J. Han, T. A. Casey, J.-Y. Chen, H. G. Im, S. M. Sarathy, and F. Bisetti. Analysis of the current–voltage curves and saturation currents in burner-stabilised premixed flames with detailed ion chemistry and transport models. *Combustion Theory and Modelling*, 22(5):939–972, 2018.

[97] Reaction Design. TRANSPORT, TRA-036-1, Chemkin Collection Release 3.6, September 2000. `https://www3.nd.edu/~powers/ame.60636/transport.pdf`.

[98] T. Kathrotia, U. Riedel, A. Seipel, K. Moshammer, and A. Brockhinke. Experimental and numerical study of chemiluminescent species in low-pressure flames. 107:571–584, 2012.

[99] A. B. S. Alquaity, J. Han, M. Chahine, H. Selim, M. Belhi, S. M. Sarathy, F. Bisetti, and A. Farooq. Measurements of positively charged ions in premixed methane-oxygen atmospheric flames. *Combustion Science and Technology*, 189(4):575–594, 2017.

[100] J.M. Goodings, D.K. Bohme, and Chun-Wai Ng. Detailed ion chemistry in methaneoxygen flames. ii. negative ions. *Combustion and Flame*, 36:45 – 62, 1979.

[101] Songhua Cao, B.A.V. Bennett, Bin Ma, D. Giassi, D.P. Stocker, Fumiaki Takahashi, M.B. Long, and M.D. Smooke. Effects of fuel dilution and gravity on laminar coflow methane-air diffusion flames: A computational and experimental investigation. *8th US National Combustion Meeting 2013*, 4:3458–3466, 01 2013.

[102] F. Weinberg, F. Carleton, R. Houdmont, D. Dunn-Rankin, and S. Karnani. Syngas formation in methane flames and carbon monoxide release during quenching. *Combustion and Flame*, 158(2):273 – 280, 2011.

[103] J.A Tinajero. *Master's Thesis. Dynamics of Chemi-Ion Driven Flows in an Applied Electric Field.* PhD thesis, 2015.

[104] M.D. Smooke, Y. Xu, R.M. Zurn, P. Lin, J.H. Frank, and M.B. Long. Computational and experimental study of oh and ch radicals in axisymmetric laminar diffusion flames. *Symposium (International) on Combustion*, 24(1):813 – 821, 1992. Twenty-Fourth Symposium on Combustion.

[105] M.D. Smooke, A. Ern, M.A. Tanoff, B.A. Valdati, R.K. Mohammed, D.F. Marran, and M.B. Long. Computational and experimental study of no in an axisymmetric laminar diffusion flame. *Symposium (International) on Combustion*, 26(2):2161 – 2170, 1996.

[106] L. Pulga, G.M. Bianchi, S. Falfari, and C. Forte. A machine learning methodology for improving the accuracy of laminar flame simulations with reduced chemical kinetics mechanisms. *Combustion and Flame*, 216:72 – 81, 2020.

[107] G.S. Settles. *Schlieren and Shadowgraph Techniques. Visualizing Phenomena in Transparent Media*. Springer-Verlag Berlin Heidelberg, 2001.

[108] A. Davidhazy. Introduction to shadowgraph and schlieren imaging. `http://scholarworks.rit.edu/article/478`, 2006.

[109] E. Luthman, N. Cymbalist, D. Lang, G. Candler, and P. Dimotakis. Simulating schlieren and shadowgraph images from les data. *Experiments in Fluids*, 60(134), 2019.

[110] Thomas H. Cochran and William J. Masica. An investigation of gravity effects on laminar gas-jet diffusion flames. *Thirteenth Symposium (International) on Combustion*, 13(1):821 – 829, 1971.

[111] A. Veshkini and S. B. Dworkin. A computational study of soot formation and flame structure of coflow laminar methane/air diffusion flames under microgravity and normal gravity. *Combustion Theory and Modelling*, 21(5):864–878, 2017.

[112] reactingFoam from OpenFOAM repository. `https://develop.openfoam.com/Development/openfoam/-/tree/master/applications/solvers/combustion/reactingFoam`.

[113] J.O. Hinze. *Turbulence*. 1987.

[114] N.R. Panchapakesan and J.L. Lumley. Turbulence measurements in axi-symmetric jets of air and helium. *Journal of Fluid Mechanics 225 246*, 1993.

[115] I. Yimer, I. Campbell, and L.Y. Jiang. Estimation of the turbulent schmidt number from experimental profiles of axial velocity and concentration for high-reynolds-number jet flows. *Canadian Aeronautics and Space Journal 195 3*, 2002.

[116] A. Albayrak, D. A Bezgin, and W. Polifke. Response of a swirl flame to inertial waves. *International Journal of Spray and Combustion Dynamics*, 10(4):277–286, 2018.

[117] Peter B. Sunderland, James E. Haylett, David L. Urban, and Vedha Nayagam. Lengths of laminar jet diffusion flames under elevated gravity. *Combustion and Flame*, 152(1):60 – 68, 2008.

[118] Kiyotaka Yamashita, Sunny Karnani, and Derek Dunn-Rankin. Numerical prediction of ion current from a small methane jet flame. *Combustion and Flame*, 156(6):1227 – 1233, 2009.

[119] P. Gillon, V. Gilard, M. Idir, and B. Sarh. Electric field influence on the stability and the soot particles emission of a laminar diffusion flame. *Combustion Science and Technology*, 191(2):325–338, 2019.

[120] M. Belhi, B.J. Lee, F. Bisetti, and H.G. Im. A computational study of the effects of dc electric fields on non-premixed counterflow methane-air flames. *J. Phys. D: Appl. Phys. 50, 494005 (12pp)*, 2017.

[121] Mario Di Renzo, Javier Urzay, Pietro De Palma, Marco D. de Tullio, and Giuseppe Pascazio. The effects of incident electric fields on counterflow diffusion flames. *Combustion and Flame*, 193:177 – 191, 2018.

[122] J.D.B.J. van den Boom, A.A. Konnov, A.M.H.H. Verhasselt, V.N. Kornilov, L.P.H. de Goey, and H. Nijmeijer. The effect of a dc electric field on the laminar burning velocity of premixed methane/air flames. *Proceedings of the Combustion Institute*, 32(1):1237 – 1244, 2009.

[123] D. G. Park, S. H. Chung, and M. S. Cha. Bidirectional ionic wind in nonpremixed counterflow flames with dc electric fields. *Combustion and Flame*, 168:138 – 146, 2016.

[124] C. Guerra-Garcia and M. Martinez-Sanchez. Counterflow nonpremixed flame dc displacement under ac electric field. *Combustion and Flame*, 162(11):4254 – 4263, 2015.

[125] M.J. Papac and D. Dunn-Rankin. Modelling electric field driven convection in small combustion plasmas and surrounding gases. *Combustion Theory and Modelling*, 12(1):23–44, 2008.

[126] A. Sayed-Kassem, P. Gillon, M. Idir, and V. Gilard. On the effect of a dc electric field on soot particles' emission of a laminar diffusion flame. *Combustion Science and Technology*, 0(0):1–12, 2019.

[127] Y. Ren, W. Cui, H. Pitsch, and S. Li. Experimental and numerical studies on electric field distribution of a premixed stagnation flame under dc power supply. *Combustion and Flame*, 215:103 – 112, 2020.

[128] J. Han, M. Belhi, F. Bisetti, and S.M. Sarathy. Numerical modeling of ion transport in flames. 19:744–772, 2017.

[129] J. Han. *PhD Dissertation. Numerical study of electric field enhanced combustion*. 2017.

[130] F. Bisetti and M. El Morsli. Calculation and analysis of the mobility and diffusion coefficient of thermal electrons in methane/air premixed flames. *Combustion and Flame*, 159(12):3518 – 3521, 2012.

[131] S. Karnani and D. Dunn-Rankin. Detailed characterization of dc electric field effects on small non-premixed flames. *Combustion and Flame*, 162(7):2865 – 2872, 2015.

[132] F. Weinberg and F. Carleton. Ionization and chemiluminescence during the progressive aeration of methane flames. *Combustion and Flame*, 156(12):2276 – 2284, 2009.

[133] B. A. Strayer, J. D. Posner, D. Dunn-Rankin, and F. J. Weinberg. Simulating microgravity in small diffusion flames by using electric fields to counterbalance natural convection. *Proceedings of the Royal Society of London A*, 458:1151–1166, 2002.

[134] M.J. Papac, D. Dunn-Rankin, C.B. Stipe, and D. Lucas. N2 cars thermometry and o2 lif concentration measurements in a flame under electrically induced microbuoyancy. *Combustion and Flame*, 133(3):241 – 254, 2003.

Appendix A

Domain independence

The domain independence test is fundamentally needed to ensure that the domain is large enough to prevent side boundaries from affecting the outcome.

A.1 Procedure

To test the domain independence, the same two-dimensional simulation is performed until it reaches steady-state for two different domains for the extruded burner geometry. The two different extruded domains tested have the same meshing – i.e., same cell size for each zone. The simulation used for the domain independence test employs a three-step global chemical kinetic model from the literature [66] with a volumetric flow rate of 20mL/min, at 1g, and without electric field applied.

The two domains employed for the comparison are shown in Figure A.1, where the right subfigure is 25% larger in its domain with respect to the left subfigure. For clarity, in this appendix the domain represented by the left subfigure will be called the "standard" domain, while the right one will be named the "larger" domain.

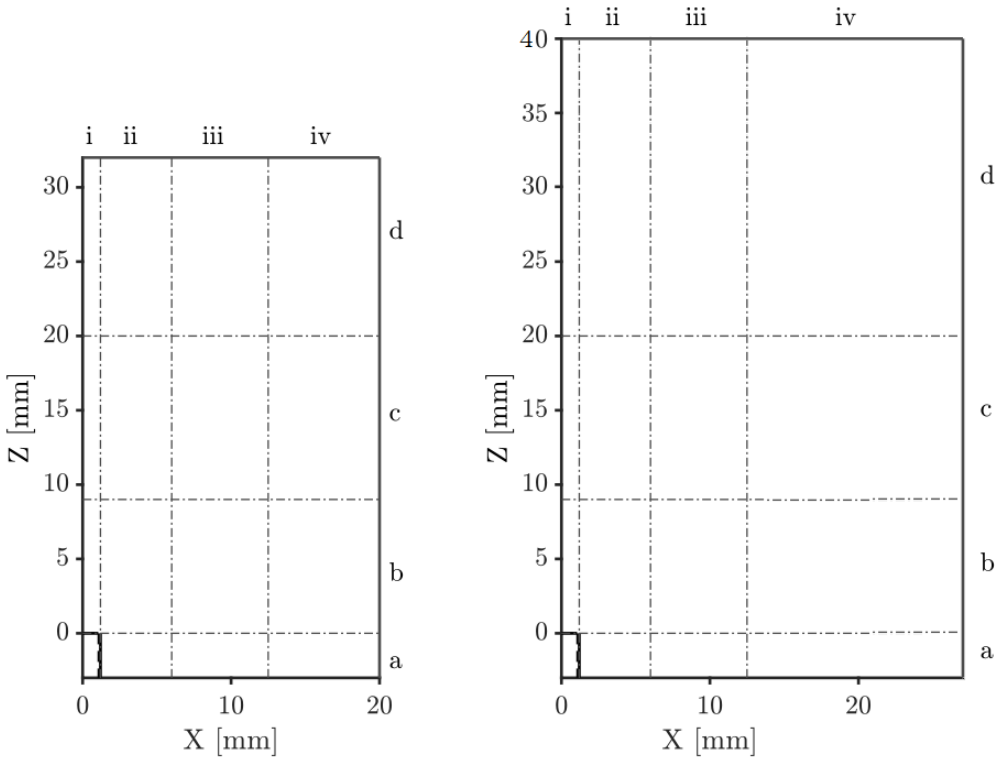

Figure A.1: OpenFOAM® mesh details and zones. Extruded burner geometries. Domain taken as standard (left) and domain with +25% of the standard domain (right).

The mesh grid detail is shown in Table A.1, which is a reproduction of Table 2.3 from Chapter 2.

The boundary conditions are set as described in Chapter 2, Section 2.3.1.

Table A.1: Reproduced from Table 2.3. Mesh grid details

Region	ΔX [mm]	ΔZ [mm]	X range [mm]	Z range [mm]
i	0.033	-	0.00 - 1.20	-
ii	0.033	-	1.20 - 6.00	-
iii	0.083	-	6.00 - 12.5	-
iv	0.150	-	12.5 - 20.0	-
a (extruded)	-	0.033	-	-3.00 - 0.00
b	-	0.033	-	0.00 - 9.00
c	-	0.150	-	9.00 - 20.0
d	-	0.300	-	20.0 - 32.0

A.2 Validation of domain independence

Since the reaction model employed for this purpose only accounts for few major species CH_4, O_2, N_2, CO_2, and H_2O and temperature, the validation by comparison between the results obtained employing both volume domains is performed by observing the distribution of these major species and temperature. A difference below 15% is expected for the local distribution of the species mass fraction, as well as for the temperature and maximum temperature achieved.

Because the effects of the boundary could be observed even if the flame is not in steady-state, the comparison between both simulations can be performed even before reaching steady-state. Notice that to be comparable, the same time steps have been run for both simulations during the ignition stage of the simulation – in this case, from 0s to 0.01s in flame real time – and once the ignition heat source is removed – in this case, from 0.01s to 0.051s. Thus, the simulations compared are for a flame real-time of 0.051s.

Figure A.2 shows that the temperature distribution can be considered the same since the maximum difference in peak temperature is 5K, and the maximum difference in location for the same temperature contours is less than 10%.

The most significant difference between the major species distribution is shown in Figure A.3, and it corresponds to the H_2O profile whose maximum variation in distribution location differs by 11.45%, which is still within the acceptable threshold. The rest of the species present lower differences in distribution location – O_2 8.4%, CO_2 10.44%, and less than 3% for N_2 and CH_4.

It is concluded that the "standard" domain is not perturbed by the close boundary by more than 12% in any case in comparison to the larger domain. Hence, this domain is chosen to proceed with the two-dimensional simulations for this work.

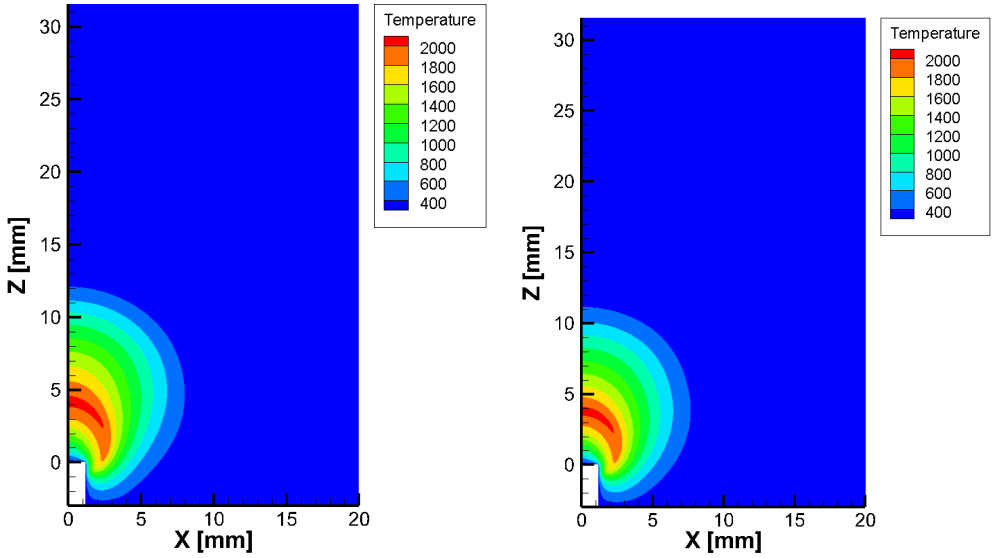

(a) "Standard" domain (b) Larger domain (close-up)

Figure A.2: Temperature profile at 0.051s of a 1g flame without e-field applied (non-steady state). 3-Step chemical kinetic model. Fuel rate = 20mL/min.

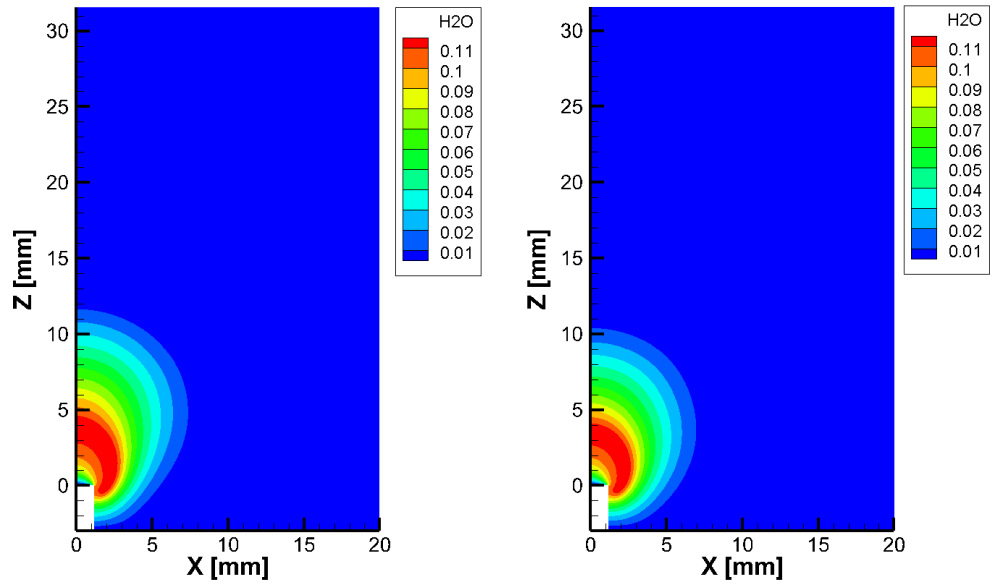

(a) "Standard" domain (b) Larger domain (close-up)

Figure A.3: H_2O profile at 0.051s of a 1g flame without e-field applied (non-steady state). 3-Step chemical kinetic model. Fuel rate = 20mL/min.

Appendix B

Mesh independence

The mesh independence test is fundamentally needed to ensure that the results of a numerical simulation are not dependent on the meshing size.

B.1 Procedure

To test the mesh independence, the same two-dimensional simulation is carried out until it reaches a steady-state for each mesh case. Three different extruded configuration meshes are tested. The simulation used for the mesh independence test employs Model 1 chemistry (see Chapter 3) with a volumetric flow rate of 27mL/min, at 1g, and without electric field applied.

The three meshes are different in number of points – and therefore, number of cells –, going from coarser to finer. For differentiation purposes, the three meshes are called *coarse*, *medium-coarse*, and *fine* mesh. The medium-coarse mesh presented is the one used in the simulations explained in this work, which details are shown in Table 2.3. The details of the coarse and finer meshes used in the mesh independence test are show in Tables B.1 and B.2. The three meshes studied share the

same domain divisions for gradual-increment-of-cell-size purpose (see Figure 2.3) and the same boundary conditions (see Table 2.4).

Table B.1: Coarse mesh grid details.

Region	ΔX [mm]	ΔZ [mm]	X range [mm]	Z range [mm]
i	0.066	-	0.00 - 1.20	-
ii	0.067	-	1.20 - 6.00	-
iii	0.167	-	6.00 - 12.5	-
iv	0.300	-	12.5 - 20.0	-
a (extruded)	-	0.067	-	-3.00 - 0.00
a (jet)	-	0.067	-	-10.00 - 0.00
b	-	0.066	-	0.00 - 9.00
c	-	0.306	-	9.00 - 20.0
d	-	0.600	-	20.0 - 32.0

Table B.2: Fine mesh grid details.

Region	ΔX [mm]	ΔZ [mm]	X range [mm]	Z range [mm]
i	0.026	-	0.00 - 1.20	-
ii	0.030	-	1.20 - 6.00	-
iii	0.072	-	6.00 - 12.5	-
iv	0.125	-	12.5 - 20.0	-
a (extruded)	-	0.030	-	-3.00 - 0.00
a (jet)	-	0.030	-	-10.00 - 0.00
b	-	0.030	-	0.00 - 9.00
c	-	0.138	-	9.00 - 20.0
d	-	0.267	-	20.0 - 32.0

B.2 Results and discussion

As discussed in Chapter 3, minor species CH*, OH*, H_3O^+ and HCO^+ are crucial for predicting and understanding the flame behavior changes under different body forces. Therefore, those species are the ones that are compared in the mesh-independence test.

B.2.1 Comparison between different mesh results

Figure B.1 shows the comparison of the results using the three different meshes and for CH*, OH*, H_3O^+ and HCO^+ being normalized by their maximum value, respectively. Figure B.1(a) shows the CH*/CH*$_{max}$ = 0.1 contour; Figure B.1(b) shows the OH*/OH*$_{max}$ = 0.1 contour; Figure B.1(c) shows the $H_3O^+/H_3O^+_{max}$ = 0.3 contour; and Figure B.1(d) shows the HCO^+/HCO^+_{max} = 0.1 contour. Deeper analysis and the comparison against experiments (Section B.2.2) clarifies which is the most suitable mesh to proceed with.

B.2.2 Comparison against experimental data

Figure 3.18 shows the simulation result for the same study case as the one detailed previously (see Section B.1), but with a fuel flow rate of 20mL/min to match with the experimental data from the literature [40]. As mentioned in Section 3.4.3, the concentration level of CH^* matching with experiments is equivalent to the intensity of light collection of the experiment.

Notice that the simulation in Figure 3.18 has the temperature boundary condition at the burner wall set equal to 300K. This figure shows that the experimental contour of CH* is very well captured by the medium-coarse mesh results, yet the zone closer to the burner's tip is over-predicted by the simulation. A priori, there are two hypotheses for that. The first hypothesis would be that the burner tube gets heated by the flame, promoting the electronic excitation of the surrounding species. Those electronically excited species relax their states, emitting the previously-mentioned chemiluminescence. The second hypothesis relies on the mesh-grid in that region, showing that the interaction between burner and flame is not fully captured.

To test the first hypothesis, Figure B.2 shows the black and white simulation result keeping the same parameters except for the burner wall temperature, which is set to 450K (increased by 150K). Although this is not a realistic increment of the burner-wall temperature, this extreme case is

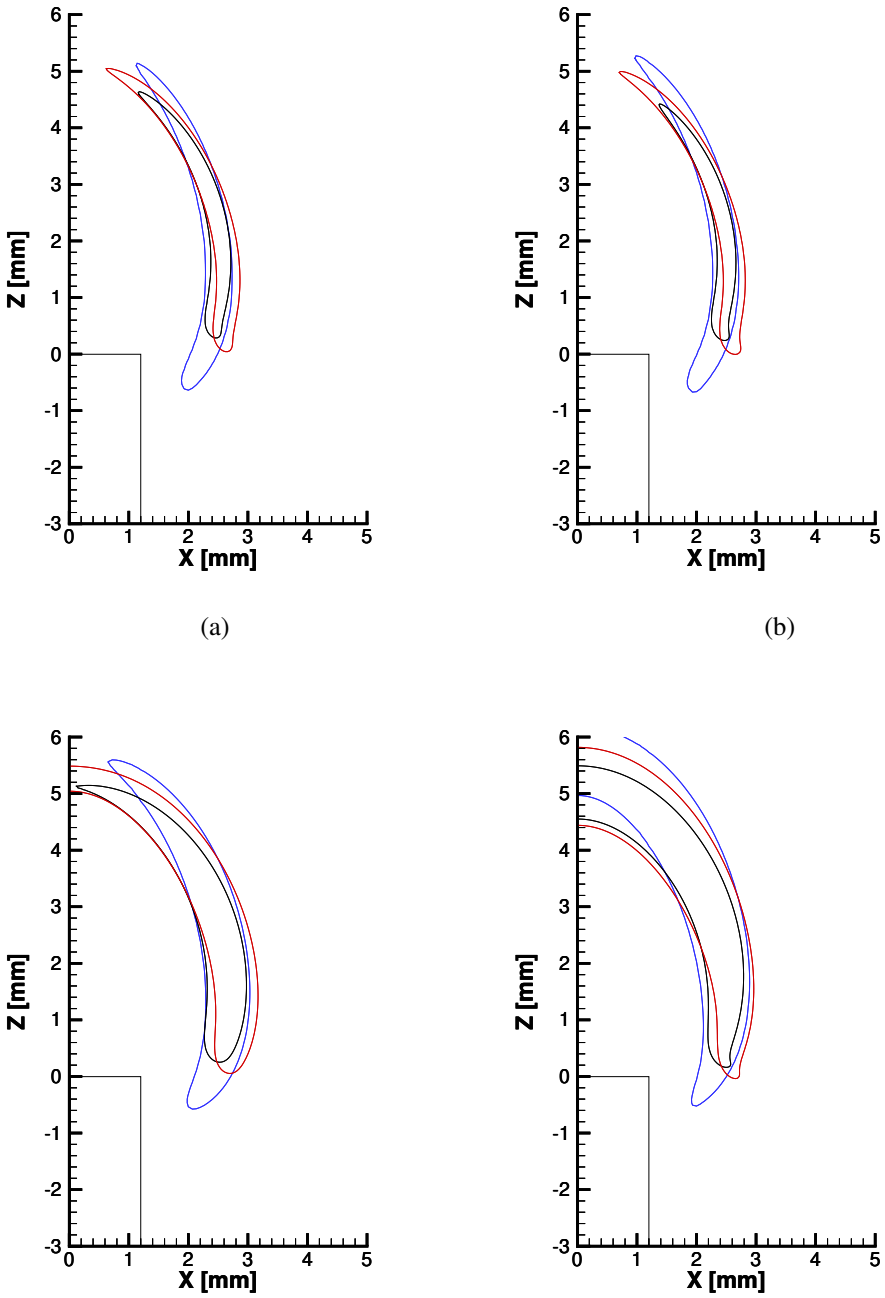

Figure B.1: Contours of 1g flame without e-field applied at steady-state. Model 1, fuel rate = 27mL/min. Meshes: coarse (blue), medium-coarse (red), fine (black). (a) CH^* (b) OH^*, (c) H_3O^+, (d) HCO^+.

simulated to clearly test this boundary condition. Following the result shown in Figure B.2, the first hypothesis is discarded. The second hypothesis is then more plausible, although Figure B.1(a) – which fuel flow rate is equal to 27mL/min– shows that the coarser is the mesh, the closer to the burner tip the CH* becomes. Having a coarser mesh capturing an experimental feature is counter-intuitive and needs to be further investigated.

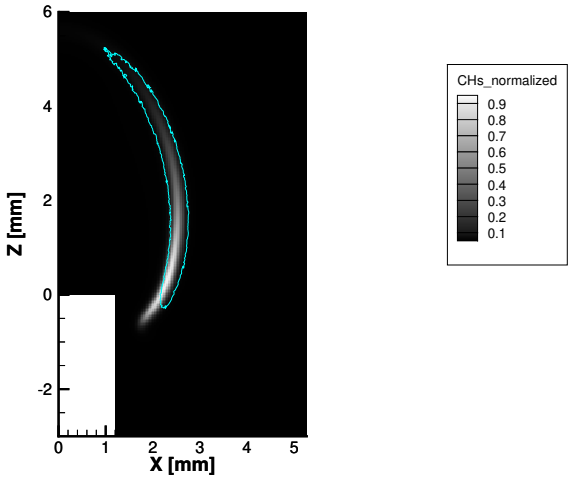

(a)

Figure B.2: Mapping of CH/CH*$_{max}$ (simulation) and contour of CH* (experiment). Extruded burner. Fuel flow rate = 20mL/min. Burner temperature (simulation) = 450K.*

Even though all these simulations are based on the same boundary conditions, the initial conditions before starting the simulation using the Model 1 chemistry are distinct. Hence, the comparison between the real time and simulation time ratio would not provide a fair correlation (see full explanation in Section 2.3.2). Nevertheless, there is a direct relationship between the number of mesh-grid points and the simulation time required to reach a steady-state, where more grid points translate into longer simulation time needed. Therefore, a compromise between computational resources and accuracy is made by choosing the medium-coarse mesh to proceed with the calculations.

Appendix C

Chemical Kinetic Models

C.1 Submodels for excited species

C.1.1 K.T. Walsh sub-model

Walsh proposed a sub-model to predict the excited species CH^* and OH^* [46]. This sub-model is meant to be added to the GRI-3.0 Mech [68]. Since the author of this document has compared the sub-model with the references given and has found errors in some of the coefficients, the corrected sub-model proposed by Walsh is presented in Table C.1. Units for rate constants are in centimetres, moles and seconds, with the formulation $k = AT^b exp[-E_a/RT]$, E_a in $[cal\, mole^{-1}]$ and R in $[cal\, mole^{-1}K^{-1}]$.

Table C.1: Walsh sub-model for CH^* and OH^*. A in $[cm^3\, mole^{-1}\, s^{-1}]$, Ea in $[cal\, mole^{-1}]$.

#	Walsh sub-model	A	b	Ea	Ref.
1	C2H+O $\rightleftharpoons$ CH*+CO	1.08E+13	0.00	0	[77]
2	C2H+O2 $\rightleftharpoons$ CH*+CO2	2.17E+10	0.00	0	[77]
3	CH* $\rightarrow$ CH+hν	1.85E+06	0.00	0	[78]
4	CH*+N2 $\rightleftharpoons$ CH+N2	3.03E+02	3.40	-381	[78]
5	CH*+O2 $\rightleftharpoons$ CH+O2	2.48E+06	2.14	-1720	[78]
6	CH*+H2O $\rightleftharpoons$ CH+H2O	5.30E+13	0.00	0	[78]
7	CH*+H2 $\rightleftharpoons$ CH+H2	1.47E+14	0.00	1361	[78]
8	CH*+CO2 $\rightleftharpoons$ CH+CO2	2.40E-01	4.30	-1694	[78]
9	CH*+CO $\rightleftharpoons$ CH+CO	2.44E+12	0.50	0	[78]
10	CH*+CH4 $\rightleftharpoons$ CH+CH4	1.73E+13	0.00	167	[78]
11	CH+O2 $\rightleftharpoons$ OH*+CO	3.25E+13	0.00	0	[83]
12	OH* $\rightarrow$ OH	1.45E+06	0.00	0	[78]
13	OH*+N2 $\rightleftharpoons$ OH+N2	1.08E+11	0.50	-1238	[78]
14	OH*+O2 $\rightleftharpoons$ OH+O2	2.10E+12	0.50	-482	[78]
15	OH*+H2O $\rightleftharpoons$ OH+H2O	5.92E+12	0.50	-861	[78]
16	OH*+H2 $\rightleftharpoons$ OH+H2	2.95E+12	0.50	-444	[78]
17	OH*+CO2 $\rightleftharpoons$ OH+CO2	2.75E+12	0.50	-968	[78]
18	OH*+CO $\rightleftharpoons$ OH+CO	3.23E+12	0.50	-787	[78]
19	OH*+CH4 $\rightleftharpoons$ OH+CH4	3.36E+12	0.50	-635	[78]

C.1.2 Model 0 (detailed model)

The Model 0 is the detailed model proposed in this work that accounts for neutral, excited species (CH^* and OH^*) and charged species. This model is a straight forward addition from the San Diego Mechanism [73] (Reactions 1-311), the sub-model proposed by K.T. Walsh for excited species chemiluminescence [46] (see previous Appendix Section C.1.1, Reactions 312-330) and the charged species reactions from the model proposed by Belhi et al. [96] (Reactions 331-394), which were previously taken from Prager's et al. model [86]. Units for rate constants are in centimetres, moles and seconds, with the formulation $k = AT^b exp[-E_a/RT]$, E_a in $[cal\, mole^{-1}]$ and R in $[cal\, mole^{-1} K^{-1}]$.

Table C.2: Model 0 (detailed model). A in $[cm^3\, mole^{-1}\, s^{-1})$], Ea in $[cal\, mol^{-1}]$.

#	**Model 0. Reactions**	**A**	**b**	**E$_a$**
1	H+O2 ⇌ OH+O	3.520e+16	-0.700	17069.79
2	H2+O ⇌ OH+H	5.060e+04	2.670	6290.63
3	H2+OH ⇌ H2O+H	1.170e+09	1.300	3635.28
4	H2O+O ⇌ 2OH	7.000e+05	2.330	14548.28
5	H+M ⇌ H2+M	1.300e+18	-1.000	0.00
	AR/0.50/ HE/0.50/ H2/2.50/ H2O/12.00/ CO/1.90/ CO2/3.80/			
6	H+OH+M ⇌ H2O+M	4.000e+22	-2.000	0.00
	AR/0.38/ HE/0.38/ H2/2.50/ H2O/12.00/ CO/1.90/ CO2/3.80/			
7	2O+M ⇌ O2+M	6.170e+15	-0.500	0.00
	AR/0.20/ HE/0.20/ H2/2.50/ H2O/12.00/ CO/1.90/ CO2/3.80/			
8	H+O+M ⇌ OH+M	4.710e+18	-1.000	0.00
	AR/0.75/ HE/0.75/ H2/2.50/ H2O/12.00/ CO/1.90/ CO2/3.80/			
9	H+O2(+M) ⇌ HO2(+M)	4.650e+12	0.440	0.00
	LOW / 5.750e+19 -1.400 0.00 /			
	TROE / 0.5 1e-30 1e+30 /			

Table C.2: Model 0 (detailed model). A in [$cm^3\, mole^{-1}\, s^{-1}$)], Ea in [$cal\, mol^{-1}$].

#	**Model 0. Reactions**	**A**	**b**	**E_a**
	AR/0.70/ HE/0.70/ H2/2.50/ H2O/16.00/ CO/1.20/ CO2/2.40/ C2H6/1.50/			
10	HO2+H ⇌ 2 OH	7.080e+13	0.000	294.93
11	HO2+H ⇌ H2+O2	1.660e+13	0.000	822.90
12	HO2+H ⇌ H2O+O	3.100e+13	0.000	1720.84
13	HO2+O ⇌ OH+O2	2.000e+13	0.000	0.00
14	HO2+OH ⇌ H2O+O2	7.000e+12	0.000	-1094.65
	DUPLICATE			
15	HO2+OH ⇌ H2O+O2	4.500e+14	0.000	10929.73
	DUPLICATE			
16	2OH(+M) ⇌ H2O2(+M)	9.550e+13	-0.270	0.00
	LOW / 2.760e+25 -3.200 0.00 /			
	TROE / 0.57 1e+30 1e-30 /			
	AR/0.70/ HE/0.40/ H2/2.50/ H2O/6.00/ H2O2/6.00/ CO/1.50/ CO2/2.00/			
17	2HO2 ⇌ H2O2+O2	1.030e+14	0.000	11042.07
	DUPLICATE			
18	2HO2 ⇌ H2O2+O2	1.940e+11	0.000	-1408.94
	DUPLICATE			
19	H2O2+H ⇌ HO2+H2	2.300e+13	0.000	7950.05
20	H2O2+H ⇌ H2O+OH	1.000e+13	0.000	3585.09
21	H2O2+OH ⇌ H2O+HO2	1.740e+12	0.000	1434.03
	DUPLICATE			
22	H2O2+OH ⇌ H2O+HO2	7.590e+13	0.000	7272.94
	DUPLICATE			
23	H2O2+O ⇌ HO2+OH	9.630e+06	2.000	3991.40
24	CO+O(+M) ⇌ CO2(+M)	1.800e+11	0.000	2384.08

Table C.2: Model 0 (detailed model). A in [$cm^3\, mole^{-1}\, s^{-1}$)], Ea in [$cal\, mol^{-1}$].

#	**Model 0. Reactions**	**A**	**b**	**E_a**
	LOW / 1.550e+24 -2.790 4190.97 /			
	TROE / 1 1 1e+07 1e+07 /			
	AR/0.70/ HE/0.70/ H2/2.50/ H2O/12.00/ CO/2.00/ CO2/4.00/			
25	CO+OH ⇌ CO2+H	4.400e+06	1.500	-740.92
26	CO+HO2 ⇌ CO2+OH	2.000e+13	0.000	22944.55
27	CO+O2 ⇌ CO2+O	1.000e+12	0.000	47700.05
28	HCO+M ⇌ CO+H+M	1.860e+17	-1.000	17000.48
	H2/1.90/ H2O/12.00/ CO/2.50/ CO2/2.50/			
29	HCO+H ⇌ CO+H2	5.000e+13	0.000	0.00
30	HCO+O ⇌ CO+OH	3.000e+13	0.000	0.00
31	HCO+O ⇌ CO2+H	3.000e+13	0.000	0.00
32	HCO+OH ⇌ CO+H2O	3.000e+13	0.000	0.00
33	HCO+O2 ⇌ CO+HO2	7.580e+12	0.000	409.89
34	HCO+CH3 ⇌ CO+CH4	5.000e+13	0.000	0.00
35	H+HCO(+M) ⇌ CH2O(+M)	1.090e+12	0.480	-260.04
	LOW / 1.350e+24 -2.570 424.95 /			
	TROE / 0.7824 271 2755 6570 /			
	AR/0.70/ H2/2.00/ H2O/6.00/ CO/1.50/ CO2/2.00/ CH4/2.00/ C2H6/3.00/			
36	CH2O+H ⇌ HCO+H2	5.740e+07	1.900	2748.57
37	CH2O+O ⇌ HCO+OH	3.500e+13	0.000	3513.38
38	CH2O+OH ⇌ HCO+H2O	3.900e+10	0.890	406.31
39	CH2O+O2 ⇌ HCO+HO2	6.000e+13	0.000	40674.00
40	CH2O+HO2 ⇌ HCO+H2O2	4.110e+04	2.500	10210.33
41	CH4+H ⇌ H2+CH3	1.300e+04	3.000	8037.76
42	CH4+OH ⇌ H2O+CH3	1.600e+07	1.830	2782.03

Table C.2: Model 0 (detailed model). A in [$cm^3\, mole^{-1}\, s^{-1}$)], Ea in [$cal\, mol^{-1}$].

#	**Model 0. Reactions**	**A**	**b**	**E$_a$**
43	CH4+O ⇌ CH3+OH	1.900e+09	1.440	8675.91
44	CH4+O2 ⇌ CH3+HO2	3.980e+13	0.000	56890.54
45	CH4+HO2 ⇌ CH3+H2O2	9.030e+12	0.000	24641.49
46	CH3+H ⇌ T-CH2+H2	1.800e+14	0.000	15105.16
47	CH3+H ⇌ S-CH2+H2	1.550e+14	0.000	13479.92
48	CH3+OH ⇌ S-CH2+H2O	4.000e+13	0.000	2502.39
49	CH3+O ⇌ CH2O+H	8.430e+13	0.000	0.00
50	CH3+T-CH2 ⇌ C2H4+H	4.220e+13	0.000	0.00
51	CH3+HO2 ⇌ CH3O+OH	5.000e+12	0.000	0.00
52	CH3+O2 ⇌ CH2O+OH	3.300e+11	0.000	8941.20
53	CH3+O2 ⇌ CH3O+O	1.100e+13	0.000	27820.03
54	2CH3 ⇌ C2H4+H2	1.000e+14	0.000	32002.87
55	2CH3 ⇌ C2H5+H	3.160e+13	0.000	14698.85
56	H+CH3(+M) ⇌ CH4(+M)	1.351e+14	0.091	87.721
	LOW / 1.59e+33 -4.761 2432.29 /			
	TROE / 0.834 36.8 778 2464.3 /			
	AR/0.70/ H2/2.00/ H2O/16.00/ CO/1.50/ CO2/2.00/ CH4/4.00/			
57	2 CH3(+M) ⇌ C2H6(+M)	1.810e+13	0.000	0.00
	LOW / 1.270e+41 -7.000 2762.91 /			
	TROE / 0.62 73 1.2e+03 /			
	AR/0.70/ H2/2.00/ H2O/6.00/ CO/1.50/ CO2/2.00/ CH4/2.00/ C2H6/3.00/			
58	S-CH2+OH ⇌ CH2O+H	3.000e+13	0.000	0.00
59	S-CH2+O2 ⇌ CO+OH+H	3.130e+13	0.000	0.00
60	S-CH2+CO2 ⇌ CO+CH2O	3.000e+12	0.000	0.00
61	S-CH2+M ⇌ T-CH2+M	6.000e+12	0.000	0.00

Table C.2: Model 0 (detailed model). A in [$cm^3\,mole^{-1}\,s^{-1}$)], Ea in [$cal\,mol^{-1}$].

#	**Model 0. Reactions**	**A**	**b**	**E_a**
	H2/2.40/ H2O/15.40/ CO/1.80/ CO2/3.60/			
62	T-CH2+H ⇌ CH+H2	6.020e+12	0.000	-1787.76
63	T-CH2+OH ⇌ CH2O+H	2.500e+13	0.000	0.00
64	T-CH2+OH ⇌ CH+H2O	1.130e+07	2.000	2999.52
65	T-CH2+O ⇌ CO+2 H	8.000e+13	0.000	0.00
66	T-CH2+O ⇌ CO+H2	4.000e+13	0.000	0.00
67	T-CH2+O2 ⇌ CO2+H2	2.630e+12	0.000	1491.40
68	T-CH2+O2 ⇌ CO+OH+H	6.580e+12	0.000	1491.40
69	2T-CH2 ⇌ C2H2+2 H	1.000e+14	0.000	0.00
70	C2H2+HO2 ⇌ CHCHO+OH	1.6e08	1.36	15420
71	CHCHO+O2 ⇌ CH2O+CO+O	1.3E06	2.4202	1604
72	CH+O ⇌ CO+H	4.000e+13	0.000	0.00
73	CH+O2 ⇌ HCO+O	1.770e+11	0.760	-478.01
74	CH+H2O ⇌ CH2O+H	1.170e+15	-0.750	0.00
75	CH+CO2 ⇌ HCO+CO	4.800e+01	3.220	-3226.58
76	CH3O+H ⇌ CH2O+H2	2.000e+13	0.000	0.00
77	CH3O+H ⇌ S-CH2+H2O	1.600e+13	0.000	0.00
78	CH3O+OH ⇌ CH2O+H2O	5.000e+12	0.000	0.00
79	CH3O+O ⇌ OH+CH2O	1.000e+13	0.000	0.00
80	CH3O+O2 ⇌ CH2O+HO2	4.280e-13	7.600	-3537.28
81	CH3O+M ⇌ CH2O+H+M	7.780e+13	0.000	13513.38
	AR/0.70/ H2/2.00/ H2O/6.00/ CO/1.50/ CO2/2.00/ CH4/2.00/			
82	C2H6+H ⇌ C2H5+H2	5.400e+02	3.500	5210.33
83	C2H6+O ⇌ C2H5+OH	1.400e+00	4.300	2772.47
84	C2H6+OH ⇌ C2H5+H2O	2.200e+07	1.900	1123.33

Table C.2: Model 0 (detailed model). A in [$cm^3\, mole^{-1}\, s^{-1}$)], Ea in [$cal\, mol^{-1}$].

#	**Model 0. Reactions**	**A**	**b**	**E_a**
85	C2H6+CH3 ⇌ C2H5+CH4	5.500e-01	4.000	8293.50
86	C2H6(+M) ⇌ C2H5+H(+M)	8.850e+20	-1.230	102222.75
	LOW / 4.900e+42 -6.430 107169.93 /			
	TROE / 0.84 125 2219 6882 /			
	AR/0.70/ H2/2.00/ H2O/6.00/ CO/1.50/ CO2/2.00/ CH4/2.00/ C2H6/3.00/			
87	C2H6+HO2 ⇌ C2H5+H2O2	1.320e+13	0.000	20469.89
88	C2H5+H ⇌ C2H4+H2	3.000e+13	0.000	0.00
89	C2H5+O ⇌ C2H4+OH	3.060e+13	0.000	0.00
90	C2H5+O ⇌ CH3+CH2O	4.240e+13	0.000	0.00
91	C2H5+O2 ⇌ C2H4+HO2	7.500e+14	-1.000	4799.95
92	C2H5+O2 ⇌ C2H4OOH	2.000e+12	0.000	0.00
93	C2H4OOH ⇌ C2H4+HO2	4.000e+34	-7.200	23000.00
94	C2H4OOH+O2 ⇌ OC2H3OOH+OH	7.500e+05	1.300	-5799.95
95	OC2H3OOH ⇌ CH2O+HCO+OH	1.000e+15	0.000	43000.00
96	C2H5(+M) ⇌ C2H4+H(+M)	1.110e+10	1.037	36768.64
	LOW / 3.990e+33 -4.990 40000.00 /			
	TROE / 0.168 1.2e+03 1e-30 /			
	AR/0.70/ H2/2.00/ H2O/6.00/ CO/1.50/ CO2/2.00/ CH4/2.00/			
97	C2H4+H ⇌ C2H3+H2	4.490e+07	2.120	13360.42
98	C2H4+OH ⇌ C2H3+H2O	5.530e+05	2.310	2963.67
99	C2H4+O ⇌ CH3+HCO	2.250e+06	2.080	0.00
100	C2H4+O ⇌ CH2CHO+H	1.210e+06	2.080	0.00
101	2C2H4 ⇌ C2H3+C2H5	5.010e+14	0.000	64700.05
102	C2H4+O2 ⇌ C2H3+HO2	4.220e+13	0.000	57623.09
103	C2H4+HO2 ⇌ C2H4O+OH	2.230e+12	0.000	17189.29

Table C.2: Model 0 (detailed model). A in [$cm^3\, mole^{-1}\, s^{-1}$)], Ea in [$cal\, mol^{-1}$].

#	**Model 0. Reactions**	**A**	**b**	**E$_a$**
104	C2H4O+HO2 ⇌ CH3+CO+H2O2	4.000e+12	0.000	17007.65
105	C2H4+M ⇌ C2H3+H+M	2.600e+17	0.000	96568.12
	AR/0.70/ H2/2.00/ H2O/6.00/ CO/1.50/ CO2/2.00/ CH4/2.00/			
106	C2H4+M ⇌ C2H2+H2+M	3.500e+16	0.000	71532.03
	AR/0.70/ H2/2.00/ H2O/6.00/ CO/1.50/ CO2/2.00/ CH4/2.00/			
107	C2H3+H ⇌ C2H2+H2	4.000e+13	0.000	0.00
108	C2H3(+M) ⇌ C2H2+H(+M)	6.380e+09	1.000	37626.67
	LOW / 1.510e+14 0.100 32685.95 /			
	TROE / 0.3 1e+30 1e-30 /			
	AR/0.70/ H2/2.00/ H2O/6.00/ CO/1.50/ CO2/2.00/ CH4/2.00/			
109	C2H3+O2 ⇌CH2O+HCO	1.700e+29	-5.312	6503.11
110	C2H3+O2 ⇌ CH2CHO+O	7.000e+14	-0.611	5262.43
111	C2H3+O2 ⇌ C2H2+HO2	5.190e+15	-1.260	3312.62
112	C2H2+O ⇌ HCCO+H	4.000e+14	0.000	10659.66
113	C2H2+O ⇌ T-CH2+CO	1.600e+14	0.000	9894.84
114	C2H2+O2 ⇌ CH2O+CO	4.600e+15	-0.540	44933.08
115	C2H2+OH ⇌ CH2CO+H	1.900e+07	1.700	999.04
116	C2H2+OH ⇌ C2H+H2O	3.370e+07	2.000	14000.96
117	CH2CO+H ⇌ CH3+CO	1.500e+09	1.430	2688.81
118	CH2CO+O ⇌ T-CH2+CO2	2.000e+13	0.000	2294.46
119	CH2CO+O ⇌ HCCO+OH	1.000e+13	0.000	2000.48
120	CH2CO+CH3 ⇌ C2H5+CO	9.000e+10	0.000	0.00
121	HCCO+H ⇌ S-CH2+CO	1.500e+14	0.000	0.00
122	HCCO+OH ⇌ HCO+CO+H	2.000e+12	0.000	0.00
123	HCCO+O ⇌ 2 CO+H	9.640e+13	0.000	0.00

Table C.2: Model 0 (detailed model). A in [$cm^3\, mole^{-1}\, s^{-1}$)], Ea in [$cal\, mol^{-1}$].

#	**Model 0. Reactions**	**A**	**b**	**E$_a$**
124	HCCO+O2 ⇌ 2 CO+OH	2.880e+07	1.700	1001.43
125	HCCO+O2 ⇌ CO2+CO+H	1.400e+07	1.700	1001.43
126	C2H+OH ⇌ HCCO+H	2.000e+13	0.000	0.00
127	C2H+O ⇌ CO+CH	1.020e+13	0.000	0.00
128	C2H+O2 ⇌ HCCO+O	6.020e+11	0.000	0.00
129	C2H+O2 ⇌ CH+CO2	4.500e+15	0.000	25095.60
130	C2H+O2 ⇌ HCO+CO	2.410e+12	0.000	0.00
131	CH2OH+H ⇌ CH2O+H2	3.000e+13	0.000	0.00
132	CH2OH+H ⇌ CH3+OH	2.500e+17	-0.930	5126.91
133	CH2OH+OH ⇌ CH2O+H2O	2.400e+13	0.000	0.00
134	CH2OH+O2 ⇌ CH2O+HO2	5.000e+12	0.000	0.00
135	CH2OH+M ⇌ CH2O+H+M	5.000e+13	0.000	25119.50
	AR/0.70/ H2/2.00/ H2O/6.00/ CO/1.50/ CO2/2.00/ CH4/2.00/			
136	CH3O+M ⇌ CH2OH+M	1.000e+14	0.000	19120.46
	AR/0.70/ H2/2.00/ H2O/6.00/ CO/1.50/ CO2/2.00/ CH4/2.00/			
137	CH2CO+OH ⇌ CH2OH+CO	1.020e+13	0.000	0.00
138	CH3OH+OH ⇌ CH2OH+H2O	1.440e+06	2.000	-838.91
139	CH3OH+OH ⇌ CH3O+H2O	4.400e+06	2.000	1505.74
140	CH3OH+H ⇌ CH2OH+H2	1.354e+03	3.200	3490.68
141	CH3OH+H ⇌ CH3O+H2	6.830e+01	3.400	7239.96
142	CH3OH+O ⇌ CH2OH+OH	3.880e+05	2.500	3080.78
143	CH3OH+HO2 ⇌ CH2OH+H2O2	8.000e+13	0.000	19383.37
144	CH3OH+O2 ⇌ CH2OH+HO2	2.000e+13	0.000	44933.08
145	CH3OH(+M) ⇌ CH3+OH(+M)	1.900e+16	0.000	91729.92
	LOW / 2.950e+44 -7.350 95460.09 /			

Table C.2: Model 0 (detailed model). A in [$cm^3\, mole^{-1}\, s^{-1}$)], Ea in [$cal\, mol^{-1}$].

#	**Model 0. Reactions**	**A**	**b**	**E_a**
	TROE / 0.414 2.8e+02 5.5e+03 /			
	AR/0.70/ H2/2.00/ H2O/6.00/ CO/1.50/ CO2/2.00/ CH4/2.00/			
146	CH2CHO ⇌ CH2CO+H	1.047e+37	-7.189	44340.34
147	CH2CHO+H ⇌ CH3+HCO	5.000e+13	0.000	0.00
148	CH2CHO+H ⇌ CH2CO+H2	2.000e+13	0.000	0.00
149	CH2CHO+O ⇌ CH2O+HCO	1.000e+14	0.000	0.00
150	CH2CHO+OH ⇌ CH2CO+H2O	3.000e+13	0.000	0.00
151	CH2CHO+O2 ⇌ CH2O+CO+OH	3.000e+10	0.000	0.00
152	CH2CHO+CH3 ⇌ C2H5+CO+H	4.900e+14	-0.500	0.00
153	CH2CHO+HO2 ⇌ CH2O+HCO+OH	7.000e+12	0.000	0.00
154	CH2CHO+HO2 ⇌ CH3CHO+O2	3.000e+12	0.000	0.00
155	CH2CHO ⇌ CH3+CO	1.170e+43	-9.800	43799.95
156	CH3CHO ⇌ CH3+HCO	7.000e+15	0.000	81700.05
157	CH3CO(+M) ⇌ CH3+CO(+M)	3.000e+12	0.000	16700.05
	LOW / 1.200e+15 0.000 12500.00 /			
	TROE / 1 1 1e+07 1e+07 /			
	AR/0.70/ H2/2.00/ H2O/6.00/ CO/1.50/ CO2/2.00/ CH4/2.00/			
158	CH3CHO+OH ⇌ CH3CO+H2O	3.370e+12	0.000	-619.98
159	CH3CHO+OH ⇌ CH2CHO+H2O	3.370e+11	0.000	-619.98
160	CH3CHO+O ⇌ CH3CO+OH	1.770e+18	-1.900	2979.92
161	CH3CHO+O ⇌ CH2CHO+OH	3.720e+13	-0.200	3559.99
162	CH3CHO+H ⇌ CH3CO+H2	4.660e+13	-0.300	2989.96
163	CH3CHO+H ⇌ CH2CHO+H2	1.850e+12	0.400	5359.94
164	CH3CHO+CH3 ⇌ CH3CO+CH4	3.900e-07	5.800	2200.05
165	CH3CHO+CH3 ⇌ CH2CHO+CH4	2.450e+01	3.100	5729.92

Table C.2: Model 0 (detailed model). A in [$cm^3\, mole^{-1}\, s^{-1}$)], Ea in [$cal\, mol^{-1}$].

#	**Model 0. Reactions**	**A**	**b**	**E_a**
166	CH3CHO+HO2 ⇌ CH3CO+H2O2	3.600e+19	-2.200	14000.00
167	CH3CHO+HO2 ⇌ CH2CHO+H2O2	2.320e+11	0.400	14900.10
168	CH3CHO+O2 ⇌ CH3CO+HO2	1.000e+14	0.000	42200.05
169	C2H5OH(+M) ⇌ CH3+CH2OH(+M)	5.000e+15	0.000	82000.00
	LOW / 3.000e+16 0.000 58000.00 /			
	TROE / 0.5 1e-30 1e+30 /			
	AR/0.70/ H2/2.00/ H2O/6.00/ CO/1.50/ CO2/2.00/ CH4/2.00/			
170	C2H5OH(+M) ⇌ C2H4+H2O(+M)	8.000e+13	0.000	65000.00
	LOW / 1.000e+17 0.000 54000.00 /			
	TROE / 0.5 1e-30 1e+30 /			
	AR/0.70/ H2/2.00/ H2O/6.00/ CO/1.50/ CO2/2.00/ CH4/2.00/			
171	C2H5OH+OH ⇌ CH2CH2OH+H2O	1.810e+11	0.400	717.02
172	C2H5OH+OH ⇌ CH3CHOH+H2O	3.090e+10	0.500	-380.02
173	C2H5OH+OH ⇌ CH3CH2O+H2O	1.050e+10	0.800	717.02
174	C2H5OH+H ⇌ CH2CH2OH+H2	1.900e+07	1.800	5099.90
175	C2H5OH+H ⇌ CH3CHOH+H2	2.580e+07	1.600	2830.07
176	C2H5OH+H ⇌ CH3CH2O+H2	1.500e+07	1.600	3039.91
177	C2H5OH+O ⇌ CH2CH2OH+OH	9.410e+07	1.700	5460.09
178	C2H5OH+O ⇌ CH3CHOH+OH	1.880e+07	1.900	1820.03
179	C2H5OH+O ⇌ CH3CH2O+OH	1.580e+07	2.000	4450.05
180	C2H5OH+CH3 ⇌ CH2CH2OH+CH4	2.190e+02	3.200	9619.98
181	C2H5OH+CH3 ⇌ CH3CHOH+CH4	7.280e+02	3.000	7950.05
182	C2H5OH+CH3 ⇌ CH3CH2O+CH4	1.450e+02	3.000	7650.10
183	C2H5OH+HO2 ⇌ CH3CHOH+H2O2	8.200e+03	2.500	10799.95
184	C2H5OH+HO2 ⇌ CH2CH2OH+H2O2	2.430e+04	2.500	15799.95

Table C.2: Model 0 (detailed model). A in [$cm^3\, mole^{-1}\, s^{-1}$)], Ea in [$cal\, mol^{-1}$].

#	**Model 0. Reactions**	**A**	**b**	**E$_a$**
185	C2H5OH+HO2 ⇌ CH3CH2O+H2O2	3.800e+12	0.000	24000.00
186	C2H4+OH ⇌ CH2CH2OH	2.410e+11	0.000	-2380.02
187	C2H5+HO2 ⇌ CH3CH2O+OH	4.000e+13	0.000	0.00
188	CH3CH2O+M ⇌ CH3CHO+H+M	5.600e+34	-5.900	25299.95
	AR/0.70/ H2/2.00/ H2O/6.00/ CO/1.50/ CO2/2.00/ CH4/2.00/			
189	CH3CH2O+M ⇌ CH3+CH2O+M	5.350e+37	-7.000	23799.95
	AR/0.70/ H2/2.00/ H2O/6.00/ CO/1.50/ CO2/2.00/ CH4/2.00/			
190	CH3CH2O+O2 ⇌ CH3CHO+HO2	4.000e+10	0.000	1099.90
191	CH3CH2O+CO ⇌ C2H5+CO2	4.680e+02	3.200	5380.02
192	CH3CH2O+H ⇌ CH3+CH2OH	3.000e+13	0.000	0.00
193	CH3CH2O+H ⇌ C2H4+H2O	3.000e+13	0.000	0.00
194	CH3CH2O+OH ⇌ CH3CHO+H2O	1.000e+13	0.000	0.00
195	CH3CHOH+O2 ⇌ CH3CHO+HO2	4.820e+13	0.000	5020.08
196	CH3CHOH+O ⇌ CH3CHO+OH	1.000e+14	0.000	0.00
197	CH3CHOH+H ⇌ C2H4+H2O	3.000e+13	0.000	0.00
198	CH3CHOH+H ⇌ CH3+CH2OH	3.000e+13	0.000	0.00
199	CH3CHOH+HO2 ⇌ CH3CHO+2 OH	4.000e+13	0.000	0.00
200	CH3CHOH+OH ⇌ CH3CHO+H2O	5.000e+12	0.000	0.00
201	CH3CHOH+M ⇌ CH3CHO+H+M	1.000e+14	0.000	25000.00
	AR/0.70/ H2/2.00/ H2O/6.00/ CO/1.50/ CO2/2.00/ CH4/2.00/			
202	C3H4+O ⇌ C2H4+CO	2.000e+07	1.800	1000.00
203	CH3+C2H2 ⇌ C3H4+H	2.560e+09	1.100	13643.88
204	C3H4+O ⇌ HCCO+CH3	7.300e+12	0.000	2250.00
205	C3H3+H(+M) ⇌ C3H4(+M)	3.000e+13	0.000	0.00
	LOW / 9.000e+15 1.000 0.00 /			

Table C.2: Model 0 (detailed model). A in [$cm^3\, mole^{-1}\, s^{-1}$)], Ea in [$cal\, mol^{-1}$].

#	**Model 0. Reactions**	**A**	**b**	**E$_a$**
	TROE / 0.5 1e+30 1e-30 /			
206	C3H3+HO2 ⇌ C3H4+O2	2.500e+12	0.000	0.00
207	C3H4+OH ⇌ C3H3+H2O	5.300e+06	2.000	2000.00
208	C3H3+O2 ⇌ CH2CO+HCO	3.000e+10	0.000	2868.07
209	C3H4+H(+M) ⇌ C3H5(+M)	4.000e+13	0.000	0.00
	LOW / 3.000e+24 -2.000 0.00 /			
	TROE / 0.8 1e+30 1e-30 /			
210	C3H5+H ⇌ C3H4+H2	1.800e+13	0.000	0.00
211	C3H5+O2 ⇌ C3H4+HO2	4.990e+15	-1.400	22428.06
212	C3H5+CH3 ⇌ C3H4+CH4	3.000e+12	-0.320	-130.98
213	C2H2+CH3(+M) ⇌ C3H5(+M)	6.000e+08	0.000	0.00
	LOW / 2.000e+09 1.000 0.00 /			
	TROE / 0.5 1e+30 1e-30 /			
214	C3H5+OH ⇌ C3H4+H2O	6.000e+12	0.000	0.00
215	C3H3+HCO ⇌ C3H4+CO	2.500e+13	0.000	0.00
216	C3H3+HO2 ⇌ OH+CO+C2H3	8.000e+11	0.000	0.00
217	C3H4+O2 ⇌ CH3+HCO+CO	4.000e+14	0.000	41826.00
218	C3H6+O ⇌ C2H5+HCO	3.500e+07	1.650	-972.75
219	C3H6+OH ⇌ C3H5+H2O	3.100e+06	2.000	-298.28
220	C3H6+O ⇌ CH2CO+CH3+H	1.200e+08	1.650	327.44
221	C3H6+H ⇌ C3H5+H2	1.700e+05	2.500	2492.83
222	C3H5+H(+M) ⇌ C3H6(+M)	2.000e+14	0.000	0.00
	LOW / 1.330e+60 -12.000 5967.97 /			
	TROE / 0.02 1097 1097 6860 /			
	AR/0.70/ H2/2.00/ H2O/6.00/ CO/1.50/ CO2/2.00/ CH4/2.00/ C2H6/3.00/			

Table C.2: Model 0 (detailed model). A in [$cm^3\, mole^{-1}\, s^{-1}$)], Ea in [$cal\, mol^{-1}$].

#	**Model 0. Reactions**	**A**	**b**	**E_a**
223	C3H5+HO2 ⇌ C3H6+O2	2.660e+12	0.000	0.00
224	C3H5+HO2 ⇌ OH+C2H3+CH2O	3.000e+12	0.000	0.00
225	C2H3+CH3(+M) ⇌ C3H6(+M)	2.500e+13	0.000	0.00
	LOW / 4.270e+58 -11.940 9770.55 /			
	TROE / 0.175 1341 6e+04 1.014e+04 /			
	AR/0.70/ H2/2.00/ H2O/6.00/ CO/1.50/ CO2/2.00/ CH4/2.00/ C2H6/3.00/			
226	C3H6+H ⇌ C2H4+CH3	1.600e+22	-2.390	11185.47
227	CH3+C2H3 ⇌ C3H5+H	1.500e+24	-2.830	18618.55
228	C3H8(+M) ⇌ CH3+C2H5(+M)	1.100e+17	0.000	84392.93
	LOW / 7.830e+18 0.000 64978.01 /			
	TROE / 0.76 1.9e+03 38 /			
229	C3H8+O2 ⇌ I-C3H7+HO2	4.000e+13	0.000	47500.00
230	C3H8+O2 ⇌ N-C3H7+HO2	4.000e+13	0.000	50932.12
231	C3H8+H ⇌ I-C3H7+H2	1.300e+06	2.400	4471.08
232	C3H8+H ⇌ N-C3H7+H2	1.330e+06	2.540	6761.47
233	C3H8+O ⇌ I-C3H7+OH	4.760e+04	2.710	2107.31
234	C3H8+O ⇌ N-C3H7+OH	1.900e+05	2.680	3718.45
235	C3H8+OH ⇌ N-C3H7+H2O	1.000e+10	1.000	1599.90
236	C3H8+OH ⇌ I-C3H7+H2O	2.000e+07	-1.600	-99.90
237	C3H8+HO2 ⇌ I-C3H7+H2O2	9.640e+03	2.600	13917.30
238	C3H8+HO2 ⇌ N-C3H7+H2O2	4.760e+04	2.550	16491.40
239	I-C3H7+C3H8 ⇌ N-C3H7+C3H8	8.400e-03	4.200	8675.91
240	C3H6+H(+M) ⇌ I-C3H7(+M)	1.330e+13	0.000	1560.71
	LOW / 8.700e+42 -7.500 4732.31 /			
	TROE / 1 1000 645.4 6844 /			

Table C.2: Model 0 (detailed model). A in [$cm^3\, mole^{-1}\, s^{-1}$)], Ea in [$cal\, mol^{-1}$].

#	**Model 0. Reactions**	**A**	**b**	**E_a**
	AR/0.70/ H2/2.00/ H2O/6.00/ CO/1.50/ CO2/2.00/ CH4/2.00/ C2H6/3.00/			
241	I-C3H7+O2 ⇌ C3H6+HO2	1.300e+11	0.000	0.00
242	N-C3H7(+M) ⇌ CH3+C2H4(+M)	1.230e+13	-0.100	30210.33
	LOW / 5.490e+49 -10.000 35778.92 /			
	TROE / -1.17 251 1e-15 1185 /			
243	H+C3H6(+M) ⇌ N-C3H7(+M)	1.330e+13	0.000	3260.04
	LOW / 6.260e+38 -6.660 7000.48 /			
	TROE / 1 1000 1310 4.81e+04 /			
	AR/0.70/ H2/2.00/ H2O/6.00/ CO/1.50/ CO2/2.00/ CH4/2.00/ C2H6/3.00/			
244	N-C3H7+O2 ⇌ C3H6+HO2	3.500e+16	-1.600	3500.00
245	N-C3H7+O2 ⇌ C3H6OOH	2.000e+12	0.000	0.00
246	C3H6OOH ⇌ C3H6+HO2	2.500e+35	-8.300	22000.00
247	C3H6OOH+O2 ⇌ OC3H5OOH+OH	1.500e+08	0.000	-7000.00
248	OC3H5OOH ⇌ CH2CHO+CH2O+OH	1.000e+15	0.000	43000.00
249	C4H10(+M) ⇌ 2C2H5(+M)	2.720e+15	0.000	75609.94
	LOW / 4.720e+18 0.000 49580.07 /			
	TROE / 0.72 1500.00 1.0000E-10			
	1.0000E+10 /			
250	C4H10+O2 ⇌ PC4H9+HO2	6.000e+13	0.000	52340.11
251	C4H10+O2 ⇌ SC4H9+HO2	4.000e+13	0.000	49799.95
252	C4H10+HO2 ⇌ PC4H9+H2O2	4.080e+01	3.590	17159.89
253	C4H10+HO2 ⇌ SC4H9+H2O2	1.264e+02	3.370	13719.89
254	C4H10+O ⇌ PC4H9+OH	1.130E+14	0.000	7850.00
255	C4H10+O ⇌ SC4H9+OH	5.620E+13	0.000	5200.00
256	C4H10+OH ⇌ PC4H9+H2O	1.054e+10	0.970	1586.04

Table C.2: Model 0 (detailed model). A in [$cm^3\, mole^{-1}\, s^{-1}$)], Ea in [$cal\, mol^{-1}$].

#	**Model 0. Reactions**	**A**	**b**	**E_a**
257	C4H10+OH ⇌ SC4H9+H2O	9.340e+07	1.610	-34.89
258	C4H10+H ⇌ H2+PC4H9	2.8000E+06	2.540	6965.4
259	C4H10+H ⇌ H2+SC4H9	1.6900E+06	2.400	4493.0
260	PC4H9 ⇌ C2H5+C2H4	3.504e+12	0.463	29469.89
261	SC4H9 ⇌ C3H6+CH3	4.803e+10	1.044	30349.90
262	C4H8 ⇌ C3H5+CH3	1.000e+16	0.000	72896.75
263	C4H8+H ⇌ H2+C2H3+C2H4	6.600e+05	2.540	6763.86
264	SC4H9+O2 ⇌ SC4H9O2	7.500e+12	0.000	0.00
265	SC4H9O2 ⇌ C4H8+HO2	5.075E+42	-9.410	41490.00
266	PC4H9+O2 ⇌ C4H8+HO2	8.370e-01	3.590	12000.00
267	PC4H9+O2 ⇌ C4H8OOH1-3	2.000E+12	0.000	0.00
268	C4H8OOH1-3 ⇌ C4H8+HO2	2.000E+12	0.000	24000.00
269	C4H8OOH1-3+O2 ⇌NC4KET13+OH	3.500E+00	2.234	-16560.00
270	NC4KET13 ⇌N-C3H7+CO2+OH	3.000E+16	0.000	41500.00
271	N2+O ⇌N+NO	1.470E13	0.30	75286.81
272	N+O2 ⇌ NO+O	6.400E09	1.00	6285.85
273	N+OH ⇌ NO+H	3.800E13	0.00	0.00
274	NH+H ⇌ N+H2	1.000E14	0.00	0.00
275	NH+O ⇌ NO+H	9.200E13	0.00	0.00
276	NH+OH ⇌ HNO+H	4.000E13	0.00	0.00
277	NH+OH ⇌ N+H2O	5.000E11	0.50	2000.48
278	NH+O2 ⇌ HNO+O	4.600E05	2.00	6500.96
279	NH+NO ⇌ N2O+H	1.800E14	-0.351	-244.00
280	NH+NO ⇌ N2+OH	2.200E13	-0.23	0.00

Table C.2: Model 0 (detailed model). A in [$cm^3\, mole^{-1}\, s^{-1}$)], Ea in [$cal\, mol^{-1}$].

#	**Model 0. Reactions**	**A**	**b**	**E_a**
281	NH2+H ⇌ NH+H2	4.000E13	0.00	3652.01
282	NH2+O ⇌ HNO+H	6.600E14	-0.50	0.00
283	NH2+O2 ⇌ H2NO+O	2.600E11	0.4872	29050.00
284	NH2+OH ⇌ NH+H2O	4.000E06	2.00	1001.43
285	NH2+N ⇌ N2+H+H	7.000E13	0.00	0.00
286	NH2+NO ⇌ N2+H2O	2.800E20	-2.654	1258.00
287	NH2+NO ⇌ N2H+OH	3.100E13	-0.48	1180.00
288	NH3+M ⇌ NH2+H+M	2.200E16	0.00	93451.24
289	NH3+H ⇌ NH2+H2	6.400E05	2.39	10181.64
290	NH3+O ⇌ NH2+OH	9.400E06	1.94	6465.11
291	NH3+OH ⇌ NH2+H2O	2.040E06	2.04	566.44
292	N2H+O2 ⇌ N2+HO2	2.000E14	0.00	0.00
293	N2H(+M) ⇌ N2+H(+M)	6.500E07	0.00	0.00
	LOW / 5.000E13 0.00 0.00 /			
294	N2H+H ⇌ N2+H2	1.000E14	0.00	0.00
295	N2H+O ⇌ N2O+H	1.000E14	0.00	0.00
296	N2H+OH ⇌ N2+H2O	5.000E13	0.00	0.00
297	H+NO(+M) ⇌ HNO(+M)	1.500E15	-0.40	0.00
	LOW / 4.300e+14 0.206 -1554.97 /			
	AR/0.50/H2O/5.00/			
298	HNO+H ⇌ NO+H2	4.400E11	0.72	650.10
299	HNO+OH ⇌ NO+H2O	3.600E13	0.00	0.00
300	N2O(+M) ⇌ N2+O(+M)	8.000E11	0.00	62619.50
	LOW / 2.000e+14 0.000 56644.36 /			
301	N2O+H ⇌ N2+OH	3.310E10	0.00	5090.00

Table C.2: Model 0 (detailed model). A in [$cm^3\,mole^{-1}\,s^{-1}$)], Ea in [$cal\,mol^{-1}$].

#	**Model 0. Reactions**	**A**	**b**	**E_a**
	DUPLICATE			
302	N2O+H ⇌ N2+OH	7.830E14	0.00	19390.00
	DUPLICATE			
303	N2O+O ⇌ NO+NO	9.150E13	0.00	27693.00
304	N2O+OH ⇌ N2+HO2	2.000E13	0.00	40000.00
305	NO2+M ⇌ NO+O+M	1.100E16	0.00	65965.58
	H2O/16.25/			
306	NO+HO2 ⇌ NO2+OH	2.100E12	0.00	-480.40
307	NO2+H ⇌ NO+OH	3.500E14	0.00	1500.96
308	NO2+O ⇌ NO+O2	1.000E13	0.00	599.90
309	H2NO+O ⇌ HNO+OH	3.000E07	2.00	2000.00
310	H2NO+O2 ⇌ HNO+HO2	3.000E12	0.00	25000.00
311	H2NO+HO2 ⇌ HNO+H2O2	2.900E04	2.69	-1600.00
312	C2H+O ⇌ CH*+CO	1.080E+13	0.000	0.000
313	C2H+O2 ⇌ CH*+CO2	2.170E+10	0.000	0.000
314	CH* → CH	1.850E+06	0.000	0.000
315	CH*+N2 ⇌ CH+N2	3.030E+02	3.400	-381.0
316	CH*+O2 ⇌ CH+O2	2.480E+06	2.100	-1720.0
317	CH*+H2O ⇌ CH+H2O	5.300E+13	0.000	0.000
318	CH*+H2 ⇌ CH+H2	1.470E+14	0.000	1361.0
319	CH*+CO2 ⇌ CH+CO2	2.400E-01	4.300	-1694.0
320	CH*+CO ⇌ CH+CO	2.440E+12	0.500	0.000
321	CH*+CH4 ⇌ CH+CH4	1.730E+13	0.000	167.0
322	CH+O2 ⇌ OH*+CO	3.250E+13	0.000	0.000
323	OH* → OH	1.450E+06	0.000	0.000

Table C.2: Model 0 (detailed model). A in [$cm^3\, mole^{-1}\, s^{-1}$)], Ea in [$cal\, mol^{-1}$].

#	**Model 0. Reactions**	**A**	**b**	**E_a**
324	OH*+N2 $\rightleftharpoons$ OH+N2	1.080E+11	0.500	-1238.0
325	OH*+O2 $\rightleftharpoons$ OH+O2	2.100E+12	0.500	-482.0
326	OH*+H2O $\rightleftharpoons$ OH+H2O	5.920E+12	0.500	-861.0
327	OH*+H2 $\rightleftharpoons$ OH+H2	2.950E+12	0.500	-444.0
328	OH*+CO2 $\rightleftharpoons$ OH+CO2	2.750E+12	0.500	-968.0
329	OH*+CO $\rightleftharpoons$ OH+CO	3.230E+12	0.500	-787.0
330	OH*+CH4 $\rightleftharpoons$ OH+CH4	3.360E+12	0.500	-635.0
331	CH+O $\rightleftharpoons$ HCO^++e^-	1.746E+18	-2.190	327.889
332	HCO^++e^- $\rightleftharpoons$ CO+H	7.399E+18	-0.690	0.00
333	HCO^++H2O $\rightleftharpoons$ $H3O^+$+CO	2.608E+16	-0.500	0.00
334	$H3O^+$+e^- $\rightleftharpoons$ H2O+H	7.395E+017	-0.500	0.00
335	$H3O^+$+e^- $\rightleftharpoons$ OH+H+H	3.181E+018	-0.500	0.00
336	$H3O^+$+e^- $\rightleftharpoons$ H2+OH	5.601E+017	-0.500	0.00
337	$H3O^+$+e^- $\rightleftharpoons$ O+H2+H	5.841E+016	-0.500	0.00
338	$H3O^+$+C $\rightleftharpoons$ HCO^++H2	6.022E+12	0.000	0.00
339	HCO^++CH2CO $\rightleftharpoons$ $C2H3O^+$+CO	1.259E+15	-0.048	0.00
340	HCO^++CH3 $\rightleftharpoons$ $C2H3O^+$+H	7.763E+14	-0.006	0.00
341	$C2H3O^+$+e^- $\rightleftharpoons$ CH2CO+H	3.129E+18	-0.500	0.00
342	$H3O^+$+CH2CO $\rightleftharpoons$ $C2H3O^+$+H2O	2.086E+16	-0.500	0.00
343	$C2H3O^+$+e^- $\rightleftharpoons$ CO+CH3	3.129E+18	-0.500	0.00
344	$C2H3O^+$+O $\rightleftharpoons$ HCO^++CH2O	2.000E+14	0.000	0.00
345	HCO^++CH3OH $\rightleftharpoons$ $CH5O^+$+CO	2.816E+16	-0.500	0.00
346	$H3O^+$+CH3OH $\rightleftharpoons$ $CH5O^+$+H2O	2.608E+16	-0.500	0.00
347	$CH5O^+$+e^- $\rightleftharpoons$ CH3OH+H	4.653E+17	-0.590	0.00
348	$CH5O^+$+CH2CO $\rightleftharpoons$ $C2H3O^+$+CH3OH	1.486E+15	-0.077	-82.93

Table C.2: Model 0 (detailed model). A in [$cm^3\, mole^{-1}\, s^{-1}$)], Ea in [$cal\, mol^{-1}$].

#	**Model 0. Reactions**	**A**	**b**	**E_a**
349	$O2^-$+H2 ⇌ H2O2+e^-	6.022E+14	0.000	0.00
350	$O2^-$+H ⇌ HO2+e^-	7.226E+14	0.000	0.00
351	$O2^-$+OH ⇌ OH^-+O2	6.022E+13	0.000	0.00
352	$O2^-$+H ⇌ OH^-+O	1.084E+15	0.000	0.00
353	OH^-+O ⇌ HO2+e^-	1.204E+14	0.000	0.00
354	OH^-+H ⇌ H2O+e^-	8.431E+14	0.000	0.00
355	OH^-+C ⇌ HCO+e^-	3.011E+14	0.000	0.00
356	OH^-+CH ⇌ CH2O+e^-	3.011E+14	0.000	0.00
357	OH^-+CH3 ⇌ CH3OH+e^-	6.022E+14	0.000	0.00
358	$CO3^-$+H ⇌ OH^-+CO2	1.020E+14	0.000	0.00
359	$CO3^-$+O ⇌ $O2^-$+CO2	4.600E+13	0.000	0.00
360	$CHO2^-$+H ⇌ CO2+H2+e^-	1.159E+14	0.000	0.00
361	OH^-+HCO ⇌ $CHO2^-$+H	2.959E+15	-0.140	-105.3
362	O^-+C ⇌ CO+e^-	3.011E+14	0.000	0.00
363	O^-+H2 ⇌ OH^-+H	1.807E+13	0.000	0.00
364	O^-+CH4 ⇌ OH^-+CH3	6.022E+13	0.000	0.00
365	O^-+H2O ⇌ OH^-+OH	8.431E+14	0.000	0.00
366	O^-+CH2O ⇌ OH^-+HCO	5.601E+14	0.000	0.00
367	O^-+CH2O ⇌ $CHO2^-$+H	1.307E+15	0.000	0.00
368	O^-+C2H6 ⇌ C2H5+OH^-	6.130E+15	-0.500	0.00
369	O^-+H ⇌ OH+e^-	3.011E+14	0.000	0.00
370	O^-+H2 ⇌ H2O+e^-	4.215E+14	0.000	0.00
371	O^-+CH ⇌ HCO+e^-	3.011E+14	0.000	0.00
372	O^-+CH2 ⇌ CH2O+e^-	3.011E+14	0.000	0.00
373	O^-+CO ⇌ CO2+e^-	3.914E+14	0.000	0.00

Table C.2: Model 0 (detailed model). A in [$cm^3\,mole^{-1}\,s^{-1}$)], Ea in [$cal\,mol^{-1}$].

#	**Model 0. Reactions**	**A**	**b**	**E_a**
374	O^-+O ⇌ O2+e^-	1.144E+14	0.000	0.00
375	O^-+C2H2 ⇌ CH2CO+e^-	7.226E+14	0.000	0.00
376	O^-+H2O ⇌ H2O2+e^-	3.613E+11	0.000	0.00
377	$O2^-$+O ⇌ On+O2	1.987E+14	0.000	0.00
378	$O2^-$+$C2H3O^+$ ⇌ O2+CH2CO+H	1.000E+18	0.000	0.00
379	$O2^-$+$CH5O^+$ ⇌ O2+CH3+H2O	1.000E+18	0.000	0.00
380	O^-+$C2H3O^+$ ⇌ O+CH2CO+H	1.000E+18	0.000	0.00
381	O^-+$C2H3O^+$ ⇌ O+CH2CHO	1.000E+18	0.000	0.00
382	O^-+$CH5O^+$ ⇌ O+CH3+H2O	1.000E+18	0.000	0.00
383	$CHO3^-$+$CH5O^+$ ⇌ CH3OH+H2O+CO2	2.000E+18	0.000	0.00
384	O2+e^-+O ⇌ $O2^-$+O	3.627E+16	0.000	0.00
385	O2+e^-+O2 ⇌ $O2^-$+O2	1.523E+21	-1.000	1191.9
386	O2+e^-+H2O ⇌ $O2^-$+H2O	5.077E+18	0.000	0.00
387	O2+e^-+N2 ⇌ $O2^-$+N2	3.590E+21	-2.000	139.0
388	e^-+OH+M ⇌ OH^-+M	1.088E+17	0.000	0.00
	H2/1.0/ H2O/6.5/ O2/0.4/ N2/0.4/ CO/0.75/ CO2/1.5/ CH4/3.0/			
389	OH^-+CO2+O2 ⇌ $CHO3^-$+O2	2.760E+20	0.000	0.00
390	OH^-+CO2+H2O ⇌ $CHO3^-$+H2O	1.104E+21	0.000	0.00
391	e^-+O+O2 ⇌ O^-+O2	3.627E+16	0.000	0.00
392	e^-+O+O ⇌ O^-+O	3.021E+17	0.000	0.00
393	O^-+CO2+O2 ⇌ $CO3^-$+O2	1.123E+20	0.000	0.00
394	C2H6+CH ⇌ C2H5+CH2	1.1E14	0.0	-2.6E2

Appendix D

Thermodynamic coefficients

The *repaired* NASA polynomial coefficients for calculating the thermodynamic properties of the species considered in the chemical kinetic models are shown next.

Listing D.1: Repaired NASA polynomial coefficients.

```
THERMO ALL
  300.0000 1000.00 5000.0000
! Refitting species CHCHO:
! max difference Cp/R = 2.5890e-02 at T = 200.0000 K
! max difference H/RT = 4.7111e-03 at T = 200.0000 K
! max difference S/R = 4.1767e-03 at T = 200.0000 K
! T_match = 1000.000000 jump
! Delta(Cp/R, H/RT, S/R) = ( 0.000e+00, 0.000e+00, 0.000e+00)
CHCHO H 2 C 2 O 1 G 200.0000 3000.0000 1000.00 1
 5.96287949e+00 7.99898746e-03-4.30605647e-06 1.11076174e-09-1.11415021
    e-13 2
 2.87282875e+04-5.17209022e+00 1.77559303e+00 2.11961976e-02-1.94427045
    e-05 3
```

```
 8.54157325e-09-1.41550216e-12 2.97656328e+04 1.59728584e+01 4
! Refitting species N2:
! max difference Cp/R = 1.4577e-06 at T = 979.4897 K
! max difference H/RT = 8.3069e-07 at T = 1000.6503 K
! max difference S/R = 1.5396e-06 at T = 1024.1621 K
! T_match = 1000.000000 jump
! Delta(Cp/R, H/RT, S/R) = (-4.441e-16,-4.441e-16, 0.000e+00)
N2 000000N 2 G 300.0000 5000.0000 1000.00 1
 2.92664000e+00 1.48797680e-03-5.68476000e-07 1.00970380e-10-6.75335100
    e-15 2
-9.22796869e+02 5.98052646e+00 3.29865872e+00 1.40837971e-03-3.96358857
   e-06 3
 5.64191194e-09-2.44500396e-12-1.02089812e+03 3.95044772e+00 4
! Refitting species AR:
! max difference Cp/R = 2.6645e-15 at T = 556.2781 K
! max difference H/RT = 1.5543e-15 at T = 1003.0015 K
! max difference S/R = 7.1054e-15 at T = 398.7494 K
! T_match = 1000.000000 jump
! Delta(Cp/R, H/RT, S/R) = ( 0.000e+00, 0.000e+00, 0.000e+00)
AR 000000AR 1 G 300.0000 5000.0000 1000.00 1
 2.50000000e+00 0.00000000e+00 0.00000000e+00 0.00000000e+00 0.00000000
    e+00 2
-7.45375000e+02 4.36600000e+00 2.50000000e+00-1.56525602e-16 4.56943616
   e-19 3
-5.17814989e-22 1.99020834e-25-7.45375000e+02 4.36600000e+00 4
! Refitting species HE:
! max difference Cp/R = 2.6645e-15 at T = 556.2781 K
! max difference H/RT = 1.5543e-15 at T = 1003.0015 K
! max difference S/R = 3.5527e-15 at T = 426.9635 K
```

```
! T_match = 1000.000000 jump
! Delta(Cp/R, H/RT, S/R) = ( 0.000e+00, 0.000e+00, 0.000e+00)
HE 000000HE 1 G 300.0000 5000.0000 1000.00 1
 2.50000000e+00 0.00000000e+00 0.00000000e+00 0.00000000e+00 0.00000000
    e+00 2
-7.45375000e+02 9.28723974e-01 2.50000000e+00-1.56525602e-16 4.56943616
   e-19 3
-5.17814989e-22 1.99020834e-25-7.45375000e+02 9.28723974e-01 4
! Refitting species H:
! max difference Cp/R = 1.2426e-09 at T = 998.2991 K
! max difference H/RT = 2.8247e-09 at T = 1000.6503 K
! max difference S/R = 8.4447e-09 at T = 1000.6503 K
! T_match = 1000.000000 jump
! Delta(Cp/R, H/RT, S/R) = ( 0.000e+00, 0.000e+00, 0.000e+00)
H 000000H 1 G 300.0000 5000.0000 1000.00 1
 2.50000001e+00-2.30842973e-11 1.61561948e-14-4.73515235e-18 4.98197357
    e-22 2
 2.54736599e+04-4.46682906e-01 2.50000001e+00-7.44840520e-11 1.92361489
    e-13 3
-2.02898893e-16 7.38682947e-20 2.54736599e+04-4.46682894e-01 4
! Refitting species O2:
! max difference Cp/R = 5.1782e-03 at T = 899.5498 K
! max difference H/RT = 7.9095e-04 at T = 993.5968 K
! max difference S/R = 1.1456e-03 at T = 1000.6503 K
! T_match = 1000.000000 jump
! Delta(Cp/R, H/RT, S/R) = ( 0.000e+00, 0.000e+00,-3.553e-15)
O2 000000O 2 G 300.0000 5000.0000 1000.00 1
 3.28253784e+00 1.48308754e-03-7.57966669e-07 2.09470555e-10-2.16717794
    e-14 2
```

```
-1.08766944e+03 5.45437693e+00 3.64943500e+00-1.96290972e-03 7.04899380
   e-06 3
-6.53404723e-09 1.99398564e-12-1.05114016e+03 4.20638308e+00 4
! Refitting species OH:
! max difference Cp/R = 2.5522e-03 at T = 899.5498 K
! max difference H/RT = 3.8984e-04 at T = 993.5968 K
! max difference S/R = 5.6461e-04 at T = 3871.4357 K
! T_match = 1000.000000 jump
! Delta(Cp/R, H/RT, S/R) = ( 0.000e+00, 0.000e+00, 0.000e+00)
OH 000000H 1O 1 G 300.0000 5000.0000 1000.00 1
 2.86472886e+00 1.05650448e-03-2.59082758e-07 3.05218674e-11-1.33195876
    e-15 2
 3.71924625e+03 5.70220534e+00 4.05974374e+00-2.71591120e-03 5.14845250
    e-06 3
-4.24736113e-09 1.44641658e-12 3.38784850e+03-4.19993086e-01 4
! Refitting species O:
! max difference Cp/R = 4.3346e-03 at T = 899.5498 K
! max difference H/RT = 6.6210e-04 at T = 993.5968 K
! max difference S/R = 9.5900e-04 at T = 1000.6503 K
! T_match = 1000.000000 jump
! Delta(Cp/R, H/RT, S/R) = (-4.441e-16, 3.553e-15, 0.000e+00)
O 000000O 1 G 300.0000 5000.0000 1000.00 1
 2.56942078e+00-8.59741137e-05 4.19484589e-08-1.00177799e-11 1.22833691
    e-15 2
 2.92182390e+04 4.78529764e+00 3.05691695e+00-2.41392018e-03 4.30064282
    e-06 3
-3.49355298e-09 1.06651908e-12 2.91329767e+04 2.51124800e+00 4
! Refitting species H2:
! max difference Cp/R = 2.1552e-02 at T = 899.5498 K
```

```
! max difference H/RT = 3.2921e-03 at T = 993.5968 K
! max difference S/R = 4.7682e-03 at T = 1539.0695 K
! T_match = 1000.000000 jump
! Delta(Cp/R, H/RT, S/R) = ( 1.776e-15, 0.000e+00, 0.000e+00)
H2 000000H 2 G 300.0000 5000.0000 1000.00 1
 3.33727920e+00-4.94024731e-05 4.99456778e-07-1.79566394e-10 2.00255376
    e-14 2
-9.53439835e+02-3.20979150e+00 2.89798528e+00 3.67759384e-03-7.83118747
   e-06 3
 7.05790885e-09-2.17450785e-12-9.71224787e+02-1.60078917e+00 4
! Refitting species H2O:
! max difference Cp/R = 1.4857e-04 at T = 899.5498 K
! max difference H/RT = 2.2694e-05 at T = 993.5968 K
! max difference S/R = 3.2896e-05 at T = 2061.0305 K
! T_match = 1000.000000 jump
! Delta(Cp/R, H/RT, S/R) = ( 8.882e-16, 0.000e+00, 3.553e-15)
H2O 000000H 2O 1 G 300.0000 5000.0000 1000.00 1
 3.03399249e+00 2.17691804e-03-1.64072518e-07-9.70419870e-11 1.68200992
    e-14 2
-3.00042744e+04 4.96680300e+00 4.19482397e+00-2.00677208e-03 6.44011434
   e-06 3
-5.39767129e-09 1.73612117e-12-3.02933594e+04-8.33288939e-01 4
! Refitting species HO2:
! max difference Cp/R = 2.7406e-02 at T = 899.5498 K
! max difference H/RT = 4.1862e-03 at T = 993.5968 K
! max difference S/R = 6.0633e-03 at T = 1141.7209 K
! T_match = 1000.000000 jump
! Delta(Cp/R, H/RT, S/R) = ( 0.000e+00, 0.000e+00, 0.000e+00)
HO2 000000H 1O 2 G 300.0000 5000.0000 1000.00 1
```

```
 4.01721090e+00 2.23982013e-03-6.33658150e-07 1.14246370e-10-1.07908535
    e-14 2
 1.16028753e+02 3.79116542e+00 3.59776869e+00 7.22502409e-04 6.34795284
    e-06 3
-7.61925359e-09 2.67785806e-12 3.62571371e+02 6.62075289e+00 4
! Refitting species H2O2:
! max difference Cp/R = 2.5340e-02 at T = 899.5498 K
! max difference H/RT = 3.8706e-03 at T = 993.5968 K
! max difference S/R = 5.6062e-03 at T = 1000.6503 K
! T_match = 1000.000000 jump
! Delta(Cp/R, H/RT, S/R) = ( 0.000e+00, 0.000e+00, 0.000e+00)
H2O2 000000H 2O 2 G 300.0000 5000.0000 1000.00 1
 4.16500285e+00 4.90831694e-03-1.90139225e-06 3.71185986e-10-2.87908305
    e-14 2
-1.78579303e+04 2.92176278e+00 3.62516505e+00 4.51625661e-03 3.03988883
   e-06 3
-6.17584399e-09 2.50885620e-12-1.76399279e+04 6.12018155e+00 4
! Refitting species CO:
! max difference Cp/R = 6.3415e-03 at T = 899.5498 K
! max difference H/RT = 9.6864e-04 at T = 993.5968 K
! max difference S/R = 1.4030e-03 at T = 1061.7809 K
! T_match = 1000.000000 jump
! Delta(Cp/R, H/RT, S/R) = ( 8.882e-16,-1.776e-15, 0.000e+00)
CO 0000000 1C 1 G 300.0000 5000.0000 1000.00 1
 2.71518561e+00 2.06252743e-03-9.98825771e-07 2.30053008e-10-2.03647716
    e-14 2
-1.41528377e+04 7.81728477e+00 3.74243760e+00-1.87642302e-03 4.44375228
   e-06 3
-2.94725970e-09 6.26068344e-13-1.43597656e+04 2.83643682e+00 4
```

```
! Refitting species CO2:
! max difference Cp/R = 7.5014e-03 at T = 899.5498 K
! max difference H/RT = 1.1458e-03 at T = 993.5968 K
! max difference S/R = 1.6595e-03 at T = 1019.4597 K
! T_match = 1000.000000 jump
! Delta(Cp/R, H/RT, S/R) = ( 0.000e+00, 7.105e-15, 0.000e+00)
CO2 000000O 2C 1 G 300.0000 5000.0000 1000.00 1
 3.85746029e+00 4.41437026e-03-2.21481404e-06 5.23490188e-10-4.72084164
    e-14 2
-4.87580241e+04 2.27329759e+00 2.16407331e+00 1.04822373e-02-1.11773067
   e-05 3
 7.01842240e-09-1.95412798e-12-4.83534222e+04 1.06959322e+01 4
! Refitting species HCO:
! max difference Cp/R = 7.8249e-03 at T = 899.5498 K
! max difference H/RT = 1.1952e-03 at T = 993.5968 K
! max difference S/R = 1.7312e-03 at T = 1000.6503 K
! T_match = 1000.000000 jump
! Delta(Cp/R, H/RT, S/R) = ( 8.882e-16, 0.000e+00, 0.000e+00)
HCO 000000H 1O 1C 1 G 300.0000 5000.0000 1000.00 1
 2.77217438e+00 4.95695526e-03-2.48445613e-06 5.89161778e-10-5.33508711
    e-14 2
 4.01310936e+03 9.80007614e+00 4.02017274e+00-1.68167800e-03 9.55132539
    e-06 3
-8.55849493e-09 2.44915922e-12 3.85891262e+03 4.22354273e+00 4
! Refitting species CH3:
! max difference Cp/R = 7.2263e-03 at T = 899.5498 K
! max difference H/RT = 1.1038e-03 at T = 993.5968 K
! max difference S/R = 1.5987e-03 at T = 1000.6503 K
! T_match = 1000.000000 jump
```

```
! Delta(Cp/R, H/RT, S/R) = (-8.882e-16, 0.000e+00, 0.000e+00)
CH3 000000H 3C 1 G 300.0000 5000.0000 1000.00 1
 2.28571772e+00 7.23990037e-03-2.98714348e-06 5.95684644e-10-4.67154394
    e-14 2
 1.67766844e+04 8.48167053e+00 3.48795564e+00 3.45368057e-03 1.82510699
    e-06 3
-2.47910857e-09 7.99809185e-13 1.64628663e+04 2.37029969e+00 4
! Refitting species CH4:
! max difference Cp/R = 3.2664e-02 at T = 899.5498 K
! max difference H/RT = 4.9893e-03 at T = 993.5968 K
! max difference S/R = 7.2264e-03 at T = 1259.2796 K
! T_match = 1000.000000 jump
! Delta(Cp/R, H/RT, S/R) = (-5.329e-15,-8.882e-16, 0.000e+00)
CH4 000000H 4C 1 G 300.0000 5000.0000 1000.00 1
 7.48514950e-02 1.33909467e-02-5.73285809e-06 1.22292535e-09-1.01815230
    e-13 2
-9.46337217e+03 1.84445444e+01 4.31079043e+00-7.14971565e-03 3.15286063
   e-05 3
-2.86217721e-08 8.78614124e-12-1.01658850e+04-1.18011161e+00 4
! Refitting species CH2O:
! max difference Cp/R = 2.7554e-02 at T = 899.5498 K
! max difference H/RT = 4.2087e-03 at T = 993.5968 K
! max difference S/R = 6.0959e-03 at T = 1035.9180 K
! T_match = 1000.000000 jump
! Delta(Cp/R, H/RT, S/R) = ( 8.882e-16,-1.776e-15, 0.000e+00)
CH2O 000000H 2O 1C 1 G 300.0000 5000.0000 1000.00 1
 1.76069008e+00 9.20000082e-03-4.42258813e-06 1.00641212e-09-8.83855640
    e-14 2
```

```
-1.39916378e+04 1.36624189e+01 4.08590675e+00-4.40727812e-03 2.24319977
   e-05 3
-2.11817893e-08 6.52729237e-12-1.42408289e+04 3.52252487e+00 4
! Refitting species T-CH2:
! max difference Cp/R = 9.1318e-03 at T = 899.5498 K
! max difference H/RT = 1.3949e-03 at T = 993.5968 K
! max difference S/R = 2.0203e-03 at T = 1066.4832 K
! T_match = 1000.000000 jump
! Delta(Cp/R, H/RT, S/R) = ( 0.000e+00, 0.000e+00, 0.000e+00)
T-CH2 000000H 2C 1 G 300.0000 5000.0000 1000.00 1
 2.87410113e+00 3.65639292e-03-1.40894597e-06 2.60179549e-10-1.87727567
    e-14 2
 4.62649941e+04 6.17321354e+00 3.52809504e+00 2.79202513e-03-2.13992788
    e-06 3
 1.69927110e-09-5.16508519e-13 4.60266189e+04 2.53017916e+00 4
! Refitting species S-CH2:
! max difference Cp/R = 2.4826e-03 at T = 899.5498 K
! max difference H/RT = 3.7921e-04 at T = 993.5968 K
! max difference S/R = 5.4922e-04 at T = 2023.4117 K
! T_match = 1000.000000 jump
! Delta(Cp/R, H/RT, S/R) = ( 0.000e+00, 0.000e+00,-3.553e-15)
S-CH2 000000H 2C 1 G 300.0000 5000.0000 1000.00 1
 2.29203842e+00 4.65588637e-03-2.01191947e-06 4.17906000e-10-3.39716365
    e-14 2
 5.09263775e+04 8.62705091e+00 4.13482906e+00-1.87096291e-03 6.89135625
    e-06 3
-5.17926016e-09 1.34397744e-12 5.05029547e+04-5.06049633e-01 4
! Refitting species C2H4:
! max difference Cp/R = 8.4863e-02 at T = 899.5498 K
```

```
! max difference H/RT = 1.2963e-02 at T = 993.5968 K
! max difference S/R = 1.8775e-02 at T = 1000.6503 K
! T_match = 1000.000000 jump
! Delta(Cp/R, H/RT, S/R) = ( 0.000e+00, 0.000e+00, 0.000e+00)
C2H4 000000H 4C 2 G 300.0000 5000.0000 1000.00 1
 2.03611116e+00 1.46454151e-02-6.71077915e-06 1.47222923e-09-1.25706061
    e-13 2
 4.95280481e+03 1.03241441e+01 1.77917700e+00 9.37233954e-03 1.12388741
    e-05 3
-1.75801140e-08 6.50699363e-12 5.29960487e+03 1.30898375e+01 4
! Refitting species CH3O:
! max difference Cp/R = 8.4698e-02 at T = 899.5498 K
! max difference H/RT = 1.2937e-02 at T = 993.5968 K
! max difference S/R = 1.8738e-02 at T = 1003.0015 K
! T_match = 1000.000000 jump
! Delta(Cp/R, H/RT, S/R) = ( 3.553e-15, 0.000e+00, 7.105e-15)
CH3O 000000H 3O 1C 1 G 300.0000 5000.0000 1000.00 1
 4.75779238e+00 7.44142474e-03-2.69705176e-06 4.38090504e-10-2.63537098
    e-14 2
 4.03032786e+02-1.94806182e+00 1.53600900e+00 1.41053661e-02-8.11610681
    e-06 3
 4.17151012e-09-1.78287623e-12 1.51714678e+03 1.55474730e+01 4
! Refitting species C2H5:
! max difference Cp/R = 6.9743e-02 at T = 899.5498 K
! max difference H/RT = 1.0653e-02 at T = 993.5968 K
! max difference S/R = 1.5430e-02 at T = 4184.1421 K
! T_match = 1000.000000 jump
! Delta(Cp/R, H/RT, S/R) = (-5.329e-15, 0.000e+00, 0.000e+00)
C2H5 000000H 5C 2 G 300.0000 5000.0000 1000.00 1
```

```
 1.95465642e+00 1.73972722e-02-7.98206668e-06 1.75217689e-09-1.49641576
    e-13 2
 1.28681370e+04 1.34778641e+01 2.51485726e+00 9.73755497e-03 1.20250517
    e-05 3
-1.75237116e-08 6.21864489e-12 1.30140701e+04 1.20975164e+01 4
! Refitting species C2H6:
! max difference Cp/R = 7.7839e-02 at T = 899.5498 K
! max difference H/RT = 1.1890e-02 at T = 993.5968 K
! max difference S/R = 1.7221e-02 at T = 1000.6503 K
! T_match = 1000.000000 jump
! Delta(Cp/R, H/RT, S/R) = ( 1.776e-15,-1.776e-15,-7.105e-15)
C2H6 000000H 6C 2 G 300.0000 5000.0000 1000.00 1
 1.07188150e+00 2.16852677e-02-1.00256067e-05 2.21412001e-09-1.90002890
    e-13 2
-1.14145438e+04 1.51328316e+01 2.29184219e+00 1.00389500e-02 1.78795417
   e-05 3
-2.35370664e-08 8.08239215e-12-1.13297442e+04 1.09150153e+01 4
! Refitting species CH:
! max difference Cp/R = 5.6158e-03 at T = 899.5498 K
! max difference H/RT = 8.5779e-04 at T = 993.5968 K
! max difference S/R = 1.2425e-03 at T = 1024.1621 K
! T_match = 1000.000000 jump
! Delta(Cp/R, H/RT, S/R) = (-4.441e-16, 0.000e+00, 0.000e+00)
CH 000000H 1C 1 G 300.0000 5000.0000 1000.00 1
 2.87846473e+00 9.70913681e-04 1.44445655e-07-1.30687849e-10 1.76079383
    e-14 2
 7.10115815e+04 5.48373754e+00 3.63407917e+00-7.97353729e-04 1.34579273
    e-06 3
-2.51037540e-10-5.07364808e-14 7.07834080e+04 1.48893444e+00 4
```

```
! Refitting species C2H2:
! max difference Cp/R = 4.4655e-03 at T = 899.5498 K
! max difference H/RT = 6.8209e-04 at T = 993.5968 K
! max difference S/R = 9.8788e-04 at T = 1007.7039 K
! T_match = 1000.000000 jump
! Delta(Cp/R, H/RT, S/R) = ( 1.776e-15, 0.000e+00, 0.000e+00)
C2H2 000000H 2C 2 G 300.0000 5000.0000 1000.00 1
 4.14756964e+00 5.96166664e-03-2.37294852e-06 4.67412171e-10-3.61235213
    e-14 2
 2.59353195e+04-1.23126909e+00 9.23394034e-01 2.24700292e-02-3.31040196
    e-05 3
 2.53011691e-08-7.42299631e-12 2.64179395e+04 1.34665192e+01 4
! Refitting species C2H4OOH:
! max difference Cp/R = 3.4405e-01 at T = 963.0315 K
! max difference H/RT = 1.0270e-01 at T = 1000.6503 K
! max difference S/R = 1.1309e-01 at T = 3793.8469 K
! T_match = 1000.000000 jump
! Delta(Cp/R, H/RT, S/R) = (-3.553e-15, 0.000e+00, 0.000e+00)
C2H4OOH 000000H 5O 2C 2 G 300.0000 5000.0000 1000.00 1
 1.16258666e+01 1.00826346e-02-3.47934362e-06 5.43394220e-10-3.16569294
    e-14 2
-8.07796609e+02-3.17392052e+01-4.12744696e+00 7.67800581e-02-1.33960138
   e-04 3
 1.24425967e-07-4.43775451e-11 2.98893781e+03 4.54160846e+01 4
! Refitting species OC2H3OOH:
! max difference Cp/R = 3.4849e-01 at T = 960.6803 K
! max difference H/RT = 9.8024e-02 at T = 1000.6503 K
! max difference S/R = 1.0983e-01 at T = 1311.0055 K
! T_match = 1000.000000 jump
```

```
! Delta(Cp/R, H/RT, S/R) = ( 7.105e-15,-7.105e-15, 0.000e+00)
OC2H3OOH 000000H 4O 3C 2 G 300.0000 5000.0000 1000.00 1
 1.24064339e+01 9.47233784e-03-3.28107928e-06 5.13772211e-10-2.99872803
    e-14 2
-3.48142260e+04-3.38381573e+01 4.11154554e-01 6.33170791e-02-1.18802845
   e-04 3
 1.18004198e-07-4.38481088e-11-3.18430441e+04 2.47294939e+01 4
! Refitting species C2H3:
! max difference Cp/R = 5.3639e-02 at T = 899.5498 K
! max difference H/RT = 8.1932e-03 at T = 993.5968 K
! max difference S/R = 1.1867e-02 at T = 1000.6503 K
! T_match = 1000.000000 jump
! Delta(Cp/R, H/RT, S/R) = ( 0.000e+00, 0.000e+00, 0.000e+00)
C2H3 000000H 3C 2 G 300.0000 5000.0000 1000.00 1
 3.01672400e+00 1.03302292e-02-4.68082349e-06 1.01763288e-09-8.62607041
    e-14 2
 3.46210393e+04 7.79919071e+00 1.83455202e+00 1.22237604e-02-3.06560031
    e-06 3
-3.16471922e-09 1.76950897e-12 3.49924721e+04 1.41943776e+01 4
! Refitting species CH2CHO:
! max difference Cp/R = 1.7415e-02 at T = 899.5498 K
! max difference H/RT = 2.6602e-03 at T = 993.5968 K
! max difference S/R = 3.8539e-03 at T = 1000.6503 K
! T_match = 1000.000000 jump
! Delta(Cp/R, H/RT, S/R) = ( 1.776e-15, 0.000e+00, 0.000e+00)
CH2CHO 000000H 3O 1C 2 G 300.0000 5000.0000 1000.00 1
 5.16620060e+00 1.08478260e-02-4.46583680e-06 8.06285480e-10-4.84101930
    e-14 2
```

```
-7.29339775e+02-1.95948223e+00 5.66035528e-01 2.61583223e-02-2.51449236
   e-05 3
 1.46336305e-08-3.90699965e-12 4.23487721e+02 2.12019118e+01 4
! Refitting species C2H4O:
! max difference Cp/R = 8.9202e-02 at T = 899.5498 K
! max difference H/RT = 1.3625e-02 at T = 993.5968 K
! max difference S/R = 1.9735e-02 at T = 3518.7594 K
! T_match = 1000.000000 jump
! Delta(Cp/R, H/RT, S/R) = ( 1.776e-15, 7.105e-15, 0.000e+00)
C2H4O 000000H 4O 1C 2 G 300.0000 5000.0000 1000.00 1
 5.40411080e+00 1.17230590e-02-4.22631370e-06 6.83724510e-10-4.09848630
    e-14 2
-2.25795421e+04-3.46105707e+00 2.43797402e+00 1.46158364e-02-6.69987266
   e-07 3
-3.24271345e-09 4.02486041e-13-2.13523209e+04 1.35552942e+01 4
! Refitting species HCCO:
! max difference Cp/R = 3.4084e-03 at T = 901.9010 K
! max difference H/RT = 5.2101e-04 at T = 993.5968 K
! max difference S/R = 7.5842e-04 at T = 1000.6503 K
! T_match = 1000.000000 jump
! Delta(Cp/R, H/RT, S/R) = (-3.553e-15, 0.000e+00, 0.000e+00)
HCCO 000000H 1O 1C 2 G 300.0000 5000.0000 1000.00 1
 5.62820580e+00 4.08534010e-03-1.59345470e-06 2.86260520e-10-1.94078320
    e-14 2
 1.93277356e+04-3.92950108e+00 2.16435678e+00 1.83339593e-02-2.55666391
    e-05 3
 1.93421680e-08-5.88690100e-12 2.00678583e+04 1.28507975e+01 4
! Refitting species CH2CO:
! max difference Cp/R = 8.0289e-03 at T = 899.5498 K
```

```
! max difference H/RT = 1.2264e-03 at T = 993.5968 K
! max difference S/R = 1.7763e-03 at T = 1000.6503 K
! T_match = 1000.000000 jump
! Delta(Cp/R, H/RT, S/R) = ( 3.553e-15,-4.441e-16, 0.000e+00)
CH2CO 000000H 2O 1C 2 G 300.0000 5000.0000 1000.00 1
 4.51129732e+00 9.00359745e-03-4.16939635e-06 9.23345882e-10-7.94838201
    e-14 2
-7.54983087e+03 6.34023532e-01 1.92958418e+00 1.97218364e-02-2.17335775
   e-05 3
 1.42238438e-08-3.95232643e-12-7.02306612e+03 1.30664291e+01 4
! Refitting species C2H:
! max difference Cp/R = 3.2677e-02 at T = 899.5498 K
! max difference H/RT = 4.9913e-03 at T = 993.5968 K
! max difference S/R = 7.2295e-03 at T = 1000.6503 K
! T_match = 1000.000000 jump
! Delta(Cp/R, H/RT, S/R) = ( 0.000e+00, 0.000e+00, 0.000e+00)
C2H 000000H 1C 2 G 300.0000 5000.0000 1000.00 1
 3.16780652e+00 4.75221902e-03-1.83787077e-06 3.04190252e-10-1.77232770
    e-14 2
 6.71160905e+04 6.62866530e+00 3.72909224e+00 6.88598386e-03-1.08181500
    e-05 3
 9.61831135e-09-3.04661568e-12 6.67585970e+04 2.76033173e+00 4
! Refitting species CH2OH:
! max difference Cp/R = 5.7689e-02 at T = 899.5498 K
! max difference H/RT = 8.8119e-03 at T = 993.5968 K
! max difference S/R = 1.2763e-02 at T = 1005.3527 K
! T_match = 1000.000000 jump
! Delta(Cp/R, H/RT, S/R) = ( 0.000e+00, 0.000e+00, 0.000e+00)
CH2OH 000000H 3O 1C 1 G 300.0000 5000.0000 1000.00 1
```

```
 5.09312037e+00 5.94758550e-03-2.06496524e-06 3.23006703e-10-1.88125052
    e-14 2
-4.04935026e+03-1.83414309e+00 2.99635913e+00 1.01669317e-02-3.32701364
   e-06 3
-1.42389018e-09 8.67547803e-13-3.38212717e+03 9.42215730e+00 4
! Refitting species CH3OH:
! max difference Cp/R = 6.5391e-02 at T = 899.5498 K
! max difference H/RT = 9.9883e-03 at T = 993.5968 K
! max difference S/R = 1.4467e-02 at T = 1000.6503 K
! T_match = 1000.000000 jump
! Delta(Cp/R, H/RT, S/R) = (-1.776e-15, 3.553e-15, 0.000e+00)
CH3OH 000000H 4O 1C 1 G 300.0000 5000.0000 1000.00 1
 1.78970791e+00 1.40938292e-02-6.36500835e-06 1.38171085e-09-1.17060220
    e-13 2
-2.53649202e+04 1.45168293e+01 4.03557601e+00-2.17557548e-03 2.99065323
   e-05 3
-3.13366288e-08 1.03532753e-11-2.54810817e+04 5.42508573e+00 4
! Refitting species CH3CHO:
! max difference Cp/R = 8.9202e-02 at T = 899.5498 K
! max difference H/RT = 1.3625e-02 at T = 993.5968 K
! max difference S/R = 1.9735e-02 at T = 3518.7594 K
! T_match = 1000.000000 jump
! Delta(Cp/R, H/RT, S/R) = ( 1.776e-15, 7.105e-15, 0.000e+00)
CH3CHO 000000H 4O 1C 2 G 300.0000 5000.0000 1000.00 1
 5.40411080e+00 1.17230590e-02-4.22631370e-06 6.83724510e-10-4.09848630
    e-14 2
-2.25795421e+04-3.46105707e+00 2.43797402e+00 1.46158364e-02-6.69987266
   e-07 3
-3.24271345e-09 4.02486041e-13-2.13523209e+04 1.35552942e+01 4
```

```
! Refitting species CH3CO:
! max difference Cp/R = 7.3023e-02 at T = 899.5498 K
! max difference H/RT = 1.1154e-02 at T = 993.5968 K
! max difference S/R = 1.6155e-02 at T = 1000.6503 K
! T_match = 1000.000000 jump
! Delta(Cp/R, H/RT, S/R) = ( 0.000e+00, 8.882e-16, 0.000e+00)
CH3CO 000000H 3O 1C 2 G 300.0000 5000.0000 1000.00 1
 5.94477310e+00 7.86672050e-03-2.88658820e-06 4.72708750e-10-2.85998610
    e-14 2
-3.77619115e+03-4.99751990e+00 2.28755291e+00 1.43464199e-02-5.19404290
   e-06 3
 2.77400704e-10-3.48316326e-13-2.47689879e+03 1.50847219e+01 4
! Refitting species C2H5OH:
! max difference Cp/R = 3.4516e-08 at T = 899.5498 K
! max difference H/RT = 5.2722e-09 at T = 993.5968 K
! max difference S/R = 7.6350e-09 at T = 998.2991 K
! T_match = 1000.000000 jump
! Delta(Cp/R, H/RT, S/R) = (-3.553e-15, 0.000e+00, 0.000e+00)
C2H5OH 000000H 6O 1C 2 G 300.0000 5000.0000 1000.00 1
 4.34717120e+00 1.86288000e-02-6.77946700e-06 8.16592600e-10 0.00000000
    e+00 2
-3.06615743e+04 3.24247304e+00 5.76536687e-01 2.89451131e-02-1.61001813
   e-05 3
 3.59162002e-09 8.33027999e-18-2.96359501e+04 2.27081263e+01 4
! Refitting species CH2CH2OH:
! max difference Cp/R = 3.0332e-01 at T = 960.6803 K
! max difference H/RT = 8.5563e-02 at T = 1000.6503 K
! max difference S/R = 9.5797e-02 at T = 1019.4597 K
! T_match = 1000.000000 jump
```

```
! Delta(Cp/R, H/RT, S/R) = ( 2.132e-14, 0.000e+00, 7.105e-15)
CH2CH2OH 000000H 5O 1C 2 G 300.0000 5000.0000 1000.00 1
 7.52244726e+00 1.10492715e-02-3.72576465e-06 5.72827397e-10-3.30061759
    e-14 2
-7.20775615e+03-1.24002784e+01-3.28406163e+00 5.89405933e-02-1.05367697
   e-04 3
 1.03408761e-07-3.83118210e-11-4.51948470e+03 4.04691437e+01 4
! Refitting species CH3CHOH:
! max difference Cp/R = 3.1993e-01 at T = 955.9780 K
! max difference H/RT = 8.1304e-02 at T = 1000.6503 K
! max difference S/R = 9.4093e-02 at T = 1000.6503 K
! T_match = 1000.000000 jump
! Delta(Cp/R, H/RT, S/R) = ( 8.882e-15, 0.000e+00, 0.000e+00)
CH3CHOH 000000H 5O 1C 2 G 300.0000 5000.0000 1000.00 1
 7.26570301e+00 1.09588926e-02-3.63662803e-06 5.53659830e-10-3.17012322
    e-14 2
-8.56235768e+03-1.05881922e+01-3.08115478e+00 5.64686247e-02-1.04535890
   e-04 3
 1.07210418e-07-4.09520720e-11-5.81739410e+03 4.05031081e+01 4
! Refitting species CH3CH2O:
! max difference Cp/R = 2.7750e-01 at T = 955.9780 K
! max difference H/RT = 7.3112e-02 at T = 1000.6503 K
! max difference S/R = 8.3674e-02 at T = 2865.1326 K
! T_match = 1000.000000 jump
! Delta(Cp/R, H/RT, S/R) = (-8.882e-15, 0.000e+00,-7.105e-15)
CH3CH2O 000000H 5O 1C 2 G 300.0000 5000.0000 1000.00 1
 8.31182392e+00 1.03426319e-02-3.39186089e-06 5.12212617e-10-2.91601713
    e-14 2
```

```
-6.05782025e+03-2.13148843e+01-4.53578225e+00 6.25453443e-02-1.06304453
   e-04 3
 1.01119684e-07-3.70791458e-11-2.74924367e+03 4.24134912e+01 4
! Refitting species C3H4:
! max difference Cp/R = 8.6459e-02 at T = 899.5498 K
! max difference H/RT = 1.3206e-02 at T = 993.5968 K
! max difference S/R = 1.9128e-02 at T = 1000.6503 K
! T_match = 1000.000000 jump
! Delta(Cp/R, H/RT, S/R) = ( 3.553e-15, 0.000e+00,-7.105e-15)
C3H4 000000H 4C 3 G 300.0000 5000.0000 1000.00 1
 6.31687220e+00 1.11337280e-02-3.96293780e-06 6.35642380e-10-3.78755400
    e-14 2
 2.01306567e+04-1.09766377e+01 3.92028872e-01 2.93840154e-02-2.81825908
    e-05 3
 1.80234594e-08-5.53148367e-12 2.17553414e+04 1.93877322e+01 4
! Refitting species C3H3:
! max difference Cp/R = 3.5784e-04 at T = 899.5498 K
! max difference H/RT = 5.4659e-05 at T = 993.5968 K
! max difference S/R = 7.9155e-05 at T = 998.2991 K
! T_match = 1000.000000 jump
! Delta(Cp/R, H/RT, S/R) = ( 7.105e-15, 0.000e+00, 0.000e+00)
C3H3 000000H 3C 3 G 300.0000 5000.0000 1000.00 1
 7.14221880e+00 7.61902005e-03-2.67459950e-06 4.24914801e-10-2.51475415
    e-14 2
 3.89087973e+04-1.25847648e+01 1.34191721e+00 3.28125617e-02-4.75760821
    e-05 3
 3.78484614e-08-1.19404516e-11 4.01066630e+04 1.52438093e+01 4
! Refitting species C3H5:
! max difference Cp/R = 9.4756e-02 at T = 899.5498 K
```

```
! max difference H/RT = 1.4473e-02 at T = 993.5968 K
! max difference S/R = 2.0972e-02 at T = 1000.6503 K
! T_match = 1000.000000 jump
! Delta(Cp/R, H/RT, S/R) = ( 0.000e+00, 7.105e-15, 0.000e+00)
C3H5 000000H 5C 3 G 300.0000 5000.0000 1000.00 1
 6.50078770e+00 1.43247310e-02-5.67816320e-06 1.10808010e-09-9.03638870
    e-14 2
 1.74968802e+04-1.12220782e+01-1.07103407e+00 3.87322554e-02-3.87105481
    e-05 3
 2.42375638e-08-7.02316531e-12 1.94799241e+04 2.72142542e+01 4
! Refitting species C3H6:
! max difference Cp/R = 6.2187e-02 at T = 899.5498 K
! max difference H/RT = 9.4977e-03 at T = 993.5968 K
! max difference S/R = 1.3761e-02 at T = 2444.2721 K
! T_match = 1000.000000 jump
! Delta(Cp/R, H/RT, S/R) = ( 3.553e-15, 0.000e+00, 0.000e+00)
C3H6 000000H 6C 3 G 300.0000 5000.0000 1000.00 1
 6.73225700e+00 1.49083400e-02-4.94989900e-06 7.21202200e-10-3.76620400
    e-14 2
-9.14093470e+02-1.32995893e+01-1.04726404e-01 3.33450189e-02-2.91311572
   e-05 3
 2.11216156e-08-7.85651270e-12 1.22863668e+03 2.27371440e+01 4
! Refitting species C3H8:
! max difference Cp/R = 8.1226e-02 at T = 899.5498 K
! max difference H/RT = 1.2407e-02 at T = 993.5968 K
! max difference S/R = 1.7970e-02 at T = 1000.6503 K
! T_match = 1000.000000 jump
! Delta(Cp/R, H/RT, S/R) = ( 0.000e+00, 0.000e+00,-7.105e-15)
C3H8 000000H 8C 3 G 300.0000 5000.0000 1000.00 1
```

```
 7.52441520e+00 1.88982820e-02-6.29210410e-06 9.21614570e-10-4.86844780
    e-14 2
-1.65520288e+04-1.78204054e+01-1.15807781e+00 4.26772574e-02-3.78613439
   e-05 3
 2.74531401e-08-1.01074526e-11-1.38570713e+04 2.78326262e+01 4
! Refitting species I-C3H7:
! max difference Cp/R = 6.0311e-02 at T = 899.5498 K
! max difference H/RT = 9.2123e-03 at T = 993.5968 K
! max difference S/R = 1.3343e-02 at T = 1024.1621 K
! T_match = 1000.000000 jump
! Delta(Cp/R, H/RT, S/R) = ( 3.553e-15, 0.000e+00, 0.000e+00)
I-C3H7 000000H 7C 3 G 300.0000 5000.0000 1000.00 1
 6.51927410e+00 1.72201040e-02-5.73642170e-06 8.41307320e-10-4.45659130
    e-14 2
 7.33190029e+03-9.06967828e+00-1.04383738e-01 3.30400941e-02-2.48883478
    e-05 3
 1.81798205e-08-7.42748527e-12 9.57149401e+03 2.65071275e+01 4
! Refitting species N-C3H7:
! max difference Cp/R = 7.8157e-02 at T = 899.5498 K
! max difference H/RT = 1.1938e-02 at T = 993.5968 K
! max difference S/R = 1.7291e-02 at T = 1842.3712 K
! T_match = 1000.000000 jump
! Delta(Cp/R, H/RT, S/R) = ( 0.000e+00, 0.000e+00, 0.000e+00)
N-C3H7 000000H 7C 3 G 300.0000 5000.0000 1000.00 1
 7.70974790e+00 1.60314850e-02-5.27202380e-06 7.58883520e-10-3.88627190
    e-14 2
 7.98812185e+03-1.54980061e+01-9.58649601e-01 4.16130734e-02-3.98822109
    e-05 3
 2.79080827e-08-9.49106566e-12 1.05055950e+04 2.94179853e+01 4
```

```
! Refitting species C3H6OOH:
! max difference Cp/R = 5.3308e-01 at T = 958.3292 K
! max difference H/RT = 1.4230e-01 at T = 1000.6503 K
! max difference S/R = 1.6211e-01 at T = 1809.4547 K
! T_match = 1000.000000 jump
! Delta(Cp/R, H/RT, S/R) = ( 1.066e-14, 1.776e-15, 0.000e+00)
C3H6OOH 000000H 7O 2C 3 G 300.0000 5000.0000 1000.00 1
 1.46139980e+01 1.43723015e-02-4.88635144e-06 7.56519620e-10-4.38364992
    e-14 2
-6.31862609e+03-4.55857108e+01-6.15700779e+00 1.02926779e-01-1.88813302
   e-04 3
 1.86031012e-07-6.91748498e-11-1.00829585e+03 5.68289013e+01 4
! Refitting species OC3H5OOH:
! max difference Cp/R = 5.4943e-01 at T = 963.0315 K
! max difference H/RT = 1.5917e-01 at T = 1000.6503 K
! max difference S/R = 1.7684e-01 at T = 1000.6503 K
! T_match = 1000.000000 jump
! Delta(Cp/R, H/RT, S/R) = ( 0.000e+00, 7.105e-15, 0.000e+00)
OC3H5OOH 000000H 6O 3C 3 G 300.0000 5000.0000 1000.00 1
 1.70285271e+01 1.30716784e-02-4.59310856e-06 7.26135156e-10-4.26658337
    e-14 2
-4.14741491e+04-5.90745166e+01-7.23875434e+00 1.15936274e-01-2.08565920
   e-04 3
 1.97147096e-07-7.10881297e-11-3.55443759e+04 5.99674470e+01 4
! Refitting species C4H8:
! max difference Cp/R = 1.8310e-04 at T = 885.4427 K
! max difference H/RT = 4.7504e-05 at T = 1000.6503 K
! max difference S/R = 7.2947e-05 at T = 3034.4172 K
! T_match = 1000.000000 jump
```

```
! Delta(Cp/R, H/RT, S/R) = (-3.553e-15, 1.776e-15,-7.105e-15)
C4H8 C 4H 80 00 0G 300.0000 5000.0000 1000.00 1
 2.05358400e+00 3.43505000e-02-1.58831960e-05 3.30896600e-09-2.53610400
    e-13 2
-2.13967546e+03 1.55432739e+01 1.17566460e+00 3.08961342e-02 4.96998818
   e-06 3
-2.45226273e-08 1.10570840e-11-1.78987509e+03 2.10850242e+01 4
! Refitting species N:
! max difference Cp/R = 3.6287e-04 at T = 899.5498 K
! max difference H/RT = 5.9714e-05 at T = 1000.6503 K
! max difference S/R = 9.1957e-05 at T = 1007.7039 K
! T_match = 1000.000000 jump
! Delta(Cp/R, H/RT, S/R) = ( 4.441e-16, 0.000e+00,-3.553e-15)
N 120186N 1 G 300.0000 5000.0000 1000.00 1
 2.45026800e+00 1.06614580e-04-7.46533700e-08 1.87965200e-11-1.02598390
    e-15 2
 5.61159802e+04 4.44866604e+00 2.51239411e+00-9.42585759e-05 2.50333766
    e-07 3
-2.77062742e-10 1.08593184e-13 5.60980026e+04 4.12910860e+00 4
! Refitting species NH:
! max difference Cp/R = 2.9750e-03 at T = 200.0000 K
! max difference H/RT = 5.4135e-04 at T = 200.0000 K
! max difference S/R = 4.7994e-04 at T = 200.0000 K
! T_match = 1000.000000 jump
! Delta(Cp/R, H/RT, S/R) = ( 0.000e+00, 0.000e+00, 3.553e-15)
NH L11/89N 1H 1 0 0G 200.0000 6000.0000 1000.00 1
 2.78369290e+00 1.32984290e-03-4.24780470e-07 7.83485040e-11-5.50444700
    e-15 2
```

```
 4.21342037e+04 5.74056959e+00 3.52658205e+00 2.76343190e-05-6.48964620
    e-07 3
 1.46178594e-09-6.05438307e-13 4.18912743e+04 1.71201144e+00 4
! Refitting species NH2:
! max difference Cp/R = 6.7500e-03 at T = 200.0000 K
! max difference H/RT = 1.2283e-03 at T = 200.0000 K
! max difference S/R = 1.0889e-03 at T = 200.0000 K
! T_match = 1000.000000 jump
! Delta(Cp/R, H/RT, S/R) = (-8.882e-16, 0.000e+00, 0.000e+00)
NH2 L12/89N 1H 2 0 0G 200.0000 6000.0000 1000.00 1
 2.84766110e+00 3.14284530e-03-8.98665570e-07 1.30323570e-10-7.48853560
    e-15 2
 2.18246186e+04 6.47229178e+00 4.12915796e+00-1.49080265e-03 5.36213399
    e-06 3
-3.61631916e-09 8.30505717e-13 2.15420743e+04 1.62655562e-01 4
! Refitting species N2O:
! max difference Cp/R = 6.9486e-03 at T = 200.0000 K
! max difference H/RT = 1.2644e-03 at T = 200.0000 K
! max difference S/R = 1.1210e-03 at T = 200.0000 K
! T_match = 1000.000000 jump
! Delta(Cp/R, H/RT, S/R) = (-1.776e-15, 0.000e+00, 0.000e+00)
N2O L 7/88N 2O 1 0 0G 200.0000 6000.0000 1000.00 1
 4.82307290e+00 2.62702510e-03-9.58508720e-07 1.60007120e-10-9.77523020
    e-15 2
 8.07412818e+03-2.20122859e+00 2.17850018e+00 1.19684226e-02-1.56334679
    e-05 3
 1.20640237e-08-3.93565749e-12 8.74882749e+03 1.10763796e+01 4
! Refitting species HNO:
! max difference Cp/R = 5.2380e-03 at T = 200.0000 K
```

```
! max difference H/RT = 9.5313e-04 at T = 200.0000 K
! max difference S/R = 8.4501e-04 at T = 200.0000 K
! T_match = 1000.000000 jump
! Delta(Cp/R, H/RT, S/R) = (-1.776e-15,-1.776e-15, 0.000e+00)
HNO L12/89H 1N 1O 1 0G 200.0000 3500.0000 1000.00 1
 3.16552290e+00 3.00008620e-03-3.94366190e-07-3.85758150e-11 7.08071890
    e-15 2
 1.11938809e+04 7.64741199e+00 4.59453544e+00-6.18570287e-03 1.99989536
    e-05 3
-1.89838984e-08 6.31586001e-12 1.10345644e+04 1.50318497e+00 4
! Refitting species NH3:
! max difference Cp/R = 2.7323e-02 at T = 200.0000 K
! max difference H/RT = 4.9717e-03 at T = 200.0000 K
! max difference S/R = 4.4078e-03 at T = 200.0000 K
! T_match = 1000.000000 jump
! Delta(Cp/R, H/RT, S/R) = (-1.776e-15,-6.661e-16, 0.000e+00)
NH3 AMONIA RUS 89N 1H 3 0 0G 200.0000 6000.0000 1000.00 1
 2.71709692e+00 5.56856338e-03-1.76886396e-06 2.67417260e-10-1.52731419
    e-14 2
-6.58167475e+03 6.09483464e+00 3.99251912e+00-2.16156694e-03 1.42188208
   e-05 3
-1.36192500e-08 4.33841754e-12-6.72033135e+03 5.61284602e-01 4
! Refitting species NO2:
! max difference Cp/R = 3.6108e-02 at T = 200.0000 K
! max difference H/RT = 6.5703e-03 at T = 200.0000 K
! max difference S/R = 5.8250e-03 at T = 200.0000 K
! T_match = 1000.000000 jump
! Delta(Cp/R, H/RT, S/R) = ( 0.000e+00, 0.000e+00, 0.000e+00)
NO2 L 7/88N 1O 2 0 0G 200.0000 6000.0000 1000.00 1
```

```
 4.88475400e+00 2.17239550e-03-8.28069090e-07 1.57475100e-10-1.05108950
    e-14 2
 2.32025808e+03-1.14858031e-01 3.53533598e+00 1.86337812e-03 6.46175178
    e-06 3
-8.09744241e-09 2.61302115e-12 2.93326748e+03 7.96645454e+00 4
! Refitting species N2H:
! max difference Cp/R = 3.1295e-02 at T = 200.0000 K
! max difference H/RT = 5.6946e-03 at T = 200.0000 K
! max difference S/R = 5.0487e-03 at T = 200.0000 K
! T_match = 1000.000000 jump
! Delta(Cp/R, H/RT, S/R) = ( 0.000e+00, 0.000e+00, 0.000e+00)
N2H T07/93N 2H 1 0 0G 200.0000 6000.0000 1000.00 1
 3.76675450e+00 2.89150810e-03-1.04166200e-06 1.68425940e-10-1.00918960
    e-14 2
 2.86539560e+04 4.47272452e+00 3.99046699e+00-1.86054587e-03 1.12222984
    e-05 3
-1.09981829e-08 3.42089801e-12 2.88237380e+04 4.41190264e+00 4
! Refitting species NO:
! max difference Cp/R = 6.4335e-03 at T = 200.0000 K
! max difference H/RT = 1.1707e-03 at T = 200.0000 K
! max difference S/R = 1.0379e-03 at T = 200.0000 K
! T_match = 1000.000000 jump
! Delta(Cp/R, H/RT, S/R) = ( 0.000e+00,-1.776e-15, 0.000e+00)
NO RUS 89N 1O 1 0 0G 200.0000 6000.0000 1000.00 1
 3.26071234e+00 1.19101135e-03-4.29122646e-07 6.94481463e-11-4.03295681
    e-15 2
 9.92210128e+03 6.36946115e+00 4.14577886e+00-4.02538298e-03 9.22760068
    e-06 3
-7.13508162e-09 1.87510129e-12 9.85162973e+03 2.57539722e+00 4
```

```
! Refitting species C4H10:
! max difference Cp/R = 2.9869e-02 at T = 1235.7679 K
! max difference H/RT = 5.1102e-03 at T = 1379.1896 K
! max difference S/R = 8.4158e-03 at T = 1390.9455 K
! T_match = 1392.000000 jump
! Delta(Cp/R, H/RT, S/R) = (-3.553e-15, 0.000e+00, 0.000e+00)
C4H10 8/ 4/ 4 THERMC 4H 10 0 0G 300.0000 5000.0000 1392.00 1
 1.24940183e+01 2.17726258e-02-7.44272215e-06 1.15487023e-09-6.69712949
    e-14 2
-2.18332626e+04-4.45474765e+01-7.49402014e-01 5.00249108e-02-3.10099224
   e-05 3
 1.09140627e-08-1.86245403e-12-1.68650026e+04 2.77315037e+01 4
! Refitting species PC4H9:
! max difference Cp/R = 2.7471e-02 at T = 1235.7679 K
! max difference H/RT = 4.7025e-03 at T = 1379.1896 K
! max difference S/R = 7.7362e-03 at T = 1390.9455 K
! T_match = 1391.000000 jump
! Delta(Cp/R, H/RT, S/R) = ( 0.000e+00, 0.000e+00, 0.000e+00)
PC4H9 8/ 4/ 4 THERMC 4H 9 0 0G 300.0000 5000.0000 1391.00 1
 1.20779744e+01 1.96264778e-02-6.71302199e-06 1.04206424e-09-6.04469282
    e-14 2
 3.23201891e+03-3.87642022e+01 5.08646378e-02 4.52970303e-02-2.81595154
    e-05 3
 9.95113578e-09-1.70645452e-12 7.74347540e+03 2.68737016e+01 4
! Refitting species SC4H9:
! max difference Cp/R = 1.4909e-02 at T = 1228.7144 K
! max difference H/RT = 2.5473e-03 at T = 1369.7849 K
! max difference S/R = 4.1788e-03 at T = 1388.5943 K
! T_match = 1381.000000 jump
```

```
! Delta(Cp/R, H/RT, S/R) = (-3.553e-15, 0.000e+00, 0.000e+00)
SC4H9 8/ 4/ 4 THERMC 4H 9 0 0G 300.0000 5000.0000 1381.00 1
 1.16934304e+01 1.96402287e-02-6.65306517e-06 1.02631895e-09-5.92826294
    e-14 2
 1.96732787e+03-3.61584884e+01 6.99964596e-01 3.92240205e-02-1.72461161
    e-05 3
 2.25782255e-09 1.90185691e-13 6.40409253e+03 2.50785516e+01 4
! Refitting species SC4H9O2:
! max difference Cp/R = 5.0659e-02 at T = 1233.4167 K
! max difference H/RT = 8.6614e-03 at T = 1376.8384 K
! max difference S/R = 1.4253e-02 at T = 1390.9455 K
! T_match = 1389.000000 jump
! Delta(Cp/R, H/RT, S/R) = ( 7.105e-15, 0.000e+00, 0.000e+00)
SC4H9O2 7/19/ 0 THERMC 4H 9O 2 0G 300.0000 5000.0000 1389.00 1
 1.64031135e+01 2.09361006e-02-7.23393011e-06 1.13058996e-09-6.58938667
    e-14 2
-1.84954757e+04-5.77189110e+01 8.26041457e-01 5.96800629e-02-4.77954648
   e-05 3
 2.25404204e-08-4.72881872e-12-1.31027118e+04 2.55291129e+01 4
! Refitting species C4H8OOH1-3:
! max difference Cp/R = 2.9372e-02 at T = 1224.0120 K
! max difference H/RT = 5.0100e-03 at T = 1365.0825 K
! max difference S/R = 8.2153e-03 at T = 1376.8384 K
! T_match = 1377.000000 jump
! Delta(Cp/R, H/RT, S/R) = (-1.421e-14, 3.553e-15, 0.000e+00)
C4H8OOH1-3 7/19/ 0 THERMC 4H 9O 2 0G 300.0000 5000.0000 1377.00 1
 1.76442170e+01 1.91706536e-02-6.57168641e-06 1.02246571e-09-5.94304735
    e-14 2
```

```
-1.01790603e+04-6.17033662e+01 1.64413741e+00 5.39024467e-02-3.55996859
   e-05 3
 1.27441434e-08-2.11480877e-12-4.31181437e+03 2.52803257e+01 4
! Refitting species NC4KET13:
! max difference Cp/R = 5.1055e-02 at T = 1231.0655 K
! max difference H/RT = 8.7262e-03 at T = 1374.4872 K
! max difference S/R = 1.4343e-02 at T = 1386.2431 K
! T_match = 1386.000000 jump
! Delta(Cp/R, H/RT, S/R) = (-7.105e-15, 1.776e-15, 0.000e+00)
NC4KET13 7/19/ 0 THERMC 4H 8O 3 0G 300.0000 5000.0000 1386.00 1
 1.96430808e+01 1.80940566e-02-6.33063232e-06 9.97860399e-10-5.85076458
    e-14 2
-4.59468437e+04-7.16761660e+01 2.24169630e+00 6.21407492e-02-5.26959462
   e-05 3
 2.52587220e-08-5.25447829e-12-4.00529581e+04 2.09556655e+01 4
! Refitting species H2NO:
! max difference Cp/R = 1.9886e-06 at T = 1499.3997 K
! max difference H/RT = 4.7413e-07 at T = 1501.2506 K
! max difference S/R = 8.3926e-06 at T = 1501.2506 K
! T_match = 1500.000000 jump
! Delta(Cp/R, H/RT, S/R) = ( 1.776e-15, 0.000e+00, 0.000e+00)
H2NO 102290H 2N 1O 1 G 300.0000 4000.0000 1500.00 1
 5.67334600e+00 2.29883700e-03-1.77444600e-07-1.10348200e-10 1.85976200
    e-14 2
 5.56932571e+03-6.15353161e+00 2.53059296e+00 8.59601653e-03-5.47099406
    e-06 3
 2.27622271e-09-4.64801256e-13 6.86802967e+03 1.12664973e+01 4
OHs RUS 78O 1H 1 G 200.000 6000.000 1000.000 1
```

```
 2.75582920E+00 1.39848756E-03-4.19428493E-07 6.33453282E-11-3.56042218
    E-15 2
 5.09751756E+04 5.62581429E+00 3.46084428E+00 5.01872172E-04-2.00254474
    E-06 3
 3.18901984E-09-1.35451838E-12 5.07349466E+04 1.73976415E+00
    4!!!!!!!!!!From Prager_plus_Walsh
CHs C 1H 1 G 200.000 6000.000 1000.000 1
 2.78220752E+00 1.47246754E-03-4.63436227E-07 7.32736021E-11-4.19705404
    E-15 2
 1.04547060E+05 5.17421018E+00 3.47250101E+00 4.26443626E-04-1.95181794
    E-06 3
 3.51755043E-09-1.60436174E-12 1.04334869E+05 1.44799533E+00
    4!!!!!!!!!!!From Prager_plus_Walsh
!E electron gas g12/98E 1. 0. 0. 0.G 298.150 6000.000 1000. 1
! 2.50000000E+00 0.00000000E+00 0.00000000E+00 0.00000000E+00
   0.00000000E+00 2
!-7.45375000E+02-1.17208122E+01 2.50000000E+00 0.00000000E+00
   0.00000000E+00 3
! 0.00000000E+00 0.00000000E+00-7.45375000E+02-1.17208122E+01
   0.00000000E+00 4
E g12/98E 1. 0. 0. 0.G 298.150 6000.000 1000. 1!!!!!!!!!!!From Prager
 2.50000000E+00 0.00000000E+00 0.00000000E+00 0.00000000E+00 0.00000000
    E+00 2
-7.45375000E+02-1.17208122E+01 2.50000000E+00 0.00000000E+00 0.00000000
   E+00 3
 0.00000000E+00 0.00000000E+00-7.45375000E+02-1.17208122E+01 0.00000000
    E+00 4
H3Op ATcT AH 3.O 1.E -1. 0.G 298.150 6000.000 1000. 1
```

```
 2.49647765E+00 5.72844840E-03-1.83953239E-06 2.73577348E-10-1.54093917
    E-14 2
 7.16244227E+04 7.45850493E+00 3.79295251E+00-9.10852723E-04 1.16363521
    E-05 3
-1.21364865E-08 4.26159624E-12 7.14027518E+04 1.47156927E+00 7.25739701
   E+04 4
HCOp ATcT/AH 1.C 1.O 1.E -1.G 298.150 6000.000 1000. 1
 3.60741725E+00 3.39655575E-03-1.20330954E-06 1.92326752E-10-1.14294843
    E-14 2
 9.89901570E+04 2.55193114E+00 2.09628893E+00 9.63027792E-03-1.21901677
    E-05 3
 9.41014765E-09-2.96498603E-12 9.93329664E+04 9.91592486E+00 1.00295507
    E+05 4
C2H3Op Acetylium TT8/11C 2.H 3.O 1.E -1.G 200.000 6000.000 1000. 1
 5.38190942E+00 9.45572763E-03-3.39695691E-06 5.48225731E-10-3.28062322
    E-14 2
 7.81855758E+04-4.94235171E+00 3.31517723E+00 6.97633081E-03 1.75092244
    E-05 3
-2.69576366E-08 1.11130038E-11 7.91705828E+04 7.74260291E+00 8.00759206
   E+04 4
CH5Op OH2CH3+ T 8/11C 1.H 5.O 1.E -1.G 298.150 6000.000 1000. 1
 4.12018251E+00 1.23179143E-02-4.21315216E-06 6.57462537E-10-3.84191498
    E-14 2
 6.73969035E+04 1.71193370E+00 2.63252920E+00 9.23812483E-03 1.43800480
    E-05 3
-2.22087922E-08 8.80207817E-12 6.81751824E+04 1.11834286E+01 6.94579899
   E+04 4
O2n L 4/89O 2E 1 0 0G 298.150 6000.000 1000. 1
```

```
 3.95666294E+00 5.98141823E-04-2.12133905E-07 3.63267581E-11-2.24989228
    E-15 2
-7.06287229E+03 2.27871017E+00 3.66442522E+00-9.28741138E-04 6.45477082
   E-06 3
-7.74703380E-09 2.93332662E-12-6.87076983E+03 4.35140681E+00-5.77639825
   E+03 4
On g 1/97O 1.E 1. 0. 0.G 298.150 6000.000 1000. 1
 2.54474869E+00-4.66695513E-05 1.84912357E-08-3.18159223E-12 1.98962956
    E-16 2
 1.15042089E+04 4.52131015E+00 2.90805921E+00-1.69804907E-03 2.98069955
    E-06 3
-2.43835127E-09 7.61229311E-13 1.14357717E+04 2.80339097E+00 1.22492116
   E+04 4
OHn g 4/02O 1.H 1.E 1. 0.G 298.150 6000.000 1000. 1
 2.80023747E+00 1.13380509E-03-2.99666184E-07 4.01911483E-11-1.78988913
    E-15 2
-1.82535298E+04 4.69394620E+00 3.43126659E+00 6.31146866E-04-1.92914359
   E-06 3
 2.40618712E-09-8.66679361E-13-1.85085918E+04 1.07990541E+00-1.74702052
    E+04 4
CHO2n Formyloxy T01/07C 1.H 1.O 2.E 1.G 298.150 6000.000 1000. 1
 4.64053354E+00 5.14243825E-03-1.93660556E-06 3.22416463E-10-1.97122674
    E-14 2
-5.87433109E+04 6.51021976E-01 3.48845650E+00-2.91890924E-04 2.01968637
   E-05 3
-2.37910014E-08 8.54664245E-12-5.79368089E+04 8.87310001E+00-5.67742417
   E+04 4
CHO3n gas T 1/12C 1.O 3.H 1.E 1.G 298.150 6000.000 1000. 1
```

```
 7.36645507E+00 5.00158276E-03-1.80067797E-06 2.91606176E-10-1.75097599
    E-14 2
-9.15702268E+04-1.23983776E+01 6.36697228E-01 2.65848228E-02-2.84827025
   E-05 3
 1.53637834E-08-3.26114474E-12-8.98573981E+04 2.16337645E+01-8.87087754
    E+04 4
CO3n gas T 1/12C 1.O 3.E 1. 0.G 298.150 6000.000 1000. 1
 7.34758057E+00 2.68967066E-03-1.04696388E-06 1.78029877E-10-1.10418552
    E-14 2
-7.25571192E+04-1.06758104E+01 2.89974919E+00 1.29850653E-02-6.35950012
   E-06 3
-2.85213660E-09 2.48409760E-12-7.12276260E+04 1.27958644E+01-6.98465694
   E+04 4
CH2 IU3-03H 2C 1 G 200.0 6000.0 1000.0 1
  3.14631886E0 3.03671259E-3 -9.96474439E-7 1.5048358E-10-8.57335515E
     -15 2
  4.60412605E4 4.72341711E0 3.71757846E0 1.2739126E-3 2.17347251E-6 3
  -3.488585E-9 1.65208866E-12 4.58723866E4 1.75297945E0 4
C L-7-88C 1 G 200.0 6000.0 1000.0 1
    2.605583E0 -1.9593434E-4 1.0673722E-7 -1.642394E-11 8.187058E-16 2
   8.5411742E4 4.1923868E0 2.5542395E0 -3.2153772E-4 7.3379223E-7 3
 -7.3223487E-10 2.6652144E-13 8.5442681E4 4.5313085E0 4
END
```

Appendix E

Repaired thermodynamic coefficients evaluation

Comparisons between the repaired/non-repaired thermodynamic coefficients (NASA polynomial) are shown here to prove that the species outcome is not affected by that change. It is important to consider that three PSR temperatures are set – 1500K, 2000K, and 2500K – in order to see how the reduced model reproduces the behavior of the detailed model at different temperature regimes.

Figure E.1 shows the plots obtained from the Mech Checker tool [91] employing the reduced chemistry developed in this work (Model 1). These plots only show the species that were affected by the refit of their NASA thermodynamic coefficients. The wording *original* corresponds to outcome obtained employing the *non-repaired* thermodynamic coefficients.

Since only two species were changed by the thermodynamic parameters re-fitting process – and because N_2 is inert and C_2H_4OOH is not a major specie in the flame – it is already expected that changing the NASA thermodynamic parameters for these two species to their corresponding *repaired* parameters will not affect any of the species profiles while overcoming potential time delays due to data discontinuity.

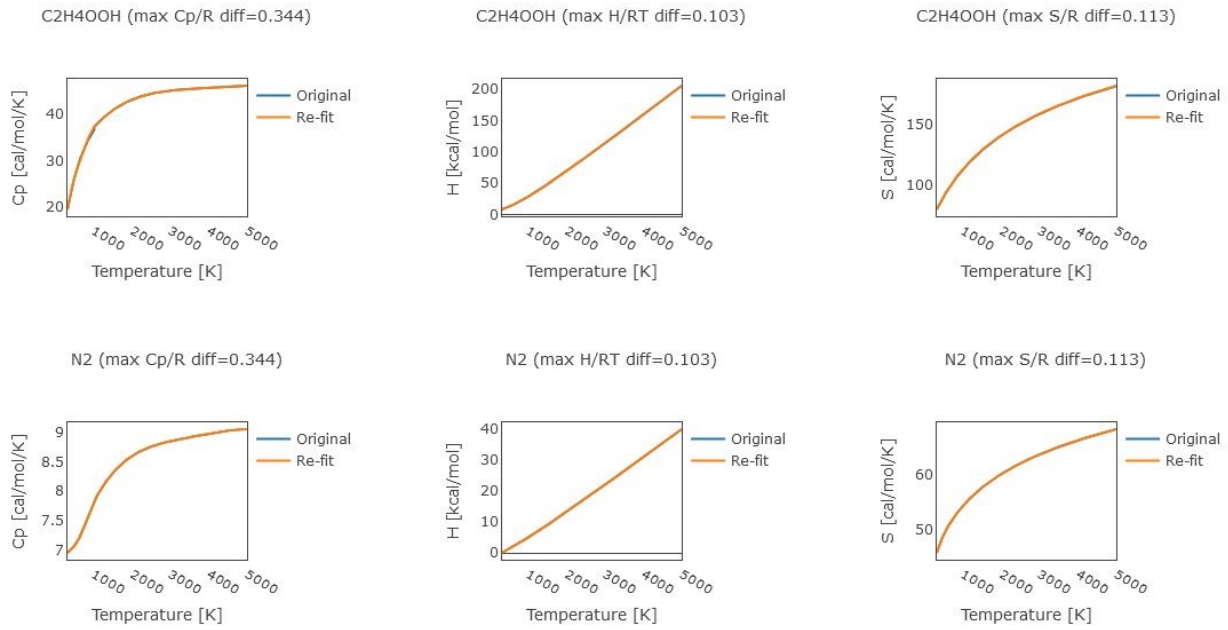

Figure E.1: Outcome comparison employing original and refitting NASA thermodynamic coefficients for C_2H_4OOH and N_2.

Figures E.2, E.3, and E.4 are shown to illustrate that the repaired thermodynamic parameters do not affect either detailed or reduced model outcomes. Figure E.2 shows the major species results for 2500K, but similar overlapping outcomes were obtained at 1500K and 2000K. Figures E.3 and E.4 correspond to the CH and OH species mole fraction, which are precursors of CH^* and OH^*, respectively.

For all the species, the results from using the repaired thermodynamic coefficients are perfectly overlapping the ones obtained with the non-repaired thermodynamic coefficients, for either detailed or reduced models.

From these results, the repaired thermodynamic coefficients are chosen to be used in further simulations, avoiding future potential discontinuities while obtaining the same converged results.

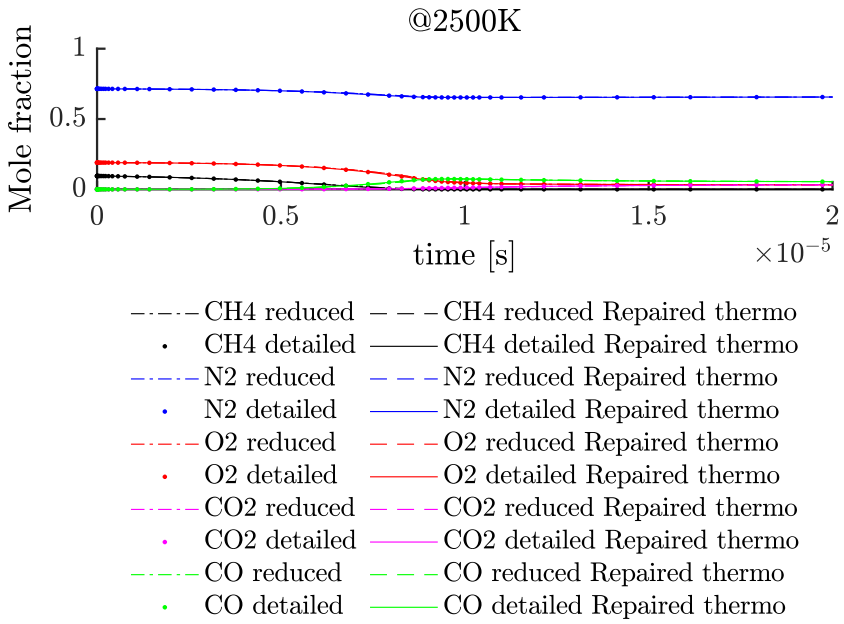

Figure E.2: PSR configuration. Major species comparison between detailed and reduced chemical kinetic models employing repaired/non-repaired thermodynamic coefficients at 2500K.

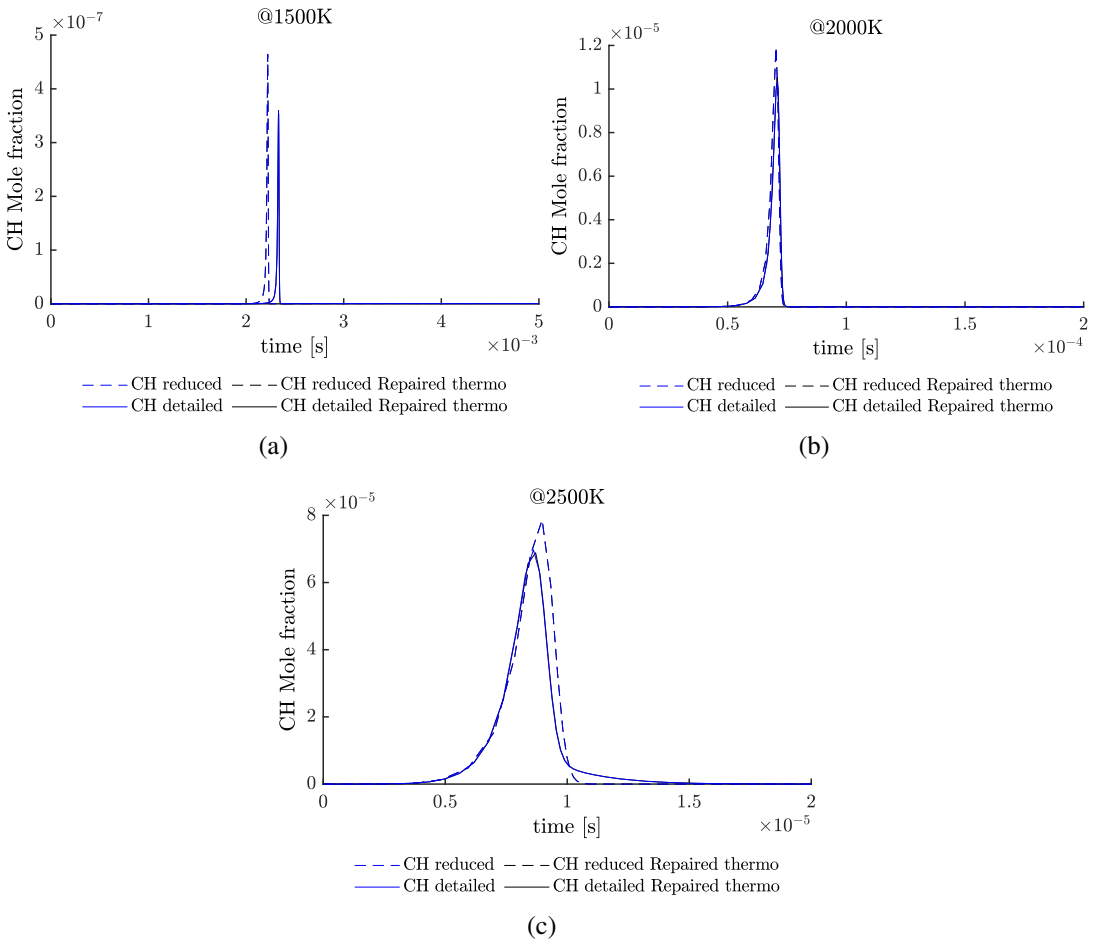

Figure E.3: PSR configuration. CH specie comparison between detailed and reduced chemical kinetic models employing repaired/non-repaired thermodynamic coefficients.

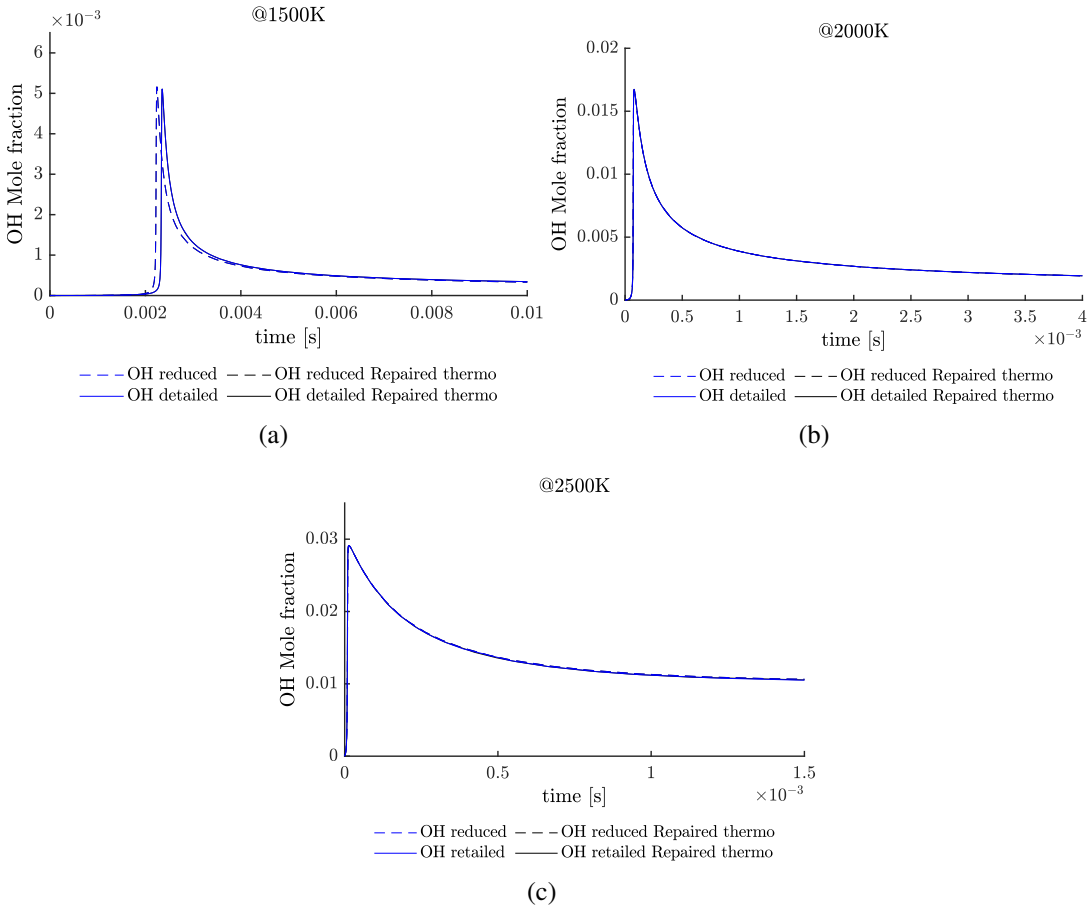

Figure E.4: PSR configuration. OH specie comparison between detailed and reduced chemical kinetic models employing repaired/non-repaired thermodynamic coefficients.

Appendix F

Transport coefficients

The transport coefficients in Chemkin format for the species considered in the chemical kinetic models 0 and 1 are shown next.

Listing F.1: Transport coefficients in Chemkin format for Model 0 and 1.

```
CHCHO 2 436.000 3.970 0.000 0.000 2.000
AR 0 136.500 3.330 0.000 0.000 0.000
RR 0 136.500 3.330 0.000 0.000 0.000
AS 0 1045.500 4.580 0.000 0.000 0.000 ! MEC
ASH 1 199.300 4.215 0.000 0.000 1.000 ! MEC
ASH2 2 229.600 4.180 0.000 0.000 1.000 ! MEC
C 0 71.400 3.298 0.000 0.000 0.000 ! *
C2 1 97.530 3.621 0.000 1.760 4.000
C2O 1 232.400 3.828 0.000 0.000 1.000 ! *
CN2 1 232.400 3.828 0.000 0.000 1.000 ! OIS
C2H 1 265.300 3.721 0.000 0.000 2.500 ! NMM
C2H2 1 265.300 3.721 0.000 0.000 2.500 ! NMM
C2H2OH 2 224.700 4.162 0.000 0.000 1.000 ! *
```

```
C2H3 2 265.300 3.721 0.000 0.000 1.000 ! NMM
C2H4 2 238.400 3.496 0.000 0.000 1.500 ! NMM
C2H5 2 247.500 4.350 0.000 0.000 1.500 ! NMM
HOCH2O 2 470.600 4.410 0.000 0.000 1.500 ! WJP
O2C2H4O2H 2 470.600 4.410 0.000 0.000 1.500 ! WJP
C2H5O2 2 470.600 4.410 0.000 0.000 1.500 ! WJP
C2H5O2H 2 470.600 4.410 0.000 0.000 1.500 ! WJP
C2H5O 2 470.600 4.410 0.000 0.000 1.500 ! NMM
PC2H4OH 2 470.600 4.410 0.000 0.000 1.500 ! NMM
SC2H4OH 2 470.600 4.410 0.000 0.000 1.500 ! NMM
O2C2H4OH 2 523.2 5.664 1.7 0.0 1.0 ! WJP
C2H4O 2 436.000 3.970 0.000 0.000 2.000 !=CH3HCO konnov
C2H4O1,2 2 387.3 4.349 0.000 0.000 1.500 ! WJP
C2H6 2 247.500 4.350 0.000 0.000 1.500 ! NMM
C2N 1 232.400 3.828 0.000 0.000 1.000 ! OIS
C2N2 1 349.000 4.361 0.000 0.000 1.000 ! OIS
C3H2 2 209.000 4.100 0.000 0.000 1.000 ! *
C3H2(S) 2 209.000 4.100 0.000 0.000 1.000 ! *
C3H3 1 324.800 4.290 0.000 0.000 1.000 ! NMM
C4H3 1 357.000 4.720 0.000 0.000 1.000 ! NMM
C3H4O 2 443.200 4.120 0.000 0.000 1.000 ! NMM
CHCHCHO 2 443.200 4.120 0.000 0.000 1.000 ! NMM
HCCCHO 2 443.200 4.120 0.000 0.000 1.000 ! NMM
HCCCO 2 443.200 4.120 0.000 0.000 1.000 ! NMM
H2CCHCO 2 443.200 4.120 0.000 0.000 1.000 ! NMM
CH3CCO 2 443.200 4.120 0.000 0.000 1.000 ! NMM
CH3CHCO 2 443.200 4.120 0.000 0.000 1.000 ! NMM
CH2CHCO 2 443.200 4.120 0.000 0.000 1.000 ! NMM
C2H3CO 2 443.200 4.120 0.000 0.000 1.000 ! NMM
```

```
!C2H5CHO 2 424.600 4.820 0.000 0.000 1.000 ! NMM
CH2CH2CHO 2 424.600 4.820 0.000 0.000 1.000 ! NMM
C2H5CO 2 424.600 4.820 0.000 0.000 1.000 ! NMM
CH3COCH3 2 435.500 4.860 0.000 0.000 1.000 ! NMM
CH3COCH2 2 435.500 4.860 0.000 0.000 1.000 ! NMM
C3H4 1 324.800 4.290 0.000 0.000 1.000 ! NMM
AC3H4 1 324.800 4.290 0.000 0.000 1.000 ! NMM
C3H4-A 1 324.800 4.290 0.000 0.000 1.000 ! NMM
PC3H4 1 324.800 4.290 0.000 0.000 1.000 ! NMM
C3H4-P 1 324.800 4.290 0.000 0.000 1.000 ! NMM
C3H4C 2 324.800 4.290 0.000 0.000 1.000 ! NMM
C3H6 2 307.800 4.140 0.000 0.000 1.000 ! NMM
C3H6OH 2 487.900 4.820 0.000 0.000 1.000 ! NMM
HOC3H6O2 2 487.900 4.820 0.000 0.000 1.000 ! NMM
!C3H6O 2 411.000 4.820 0.000 0.000 1.000 ! NMM
C3H5O 2 411.000 4.820 0.000 0.000 1.000 ! NMM
C3H7 2 303.400 4.810 0.000 0.000 1.000 ! NMM
C4H6 2 357.000 4.720 0.000 0.000 1.000 ! NMM
I-C3H7 2 303.400 4.810 0.000 0.000 1.000 ! NMM
N-C3H7 2 303.400 4.810 0.000 0.000 1.000 ! NMM
NC3H7 2 303.400 4.810 0.000 0.000 1.000 ! NMM
!IC3H7O 2 468.300 4.760 0.000 0.000 1.000 ! NMM
!NC3H7O 2 487.900 4.820 0.000 0.000 1.000 ! NMM
C3H8 2 303.400 4.810 0.000 0.000 1.000 ! NMM
C4H 1 357.000 4.720 0.000 0.000 1.000 ! NMM
C4H2 1 357.000 4.720 0.000 0.000 1.000 ! NMM
C4H2OH 2 224.700 4.162 0.000 0.000 1.000 ! *
CH3CHCCH 2 355.000 4.650 0.000 0.000 1.000 ! NMM
IC4H7 2 355.000 4.650 0.000 0.000 1.000 ! NMM
```

```
C4H7 2 355.000 4.650 0.000 0.000 1.000 ! NMM
C4H71-4 2 355.000 4.650 0.000 0.000 1.000 ! C4H8 WJP
C4H8 2 355.000 4.650 0.000 0.000 1.000 ! NMM
C4H8-1 2 355.000 4.650 0.000 0.000 1.000 ! NMM
C4H8-2 2 355.000 4.650 0.000 0.000 1.000 ! NMM
!IC4H8 2 355.000 4.650 0.000 0.000 1.000 ! NMM
PC4H9 2 352.000 5.240 0.000 0.000 1.000 ! NMM
C4H9 2 352.000 5.240 0.000 0.000 1.000 ! NMM
SC4H9 2 352.000 5.240 0.000 0.000 1.000 ! NMM
TC4H9 2 352.000 5.240 0.000 0.000 1.000 ! NMM
IC4H9 2 352.000 5.240 0.000 0.000 1.000 ! NMM
PC4H9O 2 496.000 5.200 0.000 0.000 1.000 ! NMM
TC4H9O 2 496.000 5.200 0.000 0.000 1.000 ! NMM
SC4H9O 2 496.000 5.200 0.000 0.000 1.000 ! NMM
IC4H9O 2 496.000 5.200 0.000 0.000 1.000 ! NMM
PC4H9O2 2 496.000 5.200 0.000 0.000 1.000 ! WJP
SC4H9O2 2 496.000 5.200 0.000 0.000 1.000 ! WJP
PC4H9O2H 2 496.000 5.200 0.000 0.000 1.000 ! WJP
SC4H9O2H 2 496.000 5.200 0.000 0.000 1.000 ! WJP
IC4H8OH 2 496.000 5.200 0.000 0.000 1.000 ! NMM
C4H8OH-1 2 496.000 5.200 0.000 0.000 1.000 ! WJP
C4H8OH-2 2 496.000 5.200 0.000 0.000 1.000 ! WJP
C4H8O1-2 2 496.000 5.200 0.000 0.000 1.000 ! WJP
C4H8O1-3 2 496.000 5.200 0.000 0.000 1.000 ! WJP
C4H8O1-4 2 496.000 5.200 0.000 0.000 1.000 ! WJP
C4H8O2-3 2 496.000 5.200 0.000 0.000 1.000 ! WJP
!IC4H7OH 2 496.000 5.200 0.000 0.000 1.000 ! NMM
O2C4H8OH-1 2 496.000 5.200 0.000 0.000 1.000 ! WJP
O2C4H8OH-2 2 496.000 5.200 0.000 0.000 1.000 ! WJP
```

```
C4H8OOH1-2 2 496.000 5.200 0.000 0.000 1.000 ! WJP
C4H8OOH1-3 2 496.000 5.200 0.000 0.000 1.000 ! WJP
C4H8OOH1-4 2 496.000 5.200 0.000 0.000 1.000 ! WJP
C4H8OOH2-1 2 496.000 5.200 0.000 0.000 1.000 ! WJP
C4H8OOH2-3 2 496.000 5.200 0.000 0.000 1.000 ! WJP
C4H8OOH2-4 2 496.000 5.200 0.000 0.000 1.000 ! WJP
C4H8OOH1-2O2 2 496.000 5.200 0.000 0.000 1.000 ! WJP
C4H8OOH1-3O2 2 496.000 5.200 0.000 0.000 1.000 ! WJP
C4H8OOH1-4O2 2 496.000 5.200 0.000 0.000 1.000 ! WJP
C4H8OOH2-1O2 2 496.000 5.200 0.000 0.000 1.000 ! WJP
C4H8OOH2-3O2 2 496.000 5.200 0.000 0.000 1.000 ! WJP
C4H8OOH2-4O2 2 496.000 5.200 0.000 0.000 1.000 ! WJP
IO2C4H8OH 2 496.000 5.200 0.000 0.000 1.000 ! *
C4H7O 2 496.000 5.200 0.000 0.000 1.000 ! NMM
IC4H7O 2 496.000 5.200 0.000 0.000 1.000 ! NMM
!C4H10 2 352.000 5.240 0.000 0.000 1.000 ! NMM
!IC4H10 2 352.000 5.240 0.000 0.000 1.000 ! NMM
C5H2 1 408.000 5.200 0.000 0.000 1.000 ! NMM
C5H3 1 408.000 5.200 0.000 0.000 1.000 ! NMM
C5H5 1 408.000 5.200 0.000 0.000 1.000 ! NMM
C5H6 1 408.000 5.200 0.000 0.000 1.000 ! NMM
C5H7 2 408.000 5.200 0.000 0.000 1.000 ! NMM
CYC5H7 2 408.000 5.200 0.000 0.000 1.000 !
C5H8 2 408.000 5.200 0.000 0.000 1.000 ! NMM
C6H2 1 408.000 5.200 0.000 0.000 1.000 ! NMM
C6H4 2 412.300 5.349 0.000 0.000 1.000 ! JAM
C6H5 2 412.300 5.349 0.000 0.000 1.000 ! JAM
C6H5(L) 2 412.300 5.349 0.000 0.000 1.000 ! JAM
C6H5OH 2 450.000 5.500 0.000 0.000 1.000 ! NMM
```

```
C6H5O 2 450.000 5.500 0.000 0.000 1.000 ! JAM
OKETPHNL 2 450.000 5.500 0.000 0.000 1.000 !
C6H4O2 2 450.000 5.500 0.000 0.000 1.000
C5H4O 2 450.000 5.500 0.000 0.000 1.000 ! NMM
C5H4OH 2 450.000 5.500 0.000 0.000 1.000 ! NMM
C5H5O 2 450.000 5.500 0.000 0.000 1.000 ! NMM
C5H5OH 2 450.000 5.500 0.000 0.000 1.000 ! NMM
LC6H5 2 426.300 5.510 0.000 0.000 1.000
LC3H3C3H2 2 426.300 5.510 0.000 0.000 1.000
LC3H4C3H2 2 426.300 5.510 0.000 0.000 1.000
LC3H3C3H3 2 426.300 5.510 0.000 0.000 1.000
C6H6 2 468.500 5.230 0.000 10.30 1.000 ! NMM
C6H7 2 468.500 5.230 0.000 0.000 1.000 ! NMM
CYC6H7 2 468.500 5.230 0.000 0.000 1.000 ! NMM
CYC6H8 2 468.500 5.230 0.000 0.000 1.000 ! NMM
C6H5CH2 2 495.300 5.680 0.000 0.000 1.000 ! NMM
C6H5CH3 2 495.300 5.680 0.430 12.30 1.000 ! NMM
C6H4CH3 2 495.300 5.680 0.000 0.000 1.000 ! NMM
CH3C6H4 2 495.300 5.680 0.000 0.000 1.000 ! NMM
C6H5CO 2 622.400 5.530 0.000 0.000 1.000 ! NMM
C6H5CHO 2 622.400 5.530 0.000 0.000 1.000 ! NMM
C6H5CH2OH 2 622.400 5.530 0.000 0.000 1.000 ! NMM
OC6H4CH3 2 621.100 5.640 0.000 0.000 1.000 ! NMM
HOC6H4CH3 2 621.100 5.640 0.000 0.000 1.000 ! NMM
XYLYLENE 2 523.600 6.182 0.000 0.000 1.000
XYLYLRAD 2 523.600 6.182 0.000 0.000 1.000
C6H5C2H5 2 523.600 5.960 0.000 0.000 1.000 ! NMM
ACH3C2H3 2 523.600 5.960 0.000 0.000 1.000
ACH3C2H5 2 523.600 5.960 0.000 0.000 1.000
```

```
ACH2RC2H3 2 523.600 5.960 0.000 0.000 1.000
ACH3CH3 2 523.600 5.960 0.000 0.000 1.000 !
ACH3RCH2 2 523.600 5.960 0.000 0.000 1.000
C6H9 2 426.300 5.510 0.000 0.000 1.000 ! NMM
C6H10 2 426.300 5.510 0.000 0.000 1.000 ! NMM
C8H14 2 494.000 6.170 0.000 0.000 1.000 ! NMM
C8H16-C 2 538.1 6.112 0.0 0.0 1.0 ! TCPC
C8H16-1-5 2 511.5 6.297 0.0 0.0 1.0 ! TCPC
!IC8H14 2 494.000 6.170 0.000 0.000 1.000 ! NMM
C6H5C2H3 2 546.200 6.000 0.130 15.00 1.000 ! NMM
C6H5CHCH 2 546.200 6.000 0.000 0.000 1.000 ! NMM
C6H5CCH2 2 546.200 6.000 0.000 0.000 1.000
C6H5C2H 2 534.300 5.710 0.770 0.000 1.000 ! NMM
C6H5C2 2 534.300 5.710 0.000 0.000 1.000 ! NMM
C6H4C2H3 2 546.200 6.000 0.000 0.000 1.000 ! NMM
C6H4C2H 2 534.300 5.710 0.000 0.000 1.000 ! NMM
AAC2H5 2 695.000 6.530 0.000 0.000 1.000
AAC2H3 2 689.800 6.500 0.000 0.000 1.000
AARCCH2 2 689.800 6.500 0.000 0.000 1.000
AACCH 2 689.800 6.500 0.000 0.000 1.000
ARACCH 2 689.800 6.500 0.000 0.000 1.000
ARAC2H3 2 687.200 6.490 0.000 0.000 1.000
C6H5CCO 2 588.200 5.940 0.000 0.000 1.0001
C10H7 2 630.400 6.180 0.000 0.000 1.000 ! NMM
C10H7O 2 630.400 6.180 0.000 0.000 1.000 ! NMM
AC2H3C2H5 2 630.400 6.180 0.000 0.000 1.000
AC2H3C2H3 2 630.400 6.180 0.000 0.000 1.000
C10H8 2 630.400 6.180 0.000 16.50 1.000 ! NMM
C10H9 2 630.400 6.180 0.000 0.000 1.000 ! NMM
```

```
C10H10 2 630.400 6.180 0.000 0.000 1.000 ! NMM
C10H7CH2 2 660.00 6.350 0.000 0.000 1.000 ! NMM
AACH3CH2 2 660.0 6.350 0.000 0.000 1.000
C10H7OH 2 663.45 6.362 0.000 0.000 1.000
C10H7CH3 2 660.0 6.350 0.000 0.000 1.000 ! NMM
FLRNTHN 2 812.3 7.170 0.000 0.000 1.000 ! NMM
ACEPHEN 2 812.3 7.170 0.000 0.000 1.000
ANTHRACN 2 772.0 6.960 0.000 25.40 1.000 ! NMM
CH3INDENE 2 625.0 6.150 0.000 0.000 1.000
CH3INDENYL 2 625.0 6.150 0.000 0.000 1.000
AAACH3 2 783.9 6.995 0.000 0.000 1.000
P1HENANOL 2 783.9 6.995 0.000 0.000 1.000
P5HENANOL 2 783.9 6.995 0.000 0.000 1.000
P1HANOXY 2 783.9 6.995 0.000 0.000 1.000
P5HANOXY 2 783.9 6.995 0.000 0.000 1.000
AAARCH2 2 783.9 6.995 0.000 0.000 1.000
AAAC2H5 2 816.6 7.160 0.000 0.000 1.000
AAAC2H3 2 812.0 7.137 0.000 0.000 1.000
PHNTHRN 2 772.0 6.960 0.000 38.80 1.000
PENTANAPH 2 772.0 6.960 0.000 0.000 1.000
PENAPRAD 2 772.0 6.960 0.000 0.000 1.000
P1HNTHRNYL 2 772.0 6.960 0.000 38.80 1.000 ! NMM
P5HNTHRNYL 2 772.0 6.960 0.000 38.80 1.000
PYRENE 2 834.9 7.240 0.000 0.000 1.000 ! NMM
CY5PYREN 2 862.0 7.382 0.000 0.000 1.000
H4PENTDEF 2 834.9 7.240 0.000 0.000 1.000
H4PDFRAD 2 834.9 7.240 0.000 0.000 1.000
PYRENYL 2 834.9 7.240 0.000 0.000 1.000 ! NMM
DHPYRENE 2 834.9 7.240 0.000 0.000 1.000
```

```
BENZOAP 2 832.5 7.550 1.400 0.000 1.000 ! NMM
SMILEY 2 832.5 7.550 0.000 0.000 1.000
BENZOGHI 2 832.5 7.550 0.000 0.000 1.000
CPENTACD 2 832.5 7.550 0.000 0.000 1.000
ACEC10H8 2 695.4 6.760 0.000 0.000 1.000 ! NMM
ACEC10H7 2 695.4 6.760 0.000 0.000 1.000
INDENE 2 588.6 5.960 0.650 0.000 1.000 ! NMM
INDENYL 2 588.6 5.960 0.000 0.000 1.000 ! NMM
CH3NDENE 2 588.6 5.960 0.000 0.000 1.000 ! NMM
CH3NDNYL 2 588.6 5.960 0.000 0.000 1.000 ! NMM
CH3FLRNE 2 712.6 6.890 0.000 0.000 1.000
CH3FLRNL 2 712.6 6.890 0.000 0.000 1.000
FLRENE 2 712.6 6.890 0.000 0.000 1.000
FLRNYLP 2 712.6 6.890 0.000 0.000 1.000
FLRNYLA 2 712.6 6.890 0.000 0.000 1.000
CH2FLRNE 2 712.6 6.890 0.000 0.000 1.000
C6H5C5H5 2 783.800 6.640 0.000 0.000 1.000
C6H5C5H4 2 783.800 6.640 0.000 0.000 1.000
BIBENZYL 2 783.800 6.640 0.000 0.000 1.000 ! NMM
STILBENE 2 772.0 6.960 0.000 0.000 1.000 ! NMM
STILBNRD 2 772.0 6.960 0.000 0.000 1.000 ! NMM
DHANTHRN 2 772.0 6.960 0.000 0.000 1.000
OBZYLTOL 2 772.0 6.960 0.000 0.000 1.000
OBZYLTLR 2 772.0 6.960 0.000 0.000 1.000
DMDP 2 712.6 6.890 0.000 0.000 1.000
DMDPRD 2 712.6 6.890 0.000 0.000 1.000
CH 1 80.000 2.750 0.000 0.000 0.000
CH2 1 144.000 3.800 0.000 0.000 0.000
T-CH2 1 144.000 3.800 0.000 0.000 0.000
```

```
SCH2 1 144.000 3.800 0.000 0.000 0.000
S-CH2 1 144.000 3.800 0.000 0.000 0.000
CH2CHCCH 2 373.700 4.790 0.000 0.000 1.000 ! NMM
CH2CHCCH2 2 373.700 4.790 0.000 0.000 1.000 ! NMM
CH3CHCCH2 2 357.100 4.720 0.000 0.000 1.000
CH2CH2CCH 2 373.700 4.790 0.000 0.000 1.000 ! NMM
CH2CHCH2 2 316.000 4.220 0.000 0.000 1.000 ! NMM
C3H5 2 316.000 4.220 0.000 0.000 1.000
AC3H5 2 316.000 4.220 0.000 0.000 1.000
C3H5-A 2 316.000 4.220 0.000 0.000 1.000
CH2CHCHCH 2 357.100 4.720 0.000 0.000 1.000 ! NMM
CHCHCHCH 2 357.100 4.720 0.000 0.000 1.000 ! NMM
CH2CHCHCH2 2 357.100 4.720 0.000 0.000 1.000 ! NMM
CH2CO 2 436.000 3.970 0.000 0.000 2.000
C2H3O1,2 2 436.000 3.970 0.000 0.000 2.000 ! WJP
CH2O 2 498.000 3.590 0.000 0.000 2.000
OCHO 2 498.000 3.590 0.000 0.000 2.000 ! WJP
HCOH 2 498.000 3.590 0.000 0.000 1.000
H2CO 2 498.000 3.590 0.000 0.000 2.000
CH2OH 2 417.000 3.690 1.700 0.000 2.000
CH2HCO 2 436.000 3.970 0.000 0.000 2.000
CH2CHO 2 436.000 3.970 0.000 0.000 2.000
CHOCHO 1 440.200 4.010 0.000 0.000 2.000 ! NMM
CHOCO 1 440.200 4.010 0.000 0.000 2.000 ! NMM
HCO2H 2 481.800 3.626 1.7 0.000 1.000 ! CH3OH
CH3 1 144.000 3.800 0.000 0.000 0.000
CH3CC 2 252.000 4.760 0.000 0.000 1.000 ! JAM
!CH3CHCCH 2 373.700 4.790 0.000 0.000 1.000 ! NMM
CH3CCCH2 2 357.100 4.720 0.000 0.000 1.000 ! NMM
```

```
CH3CCCH3 2 357.100 4.720 0.000 0.000 1.000 ! NMM
CH3CCH2 2 316.000 4.220 0.000 0.000 1.000 ! NMM
TC3H5 2 316.000 4.220 0.000 0.000 1.000
C3H5-T 2 316.000 4.220 0.000 0.000 1.000
CH3CHCH 2 316.000 4.220 0.000 0.000 1.000 ! NMM
SC3H5 2 316.000 4.220 0.000 0.000 1.000
C3H5-S 2 316.000 4.220 0.000 0.000 1.000
CH3CH2CCH 2 357.100 4.720 0.000 0.000 1.000 ! NMM
CH3HCO 2 436.000 3.970 0.000 0.000 2.000
CH3CHO 2 436.000 3.970 0.000 0.000 2.000
HOCHO 2 436.000 3.970 0.000 0.000 2.000 ! WJP
CH3CO 2 436.000 3.970 0.000 0.000 2.000
CH3CO2 2 436.000 3.970 0.000 0.000 2.000 ! WJP
CH3CO3 2 436.000 3.970 0.000 0.000 2.000 ! WJP
CH3CO3H 2 436.000 3.970 0.000 0.000 2.000 ! WJP
HO2CHO 2 436.000 3.970 0.000 0.000 2.000 ! WJP
O2CHO 2 436.000 3.970 0.000 0.000 2.000 ! WJP
CH3O 2 417.000 3.690 1.700 0.000 2.000
CH3OH 2 481.800 3.626 0.000 0.000 1.000 ! SVE
CH3O2 2 481.800 3.626 0.000 0.000 1.000 ! WJP
CH3O2H 2 481.800 3.626 0.000 0.000 1.000 ! WJP
CH4 2 141.400 3.746 0.000 2.600 13.000
CH4O 2 417.000 3.690 1.700 0.000 2.000
CN 1 75.000 3.856 0.000 0.000 1.000 ! OIS
CNC 1 232.400 3.828 0.000 0.000 1.000 ! OIS
CNN 1 232.400 3.828 0.000 0.000 1.000 ! OIS
CO 1 98.100 3.650 0.000 1.950 1.800
CO2 1 244.000 3.763 0.000 2.650 2.100
F 0 80.000 2.750 0.000 0.000 0.000
```

```
F2 1 125.700 3.301 0.000 1.600 3.800
H 0 145.000 2.050 0.000 0.000 0.000
GAH 1 335.500 4.240 0.000 0.000 1.000 ! MEC
H2C4O 2 357.000 5.180 0.000 0.000 1.000 ! JAM
H2 1 38.000 2.920 0.000 0.790 280.000
H2CCC 2 265.300 3.721 0.000 0.000 1.000 ! *
H2CCC(S) 2 265.300 3.721 0.000 0.000 1.000 ! *
H2CCCH 2 252.000 4.760 0.000 0.000 1.000 ! JAM
H2CCCCH 2 357.100 4.720 0.000 0.000 1.000 ! NMM
H2CCCCH2 2 357.100 4.720 0.000 0.000 1.000 ! NMM
H2CCCCCH 1 408.000 5.200 0.000 0.000 1.000 ! NMM
H2CN 1 569.000 3.630 0.000 0.000 1.000 ! OS/JM
H2NO 2 116.700 3.492 0.000 0.000 1.000 ! JAM
H2O 2 572.400 2.605 1.844 0.000 4.000
H2O2 2 107.400 3.458 0.000 0.000 3.800
H2S 2 301.000 3.600 0.000 0.000 1.000 ! OIS
HC2N2 1 349.000 4.361 0.000 0.000 1.000 ! OIS
HCCHCCH 2 357.100 4.720 0.000 0.000 1.000 ! NMM
HCCO 2 150.000 2.500 0.000 0.000 1.000 ! *
HCCOH 2 436.000 3.970 0.000 0.000 2.000
HCCCHCCH 1 408.000 5.200 0.000 0.000 1.000 ! NMM
HCN 1 569.000 3.630 0.000 0.000 1.000 ! OIS
HCO 2 498.000 3.590 0.000 0.000 0.000
CHO 2 498.000 3.590 0.000 0.000 0.000
HCO+ 1 498.000 3.590 0.000 0.000 0.000
HE 0 10.200 2.576 0.000 0.000 0.000 ! *
HF 1 330.000 3.148 1.920 2.460 1.000 ! SV/MEC
HF0 1 352.000 2.490 1.730 0.000 5.000
HF1 1 352.000 2.490 1.730 0.000 5.000
```

```
HF2 1 352.000 2.490 1.730 0.000 5.000
HF3 1 352.000 2.490 1.730 0.000 5.000
HF4 1 352.000 2.490 1.730 0.000 5.000
HF5 1 352.000 2.490 1.730 0.000 5.000
HF6 1 352.000 2.490 1.730 0.000 5.000
HF7 1 352.000 2.490 1.730 0.000 5.000
HF8 1 352.000 2.490 1.730 0.000 5.000
HCNO 2 232.400 3.828 0.000 0.000 1.000 ! JAM
HOCN 2 232.400 3.828 0.000 0.000 1.000 ! JAM
HNCO 2 232.400 3.828 0.000 0.000 1.000 ! OIS
HNNO 2 232.400 3.828 0.000 0.000 1.000 ! *
HNO 2 116.700 3.492 0.000 0.000 1.000 ! *
HNOH 2 116.700 3.492 0.000 0.000 1.000 ! JAM
HO2 2 107.400 3.458 0.000 0.000 1.000 ! *
HSO2 2 252.000 4.290 0.000 0.000 1.000 ! OIS
N 0 71.400 3.298 0.000 0.000 0.000 ! *
N2 1 97.530 3.621 0.000 1.760 4.000
N2H 2 71.400 3.798 0.000 0.000 1.000 ! *
N2H2 2 71.400 3.798 0.000 0.000 1.000 ! *
N2H3 2 200.000 3.900 0.000 0.000 1.000 ! *
N2H4 2 205.000 4.230 0.000 4.260 1.500
N2O 1 232.400 3.828 0.000 0.000 1.000 ! *
NCN 1 232.400 3.828 0.000 0.000 1.000 ! OIS
NCO 1 232.400 3.828 0.000 0.000 1.000 ! OIS
NH 1 80.000 2.650 0.000 0.000 4.000
NH2 2 80.000 2.650 0.000 2.260 4.000
NH3 2 481.000 2.920 1.470 0.000 10.000
NO 1 97.530 3.621 0.000 1.760 4.000
NCNO 2 232.400 3.828 0.000 0.000 1.000 ! OIS
```

```
NO2 2 200.000 3.500 0.000 0.000 1.000 ! *
O 0 80.000 2.750 0.000 0.000 0.000
O2 1 107.400 3.458 0.000 1.600 3.800
O3 2 180.000 4.100 0.000 0.000 2.000
OH 1 80.000 2.750 0.000 0.000 0.000
S 0 847.000 3.839 0.000 0.000 0.000 ! OIS
S2 1 847.000 3.900 0.000 0.000 1.000 ! OIS
SH 1 847.000 3.900 0.000 0.000 1.000 ! OIS
SO 1 301.000 3.993 0.000 0.000 1.000 ! OIS
SO2 2 252.000 4.290 0.000 0.000 1.000 ! OIS
SO3 2 378.400 4.175 0.000 0.000 1.000 ! OIS
SIH4 2 207.6 4.084 0.000 0.000 1.000 ! MEC
SIH3 2 170.3 3.943 0.000 0.000 1.000 ! MEC
SIH2 2 133.1 3.803 0.000 0.000 1.000 ! MEC
SIH 1 95.8 3.662 0.000 0.000 1.000 ! MEC
SI 0 3036. 2.910 0.000 0.000 0.000 ! MEC
SI2H6 2 301.3 4.828 0.000 0.000 1.000 ! MEC
SI2H5 2 306.9 4.717 0.000 0.000 1.000 ! MEC
SI2H4 2 312.6 4.601 0.000 0.000 1.000 ! MEC
SI2H3 2 318.2 4.494 0.000 0.000 1.000 ! MEC
SI2H2 2 323.8 4.383 0.000 0.000 1.000 ! MEC
SI2 1 3036. 3.280 0.000 0.000 1.000 ! MEC
SI3 2 3036. 3.550 0.000 0.000 1.000 ! MEC
SIF3 2 309.6 4.359 0.000 0.000 1.000 ! MEC
SIF3NH2 2 231.0 4.975 0.000 0.000 1.000 ! MEC
SIF4 2 171.9 4.880 0.000 0.000 1.000 ! SVE
SIHF3 2 180.8 4.681 0.000 0.000 1.000 ! MEC
H2SISIH2 2 312.6 4.601 0.000 0.000 1.000 ! MEC
H3SISIH 2 312.6 4.601 0.000 0.000 1.000 ! MEC
```

```
SI3H8 2 331.2 5.562 0.000 0.000 1.000 ! MEC
ASH3 2 259.8 4.145 0.000 0.000 1.000 ! MEC
AS2 1 1045.5 5.510 0.000 0.000 1.000 ! MEC
GAME3 2 378.2 5.52 0.000 0.000 1.000 ! MEC
GAME2 2 675.8 5.22 0.000 0.000 1.000 ! MEC
GAME 2 972.7 4.92 0.000 0.000 1.000 ! MEC
GA 0 2961.8 4.62 0.000 0.000 0.000 ! MEC
K 0 850. 4.25 0.000 0.000 1.000 ! SINGH
KOH 2 1213. 4.52 0.000 0.000 1.000 ! SINGH
KO2 2 1213. 4.69 0.000 0.000 1.000 ! SINGH
KH 1 93.3 3.542 0.000 0.000 1.000 ! SINGH
K+ 0 850. 4.25 0.000 0.000 1.000 ! SINGH
E 0 850. 425. 0.000 0.000 1.000 ! SINGH
KCL 1 1989. 4.186 0.000 0.000 1.000 ! SINGH
CL 0 130.8 3.613 0.000 0.000 1.000 ! SINGH
CL- 0 130.8 3.613 0.000 0.000 1.000 ! SINGH
HCL 1 344.7 3.339 1.084 0.000 1.000 ! SINGH
KO 1 383.0 3.812 0.000 0.000 1.000 ! SINGH
NC10H22 2 540.0 7.085 0.0 0.0 1.0 ! TCPC
NC10H22O 2 600.6 7.229 1.8 0.0 1.0 ! TCPC
335C10H22 2 522.0 6.873 0.0 0.0 1.0 ! WJP
2255C10H22 2 497.3 6.899 0.0 0.0 1.0 ! WJP
IC8H18 2 458.5 6.414 0.0 0.0 1.0 ! WJP
AC8H17 2 458.5 6.414 0.0 0.0 1.0 ! WJP
BC8H17 2 458.5 6.414 0.0 0.0 1.0 ! WJP
CC8H17 2 458.5 6.414 0.0 0.0 1.0 ! WJP
DC8H17 2 458.5 6.414 0.0 0.0 1.0 ! WJP
1C8H17OH 2 581.3 6.506 2.0 0.0 1.0 ! TCPC
AC8H17O 2 581.3 6.506 2.0 0.0 1.0 ! WJP
```

```
BC8H17O 2 581.3 6.506 2.0 0.0 1.0 ! WJP
CC8H17O 2 581.3 6.506 2.0 0.0 1.0 ! WJP
DC8H17O 2 581.3 6.506 2.0 0.0 1.0 ! WJP
1C8H16 2 485.6 6.440 0.3 0.0 1.0 ! WJP
IC8H16 2 485.6 6.440 0.3 0.0 1.0 ! WJP
JC8H16 2 485.6 6.440 0.3 0.0 1.0 ! WJP
IC8H15 2 485.6 6.440 0.3 0.0 1.0 ! WJP
IC8H14 2 485.6 6.440 0.3 0.0 1.0 ! WJP
C7H16 2 459.6 6.253 0.0 0.0 1.0 ! TCPC
C7H15-1 2 459.6 6.253 0.0 0.0 1.0 ! WJP
C7H15-2 2 459.6 6.253 0.0 0.0 1.0 ! WJP
C7H15-3 2 459.6 6.253 0.0 0.0 1.0 ! WJP
C7H15-4 2 459.6 6.253 0.0 0.0 1.0 ! WJP
NEOC7H16 2 437.3 6.168 0.0 0.0 1.0 ! WJP
2-4C7H16 2 437.3 6.168 0.0 0.0 1.0 ! WJP
QC7H15 2 437.3 6.168 0.0 0.0 1.0 ! WJP
PC7H15 2 437.3 6.168 0.0 0.0 1.0 ! WJP
OC7H15 2 437.3 6.168 0.0 0.0 1.0 ! WJP
!NC7H15 2 437.3 6.168 0.0 0.0 1.0 ! WJP
XC7H15 2 437.3 6.168 0.0 0.0 1.0 ! WJP
YC7H15 2 437.3 6.168 0.0 0.0 1.0 ! WJP
ZC7H15 2 437.3 6.168 0.0 0.0 1.0 ! WJP
1C7H15OH 2 561.0 6.317 1.7 0.0 1.0 ! TCPC
C7H15O-1 2 561.0 6.317 1.7 0.0 1.0 ! WJP
C7H15O-2 2 561.0 6.317 1.7 0.0 1.0 ! WJP
C7H15O-3 2 561.0 6.317 1.7 0.0 1.0 ! WJP
C7H15O-4 2 561.0 6.317 1.7 0.0 1.0 ! WJP
C7H15O2-1 2 561.0 6.317 1.7 0.0 1.0 ! WJP
C7H15O2-2 2 561.0 6.317 1.7 0.0 1.0 ! WJP
```

```
C7H15O2-3 2 561.0 6.317 1.7 0.0 1.0 ! WJP
C7H15O2-4 2 561.0 6.317 1.7 0.0 1.0 ! WJP
C7H15O2H-1 2 561.0 6.317 1.7 0.0 1.0 ! WJP
C7H15O2H-2 2 561.0 6.317 1.7 0.0 1.0 ! WJP
C7H15O2H-3 2 561.0 6.317 1.7 0.0 1.0 ! WJP
C7H15O2H-4 2 561.0 6.317 1.7 0.0 1.0 ! WJP
C7H14OOH1-2 2 561.0 6.317 1.7 0.0 1.0 ! WJP
C7H14OOH1-3 2 561.0 6.317 1.7 0.0 1.0 ! WJP
C7H14OOH1-4 2 561.0 6.317 1.7 0.0 1.0 ! WJP
C7H14OOH1-5 2 561.0 6.317 1.7 0.0 1.0 ! WJP
C7H14OOH2-1 2 561.0 6.317 1.7 0.0 1.0 ! WJP
C7H14OOH2-3 2 561.0 6.317 1.7 0.0 1.0 ! WJP
C7H14OOH2-4 2 561.0 6.317 1.7 0.0 1.0 ! WJP
C7H14OOH2-5 2 561.0 6.317 1.7 0.0 1.0 ! WJP
C7H14OOH2-6 2 561.0 6.317 1.7 0.0 1.0 ! WJP
C7H14OOH3-1 2 561.0 6.317 1.7 0.0 1.0 ! WJP
C7H14OOH3-2 2 561.0 6.317 1.7 0.0 1.0 ! WJP
C7H14OOH3-4 2 561.0 6.317 1.7 0.0 1.0 ! WJP
C7H14OOH3-5 2 561.0 6.317 1.7 0.0 1.0 ! WJP
C7H14OOH3-6 2 561.0 6.317 1.7 0.0 1.0 ! WJP
C7H14OOH3-7 2 561.0 6.317 1.7 0.0 1.0 ! WJP
C7H14OOH4-1 2 561.0 6.317 1.7 0.0 1.0 ! WJP
C7H14OOH4-2 2 561.0 6.317 1.7 0.0 1.0 ! WJP
C7H14OOH4-3 2 561.0 6.317 1.7 0.0 1.0 ! WJP
C7H14OOH1-2O2 2 600.6 7.229 1.8 0.0 1.0 ! NC10H22O WJP
C7H14OOH1-3O2 2 600.6 7.229 1.8 0.0 1.0 ! NC10H22O WJP
C7H14OOH1-4O2 2 600.6 7.229 1.8 0.0 1.0 ! NC10H22O WJP
C7H14OOH1-5O2 2 600.6 7.229 1.8 0.0 1.0 ! NC10H22O WJP
C7H14OOH2-1O2 2 600.6 7.229 1.8 0.0 1.0 ! NC10H22O WJP
```

C7H14OOH2-3O2 2 600.6 7.229 1.8 0.0 1.0 ! NC10H22O WJP

C7H14OOH2-4O2 2 600.6 7.229 1.8 0.0 1.0 ! NC10H22O WJP

C7H14OOH2-5O2 2 600.6 7.229 1.8 0.0 1.0 ! NC10H22O WJP

C7H14OOH2-6O2 2 600.6 7.229 1.8 0.0 1.0 ! NC10H22O WJP

C7H14OOH3-1O2 2 600.6 7.229 1.8 0.0 1.0 ! NC10H22O WJP

C7H14OOH3-2O2 2 600.6 7.229 1.8 0.0 1.0 ! NC10H22O WJP

C7H14OOH3-4O2 2 600.6 7.229 1.8 0.0 1.0 ! NC10H22O WJP

C7H14OOH3-5O2 2 600.6 7.229 1.8 0.0 1.0 ! NC10H22O WJP

C7H14OOH3-6O2 2 600.6 7.229 1.8 0.0 1.0 ! NC10H22O WJP

C7H14OOH3-7O2 2 600.6 7.229 1.8 0.0 1.0 ! NC10H22O WJP

C7H14OOH4-1O2 2 600.6 7.229 1.8 0.0 1.0 ! NC10H22O WJP

C7H14OOH4-2O2 2 600.6 7.229 1.8 0.0 1.0 ! NC10H22O WJP

C7H14OOH4-3O2 2 600.6 7.229 1.8 0.0 1.0 ! NC10H22O WJP

C7H14O1-2 2 511.5 6.297 0.0 0.0 1.0 ! C8H16-1-5 WJP

C7H14O1-3 2 511.5 6.297 0.0 0.0 1.0 ! C8H16-1-5 WJP

C7H14O1-4 2 511.5 6.297 0.0 0.0 1.0 ! C8H16-1-5 WJP

C7H14O1-5 2 511.5 6.297 0.0 0.0 1.0 ! C8H16-1-5 WJP

C7H14O2-3 2 511.5 6.297 0.0 0.0 1.0 ! C8H16-1-5 WJP

C7H14O2-4 2 511.5 6.297 0.0 0.0 1.0 ! C8H16-1-5 WJP

C7H14O2-5 2 511.5 6.297 0.0 0.0 1.0 ! C8H16-1-5 WJP

C7H14O2-6 2 511.5 6.297 0.0 0.0 1.0 ! C8H16-1-5 WJP

C7H14O3-4 2 511.5 6.297 0.0 0.0 1.0 ! C8H16-1-5 WJP

C7H14O3-5 2 511.5 6.297 0.0 0.0 1.0 ! C8H16-1-5 WJP

NC7KET12 2 581.3 6.506 2.0 0.0 1.0 ! 1C8H17OH WJP

NC7KET13 2 581.3 6.506 2.0 0.0 1.0 ! 1C8H17OH WJP

NC7KET14 2 581.3 6.506 2.0 0.0 1.0 ! 1C8H17OH WJP

NC7KET15 2 581.3 6.506 2.0 0.0 1.0 ! 1C8H17OH WJP

NC7KET21 2 581.3 6.506 2.0 0.0 1.0 ! 1C8H17OH WJP

NC7KET23 2 581.3 6.506 2.0 0.0 1.0 ! 1C8H17OH WJP

```
NC7KET24 2 581.3 6.506 2.0 0.0 1.0 ! 1C8H17OH WJP
NC7KET25 2 581.3 6.506 2.0 0.0 1.0 ! 1C8H17OH WJP
NC7KET26 2 581.3 6.506 2.0 0.0 1.0 ! 1C8H17OH WJP
NC7KET31 2 581.3 6.506 2.0 0.0 1.0 ! 1C8H17OH WJP
NC7KET32 2 581.3 6.506 2.0 0.0 1.0 ! 1C8H17OH WJP
NC7KET34 2 581.3 6.506 2.0 0.0 1.0 ! 1C8H17OH WJP
NC7KET35 2 581.3 6.506 2.0 0.0 1.0 ! 1C8H17OH WJP
NC7KET36 2 581.3 6.506 2.0 0.0 1.0 ! 1C8H17OH WJP
NC7KET37 2 581.3 6.506 2.0 0.0 1.0 ! 1C8H17OH WJP
NC7KET41 2 581.3 6.506 2.0 0.0 1.0 ! 1C8H17OH WJP
NC7KET42 2 581.3 6.506 2.0 0.0 1.0 ! 1C8H17OH WJP
NC7KET43 2 581.3 6.506 2.0 0.0 1.0 ! 1C8H17OH WJP
QC7H15O 2 561.0 6.317 1.7 0.0 1.0 ! WJP
PC7H15O 2 561.0 6.317 1.7 0.0 1.0 ! WJP
OC7H15O 2 561.0 6.317 1.7 0.0 1.0 ! WJP
NC7H15O 2 561.0 6.317 1.7 0.0 1.0 ! WJP
NC7H15 2 459.980 6.310 0.0 0.0 1.0 ! Ranzi
XC7H15O 2 561.0 6.317 1.7 0.0 1.0 ! WJP
YC7H15O 2 561.0 6.317 1.7 0.0 1.0 ! WJP
ZC7H15O 2 561.0 6.317 1.7 0.0 1.0 ! WJP
C7H14 2 457.8 6.173 0.3 0.0 1.0 ! TCPC
1C7H14 2 457.8 6.173 0.3 0.0 1.0 ! TCPC
C7H14-1 2 457.8 6.173 0.3 0.0 1.0 ! TCPC
C7H14-2 2 457.8 6.173 0.3 0.0 1.0 ! WJP
C7H14-3 2 457.8 6.173 0.3 0.0 1.0 ! WJP
C7H13 2 457.8 6.173 0.3 0.0 1.0 ! WJP
IBC7H14 2 439.2 6.151 0.0 0.0 1.0 ! TCPC
O-C7H14 2 439.2 6.151 0.0 0.0 1.0 ! WJP
PC7H14 2 439.2 6.151 0.0 0.0 1.0 ! WJP
```

```
XC7H14 2 439.2 6.151 0.0 0.0 1.0 ! WJP
YC7H14 2 439.2 6.151 0.0 0.0 1.0 ! WJP
PC7H13 2 439.2 6.151 0.0 0.0 1.0 ! WJP
XC7H13 2 439.2 6.151 0.0 0.0 1.0 ! WJP
NC6H14 2 427.4 5.946 0.0 0.0 1.0 ! WJP
NEOC6H14 2 406.1 5.842 0.0 0.0 1.0 ! WJP
XC6H14 2 416.7 5.852 0.0 0.0 1.0 ! WJP
3-C6H14 2 422.5 5.870 0.0 0.0 1.0 ! WJP
IC6H14 2 422.5 5.870 0.0 0.0 1.0 ! WJP
C2H5COC3H7-N 2 498.6 6.009 2.0 0.0 1.0 ! TCPC
FC6H13 2 406.1 5.842 0.0 0.0 1.0 ! WJP
GC6H13 2 406.1 5.842 0.0 0.0 1.0 ! WJP
HC6H13 2 406.1 5.842 0.0 0.0 1.0 ! WJP
AC6H13 2 422.5 5.870 0.0 0.0 1.0 ! WJP
BC6H13 2 422.5 5.870 0.0 0.0 1.0 ! WJP
C-C6H13 2 422.5 5.870 0.0 0.0 1.0 ! WJP
DC6H13 2 422.5 5.870 0.0 0.0 1.0 ! WJP
EC6H13 2 422.5 5.870 0.0 0.0 1.0 ! WJP
1C6H13OH 2 541.5 5.674 1.8 0.0 1.0 ! TCPC
FC6H13O 2 541.5 5.674 1.8 0.0 1.0 ! WJP
GC6H13O 2 541.5 5.674 1.8 0.0 1.0 ! WJP
HC6H13O 2 541.5 5.674 1.8 0.0 1.0 ! WJP
AC6H13O 2 541.5 5.674 1.8 0.0 1.0 ! WJP
BC6H13O 2 541.5 5.674 1.8 0.0 1.0 ! WJP
C-C6H13O 2 541.5 5.674 1.8 0.0 1.0 ! WJP
DC6H13O 2 541.5 5.674 1.8 0.0 1.0 ! WJP
EC6H13O 2 541.5 5.674 1.8 0.0 1.0 ! WJP
NEOC6H12 2 397.9 5.767 0.0 0.0 1.0 ! WJP
KC6H12 2 435.9 5.807 0.0 0.0 1.0 ! WJP
```

```
JC6H12 2 415.3 5.794 0.0 0.0 1.0 ! WJP
C-C6H12 2 414.4 5.872 0.0 0.0 1.0 ! WJP
C-C6H12-C 2 411.9 5.860 0.0 0.0 1.0 ! WJP
H-C6H12 2 430.6 5.843 0.0 0.0 1.0 ! WJP
H-C6H12-C 2 433.6 5.825 0.0 0.0 1.0 ! WJP
BC6H12 2 430.1 5.833 0.0 0.0 1.0 ! WJP
3C6H12 2 431.5 5.859 0.0 0.0 1.0 ! WJP
3C6H12-C 2 428.9 5.830 0.3 0.0 1.0 ! WJP
2C6H12 2 429.6 5.829 0.0 0.0 1.0 ! WJP
2C6H12-C 2 432.4 5.827 0.0 0.0 1.0 ! WJP
1C6H12 2 423.2 5.834 0.4 0.0 1.0 ! WJP
AC6H12 2 430.1 5.833 0.0 0.0 1.0 ! WJP
DC6H12 2 414.4 5.872 0.0 0.0 1.0 ! WJP
NEOC6H11 2 397.9 5.767 0.0 0.0 1.0 ! WJP
C6H11OOH1-4 2 561.0 6.317 1.7 0.0 1.0 ! 1C7H15OH WJP
C6H11OOH1-5 2 561.0 6.317 1.7 0.0 1.0 ! 1C7H15OH WJP
C6H11O1-4 2 541.5 5.674 1.8 0.0 1.0 ! 1C6H13OH WJP
C6H11O1-5 2 541.5 5.674 1.8 0.0 1.0 ! 1C6H13OH WJP
IC6H12 2 430.1 5.833 0.0 0.0 1.0 ! WJP
NC3H7COOC2H5 2 494.8 6.174 1.8 0.0 1.0 ! TCPC
NC5KET12 2 494.8 6.174 1.8 0.0 1.0 ! TCPC
NC5KET13 2 494.8 6.174 1.8 0.0 1.0 ! TCPC
NC5KET14 2 494.8 6.174 1.8 0.0 1.0 ! TCPC
NC5KET15 2 494.8 6.174 1.8 0.0 1.0 ! TCPC
NC5KET21 2 494.8 6.174 1.8 0.0 1.0 ! TCPC
NC5KET23 2 494.8 6.174 1.8 0.0 1.0 ! TCPC
NC5KET24 2 494.8 6.174 1.8 0.0 1.0 ! TCPC
NC5KET25 2 494.8 6.174 1.8 0.0 1.0 ! TCPC
NC5KET31 2 494.8 6.174 1.8 0.0 1.0 ! TCPC
```

```
NC5KET32 2 494.8 6.174 1.8 0.0 1.0 ! TCPC
NC3H7COOC3H7-N 2 467.0 6.548 1.8 0.0 1.0 ! TCPC
NC6KET12 2 467.0 6.548 1.8 0.0 1.0 ! WJP
NC6KET13 2 467.0 6.548 1.8 0.0 1.0 ! WJP
NC6KET14 2 467.0 6.548 1.8 0.0 1.0 ! WJP
NC6KET15 2 467.0 6.548 1.8 0.0 1.0 ! WJP
NC6KET21 2 467.0 6.548 1.8 0.0 1.0 ! WJP
NC6KET23 2 467.0 6.548 1.8 0.0 1.0 ! WJP
NC6KET24 2 467.0 6.548 1.8 0.0 1.0 ! WJP
NC6KET25 2 467.0 6.548 1.8 0.0 1.0 ! WJP
NC6KET26 2 467.0 6.548 1.8 0.0 1.0 ! WJP
NC6KET31 2 467.0 6.548 1.8 0.0 1.0 ! WJP
NC6KET32 2 467.0 6.548 1.8 0.0 1.0 ! WJP
NC6KET34 2 467.0 6.548 1.8 0.0 1.0 ! WJP
NC6KET35 2 467.0 6.548 1.8 0.0 1.0 ! WJP
NC6KET36 2 467.0 6.548 1.8 0.0 1.0 ! WJP
NC5H12 2 391.7 5.591 0.0 0.0 1.0 ! WJP
NEO-C5H12 2 357.8 5.550 0.0 0.0 1.0 ! WJP
IC5H12 2 382.1 5.548 0.0 0.0 1.0 ! WJP
NC5H11CHO 2 498.6 6.009 2.0 0.0 1.0 ! C2H5COC3H7-N WJP
NC5H11CO 2 498.6 6.009 2.0 0.0 1.0 ! C2H5COC3H7-N WJP
NC5H10CHO-1 2 498.6 6.009 2.0 0.0 1.0 ! C2H5COC3H7-N WJP
NC5H10CHO-2 2 498.6 6.009 2.0 0.0 1.0 ! C2H5COC3H7-N WJP
NC5H10CHO-3 2 498.6 6.009 2.0 0.0 1.0 ! C2H5COC3H7-N WJP
NC5H10CHO-4 2 498.6 6.009 2.0 0.0 1.0 ! C2H5COC3H7-N WJP
NC5H10CHO-5 2 498.6 6.009 2.0 0.0 1.0 ! C2H5COC3H7-N WJP
1C5H11OH 2 523.2 5.664 1.7 0.0 1.0 ! TCPC
IC5H11OH-1 2 451.9 6.041 0.0 0.0 1.0 ! WJP
IC5H11OH-2 2 431.4 5.624 1.9 0.0 1.0 ! WJP
```

```
1C5H11O 2 523.2 5.664 1.7 0.0 1.0 ! WJP
2C5H11O 2 523.2 5.664 1.7 0.0 1.0 ! WJP
3C5H11O 2 523.2 5.664 1.7 0.0 1.0 ! WJP
C5H11O-1 2 523.2 5.664 1.7 0.0 1.0 ! WJP
C5H11O-2 2 523.2 5.664 1.7 0.0 1.0 ! WJP
C5H11O-3 2 523.2 5.664 1.7 0.0 1.0 ! WJP
AC5H11O 2 523.2 5.664 1.7 0.0 1.0 ! WJP
BC5H11O 2 523.2 5.664 1.7 0.0 1.0 ! WJP
CC5H11O 2 523.2 5.664 1.7 0.0 1.0 ! WJP
DC5H11O 2 523.2 5.664 1.7 0.0 1.0 ! WJP
C5H11O2-1 2 523.2 5.664 1.7 0.0 1.0 ! WJP
C5H11O2-2 2 523.2 5.664 1.7 0.0 1.0 ! WJP
C5H11O2-3 2 523.2 5.664 1.7 0.0 1.0 ! WJP
C5H11O2H-1 2 523.2 5.664 1.7 0.0 1.0 ! WJP
C5H11O2H-2 2 523.2 5.664 1.7 0.0 1.0 ! WJP
C5H11O2H-3 2 523.2 5.664 1.7 0.0 1.0 ! WJP
C5H10OOH1-2 2 523.2 5.664 1.7 0.0 1.0 ! WJP
C5H10OOH1-3 2 523.2 5.664 1.7 0.0 1.0 ! WJP
C5H10OOH1-4 2 523.2 5.664 1.7 0.0 1.0 ! WJP
C5H10OOH2-1 2 523.2 5.664 1.7 0.0 1.0 ! WJP
C5H10OOH2-3 2 523.2 5.664 1.7 0.0 1.0 ! WJP
C5H10OOH2-4 2 523.2 5.664 1.7 0.0 1.0 ! WJP
C5H10OOH2-5 2 523.2 5.664 1.7 0.0 1.0 ! WJP
C5H10OOH3-1 2 523.2 5.664 1.7 0.0 1.0 ! WJP
C5H10OOH3-2 2 523.2 5.664 1.7 0.0 1.0 ! WJP
C5H10OOH1-2O2 2 523.2 5.664 1.7 0.0 1.0 ! WJP
C5H10OOH1-3O2 2 523.2 5.664 1.7 0.0 1.0 ! WJP
C5H10OOH1-4O2 2 523.2 5.664 1.7 0.0 1.0 ! WJP
C5H10OOH1-5O2 2 523.2 5.664 1.7 0.0 1.0 ! WJP
```

C5H10OOH2-1O2 2 523.2 5.664 1.7 0.0 1.0 ! WJP

C5H10OOH2-3O2 2 523.2 5.664 1.7 0.0 1.0 ! WJP

C5H10OOH2-4O2 2 523.2 5.664 1.7 0.0 1.0 ! WJP

C5H10OOH2-5O2 2 523.2 5.664 1.7 0.0 1.0 ! WJP

C5H10OOH3-1O2 2 523.2 5.664 1.7 0.0 1.0 ! WJP

C5H10OOH3-2O2 2 523.2 5.664 1.7 0.0 1.0 ! WJP

C5H10O1-2 2 523.2 5.664 1.7 0.0 1.0 ! WJP

C5H10O1-3 2 523.2 5.664 1.7 0.0 1.0 ! WJP

C5H10O1-4 2 523.2 5.664 1.7 0.0 1.0 ! WJP

C5H10O1-5 2 523.2 5.664 1.7 0.0 1.0 ! WJP

C5H10O2-3 2 523.2 5.664 1.7 0.0 1.0 ! WJP

C5H10O2-4 2 523.2 5.664 1.7 0.0 1.0 ! WJP

C5H9OOH-14 2 541.5 5.674 1.8 0.0 1.0 ! 1C6H13OH WJP

C5H9OOH-15 2 541.5 5.674 1.8 0.0 1.0 ! 1C6H13OH WJP

C5H9O-14 2 523.2 5.664 1.7 0.0 1.0 ! 1C5H11OH WJP

C5H9O-15 2 523.2 5.664 1.7 0.0 1.0 ! 1C5H11OH WJP

NEO-C5H11O 2 523.2 5.664 1.7 0.0 1.0 ! WJP

C2H5COC2H5 2 476.7 5.714 2.7 0.0 1.0 ! TCPC

C2H5COC2H3 2 476.7 5.714 2.7 0.0 1.0 ! WJP

PC2H4COC2H3 2 476.7 5.714 2.7 0.0 1.0 ! WJP

SC2H4COC2H3 2 476.7 5.714 2.7 0.0 1.0 ! WJP

IC3H7COCH3 2 469.0 5.632 2.8 0.0 1.0 ! WJP

NC3H7COCH3 2 477.0 5.735 2.5 0.0 1.0 ! WJP

NC4H9CHO 2 476.0 5.778 2.6 0.0 1.0 ! TCPC

NC4H9CO 2 476.0 5.778 2.6 0.0 1.0 ! WJP

C4H8CHO-1 2 476.0 5.778 2.6 0.0 1.0 ! WJP

C4H8CHO-2 2 476.0 5.778 2.6 0.0 1.0 ! WJP

C4H8CHO-3 2 476.0 5.778 2.6 0.0 1.0 ! WJP

C4H8CHO-4 2 476.0 5.778 2.6 0.0 1.0 ! WJP

```
NC4KET12 2 476.0 5.778 2.6 0.0 1.0 ! WJP
NC4KET13 2 476.0 5.778 2.6 0.0 1.0 ! WJP
NC4KET14 2 476.0 5.778 2.6 0.0 1.0 ! WJP
NC4KET21 2 476.0 5.778 2.6 0.0 1.0 ! WJP
NC4KET23 2 476.0 5.778 2.6 0.0 1.0 ! WJP
NC4KET24 2 476.0 5.778 2.6 0.0 1.0 ! WJP
C-C5H10 2 372.1 5.446 0.0 0.0 1.0 ! WJP
BC5H10 2 391.4 5.550 0.0 0.0 1.0 ! WJP
AC5H10 2 386.6 5.532 0.5 0.0 1.0 ! WJP
2C5H10 2 396.8 5.458 0.0 0.0 1.0 ! WJP
C5H10-2 2 396.8 5.458 0.0 0.0 1.0 ! WJP
1C5H10 2 386.2 5.489 0.4 0.0 1.0 ! WJP
C5H10 2 386.2 5.489 0.4 0.0 1.0 ! WJP
C5H10-1 2 386.2 5.489 0.4 0.0 1.0 ! WJP
C5H9 2 396.8 5.458 0.0 0.0 1.0 ! WJP
IC5H9 2 386.6 5.532 0.5 0.0 1.0 ! WJP
NC4H10 2 350.9 5.206 0.0 0.0 1.0 ! WJP
!C4H10 2 350.9 5.206 0.0 0.0 1.0 ! WJP
C4H10 2 352.0 5.240 0.0 0.0 1.0 ! Ranzi
IC4H10 2 335.7 5.208 0.1 0.0 1.0 ! WJP
NC4H9OH 2 502.2 5.356 1.8 0.0 1.0 ! WJP
IC4H7OH 2 502.2 5.356 1.8 0.0 1.0 ! WJP
IC4H6OH 2 502.2 5.356 1.8 0.0 1.0 ! WJP
C4H7CHO1-4 2 476.0 5.778 2.6 0.0 1.0 ! NC4H9CHO WJP
C4H7CO1-4 2 476.0 5.778 2.6 0.0 1.0 ! NC4H9CHO WJP
C4H7CHO1-43 2 476.0 5.778 2.6 0.0 1.0 ! NC4H9CHO WJP
C4H7CHO1-44 2 476.0 5.778 2.6 0.0 1.0 ! NC4H9CHO WJP
C4H7OOH1-4 2 523.2 5.664 1.7 0.0 1.0 ! 1C5H11OH WJP
C4H7O1-4 2 476.0 5.778 2.6 0.0 1.0 ! NC4H9CHO WJP
```

```
IC3H7CHO 2 436.4 5.352 0.0 0.0 1.0 ! TCPC
TC3H6O2CHO 2 436.4 5.352 0.0 0.0 1.0 ! WJP
TC3H6O2HCO 2 436.4 5.352 0.0 0.0 1.0 ! WJP
TC3H6OHCHO 2 436.4 5.352 0.0 0.0 1.0 ! WJP
IC3H5O2HCHO 2 436.4 5.352 0.0 0.0 1.0 ! WJP
NC3H7CHO 2 464.2 5.009 2.6 0.0 1.0 ! TCPC
AC3H5CHO 2 464.2 5.009 2.6 0.0 1.0 ! WJP
AC3H5CO 2 464.2 5.009 2.6 0.0 1.0 ! WJP
C2H3CHCHO 2 464.2 5.009 2.6 0.0 1.0 ! WJP
C2H5CHCHO 2 464.2 5.009 2.6 0.0 1.0 ! WJP
C3H6CHO-1 2 464.2 5.009 2.6 0.0 1.0 ! WJP
C3H6CHO-2 2 464.2 5.009 2.6 0.0 1.0 ! WJP
C3H6CHO-3 2 464.2 5.009 2.6 0.0 1.0 ! WJP
SC3H5CHO 2 464.2 5.009 2.6 0.0 1.0 ! TCPC
SC3H5CO 2 464.2 5.009 2.6 0.0 1.0 ! TCPC
C2H5OCHO 2 427.0 5.117 2.0 0.0 1.0 ! TCPC
CH3CHOCHO 2 427.0 5.117 2.0 0.0 1.0 ! TCPC
C2H5COCH3 2 454.0 5.413 3.3 0.0 1.0 ! TCPC
C2H5COCH2 2 454.0 5.413 3.3 0.0 1.0 ! WJP
C2H3COCH3 2 454.0 5.413 3.3 0.0 1.0 ! WJP
C3KET12 2 464.2 5.009 2.6 0.0 1.0 ! WJP
C3KET13 2 464.2 5.009 2.6 0.0 1.0 ! WJP
C3KET21 2 464.2 5.009 2.6 0.0 1.0 ! WJP
IC3H7CO 2 436.4 5.352 0.0 0.0 1.0 ! WJP
NC3H7CO 2 464.2 5.009 2.6 0.0 1.0 ! WJP
IC3H6CHO 2 436.4 5.352 0.0 0.0 1.0 ! WJP
TC3H6CHO 2 436.4 5.352 0.0 0.0 1.0 ! WJP
TC3H6OCHO 2 436.4 5.352 0.0 0.0 1.0 ! WJP
IC3H6CO 2 436.4 5.352 0.0 0.0 1.0 ! WJP
```

```
IC3H5CHO 2 436.4 5.352 0.0 0.0 1.0 ! WJP
IC3H5CO 2 436.4 5.352 0.0 0.0 1.0 ! WJP
IC4H8 2 344.5 5.089 0.5 0.0 1.0 ! WJP
2-C4H8 2 354.1 5.135 0.0 0.0 1.0 ! WJP
2-C4H8-S 2 359.7 5.076 0.3 0.0 1.0 ! WJP
1-C4H8 2 345.7 5.088 0.3 0.0 1.0 ! WJP
1,3-C4H6 2 350.4 4.984 0.0 0.0 1.0 ! WJP
1,2-C4H6 2 370.3 4.984 0.4 0.0 1.0 ! WJP
C3H6O 2 403.6 4.968 2.0 0.0 1.0 ! WJP
C3H6O1-3 2 403.6 4.968 2.0 0.0 1.0 ! WJP
C3H6O1-2 2 403.6 4.968 2.0 0.0 1.0 ! WJP
C2H5CHO 2 435.2 4.662 2.7 0.0 1.0 ! WJP
C3H6OOH1-2 2 435.2 4.662 2.7 0.0 1.0 ! WJP
C3H6OOH1-3 2 435.2 4.662 2.7 0.0 1.0 ! WJP
C3H6OOH2-1 2 435.2 4.662 2.7 0.0 1.0 ! WJP
C3H6OOH1-2O2 2 435.2 4.662 2.7 0.0 1.0 ! WJP
C3H6OOH1-3O2 2 435.2 4.662 2.7 0.0 1.0 ! WJP
C3H6OOH2-1O2 2 435.2 4.662 2.7 0.0 1.0 ! WJP
NC3H7OH 2 481.5 4.997 1.7 0.0 1.0 ! WJP
IC3H7OH 2 459.5 5.036 1.7 0.0 1.0 ! WJP
CH3OC2H5 2 364.6 4.998 1.2 0.0 1.0 ! WJP
IC3H5OH 2 459.5 5.036 1.7 0.0 1.0 ! WJP
TC3H6OH 2 459.5 5.036 1.7 0.0 1.0 ! WJP
NC3H7O 2 481.5 4.997 1.7 0.0 1.0 ! WJP
NC3H7O2 2 481.5 4.997 1.7 0.0 1.0 ! WJP
NC3H7O2H 2 481.5 4.997 1.7 0.0 1.0 ! WJP
IC3H7O 2 459.5 5.036 1.7 0.0 1.0 ! WJP
IC3H7O2 2 459.5 5.036 1.7 0.0 1.0 ! WJP
IC3H7O2H 2 459.5 5.036 1.7 0.0 1.0 ! WJP
```

```
C3H5OH 2 481.5 4.997 1.7 0.0 1.0 ! WJP
C2H3CHO 2 428.8 4.958 2.9 0.0 1.0 ! WJP
CH2CCH2OH 2 481.5 4.997 1.7 0.0 1.0 ! WJP
A-AC5H10O 3 492.434 5.369 0.000 0.000 0.000 !FLAMEMASTER
A-BC5H10O 3 492.434 5.369 0.000 0.000 0.000 !FLAMEMASTER
AC3H4COC2H5 3 527.994 5.587 0.000 0.000 0.000 !FLAMEMASTER
AC3H4COCH3 3 482.331 5.306 0.000 0.000 0.000 !FLAMEMASTER
AC3H5CHCOCH3 3 527.994 5.587 0.000 0.000 0.000 !FLAMEMASTER
AC5H10OOH-A 3 546.691 5.698 0.000 0.000 0.000 !FLAMEMASTER
AC5H10OOH-AO2 3 639.455 6.230 0.000 0.000 0.000 !FLAMEMASTER
AC5H10OOH-B 3 546.691 5.698 0.000 0.000 0.000 !FLAMEMASTER
AC5H10OOH-BO2 3 639.455 6.230 0.000 0.000 0.000 !FLAMEMASTER
AC5H10OOH-C 3 546.691 5.698 0.000 0.000 0.000 !FLAMEMASTER
AC5H10OOH-CO2 3 639.455 6.230 0.000 0.000 0.000 !FLAMEMASTER
AC5H10OOH-D 3 546.691 5.698 0.000 0.000 0.000 !FLAMEMASTER
AC5H10OOH-DO2 3 639.455 6.230 0.000 0.000 0.000 !FLAMEMASTER
AC5H11 3 440.735 5.041 0.000 0.000 0.000 !FLAMEMASTER
AC5H11O2 3 546.691 5.698 0.000 0.000 0.000 !FLAMEMASTER
AC5H11O2H 3 549.783 5.717 0.000 0.000 0.000 !FLAMEMASTER
A-CC5H10O 3 492.434 5.369 0.000 0.000 0.000 !FLAMEMASTER
A-DC5H10O 3 492.434 5.369 0.000 0.000 0.000 !FLAMEMASTER
BC5H10OOH-A 3 546.691 5.698 0.000 0.000 0.000 !FLAMEMASTER
BC5H10OOH-AO2 3 639.455 6.230 0.000 0.000 0.000 !FLAMEMASTER
BC5H10OOH-C 3 546.691 5.698 0.000 0.000 0.000 !FLAMEMASTER
BC5H10OOH-CO2 3 639.455 6.230 0.000 0.000 0.000 !FLAMEMASTER
BC5H10OOH-D 3 546.691 5.698 0.000 0.000 0.000 !FLAMEMASTER
BC5H10OOH-DO2 3 639.455 6.230 0.000 0.000 0.000 !FLAMEMASTER
BC5H11 3 440.735 5.041 0.000 0.000 0.000 !FLAMEMASTER
BC5H11O2 3 546.691 5.698 0.000 0.000 0.000 !FLAMEMASTER
```

```
BC5H11O2H 3 549.783 5.717 0.000 0.000 0.000 !FLAMEMASTER
B-CC5H10O 3 492.434 5.369 0.000 0.000 0.000 !FLAMEMASTER
B-DC5H10O 3 492.434 5.369 0.000 0.000 0.000 !FLAMEMASTER
C2H5CHCO 3 436.950 5.016 0.000 0.000 0.000 !FLAMEMASTER
C2H5COC2H4P 3 489.084 5.348 0.000 0.000 0.000 !FLAMEMASTER
C2H5COC2H4S 3 489.084 5.348 0.000 0.000 0.000 !FLAMEMASTER
C3H6COC2H5-1 3 534.323 5.625 0.000 0.000 0.000 !FLAMEMASTER
C3H6COC2H5-2 3 534.323 5.625 0.000 0.000 0.000 !FLAMEMASTER
C3H6COC2H5-3 3 534.323 5.625 0.000 0.000 0.000 !FLAMEMASTER
C3H6COCH3-1 3 489.084 5.348 0.000 0.000 0.000 !FLAMEMASTER
C3H6COCH3-2 3 489.084 5.348 0.000 0.000 0.000 !FLAMEMASTER
C3H6COCH3-3 3 489.084 5.348 0.000 0.000 0.000 !FLAMEMASTER
C4H6CHO1-43 3 482.331 5.306 0.000 0.000 0.000 !FLAMEMASTER
C4H6CHO1-44 3 482.331 5.306 0.000 0.000 0.000 !FLAMEMASTER
C4H8COCH3-1 3 534.323 5.625 0.000 0.000 0.000 !FLAMEMASTER
C4H8COCH3-2 3 534.323 5.625 0.000 0.000 0.000 !FLAMEMASTER
C4H8COCH3-3 3 534.323 5.625 0.000 0.000 0.000 !FLAMEMASTER
C4H8COCH3-4 3 534.323 5.625 0.000 0.000 0.000 !FLAMEMASTER
C5H10CHO-1 3 534.323 5.625 0.000 0.000 0.000 !FLAMEMASTER
C5H10CHO-2 3 534.323 5.625 0.000 0.000 0.000 !FLAMEMASTER
C5H10CHO-3 3 534.323 5.625 0.000 0.000 0.000 !FLAMEMASTER
C5H10CHO-4 3 534.323 5.625 0.000 0.000 0.000 !FLAMEMASTER
C5H10CHO-5 3 534.323 5.625 0.000 0.000 0.000 !FLAMEMASTER
C5H10OOH1-5 3 546.691 5.698 0.000 0.000 0.000 !FLAMEMASTER
C5H11-1 3 440.735 5.041 0.000 0.000 0.000 !FLAMEMASTER
C5H11-2 3 440.735 5.041 0.000 0.000 0.000 !FLAMEMASTER
C5H11-3 3 440.735 5.041 0.000 0.000 0.000 !FLAMEMASTER
C5H9O1-4 3 489.084 5.348 0.000 0.000 0.000 !FLAMEMASTER
C5H9O1-5 3 489.084 5.348 0.000 0.000 0.000 !FLAMEMASTER
```

```
C5H9OOH1-4 3 543.585 5.680 0.000 0.000 0.000 !FLAMEMASTER
C5H9OOH1-5 3 543.585 5.680 0.000 0.000 0.000 !FLAMEMASTER
C6H11 3 482.473 5.307 0.000 0.000 0.000 !FLAMEMASTER
C6H12-1 3 485.857 5.328 0.000 0.000 0.000 !FLAMEMASTER
C6H12-2 3 485.857 5.328 0.000 0.000 0.000 !FLAMEMASTER
C6H12-3 3 485.857 5.328 0.000 0.000 0.000 !FLAMEMASTER
C6H12O1-2 3 537.467 5.643 0.000 0.000 0.000 !FLAMEMASTER
C6H12O1-3 3 537.467 5.643 0.000 0.000 0.000 !FLAMEMASTER
C6H12O1-4 3 537.467 5.643 0.000 0.000 0.000 !FLAMEMASTER
C6H12O1-5 3 537.467 5.643 0.000 0.000 0.000 !FLAMEMASTER
C6H12O2-3 3 537.467 5.643 0.000 0.000 0.000 !FLAMEMASTER
C6H12O2-4 3 537.467 5.643 0.000 0.000 0.000 !FLAMEMASTER
C6H12O2-5 3 537.467 5.643 0.000 0.000 0.000 !FLAMEMASTER
C6H12O3-4 3 537.467 5.643 0.000 0.000 0.000 !FLAMEMASTER
C6H12OOH1-2 3 588.653 5.943 0.000 0.000 0.000 !FLAMEMASTER
C6H12OOH1-2O2 3 677.149 6.436 0.000 0.000 0.000 !FLAMEMASTER
C6H12OOH1-3 3 588.653 5.943 0.000 0.000 0.000 !FLAMEMASTER
C6H12OOH1-3O2 3 677.149 6.436 0.000 0.000 0.000 !FLAMEMASTER
C6H12OOH1-4 3 588.653 5.943 0.000 0.000 0.000 !FLAMEMASTER
C6H12OOH1-4O2 3 677.149 6.436 0.000 0.000 0.000 !FLAMEMASTER
C6H12OOH1-5 3 588.653 5.943 0.000 0.000 0.000 !FLAMEMASTER
C6H12OOH1-5O2 3 677.149 6.436 0.000 0.000 0.000 !FLAMEMASTER
C6H12OOH2-1 3 588.653 5.943 0.000 0.000 0.000 !FLAMEMASTER
C6H12OOH2-1O2 3 677.149 6.436 0.000 0.000 0.000 !FLAMEMASTER
C6H12OOH2-3 3 588.653 5.943 0.000 0.000 0.000 !FLAMEMASTER
C6H12OOH2-3O2 3 677.149 6.436 0.000 0.000 0.000 !FLAMEMASTER
C6H12OOH2-4 3 588.653 5.943 0.000 0.000 0.000 !FLAMEMASTER
C6H12OOH2-4O2 3 677.149 6.436 0.000 0.000 0.000 !FLAMEMASTER
C6H12OOH2-5 3 588.653 5.943 0.000 0.000 0.000 !FLAMEMASTER
```

C6H12OOH2-5O2 3 677.149 6.436 0.000 0.000 0.000 !FLAMEMASTER

C6H12OOH2-6 3 588.653 5.943 0.000 0.000 0.000 !FLAMEMASTER

C6H12OOH2-6O2 3 677.149 6.436 0.000 0.000 0.000 !FLAMEMASTER

C6H12OOH3-1 3 588.653 5.943 0.000 0.000 0.000 !FLAMEMASTER

C6H12OOH3-1O2 3 677.149 6.436 0.000 0.000 0.000 !FLAMEMASTER

C6H12OOH3-2 3 588.653 5.943 0.000 0.000 0.000 !FLAMEMASTER

C6H12OOH3-2O2 3 677.149 6.436 0.000 0.000 0.000 !FLAMEMASTER

C6H12OOH3-4 3 588.653 5.943 0.000 0.000 0.000 !FLAMEMASTER

C6H12OOH3-4O2 3 677.149 6.436 0.000 0.000 0.000 !FLAMEMASTER

C6H12OOH3-5 3 588.653 5.943 0.000 0.000 0.000 !FLAMEMASTER

C6H12OOH3-5O2 3 677.149 6.436 0.000 0.000 0.000 !FLAMEMASTER

C6H12OOH3-6 3 588.653 5.943 0.000 0.000 0.000 !FLAMEMASTER

C6H12OOH3-6O2 3 677.149 6.436 0.000 0.000 0.000 !FLAMEMASTER

C6H13-1 3 489.224 5.349 0.000 0.000 0.000 !FLAMEMASTER

C6H13-2 3 489.224 5.349 0.000 0.000 0.000 !FLAMEMASTER

C6H13-3 3 489.224 5.349 0.000 0.000 0.000 !FLAMEMASTER

C6H13O-1 3 540.597 5.662 0.000 0.000 0.000 !FLAMEMASTER

C6H13O-2 3 540.597 5.662 0.000 0.000 0.000 !FLAMEMASTER

C6H13O2-1 3 588.653 5.943 0.000 0.000 0.000 !FLAMEMASTER

C6H13O2-2 3 588.653 5.943 0.000 0.000 0.000 !FLAMEMASTER

C6H13O2-3 3 588.653 5.943 0.000 0.000 0.000 !FLAMEMASTER

C6H13O2H-1 3 591.585 5.960 0.000 0.000 0.000 !FLAMEMASTER

C6H13O2H-2 3 591.585 5.960 0.000 0.000 0.000 !FLAMEMASTER

C6H13O2H-3 3 591.585 5.960 0.000 0.000 0.000 !FLAMEMASTER

C6H13O-3 3 540.597 5.662 0.000 0.000 0.000 !FLAMEMASTER

CC4H8O 3 444.197 5.063 0.000 0.000 0.000 !FLAMEMASTER

CC5H10 3 437.102 5.017 0.000 0.000 0.000 !FLAMEMASTER

CC5H10OOH-A 3 546.691 5.698 0.000 0.000 0.000 !FLAMEMASTER

CC5H10OOH-AO2 3 639.455 6.230 0.000 0.000 0.000 !FLAMEMASTER

```
CC5H10OOH-B 3 546.691 5.698 0.000 0.000 0.000 !FLAMEMASTER
CC5H10OOH-BO2 3 639.455 6.230 0.000 0.000 0.000 !FLAMEMASTER
CC5H10OOH-D 3 546.691 5.698 0.000 0.000 0.000 !FLAMEMASTER
CC5H10OOH-DO2 3 639.455 6.230 0.000 0.000 0.000 !FLAMEMASTER
CC5H11 3 440.735 5.041 0.000 0.000 0.000 !FLAMEMASTER
CC5H11O2 3 546.691 5.698 0.000 0.000 0.000 !FLAMEMASTER
CC5H11O2H 3 549.783 5.717 0.000 0.000 0.000 !FLAMEMASTER
C-DC5H10O 3 492.434 5.369 0.000 0.000 0.000 !FLAMEMASTER
CH2CH2COCH3 3 440.584 5.040 0.000 0.000 0.000 !FLAMEMASTER
CH2CHOOHCOCH3 3 546.562 5.698 0.000 0.000 0.000 !FLAMEMASTER
CH3CHCHO 3 387.860 4.687 0.000 0.000 0.000 !FLAMEMASTER
CH3CHCOCH3 3 440.584 5.040 0.000 0.000 0.000 !FLAMEMASTER
CH3CHOOCOCH3 3 546.562 5.698 0.000 0.000 0.000 !FLAMEMASTER
CH3COCH2O 3 447.639 5.086 0.000 0.000 0.000 !FLAMEMASTER
CH3COCH2O2 3 502.115 5.429 0.000 0.000 0.000 !FLAMEMASTER
CH3COCH2O2H 3 505.403 5.449 0.000 0.000 0.000 !FLAMEMASTER
DC5H10OOH-A 3 546.691 5.698 0.000 0.000 0.000 !FLAMEMASTER
DC5H10OOH-AO2 3 639.455 6.230 0.000 0.000 0.000 !FLAMEMASTER
DC5H10OOH-B 3 546.691 5.698 0.000 0.000 0.000 !FLAMEMASTER
DC5H10OOH-BO2 3 639.455 6.230 0.000 0.000 0.000 !FLAMEMASTER
DC5H10OOH-C 3 546.691 5.698 0.000 0.000 0.000 !FLAMEMASTER
DC5H10OOH-CO2 3 639.455 6.230 0.000 0.000 0.000 !FLAMEMASTER
DC5H11 3 440.735 5.041 0.000 0.000 0.000 !FLAMEMASTER
DC5H11O2 3 546.691 5.698 0.000 0.000 0.000 !FLAMEMASTER
DC5H11O2H 3 549.783 5.717 0.000 0.000 0.000 !FLAMEMASTER
IC3H5COC2H4P 3 527.994 5.587 0.000 0.000 0.000 !FLAMEMASTER
IC3H5COC2H4S 3 527.994 5.587 0.000 0.000 0.000 !FLAMEMASTER
IC3H5COC2H5 3 531.165 5.606 0.000 0.000 0.000 !FLAMEMASTER
IC3H5COCH2 3 482.331 5.306 0.000 0.000 0.000 !FLAMEMASTER
```

```
IC3H5COCH3 3 485.716 5.327 0.000 0.000 0.000 !FLAMEMASTER
IC3H6CHCOCH2 3 527.994 5.587 0.000 0.000 0.000 !FLAMEMASTER
IC3H6CHCOCH3 3 531.165 5.606 0.000 0.000 0.000 !FLAMEMASTER
IC3H6COC2H3 3 527.994 5.587 0.000 0.000 0.000 !FLAMEMASTER
IC3H6COC2H5 3 534.323 5.625 0.000 0.000 0.000 !FLAMEMASTER
IC3H6COCH3 3 489.084 5.348 0.000 0.000 0.000 !FLAMEMASTER
IC3H7COC2H3 3 531.165 5.606 0.000 0.000 0.000 !FLAMEMASTER
IC3H7COC2H4P 3 534.323 5.625 0.000 0.000 0.000 !FLAMEMASTER
IC3H7COC2H4S 3 534.323 5.625 0.000 0.000 0.000 !FLAMEMASTER
IC3H7COC2H5 3 537.467 5.643 0.000 0.000 0.000 !FLAMEMASTER
IC3H7COCH2 3 489.084 5.348 0.000 0.000 0.000 !FLAMEMASTER
IC4H6Q2-II 3 597.176 5.992 0.000 0.000 0.000 !FLAMEMASTER
IC4H7-I1 3 380.022 4.633 0.000 0.000 0.000 !FLAMEMASTER
IC4H7OOH 3 498.949 5.410 0.000 0.000 0.000 !FLAMEMASTER
IC4H8O 3 444.197 5.063 0.000 0.000 0.000 !FLAMEMASTER
IC4H8OOH-I 3 502.252 5.430 0.000 0.000 0.000 !FLAMEMASTER
IC4H8OOH-IO2 3 600.078 6.009 0.000 0.000 0.000 !FLAMEMASTER
IC4H8OOH-T 3 502.252 5.430 0.000 0.000 0.000 !FLAMEMASTER
IC4H8OOH-TO2 3 600.078 6.009 0.000 0.000 0.000 !FLAMEMASTER
IC4H9O2 3 502.252 5.430 0.000 0.000 0.000 !FLAMEMASTER
IC4H9O2H 3 505.540 5.450 0.000 0.000 0.000 !FLAMEMASTER
IC4KETII 3 549.655 5.716 0.000 0.000 0.000 !FLAMEMASTER
IC4KETIT 3 549.655 5.716 0.000 0.000 0.000 !FLAMEMASTER
IC5KETAA 3 591.463 5.959 0.000 0.000 0.000 !FLAMEMASTER
IC5KETAB 3 591.463 5.959 0.000 0.000 0.000 !FLAMEMASTER
IC5KETAC 3 591.463 5.959 0.000 0.000 0.000 !FLAMEMASTER
IC5KETAD 3 591.463 5.959 0.000 0.000 0.000 !FLAMEMASTER
IC5KETCA 3 591.463 5.959 0.000 0.000 0.000 !FLAMEMASTER
IC5KETCB 3 591.463 5.959 0.000 0.000 0.000 !FLAMEMASTER
```

```
IC5KETCD 3 591.463 5.959 0.000 0.000 0.000 !FLAMEMASTER
IC5KETDA 3 591.463 5.959 0.000 0.000 0.000 !FLAMEMASTER
IC5KETDB 3 591.463 5.959 0.000 0.000 0.000 !FLAMEMASTER
IC5KETDC 3 591.463 5.959 0.000 0.000 0.000 !FLAMEMASTER
NC3H7COC2H4P 3 534.323 5.625 0.000 0.000 0.000 !FLAMEMASTER
NC3H7COC2H4S 3 534.323 5.625 0.000 0.000 0.000 !FLAMEMASTER
NC3H7COC2H5 3 537.467 5.643 0.000 0.000 0.000 !FLAMEMASTER
NC3H7COCH2 3 489.084 5.348 0.000 0.000 0.000 !FLAMEMASTER
NC4H9COCH2 3 534.323 5.625 0.000 0.000 0.000 !FLAMEMASTER
NC4H9COCH3 3 537.467 5.643 0.000 0.000 0.000 !FLAMEMASTER
NEO-C5H10O 3 492.434 5.369 0.000 0.000 0.000 !FLAMEMASTER
NEOC5H10OOH 3 546.691 5.698 0.000 0.000 0.000 !FLAMEMASTER
NEOC5H10OOH-O2 3 639.455 6.230 0.000 0.000 0.000 !FLAMEMASTER
NEOC5H11 3 440.735 5.041 0.000 0.000 0.000 !FLAMEMASTER
NEOC5H11O 3 495.769 5.390 0.000 0.000 0.000 !FLAMEMASTER
NEOC5H11O2 3 546.691 5.698 0.000 0.000 0.000 !FLAMEMASTER
NEOC5H11O2H 3 549.783 5.717 0.000 0.000 0.000 !FLAMEMASTER
NEOC5H12 3 444.347 5.064 0.000 0.000 0.000 !FLAMEMASTER
NEOC5H9Q2 3 639.455 6.230 0.000 0.000 0.000 !FLAMEMASTER
NEOC5H9Q2-N 3 639.455 6.230 0.000 0.000 0.000 !FLAMEMASTER
NEOC5KEJOL 3 540.467 5.661 0.000 0.000 0.000 !FLAMEMASTER
NEOC5KET 3 591.463 5.959 0.000 0.000 0.000 !FLAMEMASTER
NEOC5KETOX 3 540.467 5.661 0.000 0.000 0.000 !FLAMEMASTER
O2C4H8CHO 3 588.531 5.942 0.000 0.000 0.000 !FLAMEMASTER
O2HC4H8CO 3 588.531 5.942 0.000 0.000 0.000 !FLAMEMASTER
SC3H5COCH2 3 482.331 5.306 0.000 0.000 0.000 !FLAMEMASTER
TC3H6COC2H3 3 527.994 5.587 0.000 0.000 0.000 !FLAMEMASTER
TC3H6COC2H5 3 534.323 5.625 0.000 0.000 0.000 !FLAMEMASTER
TC3H6COCH3 3 489.084 5.348 0.000 0.000 0.000 !FLAMEMASTER
```

```
TC4H8CHO 3 489.084 5.348 0.000 0.000 0.000 !FLAMEMASTER
TC4H8OOH-I 3 502.252 5.430 0.000 0.000 0.000 !FLAMEMASTER
TC4H8OOH-IO2 3 600.078 6.009 0.000 0.000 0.000 !FLAMEMASTER
TC4H9O2 3 502.252 5.430 0.000 0.000 0.000 !FLAMEMASTER
TC4H9O2H 3 505.540 5.450 0.000 0.000 0.000 !FLAMEMASTER
JP10 3 642.441 6.246 0.000 0.000 0.000 !FLAMEMASTER
C2H5OH 2 470.600 4.410 0.000 0.000 1.500 ! NMM
CH3CHOH 2 362.600 4.530 0.000 0.000 1.500 ! MI
CH3CH2O 2 470.600 4.410 0.000 0.000 1.500 ! NMM !JLI_MV
HOC2H4O2 2 523.2 5.664 1.7 0.0 1.0 ! WJP !JLI_MV
CH2CH2OH 2 362.600 4.530 0.000 0.000 1.500 ! MI
C2H4OH 2 362.600 4.530 0.000 0.000 1.500 ! MI
C3H6OOH 2 487.900 4.820 0.000 0.000 1.000 !adopted from MI
OC3H5OOH 2 487.900 4.820 0.000 0.000 1.000
C2H4OOH 2 470.600 4.410 0.000 0.000 1.500
OC2H3OOH 2 470.600 4.410 0.000 0.000 1.500
NC7H15 2 459.980 6.310 0.000 0.000 1.000 !Ranzi
C7H14 2 459.980 6.310 0.000 0.000 1.000 !Ranzi
NC7-QOOH 2 561.000 6.317 1.700 0.000 1.000 !WJP
NC7-OQOOH 2 581.300 6.506 2.000 0.000 1.000 !1c8h17oh wjp
CH3OCH3 2 329.400 4.624 0.000 0.000 1.000 !loc_est
CH3OCH2 2 329.400 4.624 0.000 0.000 1.000 !=CH3OCH3
CH3OCH2O2 2 329.400 4.624 0.000 0.000 1.000 !=CH3OCH3
CH2OCH2O2H 2 329.400 4.624 0.000 0.000 1.000 !=CH3OCH3
CH3OCH2O2H 2 329.400 4.624 0.000 0.000 1.000 !=CH3OCH3
HO2CH2OCHO 2 329.400 4.624 0.000 0.000 1.000 !=CH3OCH3
O2CH2OCH2O2H 2 329.400 4.624 0.000 0.000 1.000 !=CH3OCH3
HOCHO 2 470.600 4.410 0.000 0.000 1.500
OCH2OCHO 2 329.400 4.624 0.000 0.000 1.000 !=CH3OCH3
```

```
CH3OCHO 2 406.500 4.709 0.000 0.000 1.000 !loc_est
CH3OCH2OH 2 329.400 4.624 0.000 0.000 1.000 !=CH3OCH3
CH3OCH2O2H 2 329.400 4.624 0.000 0.000 1.000 !=CH3OCH3
CH3OCH2O 2 470.900 4.862 0.000 0.000 1.000 !loc_est
CH3OCO 2 406.500 4.709 0.000 0.000 1.000 !=CH3OCHO
HCOOH 2 470.600 4.410 0.000 0.000 1.500 !ZHAO
HOCH2OCO 2 329.400 4.624 0.000 0.000 1.000 !=CH3OCH3
CH* 1 80.000 2.750 0.000 0.000 0.000
OH* 1 80.000 2.750 0.000 0.000 0.000
H3O+ 2 572.4 2.605 1.844 0.897 4.0
HCO+ 2 498.000 3.590 0.000 1.356 0.000
CH5O+ 2 107.4 3.458 0.0 2.462 1.0
C2H3O+ 2 436.0 3.97 0.0 3.141 2.0
O2- 1 107.400 3.458 0.000 1.424 3.800
OH- 1 80.0 2.75 0.0 1.258 0.0
O- 0 80.000 2.750 0.000 0.482 0.000
CHO2- 2 436.0 3.97 0.0 3.345 2.0
CO3- 2 481.800 3.626 1.700 3.620 1.000
CHO3- 2 481.800 3.626 1.700 3.712 1.000
E 0 850. 425. 0.000 0.000 1.000 !(singh)
END
```

Appendix G

Effect of the temperature boundary condition at the burner walls in 2D simulations.

Since the flame may transfer heat to the burner, causing an increase in the burner temperature, the temperature boundary condition applied at the burner walls is tested. Hence, two identical simulations are run with the only difference that the temperature boundary condition at the burner walls is set at 300K and 400K, respectively. Both simulations use Model 1 chemistry and are for the extruded burner at 1g and without electric field, with the inlet fuel flow set at 20mL/min.

Figure G.1 shows the profiles of the normalized CH^* with the corresponding contours at 0.05. Undoubtedly, an increase of 100K at the burner wall makes the region closer to the burner to be heated up, and therefore, the chemistry pathways activated in that region are different than when the burner temperature is set to be at 300K.

When the burner wall temperature is set to 400K, the CH^* is placed closer to the burner. However, it is improbable that the flame will heat up the burner's temperature by 100K. Even more unlikely,

the whole burner wall will be at 400K in all its points; instead, the burner wall temperature will be distributed from high temperatures to lower temperatures as the wall zone is further from the flame.

In conclusion, the flame heating the burner can change the flame chemistry itself, leading to changes in the flame location, especially at the region closer to the burner tip. However, for a short time experiments as the ones used for the comparisons employed in this work, the heating of the burner is not expected to be increasing the burner wall temperature by 100K, and therefore, the flame is not expected to change noticeably due to the flame itself heating the burner.

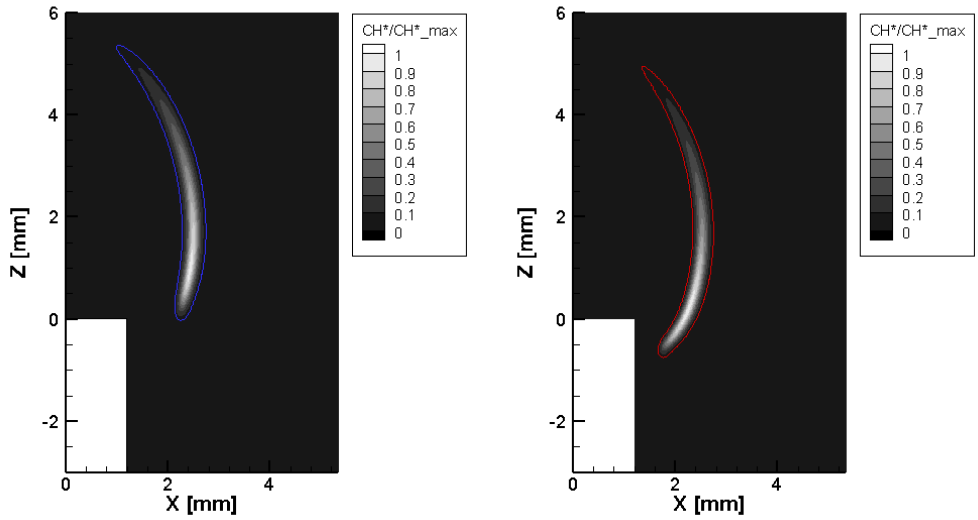

(a) T_{burner} = 300K

(b) T_{burner} = 400K

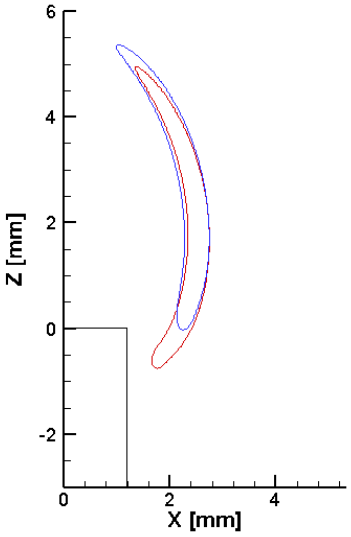

(c) T_{burner} = 300 (blue), 400K (black)

Figure G.1: Effect of temperature boundary condition at the burner wall. Extruded burner geometry at 1g without electric field applied. Q_{fuel}=20mL/min.